TU/e EINDHOVEN UNIVERSITY OF TECHNOLOGY

Hydrogen storage in Mg-Ti thin film alloys : an in situ characterization study

Citation for published version (APA):
Vermeulen, P. (2009). *Hydrogen storage in Mg-Ti thin film alloys : an in situ characterization study*. [Phd Thesis 1 (Research TU/e / Graduation TU/e), Chemical Engineering and Chemistry]. Technische Universiteit Eindhoven. https://doi.org/10.6100/IR641658

DOI:
10.6100/IR641658

Document status and date:
Published: 01/01/2009

Document Version:
Publisher's PDF, also known as Version of Record (includes final page, issue and volume numbers)

Please check the document version of this publication:

• A submitted manuscript is the version of the article upon submission and before peer-review. There can be important differences between the submitted version and the official published version of record. People interested in the research are advised to contact the author for the final version of the publication, or visit the DOI to the publisher's website.
• The final author version and the galley proof are versions of the publication after peer review.
• The final published version features the final layout of the paper including the volume, issue and page numbers.

Link to publication

General rights
Copyright and moral rights for the publications made accessible in the public portal are retained by the authors and/or other copyright owners and it is a condition of accessing publications that users recognise and abide by the legal requirements associated with these rights.

• Users may download and print one copy of any publication from the public portal for the purpose of private study or research.
• You may not further distribute the material or use it for any profit-making activity or commercial gain
• You may freely distribute the URL identifying the publication in the public portal.

If the publication is distributed under the terms of Article 25fa of the Dutch Copyright Act, indicated by the "Taverne" license above, please follow below link for the End User Agreement:

www.tue.nl/taverne

Take down policy
If you believe that this document breaches copyright please contact us at:

openaccess@tue.nl

providing details and we will investigate your claim.

Download date: 17. Nov. 2023

Hydrogen storage in Mg-Ti thin film alloys

An *in situ* characterization study

Paul Vermeulen

Samenstelling van de promotiecommissie:

prof.dr. P.J. Lemstra	Technische Universiteit Eindhoven, *voorzitter*
prof.dr. P.H.L. Notten	Technische Universiteit Eindhoven, *promotor* Philips Research Laboratories
dr. H.T.J.M. Hintzen	Technische Universiteit Eindhoven, *copromotor*
prof.dr. J.J. Kelly	Universiteit Utrecht
prof.dr. J.J.C. Geerlings	Technische Universiteit Delft
prof.dr R.A. van Santen	Technische Universiteit Eindhoven
prof.dr. R.P. Griessen	Vrije Universiteit Amsterdam
dr. B.A. Boukamp	Technische Universiteit Twente

A catalogue record is available from the Eindhoven University of Technology Library

ISBN: 978-90-386-1632-2

Copyright © 2009 by Paul Vermeulen

The research described in this thesis has been financially supported by NWO within the framework of the Sustainable Hydrogen Program of Active Chemical Technologies for Sustainability (ACTS)

Cover design: Jeroen Kooij

Printed by: Van Son Media, Son

Hydrogen storage in Mg-Ti thin film alloys
An *in situ* characterization study

PROEFSCHRIFT

ter verkrijging van de graad van doctor aan de
Technische Universiteit Eindhoven, op gezag van de
Rector Magnificus, prof.dr.ir. C.J. van Duijn, voor een
commissie aangewezen door het College voor
Promoties in het openbaar te verdedigen op
dinsdag 31 maart 2009 om 16.00 uur

door

Paul Vermeulen

geboren te Eindhoven

Dit proefschrift is goedgekeurd door de promotor:

prof.dr. P.H.L. Notten

Copromotor:
dr. H.T.J.M. Hintzen

Aan mijn grootouders

Table of Contents

1 Introduction 1

1.1 The hydrogen economy 1

1.2 Other applications of metal hydrides 4

1.3 Recent progress in Mg-based alloys 5

1.4 Scope 8

1.5 References 9

2 Experimental 13

2.1 Introduction 14

2.2 Thin film deposition and characterization 14

2.3 Electrochemical characterization 16

2.3.1 Background 16
2.3.2 The electrochemical setup 19
2.3.3 Galvanostatic control 23
2.3.4 GITT charging and discharging 24
2.3.5 Amperometry and cyclic voltammetry 26
2.3.6 Electrochemical impedance spectroscopy 27

2.4 X-ray Diffraction 33

2.4.1 Background 33
2.4.2 Grain size 34
2.4.3 Texture formation 35
2.4.4 *In situ* electrochemical X-ray diffraction 36

2.5 References 38

3 Hydrogen storage in Pd thin films 41

3.1 Introduction 42

3.2 Results & discussion 42

3.2.1 Thermodynamics of Pd hydride thin film electrodes 42
3.2.2 Kinetics of Pd hydride thin film electrodes 49

3.3 Conclusions 53

3.4 References 54

4 Electrochemical hydrogen storage in thin film Mg_yTi_{1-y} alloys 57

4.1 Introduction 58

4.2 Results & discussion 58

4.2.1 Structural characterization of the as-prepared thin films 59

4.2.2 Galvanostatic (dis)charging behavior 61

4.2.3 Thermodynamics and kinetics 67

4.2.4 Effects of the deposition technique 84

4.3 Conclusions 90

4.4 References 92

5 *In situ* XRD study of $MgyTi_{1-y}$ alloys 97

5.1 Introduction 98

5.3 Results & discussion 99

5.3.1 Structural characterization via *in situ* XRD gas loading 99

5.3.2 Structural characterization using *in situ* electrochemical XRD 107

5.4 Conclusions 118

5.5 References 119

6 Hydrogen storage in ternary MgTiX alloys 121

6.1 Introduction 122

6.2 Results & discussion 122

6.2.1 The Miedema model 123

6.2.2 Thermodynamics of MgTiX hydride thin film electrodes 124

6.3 Conclusions 129

6.4 References 129

Summary 131

Samenvatting 135

List of publications 141

Curriculum Vitae 143

Dankwoord 145

1
Introduction

1.1 The hydrogen economy

Depleting fossil fuel reserves and growing climate threats urge us towards a sustainable society.[1] The results of the annual assessment by BP of the fossil fuel reserves-to-production ratio is depicted in Fig. 1.1 and show that the oil and natural gas reserves will run out in a couple of decades.[2] Although coals will be available for a somewhat longer period of time, it will inevitably become scarcer in the near future. Another important reason why we should preferably not solely rely on fossil fuels for our future energy needs is that part of the fossil fuels are imported from politically unstable regions. We should therefore think of new ways to ensure our energy needs in the near future. These resources should preferable be renewable in nature, *e.g.* solar, biomass, wind, water and geothermal, and can typically be used for stationary applications.

For mobile applications, like a fuel-cell driven vehicle, however, the use of an on-board energy system is indispensible. Hydrogen is expected to play a dominant role in future energy scenarios.[3,4] One of the important aspects of hydrogen is that only environmentally friendly combustion products are emitted in the exothermic reaction of hydrogen with oxygen or when hydrogen is oxidized in a fuel cell. However, the feasibility of hydrogen production, storage and the consumption are still under debate.

Hydrogen is usually produced by steam reforming of fossil fuels, by partial oxidation of natural gas or by coal gasification. These methods, however, still rely on fossil fuels and therefore do not address the problems related to our declining energy sources. An alternative method to generate hydrogen is by electrolysis of water, but it is generally considered to be inefficient. Other techniques to produce hydrogen include high-temperature electrolysis, which can increase the efficiency significantly, and hydrogen generation by chemical reactions of certain algae (*e.g. Scenedesmus*).[5,6]

In prototype fuel cell-driven vehicles, hydrogen is generally stored in high-pressure cylinders to increase the density of hydrogen as much as possible. New lightweight composite cylinders have been developed which are able to withstand pressures of up to 800 bars. Even though hydrogen cylinders are expected to withstand even higher pressures in the near future, their large volumes and the energy required to compress hydrogen will limit their

practical applicability. A way to increase the density of hydrogen to 70 kg/m^3 is to liquefy it under cryogenic conditions. A significant increase of the density and a strong reduction of the necessary volume for a certain amount of hydrogen can be achieved by storing hydrogen atomically in a metal, forming a metal hydride (MH). In addition, MHs provide relatively safe storage as they can be handled without extensive safety precautions unlike, for example, compressed hydrogen gas.

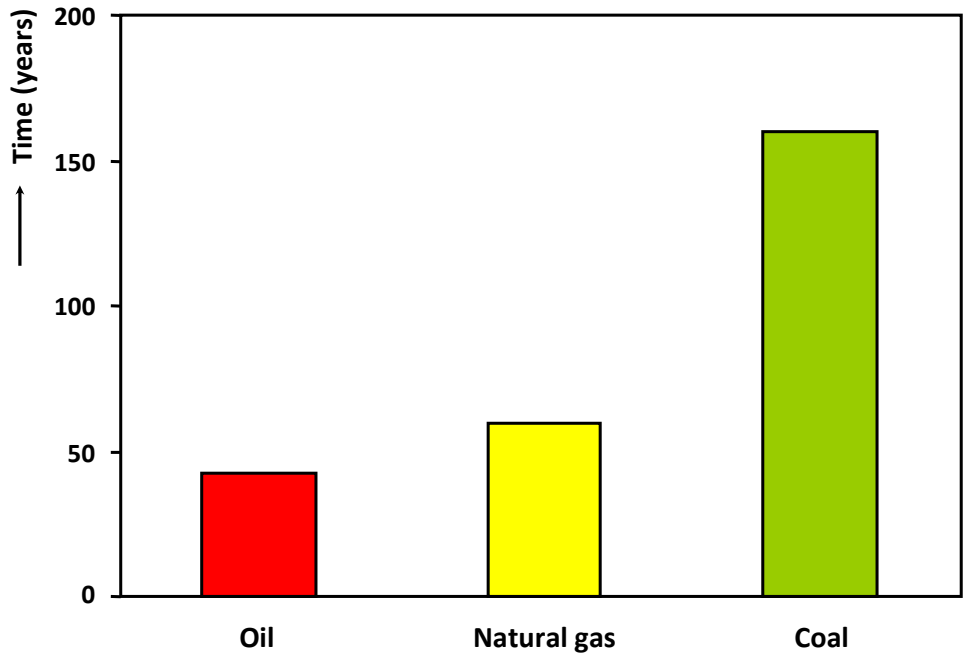

Fig. 1.1 Fossil fuel reserves-to-production ratios at the end of 2006. Data are compiled from Ref. 2.

Table 1.1 lists the technical requirements for an on-board hydrogen storage system as determined by the U.S. Department of Energy. Currently, the foremost problem of solid state storage is to find a metal-hydrogen system with a gravimetric capacity that exceeds 6 wt.% H and absorbs/desorbs hydrogen at atmospheric pressures at slightly elevated or ambient temperatures.[7]

Table 1.1 U.S. Department of Energy Technical Targets: On-Board Hydrogen Storage Systems.[7]

Storage Parameter	Deadline: 2010
Gravimetric capacity	At least 6 wt.%
Fill time (5 kg H_2)	Within 3 minutes
Volumetric capacity	45 kg m^{-3}
Equilibrium pressure	~1 bar @ 353 K
Cycle life	>1000
Storage System Cost	$ 133

In Fig. 1.2 the most common hydrides of the elements are listed, which can be found in the reports of Griessen *et al.* and Huheey.[8,9] The different colors indicate the difference in the nature of the bond between the element and hydrogen going from a high degree of ionic bonding character for groups *I* and *II* (alkali metals and alkaline earth metals) to covalently

bonding for the elements in groups *XIV* to *XVII*. The bond to hydrogen for the elements in groups *III* to *X* (transition metals, lanthanides and actinides) strongly depends on the element, however, many are interstitial in nature. Finally, the hydrogen bonding character to the elements in groups *XI* to *XIII* is covalent and these hydrides are elusive species and some polymerize. The values below the hydride compositions in Fig. 1.2 correspond to the gravimetric capacity.

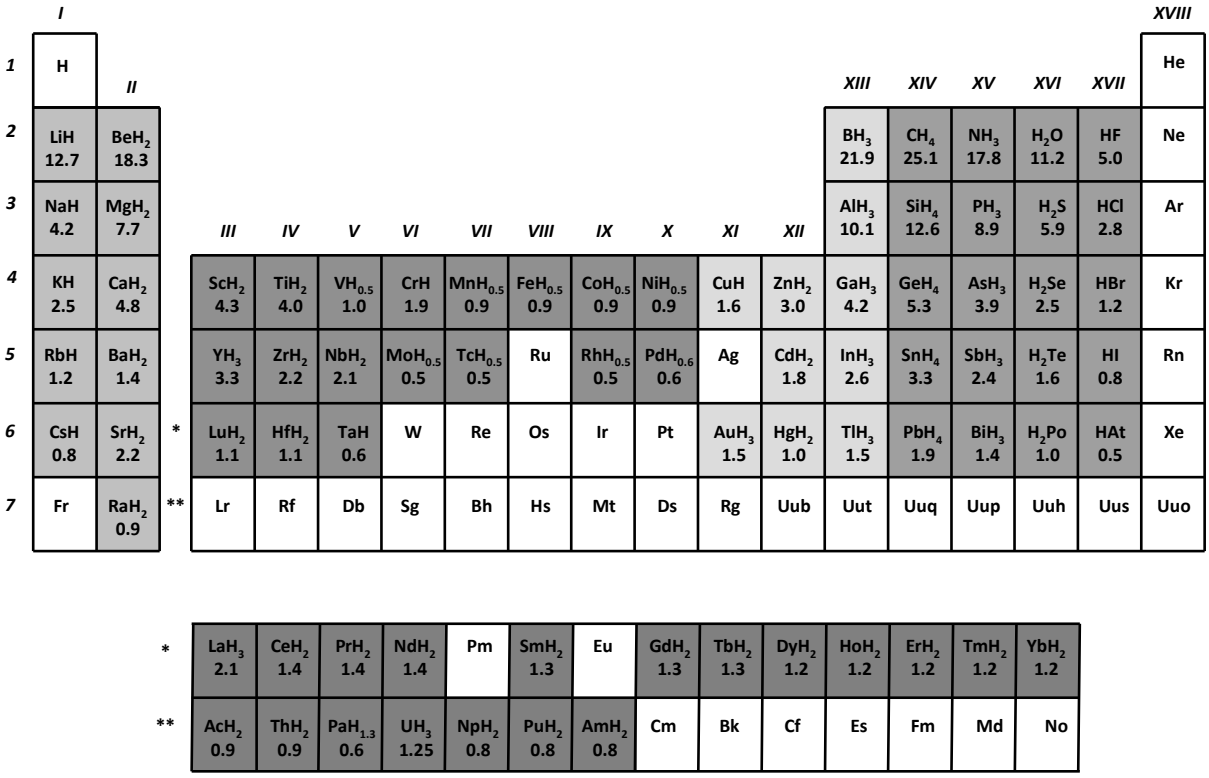

Fig. 1.2 Periodic table of elements with per element the most common hydrides and corresponding gravimetric capacity in wt.% H. Data have been compiled from Refs. 8 and 9.

Based on the weight constraints for on-board hydrogen storage systems, most of the elements presented in Fig. 1.2 are not particularly suitable as effective hydrogen storage medium. Hence, only the lightweight elements that can store a significant amount of hydrogen are of prime interest. Also, the phase of the hydride is important as it has a profound effect on the volumetric capacity. For example, CH_4 is a gas at ambient temperatures, which will lower the volumetric capacity significantly as compared to storing hydrogen in a solid. In this respect, Mg is one of the most promising elements as it exhibits a high gravimetric storage capacity of 7.7 wt.% of hydrogen and a high volumetric capacity of 110 kg/m^3.[10,11] In spite of its excellent storage capacity, the high desorption temperature (279 °C) and extremely slow hydrogen (de)sorption kinetics prevent Mg from being employed commercially.[12] It is generally accepted that the formation of a MgH_2 layer blocks further hydrogen diffusion, effectively decreasing the high storage capacity.[13-22]

In spite of its apparent drawbacks Mg is often a large constituent of new hydrogen storage materials as it enhances the gravimetric capacity. The properties of these systems, however,

should not be influenced too much by the poor diffusion properties of Mg and a fine line between hampered Mg-like behavior and enhanced properties is often found.

1.2 Other applications of metal hydrides

Large scale application of metal hydrides as solid state hydrogen storage medium for the hydrogen economy is by no means the only possibility to commercialize metal hydrides. In this paragraph an overview is given of some other types of utilization of metal hydrides.

Rechargeable batteries

An application of solid state hydrogen storage, which is already used on a large scale, is as anode material in rechargeable Nickel Metal-Hydride (NiMH) batteries. For a detailed description of this battery see paragraph 2.3.1. A metal hydride electrode was used primarily to replace the Cd-electrode in widely used Ni-Cd batteries, for which the obvious reason was to replace toxic Cd. Other advantages of a MH electrode instead of a Cd electrode include higher (dis)charge rates, a 50% higher capacity and the absence of a memory effect.[23,24] The hydrogen storage alloy currently used in NiMH batteries is a MischMetal-based $LaNi_5$ compound. Much research effort is still aimed at improving properties of this electrode material, such as corrosion resistance, rate-capability and reversible hydrogen storage capacity.[25-27] Yet, the gravimetric capacity is nowadays in the order of 1.2 wt.% H and it is not expected to rise significantly, simply because the intrinsic capacity is not much higher. In spite of their low gravimetric capacity, large NiMH packs are nowadays used in hybrid electric vehicles, like the well-known Toyota Prius and Honda Civic Hybid. Large scale implementation of NiMH will of course benefit from improving the gravimetric capacity of the anode. But also small electronic devices, such as mobile phones, personal digital assistants and navigation systems, that are nowadays mainly powered by Li-ion batteries might benefit from improving the capacity of the NiMH battery. Replacing Li-ion batteries is preferable as these batteries require expensive special safety equipment that prevents over(dis)charging the battery, whereas NiMH batteries do not require any special safety equipment.

Gas purification and (isotope) separation & reversible gettering

Metal hydrides can be used as membranes to separate H_2 from other gaseous compounds or to purify H_2. This can be achieved by, for example, employing PdAg alloy membranes, which is permeable to hydrogen, but not (in any reasonable length of time) to other gases. Metal hydrides do not only absorb hydrogen, but also deuterium (D) and tritium (T). The properties change according to the absorbing/desorbing species, which can effectively be exploited to separate the isotopes. Requirements for the MH system are fast kinetics, ease of activation, resistance to impurities, reaction efficiency, stability, durability and safety.

Another application of metal hydrides is as reversible getter in vacuum systems, which can be employed to remove trance amounts of H_2. The foremost requirements for the metal hydrogen system in this application are a low pressure, fast kinetics, ease of activation, pumping speed and durability.

Electrochromic windows and hydrogen sensors

The optical switching behavior of rare earth metals (Y and La) as a function of hydrogen content was first reported in 1996.[28] Soon after this discovery it was realized that an interesting field of new futuristic applications could be exploited with these switchable mirrors, ranging from smart windows and optical shutters to active displays. In many cases gas phase switching is not the most attractive one, especially, when a highly reactive gas, such as hydrogen, is involved. It is therefore much more attractive to use devices that are electronically driven. The concept of electrochemical switching has been investigated thoroughly for so-called inorganic electrochromic electrode materials by Grundvist.[29] Notten *et al.* investigated the electro-optical properties of rare earth (RE) thin films, which has the advantage over gas phase loading that the hydrogen concentration can be carefully controlled by the electrical current.[30] A disadvantage of these films is that their trihydrides are colored, while, from an application point-of view, transparent films are desirable. Van de Sluis *et al.* reported that alloying Gd, Sm, Lu, Y with Mg allows one to control both the film transmission and reflectivity properties.[31]

The next generation of switchable mirrors started with the study of Richardson and co-workers on Mg-transition metal (TM) alloys, revealing that the optical switching behavior of alloys of Mg and Ni is similar as found for Mg-RE alloys.[32,33] Hereafter it was shown that alloys of Mg and Co, Fe, Mn and V also switch as a function of hydrogen content.[34]

Recently, Niessen *et al.* showed that alloys that consist of elements that are immiscible with Mg, like Ti, V and Cr, can be prepared via a thin film approach.[35] These compounds are capable of absorbing a substantial amount of hydrogen. Moreover, the hydrogen content in these materials strongly affects the optical properties, which can, for instance, be exploited in hydrogen sensor applications, smart solar collectors or switchable mirrors.[36-40]

1.3 Recent progress in Mg-based alloys

In paragraph 1.1 it was pointed out that Mg is a promising element for hydrogen storage since MgH_2 has a gravimetric capacity of 7.7 wt.% H.[10] Mg is also cheap and readily available and has a medium reactivity towards air and oxygen, which is an advantage over most other lightweight metal hydrides.[41,42] However, a major impediment toward practical applications is the high thermodynamic stability of MgH_2 and the slow diffusion of hydrogen through the hydride layer, which effectively blocks hydrogen.[13-22]

Unfortunately, the history of enhancing the thermodynamics of MgH_2 to an appreciable degree is quite dismal. Among the improvements is Mg_2Ni that enables 1 bar H_2 pressure at 255°C, which is only 24°C lower compared to MgH_2.[43,44] Wagemans *et al.* showed that the hydrogen storage properties of Mg can be enhanced by decreasing the particle size of the crystallites.[45] They calculated that decreasing the grain size of magnesium hydride below approximately 1.3 nm results in a substantial decrease of the hydrogen desorption enthalpy. For these small Mg particles the hydrogen diffusion rate is of minor importance as the diffusion lengths are short.

Ouwerkerk showed that the hydrogen diffusion rate in Mg can be improved significantly by alloying Mg with Sm.[46] This work was based on the results of Cui *et al.* who reported on the kinetics of Mg-based alloys that was significantly enhanced by the addition of yttrium, which is chemically a kin to the rare earth element samarium.[47] In line with these results, a

systematic study by Van der Sluis *et al.* revealed that thin layers of magnesium can reversibly absorb and desorb hydrogen provided that they contain Gd, Sm, Lu or Y, whereas pure Mg did not absorb any appreciable amount.[31,48]

Sc, also a rare earth element, was alloyed with Mg by Notten and co-workers and it was shown that again the binary alloys reveal excellent sorption kinetics.[49-52] It was argued that fast kinetics was due to a face centered cubic (fcc) structure of the hydride, whereas the Mg_ySc_{1-y} alloys with slow kinetics revealed the body centered tetragonal (bct) MgH_2 structure. The $Mg_{0.80}Sc_{0.20}$ composition revealed excellent kinetic properties and the highest reversible hydrogen capacity of 6.7 wt.% of H. The high costs of Sc, however, prevent Mg_ySc_{1-y} alloys from being employed commercially as hydrogen storage medium.

In view of the gravimetric capacity promising substitutes for Sc should preferably be lightweight and in order to tune the properties of the magnesium-hydrogen system, it is desirable that the elements show a wide spread in hydrogen storage properties. To limit the gravimetric capacity loss by substituting a heavier element for Sc, the first row transition metals are most promising (see Fig. 1.2). Ti, V and Cr would be exceptionally suitable, as these elements not only have a reasonably high gravimetric capacity, but also form a fcc-structure hydride. This latter property might be advantageous as $Mg_ySc_{1-y}H_x$ with a fcc-symmetry revealed a high hydrogen diffusion rate. The thermodynamic properties of the hydrides of Sc, Ti, V and Cr are listed, together with the data of MgH_2, in Table 1.2.

Table 1.2 Thermodynamic properties of several metal hydrides.[8]

Metal-hydrogen system	Enthalpy of formation (kJ/mol H)	Gravimetric capacity (wt.% H)
ScH_2	-100	4.3
TiH_2	-68	4.0
V_2H	-42	1.0
CrH	-6	1.9
MgH_2	-37	7.7

Unfortunately, Ti, V and Cr are immiscible with Mg and alloys can therefore not be prepared by conventional methods.[53] As an example the phase diagram of Mg and Ti is shown in Fig. 1.3. To enforce alloying of Mg with Ti, V or Cr a complex anvil-cell technique was used to prepare hydrides of these Mg-based alloys, which required extreme temperatures and pressures and yielded Mg_7TiH_x, Mg_6VH_x and Mg_3CrH_x.[54-56] Although the complexity of the anvil-cell technique is very high and the conditions applied very extreme, it shows that crystalline MgX hydrides (X = Ti, V, Cr) can exist in bulk form. Until now, only a few researchers have tried to synthesize and characterize the same compounds via a thin film approach.

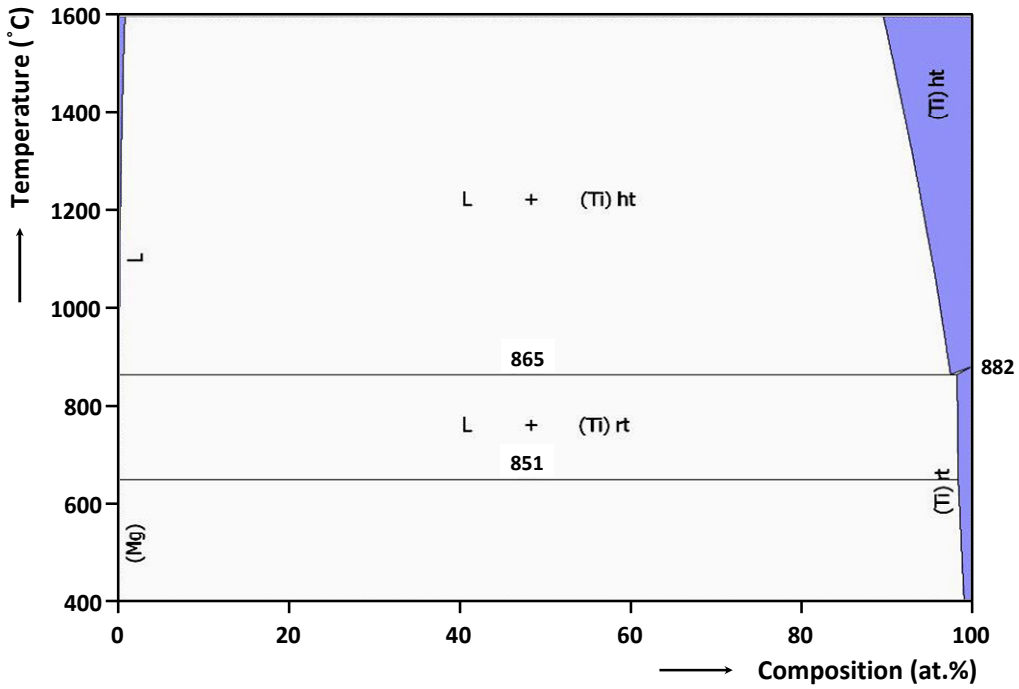

Fig. 1.3 Binary phase diagram of Mg and Ti.

Mitchell *et al.* studied MgTi thin film alloys processed by physical vapor deposition. The main focus of these new systems was to increase the corrosion resistance of Mg by introducing a solute element (Ti), which should selectively oxidize.[57] For hydrogen storage and switchable mirror applications, Richardson *et al.* synthesized binary Mg_yTi_{1-y} thin films by means of dc magnetron sputtering.[58] XRD results indicated that the as-deposited films were X-ray amorphous. In addition, no information about the stoichiometry of the hydride was given. Using the same deposition technique, Farangis and co-workers performed Extended X-ray Absorption Fine Structure (EXAFS) measurements on $Mg_{0.73}Ti_{0.27}$ and $Mg_{0.84}Ti_{0.16}$ thin films.[59] The results revealed that there was no alloy formation in the metallic state and that the hydrides were present as distinct binary phases. Niessen *et al.* recently reported that crystalline single-phase thin film $Mg_{0.80}X_{0.20}$ alloys with X=Sc, Ti, V or Cr could be prepared by electron beam evaporation.[35] The results implied that, at a first glance, alloy formation of Mg and Ti, V or Cr was achieved. In this study, the alloys were electrochemically hydrogenated using a current of -0.6 mA (~5000 mA/g) until hydrogen gas evolved at the surface of the electrode. Hereafter, the metal hydrides were dehydrogenated using firstly a discharge current of +0.12 mA (~1000 mA/g) and secondly a so-called deep-discharging current of +0.012 mA (~100 mA/g). The reversible hydrogen storage capacities for the alloys are depicted in Fig. 1.4.

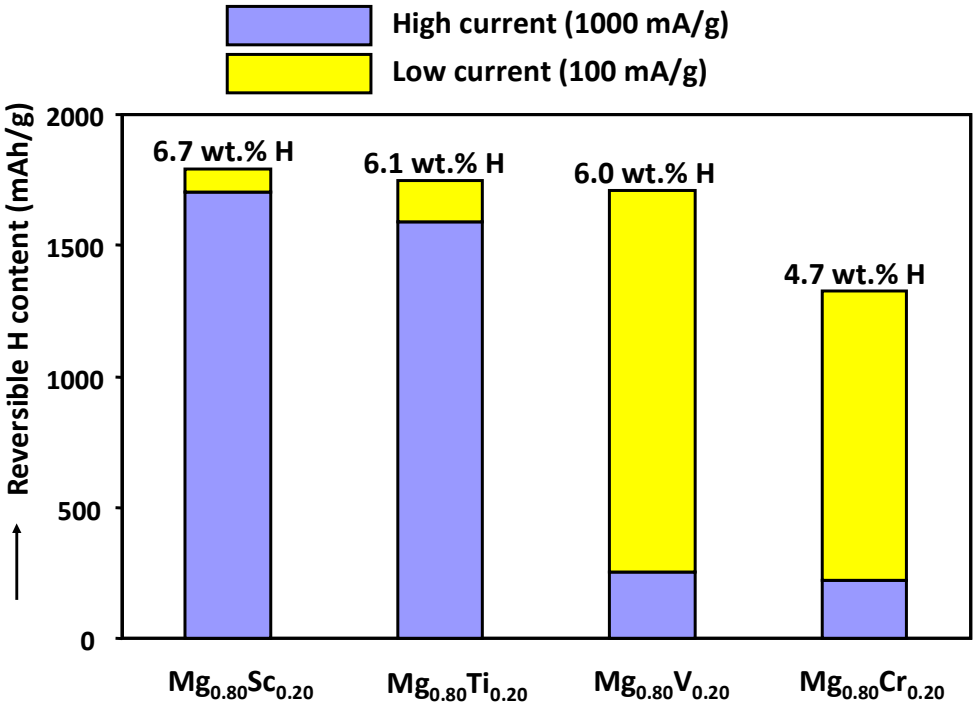

Fig. 1.4 Dehydrogenation capacities of $Mg_{0.80}Sc_{0.20}$, $Mg_{0.80}Ti_{0.20}$, $Mg_{0.80}V_{0.20}$ and $Mg_{0.80}Cr_{0.20}$ obtained by discharging the hydrogenated films at a high current (1000 mA/g) and subsequently a low current (100 mA/g). Reproduced from the data presented in Ref. 35.

Except for the $Mg_{0.80}Cr_{0.20}$ alloy, the results in Fig. 1.4 show that all alloys satisfy the requirement set by the US Department of Energy (see Table 1.1). Although the $Mg_{0.80}V_{0.20}$ has a reasonable high reversible hydrogen storage capacity, the measurements show that most of the absorbed hydrogen atoms can be released only at a low rate, whereas a substantial part of the hydrogen atoms absorbed by the $Mg_{0.80}Sc_{0.20}$ and $Mg_{0.80}Ti_{0.20}$ can be released at a high rate. From Fig. 1.4 it can therefore be concluded that only the $Mg_{0.80}Ti_{0.20}$ behaves similar to $Mg_{0.80}Sc_{0.20}$ and the magnesium-titanium system is therefore subject to an in-depth study and is presented in this thesis.

1.4 Scope

The general scope of this thesis is to characterize lightweight Mg-based materials to find new opportunities in the field of solid state hydrogen storage.

Chapter 2 describes the theory of gas phase and electrochemical hydrogen storage. It also shows how metal hydrides are employed on a large scale in rechargeable Nickel Metal-Hydride (NiMH) batteries. The electrochemical setup is discussed in detail together with several electrochemical techniques, for example, amperometry and electrochemical impedance spectroscopy. Special attention is paid to the pitfalls of electrochemical hydrogen storage analyses. Also, X-ray diffraction (XRD) is explained as it is used throughout this thesis to characterize the phases of the materials.

Chapter 3 deals with the electrochemical behavior of Pd thin films, which are often used as a topcoat of Mg-based thin films to prevent them from oxidation, to promote hydrogen

uptake from a H_2 gas phase and to electrocatalyze the reduction of water. Therefore, it is particularly interesting to determine the properties of Pd films to understand how these influence the total system. Moreover, the palladium-hydrogen system is one of the most thoroughly investigated metal hydrides, making it a perfect candidate to use the data for a recently developed Lattice Gas Model (LGM).[60]

In the next chapter, the effects of the Mg-to-Ti ratio in thin film Mg_yTi_{1-y} alloys are determined. Firstly, the crystallography properties of the as-prepared state are investigated by XRD. Secondly, the impact of the alloy composition on the hydrogen storage properties is determined by electrochemical measurements.

In chapter 5 the crystal structure of both the as-prepared state and hydrogenated under 1 bar H_2 is examined. To monitor the crystallographic changes as a function of hydrogen content, X-ray diffraction experiments were performed *in situ* under electrochemical control.

Chapter 6 takes the development of new lightweight Mg-based thin film systems a step further by incorporating not only Ti, but also a third element like Al and Si. The pronounced effects of adding a third element to the thermodynamics of the metal-hydrogen system are described in detail.

1.5 References

1 F.E. Pinkerton and B.G. Wicke, *Bottling the hydrogen genie*, Ind. Phys. **2004**, *10*, 20-23.

2 B.P. statistical review of world energy, http://www.bp.com/statisticalreview (December **2008**) http://www.bp.com/liveassets/bp_internet/globalbp/globalbp_uk_english/reports_and_publications/statistical_energy_review_2007/STAGING/local_assets/downloads/pdf/statistical_review_of_world_energy_full_report_2007.pdf.

3 L. Schlapbach and A. Züttel, *Hydrogen-storage materials for mobile applications*, Nature (London) **2001**, *414*, 353-358.

4 A. Züttel, A. Borgschulte and L. Schlapbach, *Hydrogen as a future energy carrier*, Wiley-VCH Verlag GmbH & Co. KGaA **2008**.

5 W. Doenitz, R. Schmidberger, E. Steinheil and R. Streicher, *Hydrogen production by high temperature electrolysis of water vapour*, Int. J. Hydrogen Energy **1998**, *5*, 55-63.

6 H. Gaffron and J.J. Rubin, *Fermentative and photochemical production of hydrogen in algae*, J. Gen. Physiol. **1942**, *26*, 219-240.

7 U.S. Department of Energy, Multi-Year Research, Development and Demonstration, Plan: Planned program activities for 2003-2010, http://www.eere.energy.gov/hydrogenandfuelcells/mypp/ (December **2008**).

8 R. Griessen and T. Riesterer, *Topics in Applied Physics Hydrogen in Intermetallic Compounds*, *Chapter 6: Heat of Formation Models*, Vol. 63 (Ed. L. Schlapbach), Springer-Verlag, Berlin, **1988**, 219-284.

9 E. Huheey, *Inorganic Chemistry*, Harper & Row, New York **1983**.

10 F. Stampfer, C.E. Holley and J.F. Suttle, *The magnesium-hydrogen system*, J. Am. Chem. Soc. **1960**, *82*, 3504-3508.

11 A. Andreasen, *PhD thesis: Hydrogen storage materials with focus on main group I-II elements*, Risø National Laboratory, Denmark, **2005**.

12 K.H.J. Buschow, P.C.P. Bouten and A.R. Miedema, *Hydrides formed from intermetallic compounds of two transition metals: a special class of ternary alloys,* Rep. Prog. Phys. **1982**, *45*, 937-1039.

13 C.M. Stander, *Kinetics of the formation of magnesium hydride from magnesium and hydrogen*, Phys. Chem. Neue Folge **1977**, *104*, 229-238.

14 A. Krozer and B. Kasemo, *Unusual kinetics due to interface hydride formation in the hydriding of Pd/Mg sandwich layers*, J. Vac. Sci. Technol. A **1987**, 5, 1003-1005.

15 J. Rydén, B. Hjörvarsson, T. Ericsson, E. Karlsson, A. Krozer and B. Kasemo, *Unusual kinetics of hydride formation in Mg-Pd sandwiches, studied by hydrogen profiling and quartz crystal microbalance measurements*, J. Less-common Met. **1989**, *152*, 295-309.

16 V.P. Zhdanov, A. Krozer and B. Kasemo, *Kinetics of first-order phase transitions initiated by diffusion of particles from the surface into the bulk*, Phys. Rev. B **1993**, *47*, 11044-11048.

17 K.B. Gerasimov and E.Y. Ivanov, *The mechanism and kinetics of formation and decomposition of magnesium hydride*, Mater. Lett. **1985**, *3*, 497-499.

18 Z. Luz, J. Genossar and P.S. Rudman, *Identification of the diffusing atom in MgH_2*, J. Less-common Met. **1980**, *73*, 113-118.

19 J. Töpler, H. Buchner and H. Säufferer, *Measurements of the diffusion of hydrogen atoms in magnesium and Mg2Ni by neutron scattering* J. Less-common Met. **1982**, *88*, 397-404.

20 P. Spatz, H.A. Aebischer, A. Krozer and L. Schlapbach, *The diffusion of H in Mg and the nucleation and growth of MgH_2 in thin films*, Z. Phys. Chem. **1993**, *181*, 393-397.

21 B. Vigeholm, K. Jensen, B. Larsen and A.S. Pedersen, *Elements of hydride formation mechanisms in nearly spherical magnesium powder particles*, J. Less-common Met. **1987**, *131*, 133-141.

22 M. Stioui, A. Grayevski, A. Resnik, D. Shaltiel and N. Kaplan, *Macroscopic kinetics of hydrogen in magnesium-rich compounds*, J. Less-common Met. **1986**, *123*, 9-24.

23 H.F. Bittner and C.C. Badcock, *Electrochemical utilization of metal-hydrides*, J. Electrochem. Soc. **1983**, *130*, 193C-198C.

24 J.J.G. Willems, *Metal hydrides electrodes stability of $LaNi_5$-related compounds*, Philips J. Res. Suppl. **1984**, *39*, 1-94.

25 O. Arnaud, P. Barbic, P. Bernard, A. Bouvier, B. Knosp, B. Riegel and M. Wohlfahrt-Mehrens, *Study of the corrosion resistance of Cr, Zr, Y doped AB_5 type alloys in KOH*, J. Alloys Compd. **2002**, *330-332*, 262-267.

26 H. Ye, B. Xia, W. Wu, K. Du and H. Zhang, *Effect of rare earth composition on the high-rate capability and low-temperature capacity of AB_5-type hydrogen storage alloys*, J. Power Sources **2002**, *111*, 145-151.

27 A. Singh, B.K. Singh, D.J. Davidson and O.N. Srivastava, *Studies on improvement of hydrogen storage capacity of AB_5 type: =$MmNi_{4.6}Fe_{0.4}$ alloy*, Int. J. Hydrogen Energy **2004**, *29*, 1151-1156.

28 J.N. Huiberts, R. Griessen, J.H. Rector, R.J. Wijngaarden, J.P. Dekker, D.G. de Groot and N.J. Koeman, *Yttrium and lanthanum hydride films with switchable optical properties*, Nature **1996**, *380*, 231-234.

29 C.G. Granqvist, *Handbook of Inorganic Electrochromic Materials*, Amsterdam, Elsevier **1995**.

30 P.H.L. Notten, M. Kremers M and R. Griessen, *Optical switching of Y-hydride thin film electrodes: a remarkable electrochromic phenomenon*, J. Electrochem. Soc. **1996**, *143*, 3348-3353.

31 P. van der Sluis, M. Ouwerkerk and P.A. Duine, *Optical switches based on magnesium lanthanide alloy hydrides*, Appl. Phys. Lett. **1997**, *70***,** 3356-3358.

32 T.J. Richardson, R.D. Armitage, J.L. Slack and M.D. Rubin, *Alternative materials for electrochromic mirror devices*, poster presentation at the Fourth International Meeting on Electrochromism (IME-4), August 21-23 **2000**, Uppsala, Sweden.

33 T.J. Richardson, J.L. Slack, R.D. Armitage, R. Kostecki, B. Farangis and M.D. Rubin, *Switchable mirrors based on nickel-magnesium films*, Appl. Phys. Lett. **2001**, *78*, 3047-3049.

34 T.J. Richardson, J.L. Slack, B. Farangis and M.D. Rubin, *Mixed metal films with switchable optical properties*, Appl. Phys. Lett. **2002**, *80*, 1349–1351.

35 R.A.H. Niessen and P.H.L. Notten, *Electrochemical hydrogen storage characteristics of thin film MgX (X=Sc,Ti,V,Cr) compounds*, Electrochem. Solid-State Lett. **2005**, *8*, A534-A538.

36 M. Slaman, B. Dam, M. Pasturel, D.M. Borsa, H. Schreuders, J.H. Rector and R. Griessen, *Fiber optic hydrogen detectors containing Mg-based metal hydrides***,** Sens. Actuators B **2006**, *123,* 538-545.

37 D.M. Borsa, A. Baldi, M. Pasturel, H. Schreuders, B. Dam, R. Griessen, P. Vermeulen and P.H.L. Notten, *Mg-Ti-H thin films for smart solar collectors*, Appl. Phys. Lett. **2006**, *88*, 241910/1-3.

38 S. Bao, K. Tajima, Y. Yamada, M. Okada and K. Yoshimura, *Color-neutral switchable mirrors based on magnesium-titanium thin films***,** Appl. Phys. A **2007**, *87*, 621-624.

39 S. Bao, K. Tajima, Y. Yamada, M. Okada and K. Yoshimura, *Magnesium-titanium alloy thin-film switchable mirrors*, Solar Energy Materials & Solar Cells **2008**, *92*, 224-227.

40 A. Baldi, D.M. Borsa, H. Schreuders, J.H. Rector, T. Atmakidis, M. Bakker, H.A. Zondag, W.G.J. van Helden, B. Dam and R. Griessen, *Mg-Ti-H thin films as switchable solar absorbers*, Int. J. Hydrogen Energy **2008**, *33*, 3188-3192.

41 A. Zaluska, L. Zaluski and J.O. Strom-Olsen, *Nanocrystalline magnesium for hydrogen storage*, J. Alloys Compd **1999**, *288*, 217-225.

42 G. Barkhordarian, T. Klassen and R. Bormann, *Effect of Nb_2O_5 content on hydrogen reaction kinetics of Mg*, J. Alloys Compd. **2004**, *364*, 242-246.

43 J.J. Reilly and R. H. Wiswall, Jr., *Reaction of hydrogen with alloys of magnesium and nickel and the formation of Mg_2NiH_4*, Inorg. Chem. **1968**, *7*, 2254-2256.

44 J.F. Stampfer, Jr., C.E. Holley, Jr. and J.F. Suttle, *The magnesium hydrogen* system, J. Am. Chem. Soc. **1960**, *82*, 3504-3508.

45 R.W.P. Wagemans, J.H. van Lenthe, P.E. de Jongh, A.J. van Dillen and K.P. de Jong, *Hydrogen storage in magnesium clusters: Quantum chemical study*, J. Am. Chem. Soc. **2005**, *127*, 16675-16680.

46 M. Ouwerkerk, *Electrochemically induced optical switching of $Sm_{0.3}Mg_{0.7}H_x$ thin layers*, Solid State Ionics **1998**, *113-115*, 431-437.

47 N. Cui, B. Luan, H.J. Zhao, H.K. Liu and S.X. Dou, *Effects of yttrium additions on the electrode performance of magnesium-based hydrogen storage alloys*, J. Alloys Compd. **1996**, *233*, 236-240.

48 P. Hjort, A. Krozer and B. Kasemo, *Resistivity and hydrogen uptake measurements in evaporated Mg films at 350 K*, J. Alloys Compd. **1996**, *234*, L11-L15

49 P.H.L. Notten, M. Ouwerkerk, H. van Hal, D. Beelen, W. Keur, J. Zhou and H. Feil, *Hydride-forming electrode materials seen from a kinetic perspective*, J. Power Sources **2004**, *29*, 45-54.

50 R.A.H. Niessen and P.H.L. Notten, *Hydrogen storage in thin film magnesium–scandium alloys***,** J. Alloys Compd. **2005**, *404-406*, 457-460.

51 W.P. Kalisvaart, R.A.H. Niessen and P.H.L. Notten, *Electrochemical hydrogen storage in MgSc alloys: A comparative study between thin films and bulk materials*, J. Alloys Compd. **2006**, *417*, 280–291.

52 W.P. Kalisvaart, P. Vermeulen, A.V. Lyedovskikh, D. Danilov and P.H.L. Notten, *The electrochemistry and modelling of hydrogen storage materials*, J. Alloys Compd. **2007**, *446-447*, 648–654.

53 H. Baker (Edt), *ASM Handbook – Alloy Phase Diagrams*, Vol. 3, ASM International **1992**.

54 D. Kyoi, T. Sato, E. Rönnebro, N. Kitamura, A. Ueda, M. Ito, S. Katsuyama, S. Hara, D. Noreus and T. Sakai, *A new ternary magnesium–titanium hydride Mg_7TiH_x with hydrogen desorption properties better than both binary magnesium and titanium hydrides*, J. Alloys Compd. **2004**, *372*, 213-217.

55 D. Kyoi, T. Sato, E. Rönnebro, Y. Tsuji, N. Kitamura, A. Ueda, M. Ito, S. Katsuyama, S. Hara, D. Noreus and T. Sakai, *A novel magnesium–vanadium hydride synthesized by a gigapascal-high-pressure technique*, J. Alloys Compd. **2004**, *375*, 253-258.

56 D. Kyoi, E. Rönnebro, N. Kitamura, A. Ueda, M. Ito, S. Katsuyama and T. Sakai, *The first magnesium–chromium hydride synthesized by the gigapascal high-pressure technique*, J. Alloys Compd. **2003**, *361*, 252-256.

57 T. Mitchell, S. Diplas, P. Tsakiropoulos, J.F. Watts and J.A.D. Matthew, *Study of alloying behavior in metastable Mg-Ti solid solutions using Auger parameter measurements and charge-transfer calculations*, Philos. Mag. A **2002**, *82*, 841-855.

58 T.J. Richardson, B. Farangis, J.L. Slack, P. Nachimuthu, R. Perera, N. Tamura and M. Rubin, *X-Ray absorption spectroscopy of transition metal-magnesium hydride thin films*, J. Alloys Compd. **2003**, *356-357*, 204-207.

59 B. Farangis, P. Nachimuthu, T.J. Richardson, J.L. Slack, B.K. Meyer, R.C.C. Perera and M.D. Rubin, *Structural and electronic properties of magnesium-3D transition metal switchable mirrors*, Solid State Ionics **2003**, *165*, 309-314.

60 A. Ledovskikh, D. Danilov, W.J.J. Rey and P.H.L. Notten, *Modeling of hydrogen storage in hydride-forming materials: Statistical thermodynamics,* Phys. Rev. B **2006**, *73*, 014106/1-12.

2
Experimental

Abstract

In this chapter the preparation methods and characterization techniques of the thin film systems are discussed in detail. Most of the experimental studies are based on electrochemical control as it offers several important advantages. For instance, the pressure-composition isotherms of the films can accurately be assessed by advanced electrochemical techniques. Electrochemical control also offers the possibility to tune the hydrogen content with high precision, which in combination with other characterization techniques, like for example X-ray diffraction, provides new insights into the effects of the hydrogen content on the host material. Other electrochemical methods used to determine the hydrogen storage properties of thin films include galvanostatic measurements, cyclic voltammetry and impedance spectroscopy. To resolve the crystallographic phases present in as-prepared and hydrogenated Mg-based alloys *in situ* X-ray diffraction is performed using a special setup that allows atmospheric control of the environment.

2.1 Introduction

The techniques and methods used to prepare and characterize the thin films are discussed thoroughly in this chapter. Firstly, the details of the thin film deposition are described in paragraph 2.2. Basically, two techniques are used, *i.e.* electron beam deposition and magnetron co-sputtering. Secondly, the electrochemical setup, along with several electrochemical techniques, is discussed in paragraph 1.1. Electrochemical characterization is turned out to be very beneficial for determining the hydrogen absorption and desorption properties of thin film alloys, *e.g.* electrochemical control offers the possibility to calculate and tune the hydrogen content in the hydride-forming material with high precision. Moreover, thin film pressure-composition isotherms are generally difficult to obtain, mainly because of the small amount of material. The relation between the electrochemical and gas phase properties is therefore beneficially exploited to obtain accurate isotherms. In paragraph 2.3 the background and experimental details of X-ray diffraction (XRD) analysis is explained, which is used throughout this thesis to resolve the crystallographic phases present in the material after preparation.

2.2 Thin film deposition and characterization

The thin films discussed in this thesis are prepared by electron beam deposition and magnetron co-sputtering, which are forms of physical vapor deposition. Most of the thin films presented in this thesis are prepared by electron beam evaporation, however, it was experimentally found that sputtered films show a larger degree of crystallinity making them more suitable for in-depth X-ray diffraction analysis. Below the experimental details of the thin film deposition techniques are presented.

Electron beam evaporated Pd, Mg_yTi_{1-y}, $Mg_yTi_zAl_{1-y-z}$ and $Mg_yTi_zSi_{1-y-z}$ thin films were prepared at room temperature at a base pressure of 10^{-8}-10^{-7} mbar in a Balzers BAK 550. The films were deposited on quartz substrates (Ø 20 mm, Hareaus Suprasil), which were continuously rotated for optimal alloying conditions. The film thickness was set at 200 nm for all Mg-based alloys. The thickness of the films consisting of solely a Pd layer was varied from 10 to 200 nm, which were deposited at a rate of 1 Å/s. Preliminary results showed that the direct adhesion of Pd to quartz was quite poor and therefore a 1 nm Gd adhesion layer was deposited beforehand.

For thin film Mg_yTi_{1-y} alloys the deposition rates of the individual metals strongly depend on the desired composition and range from a rate of 1.4 Å Mg/s and 1.1 Å Ti/s for $Mg_{0.50}Ti_{0.50}$ to 2.4 Å Mg/s and 0.1 Å Ti/s for $Mg_{0.95}Ti_{0.05}$. Depending on the desired alloy composition of the Al- and Si-containing ternary systems the deposition rate was 0.1-1 Å Al/s and 0.2 Å Si/s, respectively. A 10 nm thick Pd topcoat, applied to all Mg-based films to prevent oxidation and promote hydrogen gas dissociation or electrocatalyze the reduction of H_2O, was deposited at a rate of 1 Å/s.

Sputtered Mg_yTi_{1-y} films containing 70, 80 and 90 at.% Mg with a nominal thickness of 200 nm were deposited in a ultra high vacuum (UHV) system by dc/rf magnetron co-sputtering of Mg and Ti targets in an argon atmosphere. The films were again covered with 10 nm of Pd. Quartz substrates (Ø 20 mm, Hareaus Suprasil) were used for general electrochemical and gas phase characterization, while for the *in situ* electrochemical XRD

study 125 μm thick X-ray transparent PEEK foils (2.5x4 cm, Goodfellow) were used. Typical deposition rates were 2.2 Å/s for Mg at 150 W (rf), 0.2-1.8 Å/s for Ti at 60-400 W (dc) and 1.1 Å/s for Pd at 50 W (dc). In order to obtain a homogenous composition the substrates were continuously rotated during sputtering. Again, a 1 nm Cr adhesion layer was applied to the PEEK foils to ensure no delamination occurred during long-term measurements.

The thickness and homogeneity of the as-prepared films was checked by Rutherford Backscattering Spectrometry (High Voltage Engineering RBS device, Model AN-2500) analysis. The measured data was fitted using RUMP software. Fig. 2.1 shows the Rutherford Backscattering Spectroscopy (RBS) spectrum of as-prepared 200 nm thick $Mg_{0.80}Ti_{0.20}$ film capped with 10 nm Pd on a quartz substrate. It is clear that, besides the response of the quartz substrate (a), only the elements are visible that were deposited by means of electron beam deposition. Peaks (b) and (c) can be correlated to Mg and Ti, respectively, while peak (d) corresponds to the Pd capping layer. Evidently, the Pd topcoat successfully protects the Mg-based thin film from corrosion, as no oxygen traces are observed. Additionally, no other responses are present that point to contamination by other elements.

The RBS fit gives information about the composition and thickness of the films, which can be used to determine the mass (m) of the sample by

$$m = dA\rho \tag{2.1}$$

where d is the thickness of the film, A is the area (estimated to be about 3 cm^2) and ρ is the density known from literature. Note that for calculating the mass of an alloy, ρ is estimated from a linear combination of the densities of the elements involved. The specific contribution of the density of the individual elements to the estimated density is based on the measured alloy composition. This approach is based on *Vegard's* law that states that a linear relation exists between the composition and lattice parameters of an alloy.[1] In paragraphs 4.2.1 and 4.2.4.1 it will be shown that indeed an almost linear relation between the lattice parameter and the composition of the as-prepared Mg_yTi_{1-y} thin films with $0.50 \leq y \leq 1.00$ is found experimentally, thus confirming that estimating the density of the alloys from the densities of the individual elements is allowed.

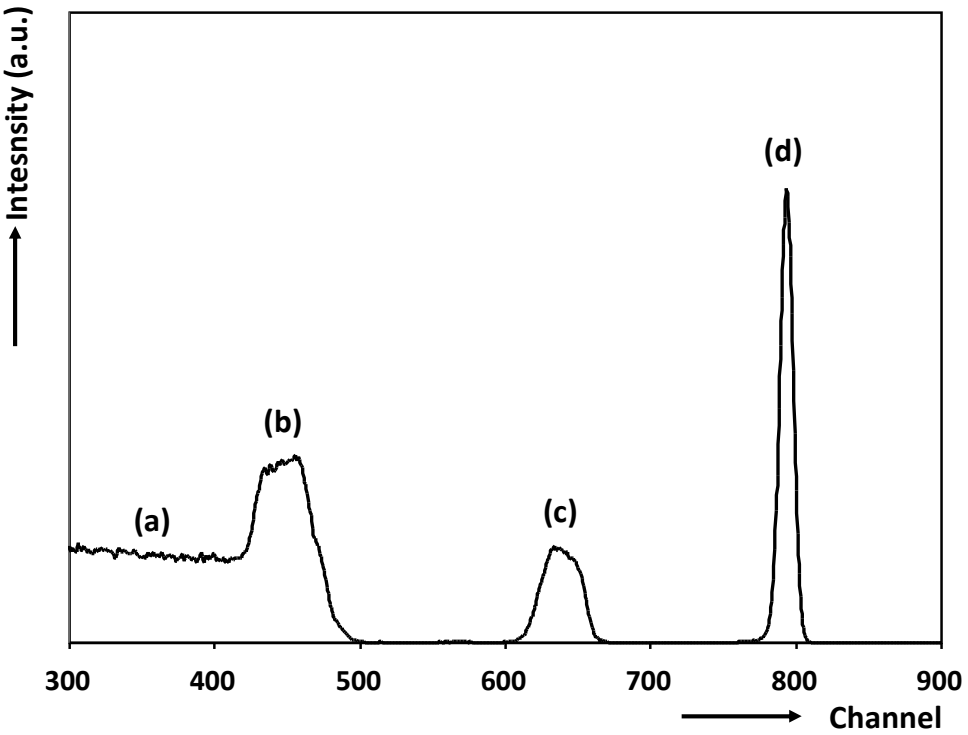

Fig. 2.1 RBS spectrum of a freshly prepared Pd-coated $Mg_{0.80}Sc_{0.20}$ thin film. The responses of interest are indicated: (a) quartz substrate, (b) Mg, (c) Ti and (d) Pd.

2.3 Electrochemical characterization

Most of the experimental techniques used in this thesis to characterize the hydrogen storage properties of the Mg-based compounds are completely based on or combined with electrochemistry. Electrochemistry offers a unique approach to determine several properties that are otherwise difficult to assess. In this paragraph the background of electrochemical control and the experimental techniques are discussed in detail.

2.3.1 Background

Electrochemical (de)hydrogenation of hydride-forming materials is used on a large scale in rechargeable Nickel Metal Hydride (NIMH) batteries. These batteries were introduced to replace the environmentally unfriendly NiCd batteries. Moreover, NiMH is reported to have a more than 50% higher volumetric and gravimetric energy density than conventional NiCd batteries.[2] Nowadays, they are primarily used in large scale devices, for instance hybrid electric vehicles, since Li-ion batteries have taken over the market in portable electronics. In Fig. 2.2 a schematic representation of a NiMH battery is depicted. The battery consists of a nickel hydroxide electrode (generally denoted as the nickel electrode) and a metal hydride (MH) electrode.[3] The electrodes are electrically insulated from each other by a separator, which is impregnated with an alkaline solution to provide ionic conductivity. Charging the

battery enforces 2 electrochemical reactions, *i.e.* oxidation of nickel(II) to the trivalent state, forming nickeloxyhydroxide, according to

$$Ni(OH)_2 + x\ OH^- \rightleftarrows x\ NiOOH + x\ H_2O + x\ e^- \quad (2.2)$$

Simultaneously, at the metal hydride electrode, water is reduced to form hydroxyl ions and hydrogen atoms, the latter are absorbed by $LaNi_5$. This reaction can be represented by

$$LaNi_5 + x\ H_2O + e^- \rightleftarrows LaNi_5H_x + x\ OH^- \quad (2.3)$$

Reactions 2.2 and 2.3 show that no electrolyte is consumed in the charging and discharging reactions.

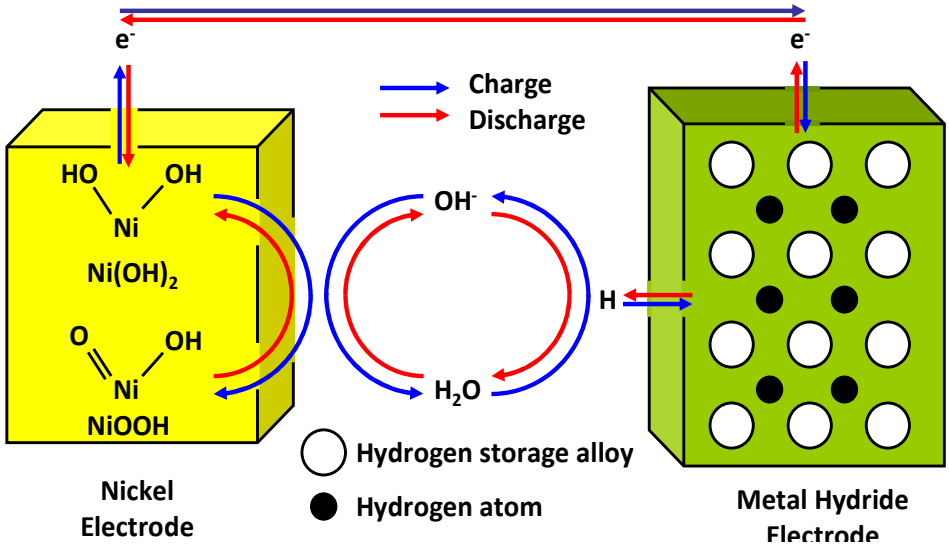

Fig. 2.2 Schematic representation of the chemistry in a rechargeable NiMH battery (modified from Ref. 4).

Once hydrogen atoms are absorbed they can occupy the tetrahedral and octahedral sites in the crystal lattice, which is shown in Fig. 2.3. Whether hydrogen prefers to occupy a tetrahedral or octahedral interstitial depends on the energy. This energy depends upon the hydride-forming material, *e.g.* in MgH_2 the hydrogen atoms occupy the tetrahedral sites, whereas in Pd hydride atoms prefer to reside in the octahedral sites. Several studies show that the distribution of hydrogen over the two types of interstices changes with the hydrogen content. For instance in $LaNi_5D_7$ it was found that deuterium occupies two tetrahedral sites (coordinated with Ni_4 and La_2Ni_2) and one octahedral site with La_2Ni_4 neighbors.[5,6] The Ni_4 tetrahedron has the smallest interstitial volume with a spherical hole radius of 0.27 Å, which is much to small to accommodate a D atom. However, if the La_2Ni_2 and La_2Ni_4 sites are occupied first then it was calculated that the radius of the Ni_4 site is increased to 0.38 Å due to expansion of the unit cell. This is found to be large enough for the insertion of a D atom after which the radius is increased even more. This example illustrates beautifully that the site distribution of deuterium is a function of the degree of loading.

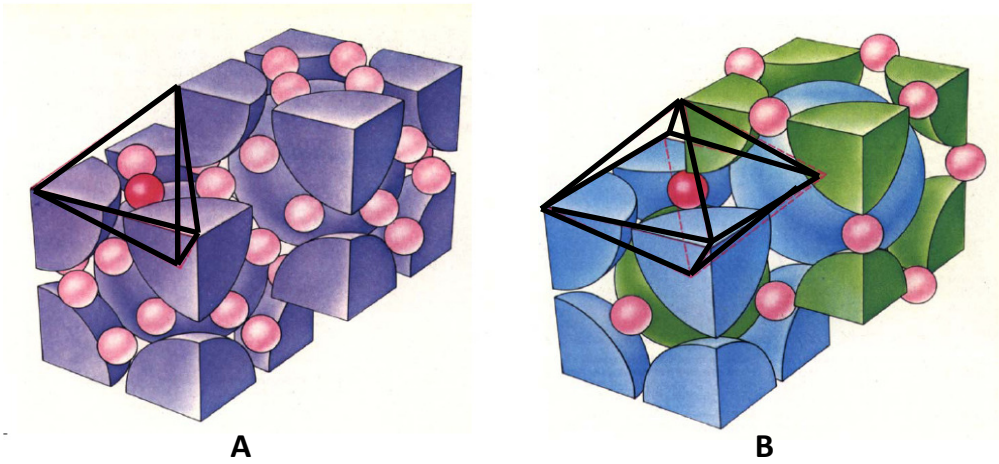

Fig. 2.3 Hydrogen atoms indicated in red occupying (A) a tetrahedral and (B) an octahedral site.

Hydrogen absorption by a metal hydride is often accompanied by a phase transition from a hydrogen-poor α-phase, where hydrogen is dissolved in the matrix, to a hydrogen-rich β-phase, where hydrogen occupies specific sites in the host lattice. The absorption and desorption of hydrogen by a metal is typically represented by a pressure-composition isotherm (PCI). PCI-curves of an ideal hydride-forming material are shown in Fig. 2.4 as a function of temperature.

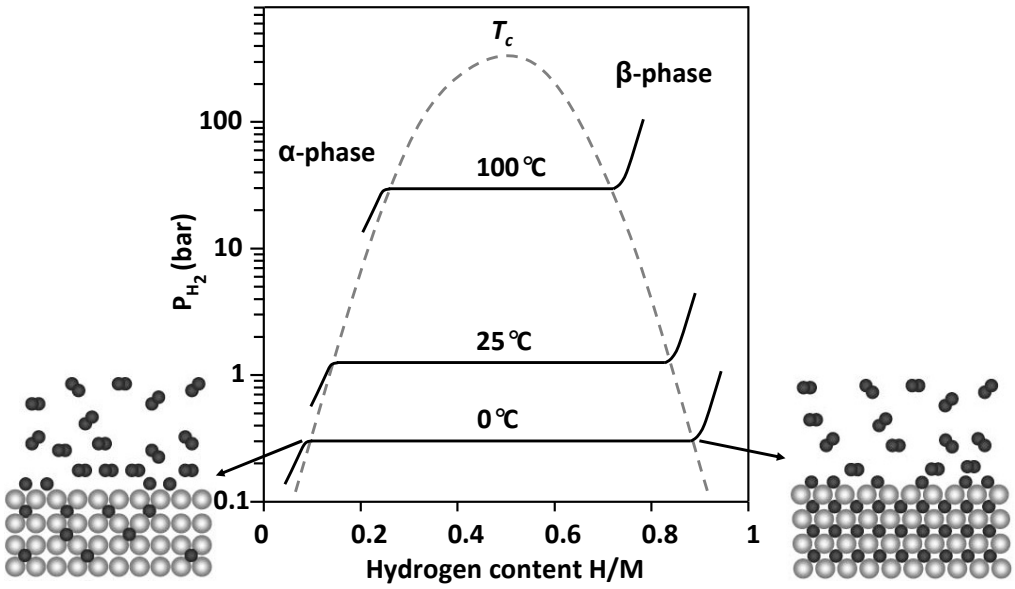

Fig. 2.4 Pressure-composition isotherms of an ideal hydride-forming material showing the influence of the temperature on the miscibility of the α and β phases as well as the increase of the plateau pressure governed by the Van 't Hoff relation (see Eq. 2.4). Reproduced from Ref. 7.

In the α-solid solution it is clear that the hydrogen concentration strongly depends on the hydrogen pressure. Once the solid solution is saturated at a critical H concentration (x_α) a second phase (β) nucleates and grows. The miscibility of two well-defined phases is apparent by the development of a plateau. After the α-phase is completely converted into the β-phase

at a H concentration denoted as x_β, further increase of the hydrogen concentration is accompanied by an increasing hydrogen partial pressure (P_{H_2}). The miscibility gap becomes smaller with rising temperature as is shown in Fig. 2.4. Ultimately, it disappears completely at a critical temperature T_c. The plateau pressures increase with increasing temperature according to the Van 't Hoff relation[7-9]

$$ln\, P_{H_2} = \frac{\Delta H_f}{RT} - \frac{\Delta S_0}{R} \tag{2.4}$$

where ΔH_f is the enthalpy of formation, R the universal gas constant, T the absolute temperature, ΔS_0 is the entropy of formation in J/(K mol H_2). In a first approximation, ΔS_0 is mainly determined by the loss of entropy when gaseous H_2 is absorbed in the solid, *i.e.* $\Delta S_0 \cong - S_{H_2}$ = -130.8 J/(K mol H_2).

The hydrogen partial pressure can be related to the electrochemical equilibrium potential according to[3,10]

$$E^{eq} = -\frac{R\,T}{2F}\, ln\left(\frac{P_{H_2}}{P_{ref}}\right) \; vs.\ \text{RHE} \tag{2.5}$$

where F is the Faraday constant (96485 C/mol), P_{ref} is the reference pressure (1 bar) and *RHE* refers to the reversible hydrogen electrode. For $LaNi_5$ the phase transition occurs in a narrow pressure window. Hence, the fundamental reason why $LaNi_5$ is particularly suitable for the use as electrode material in NiMH batteries is that its electrochemical potential is constant over a large capacity range, resulting in a stable battery voltage.

2.3.2 The electrochemical setup

For electrochemical analysis, a silver lead (Ø 1 mm, Alfa Aesar Premion®) was attached to the surface of the as-deposited thin film alloys with a conductive adhesive silver paste (E-solder™ 3021, 2 comp. conductive adhesive, Epoxy Produkte). The Ag wire was coated using a chemical inert lacquer (W40, Apiezon) to isolate it from the electrolyte to avoid any interference with the electrochemical measurements. To prevent lateral hydrogen uptake also the edges of the metallic layer were covered by the lacquer.

The electrochemical measurements were carried out in a so-called three-electrode configuration (see Fig. 2.5) comprised of a working electrode, reference electrode and counter electrode. The working electrode consists of the thin film material under investigation. The electrochemical potential of the working electrode is measured versus a reference electrode. As the electrochemical experiments are performed in strong alkaline solutions (6 M KOH) it limits the choice of a suitable reference electrode. Recently, Niessen *et al*. showed that Hg/HgO reference electrodes manufactured by Radiometer, which are specifically designed to operate in alkaline electrolytes, interfered with thin film measurements.[11] Small amounts of contaminants leached out of Pb-containing glass casing of the Hg/HgO reference electrode. Soon Pb-complexes covered the surface of the electrodes,

changing the charge transfer kinetics dramatically. This problem was solved by using Hg/HgO reference electrodes made out of polyethylene (Koslow Scientific Company, USA).

As it is clear that small traces of metals can potentially disturb the electrodes surface and create redox couples that can interfere with the electrochemical reactions the alkaline electrolyte was prepared by dissolving high purity KOH (P.A. grade) pellets in Millipore Milli-Q water (resistivity >18.2 MΩ/cm). Unless stated otherwise the setup is thermostated at 298 K by means of a water jacket surrounding the cell and the experiments are conducted in a 6 M KOH electrolyte. Electrochemical control is performed using an Autolab PGSTAT30 (Ecochemie) or Maccor M2300 battery tester (Maccor, USA) depending on the desired experimental conditions.

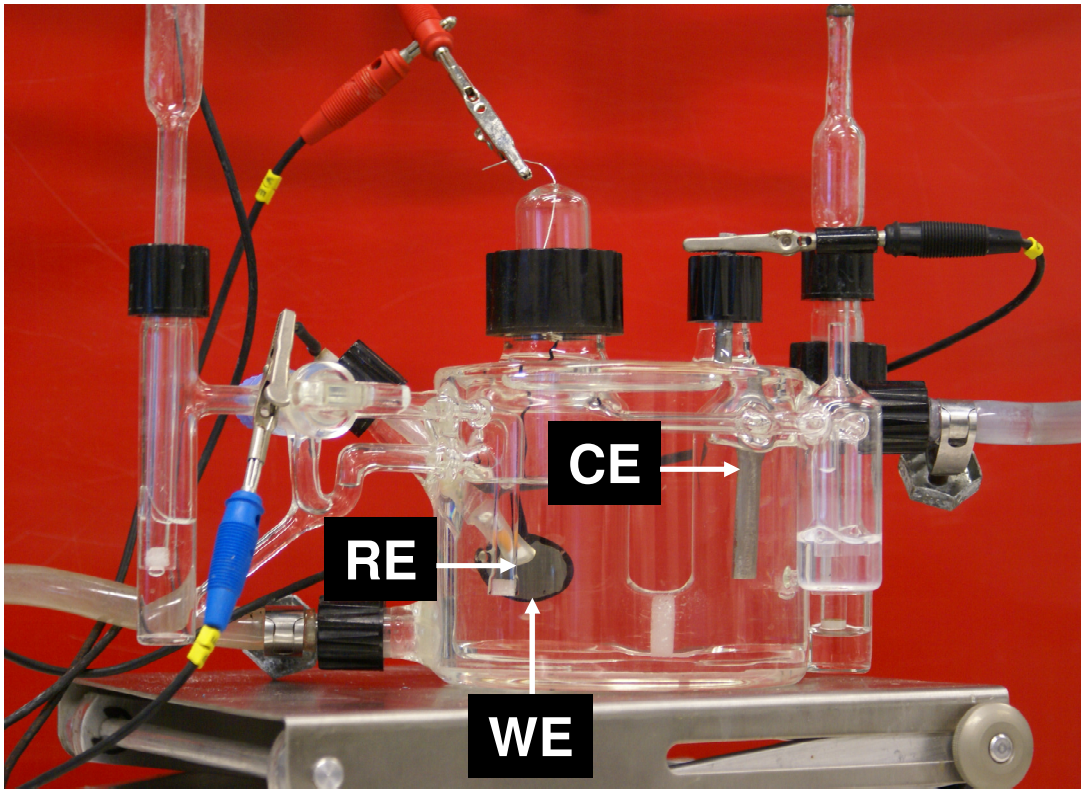

Fig. 2.5 Photograph of the three-electrode thin film cell. The positions of the working electrode (WE), counter electrode (CE) and reference electrode (WE) are indicated. The purging gas inlets ('water locks') are on either sides of the cell. The valve on the left-hand side of the WE-compartment can be used to regulate whether the purging gas flows through or over the electrolyte.

A three-electrode configuration is often used in experiments where the Ohmic drop in the electrolyte is large. However, in our experiments the electrolyte is a strong alkaline KOH solution, therefore the main advantage of a three-electrode setup is the broader choice of the counter electrode. Obviously, in a two-electrode configuration it is important that the counter electrode has a stable potential in the voltage window of the experiment. As a reaction will inevitably take place at the counter electrode during cell operation it is expected that it will change the potential of the counter electrode, which, as a result, cannot be used as a reliable

reference anymore. It is essential that during operation of the cell no O_2 is formed at the counter electrode, according to

$$4\ OH^- \rightarrow\ O_2 + 2\ H_2O + 4\ e^- \qquad E^0 = +0.3\ V\ vs.\ Hg/HgO \qquad (2.6)$$

O_2 formation needs to be avoided at all times as it can affect the hydrogen content by oxidizing the metal hydride, according to[12,13]

$$MH_x + \frac{1}{4}\ x\ O_2 \rightarrow M + \frac{1}{2}\ x\ H_2O \qquad (2.7)$$

This reaction shows that even minute amounts of oxygen can seriously affect the hydrogen content. Moreover, the reduction of O_2, which proceeds via

$$O_2 + H_2O + 4\ e^- \rightarrow\ 4\ OH^- \qquad (2.8)$$

can interfere with the electrochemical potential of H_2O reduction resulting in a mixed electrode potential and, consequently, will lead to experimental errors.

To avoid O_2 formation a Pd rod is used as counter electrode. Before starting the experiment, this electrode is precharged with hydrogen, according to

$$Pd + x\ H_2O + x\ e^- \rightarrow PdH_x + x\ OH^-\ . \qquad (2.9)$$

The total amount of charge needed to extract all the hydrogen from this rod far exceeds the charge needed to fully hydrogenate the working electrode. This ensured that during the electrochemical experiments no oxygen is produced at the palladium counter electrode.

As even small amounts of O_2 need to be removed, also the electrolyte is deaerated by vigorously purging the electrolyte with argon for 1 hour before proceeding with the electrochemical analyses. To avoid interference from the Ar bubbles during the electrochemical measurement, the gas is led over, instead of through, the solution. To remove possible oxygen traces from the argon feed, the argon was purified in a oxygen-scrubber system, which is explained in detail below.

The oxygen-scrubber system is based on the high reactivity of the methylviologen (MV) single radical towards oxygen.[14] MV is the common name for 1,1-dimethyl-4,4-bipyridiniumdichloride, of which the molecular structure is shown in Fig. 2.6.

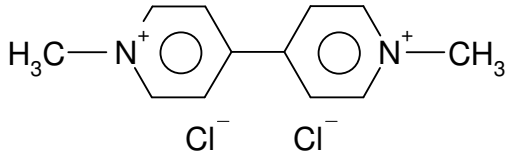

Fig. 2.6 Structural formula of the methylviologen molecule.

To prepare the MV solution, the MV salt is dissolved, forming MV^{2+} ions, in a buffer solution of pH = 6, consisting of 0.1 M KH_2PO_4 and 0.1 M NaOH. A glass column (h = 900 mm and ∅ 50 mm) is filled with the solution. Obviously, the height of the column should be

large enough to enforce the complete removal of O_2 from the Ar feed. The Ar feed was also led through small glass marbles to breakup any large bubbles into smaller ones to enforce a sufficiently large contact area of the bubbles with the solution, which obviously facilitates the removal of O_2 from the Ar feed.

Fig. 2.7 shows a schematic representation of the glass column together with the three-electrode setup used to generate $MV^{+\bullet}$ ions. MV^{2+} ions are reduced potentiostatically at -0.7 V *vs.* SCE to a single radical state ($MV^{+\bullet}$) at a platinum gauze (99.999 % Pt) working electrode, according to

$$MV^{2+} + e^- \rightarrow MV^{+\bullet} \qquad E^0 = -0.68 \text{ V } vs. \text{ SCE} \qquad (2.10)$$

The $MV^{+\bullet}$ radicals, which color the buffer solution in deep-blue, react with the oxygen traces present in the Ar feed according to

$$2\,MV^{+\bullet} + O_2 + 2\,H^+ \rightarrow 2\,MV^{2+} + H_2O_2 \qquad (2.11)$$

Reaction 2.11 shows that once $MV^{+\bullet}$ oxidizes to MV^{2+}, by reacting with oxygen, the formed MV^{2+} ion can be reduced again to $MV^{+\bullet}$ at the working electrode according to reaction 2.10. As long as the solution has a deep-blue color it can be assumed that the solution is saturated with $MV^{+\bullet}$ ions, thus, providing sufficient reactants for the complete removal of O_2 traces from the Ar feed. The oxygen-purified argon gas is transported to the electrochemical cell using stainless steel Swagelok™ tubing (∅ 0.25 in.). Interesting to note is that the purging gas, which has passed through the MV setup, is not only purified of oxygen but also saturated with water. It is therefore not expected that any electrolyte will evaporate, which ensures that the pH of the electrolyte remains unchanged, even when performing long-term experiments.

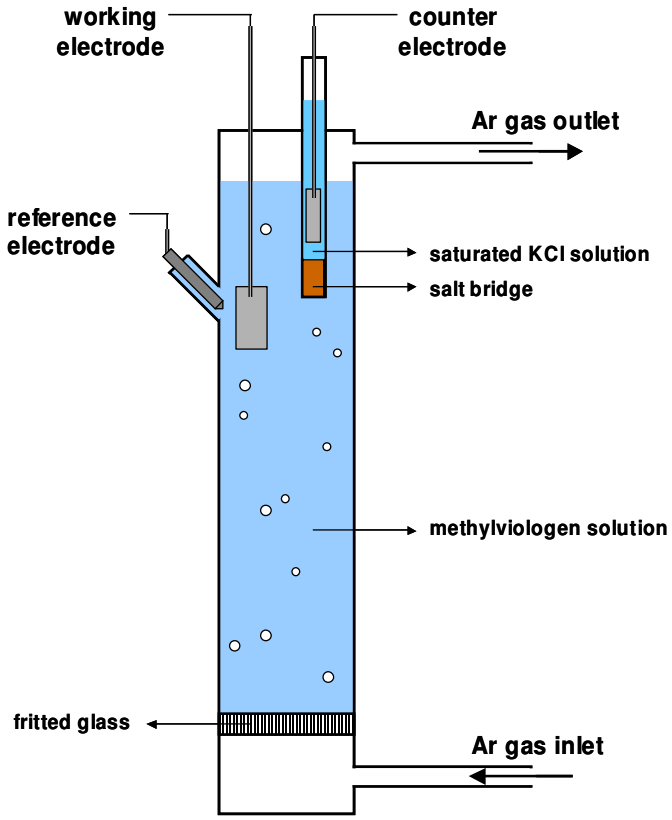

Fig. 2.7 Schematic representation of the oxygen-scrubbing methylviologen setup.[12,13]

2.3.3 Galvanostatic control

Galvanostatic measurements are based on applying a constant current to the system and measuring the resulting electrochemical potential. During charging the current drives the reduction reaction of H_2O at the surface of the electrode according to

$$M + H_2O + e^- \rightleftarrows MH_{ad} + OH^- \qquad (2.12)$$

Subsequently, the adsorbed hydrogen atoms (H_{ad}) are either absorbed (H_{abs}) by the hydride forming material represented by

$$MH_{ad} \rightleftarrows MH_{abs} \qquad (2.13)$$

or they recombine at the metal surface to form a hydrogen molecule according to the *Tafel step*

$$2\,MH_{ad} \rightleftarrows 2\,M + H_2(g) \qquad (2.14)$$

The latter reaction is also known as the hydrogen evolution reaction (HER). Another possible route for hydrogen gas formation is

$$MH_{ad} + H_2O + e^- \rightleftarrows 2\,M + H_2(g) + OH^- \quad (2.15)$$

which is known as the *Heyrovski step*. Yet, a previous study shows that this reaction proceeds at a very low rate and can therefore be omitted.[15]

Although hydrogen evolution can often be distinguished from the hydrogen absorption process by studying the potential response thoroughly, it can obviously lead to inaccuracies in the calculations of the hydrogen content. To avoid any influences of this competing reaction the hydrogen storage properties are often determined from discharging experiments only. Discharging occurs by simply changing the polarity of the current. However, discharging should stop in time to prevent oxidation of OH^- ions (see Reaction Eq. 2.6), as it can lead to errors in the dehydrogenation capacity and, moreover, O_2 formation should always be avoided as it can lead to self-discharge behavior (see reaction (2.7). Therefore, a cut-off potential at 0 V is used to ensure no O_2 is formed.

One of the advantages of electrochemistry is that the hydrogen content can be exactly calculated from the amount of charge (Q) that is used during the galvanostatic mode. Q can be quantified by integrating the current (I) with respect to time (t), according to

$$Q = \int_0^{t_{end}} |I|\, dt \quad (2.16)$$

Using the Faraday constant, the number of absorbed/desorbed moles of H can easily be calculated from the value of Q, as every electron corresponds to a single H atom that is inserted or extracted (see Reaction 2.12) via

$$\frac{Q}{F} = \text{mole H} \quad (2.17)$$

Together with the results of the RBS measurement, which gives insight into the exact composition and thickness of the thin film material (see paragraph 2.2), it can be used to calculate the hydrogen storage capacity per mass unit very accurately.

2.3.4 GITT charging and discharging

To obtain equilibrium data that can be used to construct pressure-composition isotherms (PCI), often requires advanced techniques. To assess the properties of thin film rules out the most common techniques, *e.g.* gravimetric analysis and volumetric Sievert's apparatus analysis, to determine PCI's as the equipment is not sensitive enough for the small weight and volume changes of the system as a function of hydrogen content. Fortunately, electrochemistry offers a method to assess the equilibrium properties of thin film hydride-forming materials, even for materials with an extremely low hydrogen partial pressures (down to 10^{-32} bar H_2 at room temperature). This method is known as the Galvanostatic Intermittent Titration Technique (GITT) and is used to obtain values for E^{eq} as a function of hydrogen content.[16] GITT is based on collecting equilibrium potential data by successively applying a current pulse followed by a current-off relaxation period. A single

current step and resulting electrochemical potential response are schematically illustrated in Fig. 2.8.

Starting at an equilibrium state, characterized by E_1^{eq}, the potential of the metal hydride (E) changes when the current is switched on at $t = 0$. At $t = t_{end}$ the current is interrupted and E relaxes toward a new equilibrium state (E_2^{eq}). The difference between E_1^{eq} and E_2^{eq} is due to the difference in hydrogen content which can be exactly calculated from the amount of charge (Q; Eq. 2.17) that is inserted or extracted during the current pulse. As was pointed out in paragraph 2.3.1, the electrochemical equilibrium potential can be converted into a partial hydrogen pressure (see Eq. 2.5). Using the RHE electrode is, however, not convenient and therefore, in the experiments described in this thesis, the more practical Hg/HgO reference electrode immersed in a 1 or 6 KOH solution is used. Consequently, a constant to account for the equilibrium potential of the HgO/Hg couple has to be added to Eq. 2.5, resulting in[9,17]

$$E^{eq} = -\frac{R\,T}{nF}\,ln\left(\frac{P_{H_2}}{P_{ref}}\right) - 0.926 \tag{2.18}$$

for a 1 M KOH solution and

$$E^{eq} = -\frac{R\,T}{nF}\,ln\left(\frac{P_{H_2}}{P_{ref}}\right) - 0.931 \tag{2.19}$$

for a solution with 6 M KOH.

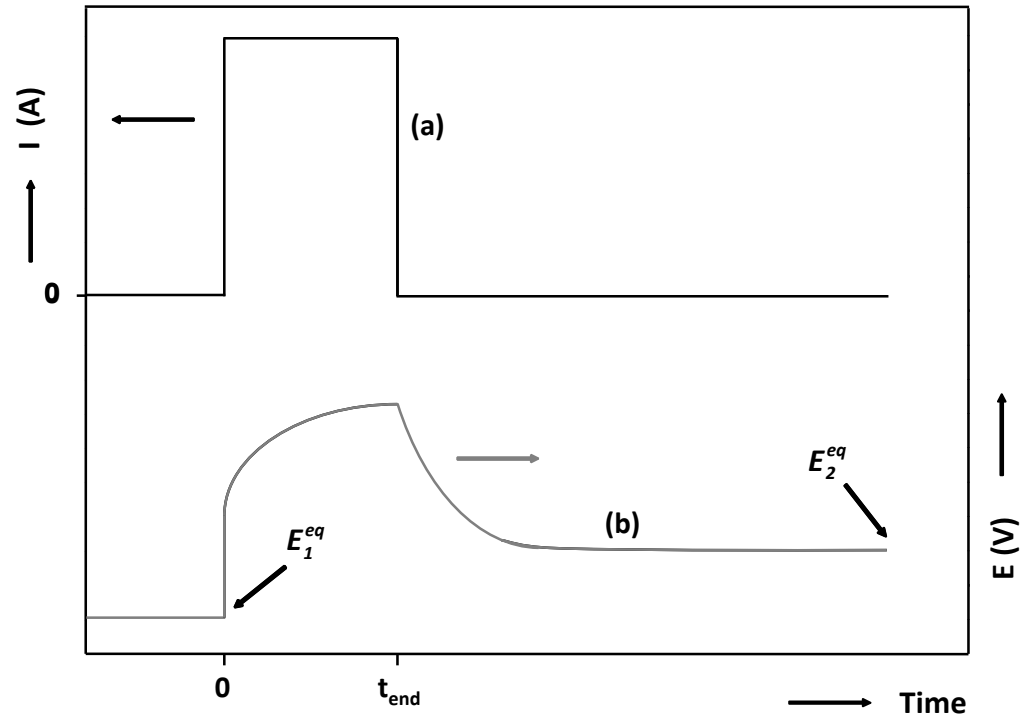

Fig. 2.8 Current pulse applied to the metal hydride electrode (a) and the resulting potential response (b). Indicated are the equilibrium potentials before (E_1^{eq}) and after (E_2^{eq}) the current pulse.

Plotting these values as a function of H-content yields the desired pressure-composition isotherms, which can be used to assess the thermodynamic stability of the metal-hydrogen system. Electrochemically obtained isothermal curves are generally determined under dehydrogenation conditions as incorrect calculations of the H content caused by the parasitic HER (see reaction 2.14) are then avoided. To avoid reaction 2.6 to occur, again a cut-off voltage of 0 V *vs.* Hg./HgO is used. Since conventional gas phase pressure-composition-temperature (PCT) isotherms are generally represented with increasing hydrogen content, the electrochemically determined isotherms in this thesis are, unless stated otherwise, plotted in accordance with this convention. In this thesis the time of a single current pulse was determined based on the hydrogenate/dehydrogenate in about 20 pulses. The relaxation time in all experiments was 1 hour.

2.3.5 Amperometry and cyclic voltammetry

An amperometric measurement is performed at a fixed electrochemical potential and is often referred to as a potentiostatic measurement. In this report we mostly use potentiostatic measurements to enable us to measure at a preselected equilibrium voltage. In the three-electrode setup used in our experiments, the potentiostat controls the voltage between the working electrode and the reference electrode. The potentiostat forces through the working electrode, at any time, the current that is required to achieve a constant potential between the working and reference electrode. Furthermore, it assures that current is only flowing through both the working- and counter electrode, whereas the current passing through the reference electrode remains infinitesimally small at all times.

A cyclic voltammetry measurement is a transient technique performed between two chosen electrochemical potential limits (E_1 and E_2) at a known linear sweep rate, υ (V/s), and measuring the current response at the working electrode. After reaching E_2, the potential is reversed back to E_1 or another chosen potential limit. A typical cyclic voltammetry measurement is shown in Fig. 2.9A and the resulting current response is depicted in Fig. 2.9B. It shows that scanning towards positive potentials and reaching the vicinity of E^0 initiates an oxidation reaction. Scanning the potential towards more positive values, leads to a drop of the surface concentration of the reacting agent, this increases the flux of the reactants to the electrode surface and, consequently, the current increases. Upon further increasing the potential, the surface concentration drops nearly to zero and the mass transfer to the surface reaches a maximum rate before it declines. The observation is therefore a peaked current-potential curve like that depicted in Fig. 2.9B. When changing the polarity of the electrode, when the scan direction is reversed towards E_1, the reactant will be reduced leading to a reduction current. The *I-E* curve for the reduction reaction has nearly the same shape as the oxidation reaction for essentially the same reasons. Assuming that the same, but reversed, reaction occurs during the potentials scans, the position of the peak current is then a measure for the reversibility of the reaction. Moreover, cyclic voltammetry gives information about the mechanism, equilibrium potential and rate of the reaction.

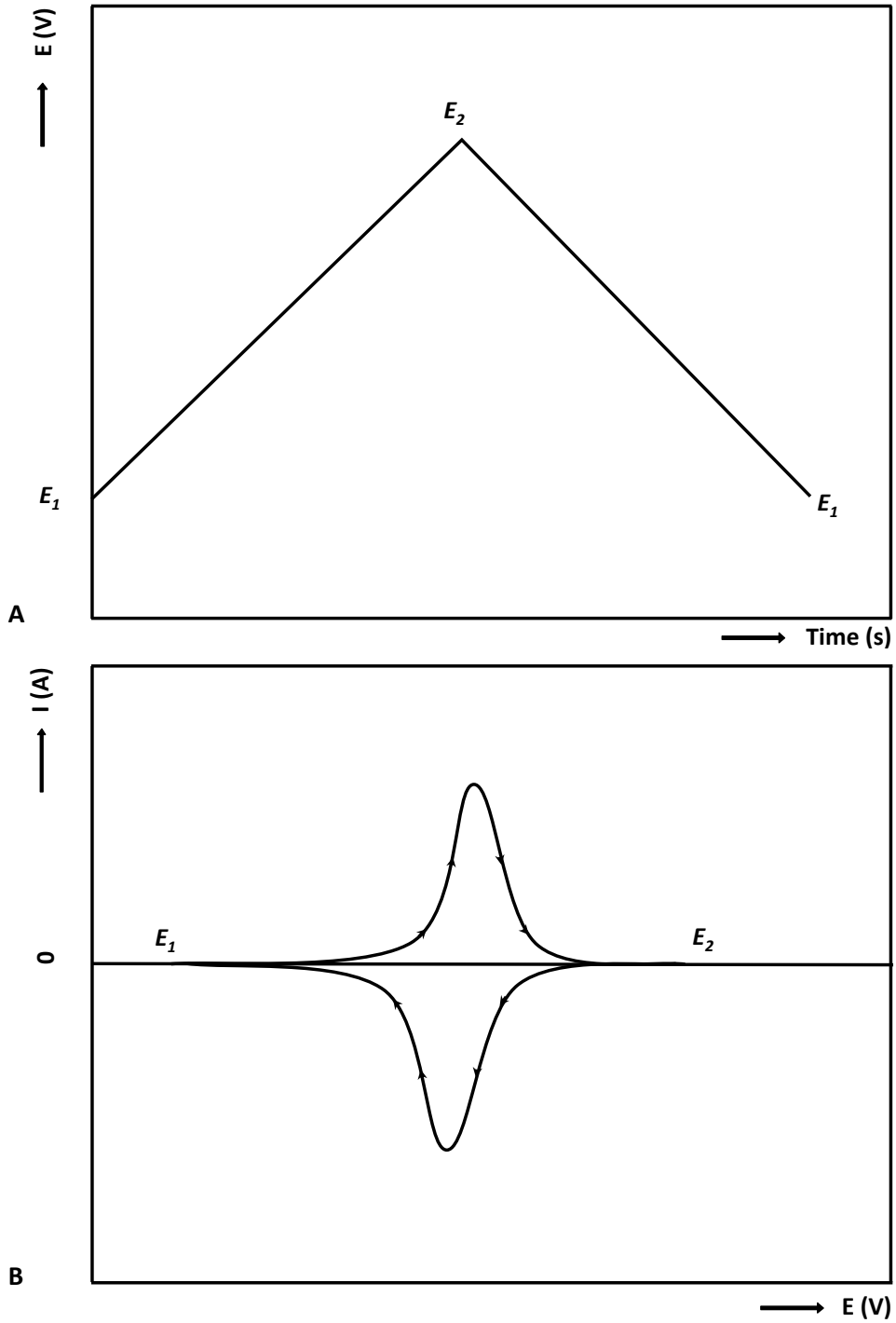

Fig. 2.9 (A) Schematic representation of the applied potential sweep during a cyclic voltammetry experiment and (B) an example of the resulting current response for a reversible electrochemical reaction.

2.3.6 Electrochemical impedance spectroscopy

Electrochemical impedance spectroscopy (EIS) is a technique that is generally used to *separate* and *quantify* the impedance of (electro)chemical processes and reactions.[18,19] EIS

monitors the system response to the application of an electrical perturbation to the system. The impedance (Z) of a system is defined as

$$Z = \frac{E}{I} \tag{2.20}$$

where E is the electrochemical potential and I is the current. Eq. 2.20 shows that the impedance of the system can be measured both under potentiostatic and galvanostatic control. A typical impedance spectroscopy experiment is performed under potentiostatic control and the resulting current is monitored. Then, one puts a direct current voltage across the working- and reference electrode (E_{DC}) and superimposes an oscillating alternating current potential (E_{AC}) according to

$$E = E_{DC} + E_{AC} = E_{DC} + E_m sin(\omega t) \tag{2.21}$$

where E_m is the amplitude of the sinusoidal perturbation and ω is the angular frequency. ω (radians/s) is defined as

$$\omega = 2\pi f \tag{2.22}$$

where is f is the frequency expressed in Hz. The amplitude of the electrical perturbation should be small enough to ensure (pseudo)linear I-E behavior (*i.e.* $I \propto E$), which is shown in Fig. 2.10. For an EIS measurement with potentiostatic control a typical value of the amplitude of the sinusoidal potential perturbation is 10 mV or less. Moreover, using a small amplitude perturbation limits the occurrence of harmonics of the excitation frequency.

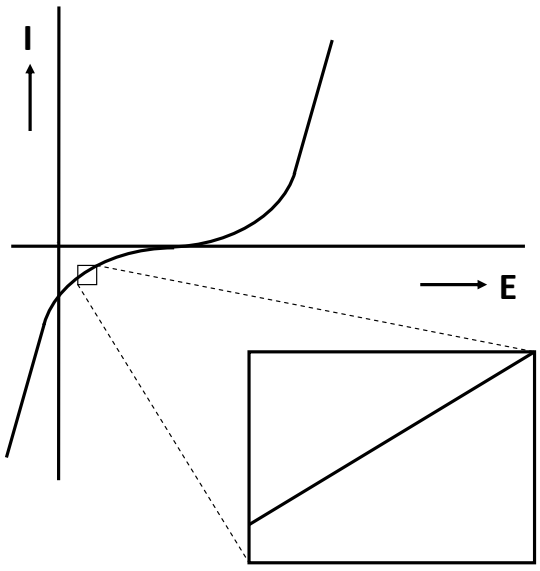

Fig. 2.10 Current versus voltage curves showing pseudo-linearity.

The current response to the sinusoidal potential perturbation (Eq. 2.21) consists of two parts, *i.e.* a constant current (I_{DC}) and an alternation current (I_{AC}), according to

$$I = I_{DC} + I_{AC} = I_{DC} + I_m sin(\omega t + \varphi) \quad (2.23)$$

In case of (pseudo)linear *I-E* behavior, I_{AC} reveals the same sinusoidal behavior as the potential perturbation, where the amplitude of the current oscillation (I_m) is distinct for the system. Depending on the electrochemical system the current response can be in phase with the potential perturbation or shifted by a phase angle (φ). The current or voltage response by a voltage or current perturbation, respectively, for a system where φ=0° (Fig. 2.11A) and φ=90° (Fig. 2.11B).

The possible occurrence of a phase shift is discussed by evaluating the response of some typical electrical components, which can be used to mimic the behavior of the electrochemical cell. Often a combination of these components is used to fit the experimental data, also known as an equivalent circuit (EQC), to obtain relevant physical properties of the system. Here, we discuss two circuit elements in detail, *i.e.* a resistor and a capacitor.

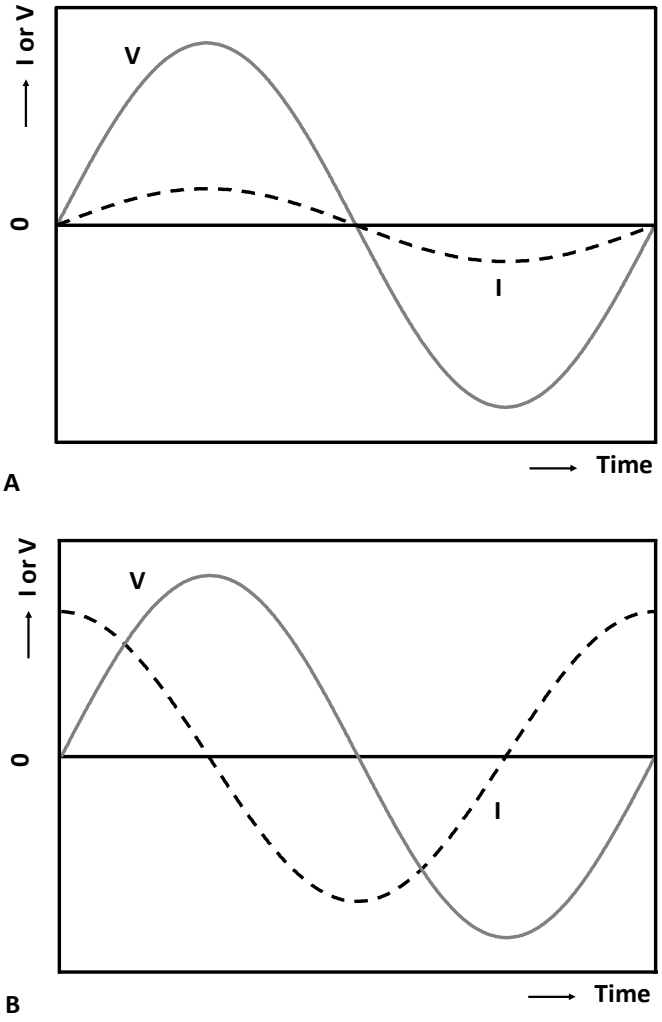

Fig. 2.11 Sinusoidal current and voltage behavior where φ=0° (A) and φ=90° (B). .

The current across a resistor is defined as

$$I_R = \frac{E}{Z} = \frac{E_{DC}}{Z} + \frac{|E_m|}{Z} sin(\omega t) \tag{2.24}$$

The impedance is

$$Z_R = \frac{|E_m| sin(\omega t)}{|j_m| sin(\omega t)} = \frac{|E_{AC}|}{|j_{DC}|} = R \tag{2.25}$$

which shows that the response is purely Ohmic (*i.e.* the current is in phase with the potential). This behavior is typical for a poorly conducting ionic electrolyte.

For a capacitor the current is equal to the time derivative of the potential

$$I_C = C\frac{dE}{dt} = I_{AC} = C|E_m|\omega cos(\omega t) = C|E_m|\omega sin\left(\omega t + \frac{\pi}{2}\right) \tag{2.26}$$

The current response is purely capacitive, the current is $\pi/2$ or 90° out of phase with the potential. This behavior is typical for the solid liquid interface and a capacitor is often used to mimic the effect of the double layer, hence the name double layer capacitance. The impedance of a capacitor (Z_C) is

$$Z_C = \frac{|E_m| sin(\omega t)}{C|E_m|\omega sin\left(\omega t + \frac{\pi}{2}\right)} \tag{2.27}$$

To acquire a phase shift in the original expression of the impedance, a complex impedance is defined that exists of a real and an imaginary part. Eq. 2.21 is therefore redefined as

$$E = E_{DC} + E_{AC} = E_{DC} + E_m exp(i\omega t) \tag{2.28}$$

where $i = \sqrt{-1}$, and $exp(i\omega t) = cos(\omega t) + isin(\omega t)$ (Euler's equation). For the capacitor current we now find

$$I_C = iCE_m\omega exp(i\omega t) \tag{2.29}$$

The impedance of the capacitor is

$$Z_C = \frac{E_{AC}}{j_{DC}} = \frac{1}{i\omega C} = -\frac{i}{\omega C} \tag{2.30}$$

Note that at high frequencies Z_C is small, whereas at low frequencies Z_C is large, therefore the impedance of a capacitor behaves like a resistor that varies with frequency.

If we now put a resistor and capacitor in series, which is the equivalent circuit for an ideally polarizable electrode in series with a finite Ohmic resistance of the electrolyte, the total impedance is the summation of the two, represented by

$$Z_{tot} = Z_R + Z_C = R - \frac{i}{\omega C} \tag{2.31}$$

Eq. 2.31 shows that the impedance consists of a real (Z') and an imaginary part (Z''). In Cartesian coordinates the impedance is written as

$$Z_{tot} = Z' + iZ'' \tag{2.32}$$

The impedance results are often presented in a Bode or Nyquist plot. In a Bode plot, Z', Z'', $|Z|$ or φ are plotted as a function of the excitation frequency. A Nyquist plot shows the results by plotting $-Z''$ as a function of Z'.

Placing a resistor and a capacitor in parallel gives

$$\frac{1}{Z_{tot}} = \frac{1}{Z_R} + \frac{1}{Z_C} = \frac{1}{R} + i\omega C \tag{2.33}$$

Rewriting Eq. 2.33 leads to

$$Z_{tot} = \left(\frac{1}{R} + i\omega C\right)^{-1} = \frac{R(1 - i\omega CR)}{(1 + \omega^2 C^2 R^2)} \tag{2.34}$$

which is the equation of a semi-circle in a Nyquist plot. The real part of Eq. 2.34 is given by

$$Z_{Re} = \frac{R}{(1+\omega^2 C^2 R^2)} \tag{2.35}$$

The value of R can easily be obtained at very low frequencies, where $Z_{Re} = R$.
The imaginary part of Eq. 2.34 is

$$-Z_{im} = \frac{\omega CR^2}{(1+\omega^2 C^2 R^2)} \tag{2.36}$$

From the maximum of the semi-circle in the Nyquist plot (or at $\frac{d\text{-}Z_{im}}{d\omega} = 0$) we get the value of $\frac{1}{RC}$. As the resistance is known from the analysis at low frequencies, the capacitance can now be calculated easily.

Mass transport is often modeled with a Warburg impedance (*W*). For this, the Cottrell equation is used, which is represented by

$$I=nFAc_0\sqrt{\frac{D}{\pi t}} \tag{2.37}$$

where c_0 is the initial concentration of the species being reduced or oxidized and D is the diffusion coefficient. Rewriting Eq. 2.37 into the frequency domain leads to

$$I = nFAc_o\sqrt{\frac{Df}{\pi}} \tag{2.38}$$

From Eq. 2.38 it is clear that for $f \uparrow$, $I \uparrow$ (and Z $\downarrow$) and for $f \downarrow$, I $\downarrow$ and consequently Z $\uparrow$. Hence, the Warburg diffusion appears only at low frequencies. To get Z_W, the diffusion equation is solved with sinusoidal boundary conditions, the resulting equation is

$$Z_W = \sigma\omega^{-\frac{1}{2}} - i\sigma\omega^{-\frac{1}{2}} \text{ with } \sigma = f(c_o, D_o, c_R, D_R) \tag{2.39}$$

Eq. 2.39 shows that $Z_{\mathrm{Re}} = -Z_{im}$, therefore it will give a line with a 45° angle is a Nyquist plot. An example of a Nyquist plot for the electric circuit depicted in Fig. 2.12A, also known as the Randles circuit, is shown in Fig. 2.12B.

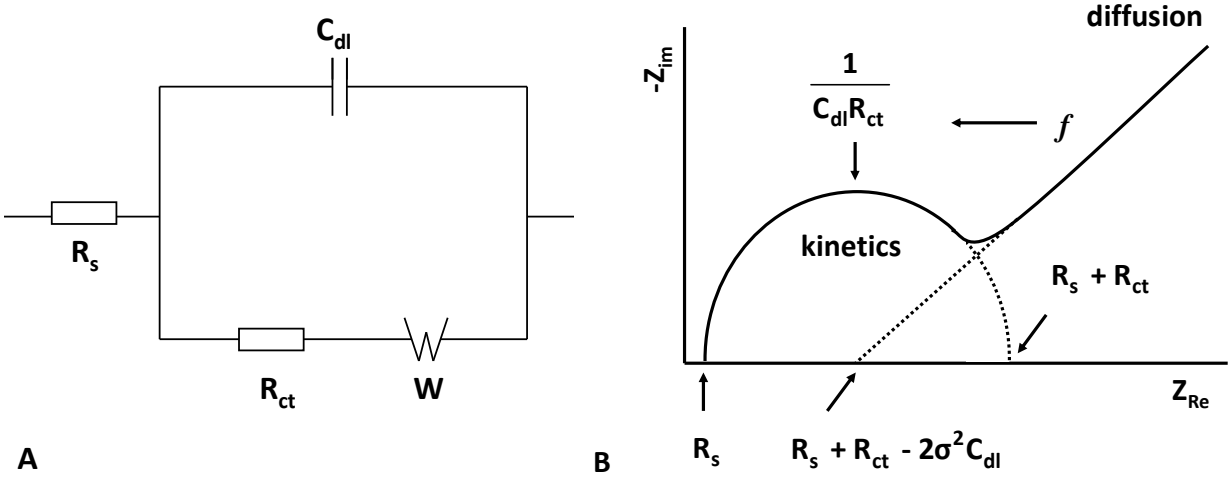

Fig. 2.12 (A) Randles equivalent circuit and (B) corresponding Nyquist plot showing the frequency dependence of the impedance.

The impedance measurements performed in this thesis are combined with GITT to obtain data as a function of hydrogen content. For example, the exchange current density that results from the Butler-Volmer curves can be assessed. The EIS experiments were conducted at equilibrium voltage conditions using a ac amplitude of 5 mV rms and scanning the frequency from 50 kHz to 1 mHz. A non-linear least squares fitting program (EQUIVCRT) was used to analyze the EIS data.[20,21]

2.4 X-ray Diffraction

The phases present in solid state materials are often characterized by XRD which is a versatile and non-destructive technique that reveals detailed information about the crystallographic structure.

2.4.1 Background

X-ray diffraction is observed when electromagnetic radiation impinges on periodic structures with geometrical variations on the length scale of the wavelength of the radiation. The interatomic distances in crystals typically amount to 0.15-4.0 nm. Only when X-rays with a wavelength (λ) and an angle of incidence (θ) exactly fit once or n times, where n is an integer, between the crystal planes separated by a distance d, constructive interference is observed in the form of a diffraction peak (see Fig. 2.13). This is represented by the Bragg equation, according to

$$n\,\lambda = 2\,d\,\sin\theta \tag{2.40}$$

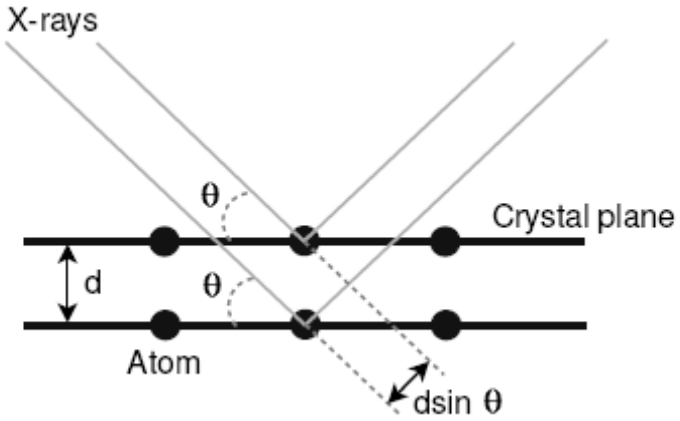

Fig. 2.13 Illustration of diffraction of parallel X-rays with a wavelength of λ from atoms in a set of crystal planes separated by a distance of d. The diffraction angle is θ.

In a crystal the positions of the atoms are periodic in all three dimensions and form the crystal lattice. Within the lattice it is possible to determine the unit cell, which is the smallest unit that describes the structure of the entire crystal by translation into the three dimensions. The unit cell is characterized by the lattice parameter a, b and c that represent the lengths of the crystallographic unit cell, while α, β and γ are the angles between them. Directions with repeating units in crystals are described by the Miller indices h, k and l, which define a set of lattice planes (hkl) in that direction. The Miller indices specify the points of intersection of the lattice planes with the unit cell axes. As an example, the lattice planes with Miller indices (100) en (111) are depicted in Fig. 2.14 for a simple cubic lattice.

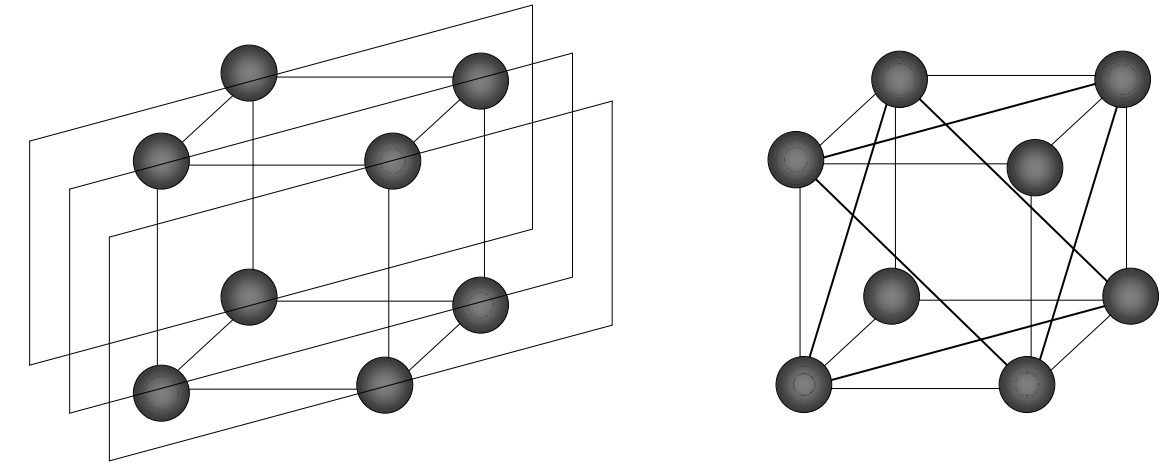

Fig. 2.14 Lattice planes with Miller indices (110) (A) and (111) (B) in a simple cubic lattice.

The distance between two adjacent planes is given by the interplanar distance (d_{hkl}) with the indices specifying the Miller indices of the appropriate lattice planes. For orthogonal lattices (*i.e.* cubic, orthorhombic and tetragonal) the d_{hkl} spacing can be calculated with

$$d_{hkl} = \frac{a}{\sqrt{h^2 k^2 l^2}} \tag{2.41}$$

2.4.2 Grain size

The as-prepared states of the thin film alloys are investigated by XRD using a Panalytical X'Pert MPD PRO diffractometer, equipped with a Cu source and a X'Celerator detector. Besides the dimensions and symmetry of the unit cells in the crystalline solid, another property that can be analyzed by XRD is the grain size. To quantify the grain size, the Scherrer equation can be used, according to

$$D = \frac{K\lambda}{B_{1/2}\ cos\theta} \tag{2.42}$$

where D is the diameter of the grain, K is the shape factor (typical value is 0.9), λ is the wavelength of the incident beam (1.54 Å), $B_{1/2}$ is the line-width in radians at half maximum peak intensity and θ is the Bragg angle.[22] $B_{1/2}$ must be corrected for broadening originating from the instrument (B_{instr}) and takes the form

$$B_{1/2}^2 = B_{obs}^2 - B_{instr}^2 \tag{2.43}$$

where B_{obs} is the observed width. However, since in our case

$$B_{obs} >> B_{instr} \tag{2.44}$$

Eq. 2.42 simplifies to

$$D = \frac{K\lambda}{B_{obs}\ cos\theta} \tag{2.45}$$

2.4.3 Texture formation

For a powder it is generally assumed that all grain orientations occur with the same probability. For thin polycrystalline films the distribution of crystallite orientation is only rarely isotropic.[23] The anisotropy of crystallite orientation is called texture or preferred orientation. This phenomenon can significantly affect the diffraction pattern, as a pronounced enhancement of certain Bragg reflections, whereas others completely vanish. Obviously, if only a limited number of reflections are observed in the diffraction pattern it can be difficult, if not impossible, to determine the crystal structure of the lattice.

A way to determine all the lattice parameters is therefore to determine the position of the other reflections under various orientations. By changing the tilt angle (ψ) of the sample other reflections appear in the diffraction patterns, while others disappear.

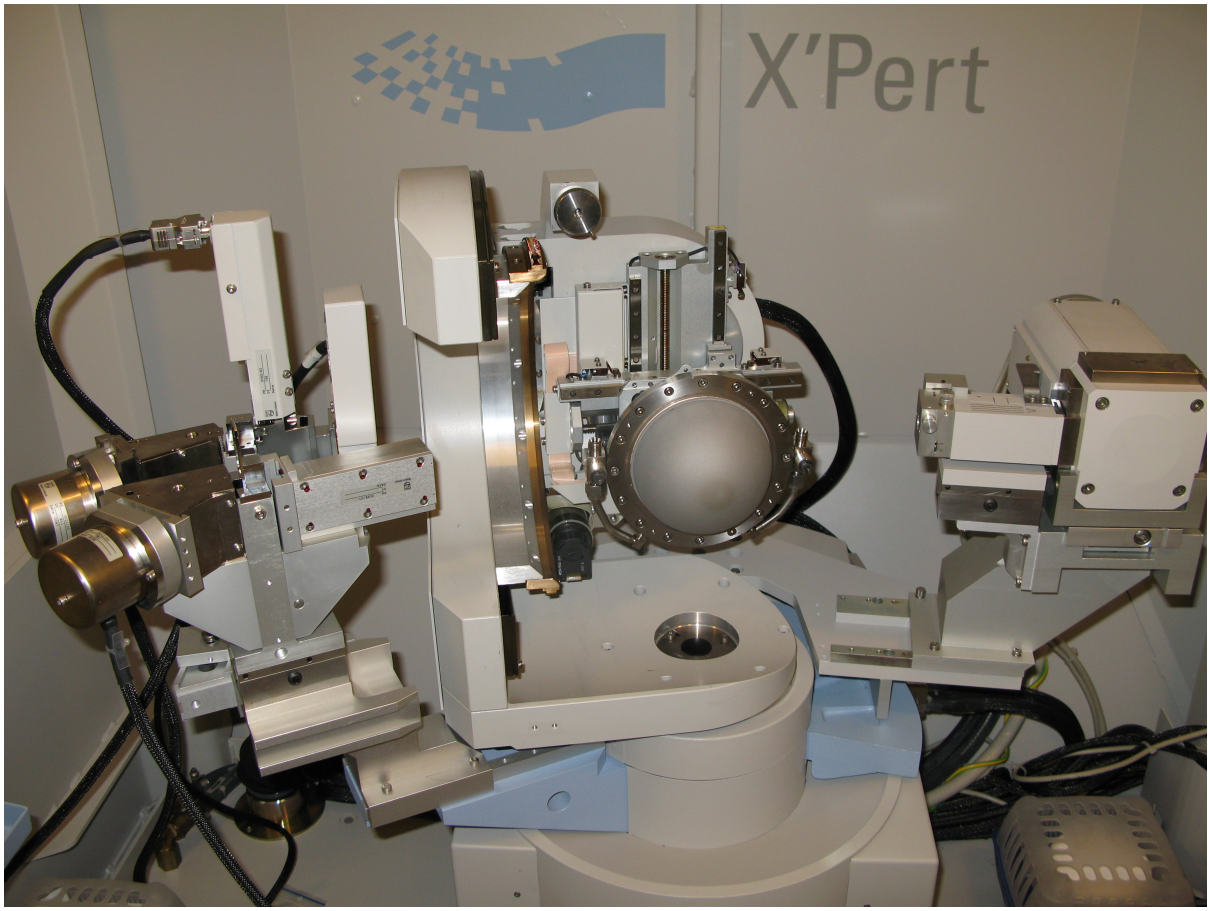

Fig. 2.15 X-ray diffractometer equipped with a Be dome.

XRD gas phase measurements were performed to identify the crystal structures that are present in the Mg-Ti layers in both the as-deposited and hydrogenated state. For each XRD experiment a sample was placed in a container that consisted of a stainless steel backplate, with gas inlet and outlet, and a Be dome (wall thickness 0.51 mm; inner radius 53.34 mm) that was brazed to a stainless steel ring, serving as a gas seal. XRD measurements were performed before and after hydrogenation. The latter was attained by flushing the container with H_2 at 10^5 Pa for at least 5 minutes before the inlet and outlet valves were closed. Hereafter, the sample holder was installed on the 4-circle goniometer (open Eulerian cradle) of a Philips X'Pert PRO MRD diffractometer. The diffractometer was equipped with a Cu X-ray source, a polycapillary X-ray lens in the incident beam and a 0.27° parallel plate collimator and graphite monochromator in the diffracted beam. The incident beam size was manually set at 2×2 mm^2 or 3×3 mm^2 using a cross slit collimator at the end of the X-ray lens. Continuous 2θ-θ scans were recorded at tilt angles (ψ) between 0° and 84° with a step size of 6°. Each scan ranged from at least 25° to 55° 2θ with a step size of 0.04° 2θ and a measurement time of 20 s/step. Additionally, ψ scans were recorded around some of the detected diffraction peaks to determine a more accurate ψ-position of the peak. It was verified that the crystallites of the Mg-Ti and Pd layers have a crystallographic fiber texture with axes normal to the substrate, which implies that the measurements should be independent of the rotation angle (φ) around the sample normal.

2.4.4 *In situ* electrochemical X-ray diffraction

The advantages of the combination of X-ray diffraction and electrochemistry were first realized by Uno Falk and co-workers around 1960.[24,25] The *in situ* technique was used to investigate the phases present in the nickel-cadmium battery and the negative electrode of the alkaline iron battery. Prior studies, which were all conducted *ex situ*, gave no conclusive evidence about the chemical formulas of the materials. In fact, some of the results were difficult to interpret owing to possible atmospheric reactions. *In situ* XRD measurements showed unambiguously the existence of, amongst others, $Fe(OH)_2$, Fe_3O_4, $Cd(OH)_2$, $Ni(OH)_2$ and NiOOH. Surprisingly, these results did not lead to a combined use of XRD and electrochemistry. Only in the late 1970s the potential of this technique was rediscovered by electrochemists.[26]

The foremost problem in designing an electrochemical cell that allows simultaneous XRD measurements and electrochemical control is the limited penetration depth of X-rays. Therefore, experiments are either done in reflection mode, in which case the electrode is located close to an X-ray transparent window, or in transmission mode using very thin (two-electrode) cells.

Fig. 2.16 Schematic representation of the layered structure of a 200 nm thick Mg_yTi_{1-y} thin film alloy capped with a 10 nm thick Pd layer deposited on PEEK using a 1 nm Cr adhesion layer.

The X-ray transparent windows reported in the literature include beryllium, thin metal foils (*e.g.* Al and Ni) and polymers such as polyimide (Kapton) and polyester (Mylar). Our *in situ* electrochemical X-ray diffraction measurements are conducted in a strong alkaline solution (1 M KOH), which obviously limits the choice of the window material. For the experiments described in this thesis a Poly-Ether-Ether-Ketone (PEEK) foil with a thickness of 125 μm was used, owing to its particularly high resistance to alkaline solutions. Moreover, its mechanical strength is high enough to ensure that no *height error* arises from possible strains that build up during the hydrogenation process of the material. A small amount of finely powdered Ni, adhered to the outside of the PEEK foil, served as reference to monitor any displacement of the foil during hydrogen absorption and desorption. No displacement was observed during the measurements and therefore no corrections for the height of the sample were required. Another important property of PEEK is that it is amorphous, which avoids any interference to the Bragg reflections of the material under investigations. The adhesion of Mg-Ti alloys to PEEK foil was found to be quite poor, therefore a 1 nm thick Cr adhesion layer was applied. Note that Cr hydride is not stable under experimental conditions of the *in situ* XRD measurements and consequently any hydrogen absorption by the Cr adhesion layer can be neglected.[8] A schematic representation of the foil and sputtered layers is depicted in Fig. 2.16.

The *in situ* electrochemical measurements were performed using a three-electrode cell made out of polyvinylidene fluoride (PVDF), which is depicted in Fig. 2.17. The design of this cell is based on the work of Meulenkamp.[27] The working electrode was positioned at the front of the cell and pressed onto a copper ring to provide electrical contact. To prevent contact between the copper ring and the electrolyte, and to avoid leakage, O-rings were placed inside and outside the copper ring. The surface area of the MgTi layer exposed to the electrolyte was 8 cm^2. The electrochemical experiments were carried out in a 1 M KOH solution at room temperature. Again, special care was taken to avoid any interference of oxygen by purging the electrolyte prior to the experiment for 1 hour with O_2-scrubbed Ar, using the methylviologen setup described in paragraph 2.3.2. The *in situ* electrochemical XRD cell was mounted on a Philips PW 1835 horizontal diffractometer. Gonio (θ-2θ) scans

were recorded using a Cu source to generate Kα radiation (λ=1.54 Å). To increase the peak-to-noise ratio the XRD patterns were smoothed.

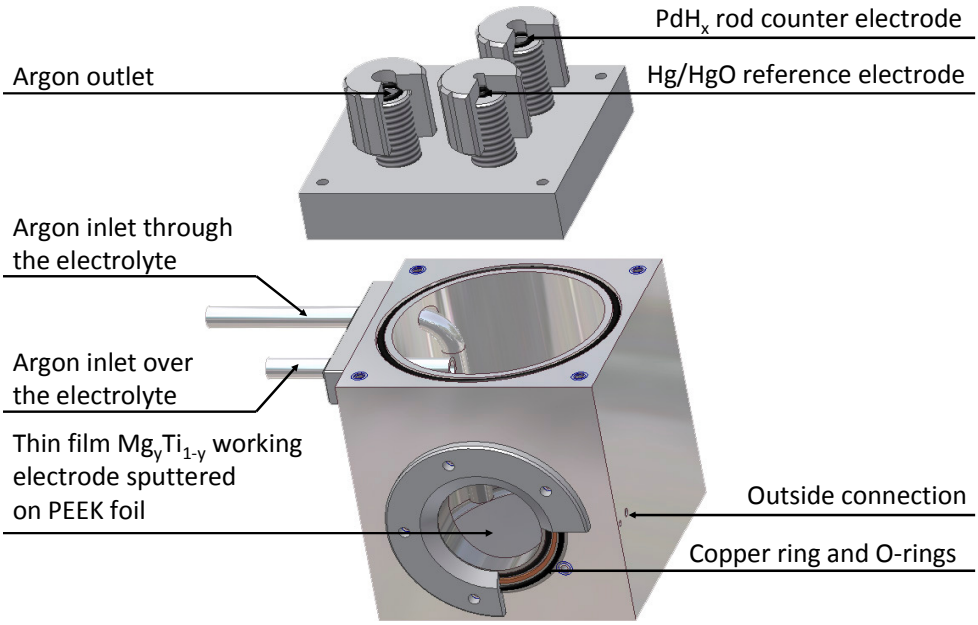

Fig. 2.17: Schematic representation of the *in situ* electrochemical XRD cell, indicating the positions of the Mg_yTi_{1-y} working electrode sputtered on PEEK foil, the PdH_x counter electrode and the Hg/HgO reference electrode. Also the argon inlets (through and over the electrolyte) and argon outlet are shown. The working electrode was pressed onto a copper ring that is connected to the outside.

2.5 References

1 L. Vegard, *The constitution of mixed crystals and the space occupied by atoms*, Z. Physik **1921**, *5*, 17-26.

2 P.H.L. Notten and J.R.G. van Beek, *Nickel-metal hydride batteries: from concept to characteristics*, Hemijska Industrija **2000**, 54, 102-115.

3 P.H.L. Notten, *Rechargeable nickel-metalhydride batteries: a successful new concept* in *Interstitial Intermetallic Alloys*, NATO ASI Series E, Vol. 281 (Eds. F. Grandjean, G. L. Long, K. H. J. Buschow), Kluwer Academic Publishers, Dordrecht, **1995**, 151-195.

4 M. Ikoma, S. Hamada, N. Morishita, Y. Hoshina, H. Matsuda, K. Ohta and T. Kimura, *Development of a nickel/metal hydride battery (Ni/MH) system for EV application*, Proceedings of the symposium in hydrogen and metal hydride batteries **1994**, *94*, 371.

5 C. Lartigue, A. Percheron-Guegan, J.C. Achard and J.L. Soubeyoux, *Hydrogen (deuterium) ordering in the β-$LaNi_5D_{x>5}$ phases - a neutron diffraction study*, J. Less-common Metals **1985**, *113*, 127-148.

6 P. Thompson, J.J. Reilly, L.M. Corlis, J.M. Hastings and R. Hempelmann, *The crystal-structure of $LaNi_5D_7$*, J. Phys. F **1986**, *16*, 679-685.

7 L. Schlapbach and A. Züttel, *Hydrogen-storage materials for mobile applications*, Nature (London) **2001**, *414*, 353-358.

8 K.H.J. Buschow, P.C.P Bouten and A.R. Miedema, *Hydrides formed from intermetallic compounds of two transition metals: a special class of ternary alloys,* Rep. Prog. Phys. **1982**, *45*, 937-1039.

9 R. Griessen and T. Riesterer, *Topics in Applied Physics Hydrogen in Intermetallic Compounds*, *Chapter 6: Heat of Formation Models*, Vol. 63 (Ed. L. Schlapbach), Springer-Verlag, Berlin, **1988**, 219-284

10 J.J.G. Willems, *Metal hydrides electrodes stability of $LaNi_5$-related compounds*, Philips J. Res. Suppl. **1984**, *39*, 1-94.

11 R.A.H. Niessen and P.H.L. Notten, *Reference electrode-induced surface poisoning of thin film electrodes*, J. Electrochem. Soc. **2005**, *152*, A2051-A2057.

12 R.A.H. Niessen and P.H.L. Notten, *The influence of O_2 on the electrochemistry of thin film, hydrogen storage, electrodes,* Electrochim. Acta **2005**, *50*, 2959-2965.

13 R.A.H. Niessen, *Electrochemical hydrogen storage in lightweight electrode materials*, Ph.D. Thesis, Eindhoven University of Technology, **2006**.

14 P.B. Sweetster, *Calorimetric determination of trace levels of oxygen in gases with the photochemically generate methyl viologen radical-cation*, Anal. Chem. **1967**, *39*, 979-982.

15 K. Machida, M. Enyo, G. Adachi and J. Shiokawa, *The hydrogen electrode reaction characteristics of thin film electrodes of Ni-based hydrogen storage alloys*, Electrochim. Acta **1984**, *29*, 807-815.

16 W. Weppner and R.A. Huggins, *Determination of the kinetic parameters of mixed-conducting electrodes and application to the system Li_3Sb*, J. Electrochem. Soc. 1977, *124*, 1569-1578.

17 H. Senoh, K. Morimoto, H. Inoue, C. Iwakura and P.H.L. Notten, *Relationship between equilibrium hydrogen pressure and exchange current for the hydrogen electrode reaction at $MmNi_{3.92-x}Mn_{0.4}Al_xCo_{0.7}$ alloy electrodes*, J. Electrochem. Soc. **2000**, *147*, 2451-2455.

18 J.R. Macdonald, *Impedance Spectroscopy: emphasizing solid materials and systems*, John Wiley & Sons, **1987**.

19 A.J. Bard and L.R. Faulkner, *Electrochemical methods, fundamentals and applications*, 2nd Ed., John Wiley & Sons, Inc., Chapter 10, **2001**.

20 B.A. Boukamp, *A package for impedance/admittance data analysis*, Solid State Ionics **1986**, *18-19*, 136-140.

21 B.A. Boukamp, *A nonlinear least squares fit procedure for analysis of immitance data of electrochemical systems,* Solid State Ionics **1986**, *20*, 31-44.

22 L.S. Birks and H. Friedman, *Particle size determination from X-ray line broadening*, J. Appl. Phys. **1946**, *17*, 687-692.

23 M. Birkholz, *Thin film analysis by X-ray scattering*, Wiley-VCH Verlag GmbH & Co. KGaA, **2006**.

24 S. Uno Falk, *Investigations of the reaction mechanism of the nickel-cadmium cell*, J. Electrochem. Soc. **1960**, *107*, 661-667.

25 A.J. Salkind, C.J. Venuto and S. Uno Falk, *The reaction at the iron alkaline electrode*, J. Electrochem. Soc. **1964**, *111*, 493-495.

26 R.R. Chianelli, J.C. Scanlon and B.M.L. Rao, *Dynamic X-ray diffraction***,** J. Electrochem. Soc. **1987**, *125*, 1563-1566.

27 E.A. Meulenkamp, *An electrochemical cell for simultaneous in situ X-ray diffraction and optical measurements*, J. Electrochem. Soc. **1998**, *145*, 2759-2762.

3

Hydrogen storage in Pd thin films

Abstract

A lattice gas model was presented recently and successfully applied to simulate the absorption/desorption isotherms of various hydride-forming materials. The simulation results are expressed by parameters corresponding to several energy contributions, *e.g.* interaction energies. However, the use of a model-system is indispensable in order to show the strength of the simulations. The palladium-hydrogen system is one of the most thoroughly described metal hydrides found in the literature and is therefore ideal for this purpose. The effects of decreasing the thickness of Pd thin films on the isotherms have been monitored experimentally and subsequently simulated. An excellent fit of the lattice gas model to the experimental data is found and the corresponding parameters are used to describe several thermodynamic properties. It is found that the contribution of H-H interaction energies to the total energy and the influence of the host lattice energy are significantly and systematically changing as a function of Pd thickness. Conclusively, it has been verified that the lattice gas model is a useful tool to analyze thermodynamic properties of hydrogen storage materials.

A Pd topcoat is often applied to hydride-forming thin film materials to protect them from oxidation and electrocatalyze the reduction of H_2O, which is one of the essential steps in electrochemical hydrogenation. As a 10 nm Pd caplayer is applied to the Mg-based alloys throughout the remainder of this thesis, it is useful to determine its electrocatalytic properties separately.[*]

---

[*] Part of this chapter is based on:

P. Vermeulen, A. Leydovskikh, D. Danilov and P.H.L. Notten, *Impact of the layer thickness on the thermodynamics of Pd thin film electrodes*, J. Phys. Chem. B **2006**, 20350-20353.

R.A.H. Niessen, P. Vermeulen and P.H.L. Notten, *The electrochemistry of Pd-coated $Mg_ySc_{(1-y)}$ thin film electrodes: A thermodynamic and kinetic study,* Electrochim. Acta **2006**, *51*, 2427-2436.

A. Leydovskikh, D. Danilov, P. Vermeulen and P.H.L. Notten, *Electrochemical modeling of hydrogen storage in hydride-forming electrodes*, Electochim. Acta **2008**, submitted.

A. Ledovskikh, D. Danilov, P. Vermeulen and P.H.L. Notten, *Surface kinetic effects of hydrogen storage: Complete electrochemical kinetic model*, in preparation.

3.1 Introduction

Recently, a theoretical lattice gas model based on the principles of statistical thermodynamics has been proposed to calculate the thermodynamic properties of hydride-forming materials.[1] The model can be used to describe the equilibrium electrode potentials and pressure-composition isotherms of metal hydrides (MH) as a function of hydrogen concentration in both the α- and β-solid solutions and two-phase coexistence region. In particular, equilibrium characteristics of $LaNi_yCu_{1.0}$ alloys with $4.0 \leq y \leq 5.0$ and MischMetal-based AB_5 compounds at various temperatures were simulated. A good agreement between calculated and experimental isotherms was found.

The use of a so-called model-system is, however, indispensable to verify and ultimately show the strength of this model. Palladium hydride is ideal for this purpose as it is one of the most thoroughly described metal-hydrogen systems found in the literature, *e.g.* a comprehensive monograph by Lewis is fully devoted to this system.[2]

In 1980, Frazier and Glosser reported a narrowing of the plateau width of isotherms of PdH_x layers as well as an increasing slope of the α-to-β phase transition region with decreasing film thickness.[3] Extensive studies were carried out by Griessen and co-workers also showed that the critical temperature (T_c) decreased as a function of film thickness.[4,5] While the former results were obtained from gas phase experiments, Nicolas *et al.* used electrolytic (de)hydrogenation and showed the impact of the thickness of thin Pd layers (6-60 nm) with respect to T_c, *i.e.* T_c decreased with decreasing film thickness.[6] The marked drop of T_c with decreasing film thickness was attributed to clamping effects of the thin film to the substrate. More elaborate studies on the influence of the thickness of Pd films, with a nominal thickness of 10, 50, 100, 150 and 200 nm, on the isotherms and corresponding thermodynamics have been performed and are discussed in paragraph 3.2.1.

Extending the knowledge of PdH_x thin films is desirable as, especially in thin film research aimed on developing high-energy density metal hydrides and switchable mirror materials, a thin Pd topcoat is often applied to prevent the underlying layer from oxidizing.[7-10] Additionally, the Pd overlayer catalyzes H_2 dissociation in gas phase loading and electrocatalyzes the charge transfer process in electrochemical (de)hydrogenation. To assess the electrocatalytic properties of Pd thin film electrodes with a typical thickness of 10 nm Electrochemical Impedance Spectroscopy (EIS; see paragraph 2.3.6) is used. The results are described in paragraph 3.2.2.

3.2 Results & discussion

3.2.1 Thermodynamics of Pd hydride thin film electrodes

The isotherms of Pd layers with various thicknesses were determined electrochemically. Generally, isotherms are obtained during hydrogenation, however, the hydrogen evolution reaction (HER, see reaction (2.14)) can seriously intervene with the hydrogenation reaction resulting in inaccurate hydrogen storage capacities. Therefore, to avoid the HER and to monitor the hydrogen content accurately, the electrochemically determined isotherms are measured during dehydrogenation. To this end, the thin films were first galvanostatically

charged to their fully hydrogenated state using a current of -0.12 mA. Subsequently, the electrodes were allowed to equilibrate for 1 h. Hereafter, the PdH_x electrodes were discharged by means of GITT in approximately 20 pulses using a current of +0.12 mA.

Fig. 3.1 shows the experimentally determined equilibrium points (symbols) together with the corresponding equilibrium curve (curve (a)), as well as the dynamic potential responses of a 150 nm thick Pd film during each current pulse (curves (b)). From the latter it is evident that during the hydrogen-rich β-solid solution and the β-to-α phase transformation plateau, the overpotential (η) remains nearly constant, only to increase significantly at the hydrogen depleted state. In the electrochemical experiments, a 1 nm thick Gd layer, used to enforce a good adhesion, is assumed not to influence the electrochemical response as it is known from experiment that films of less then 3 monolayers do not absorb any appreciable amount of hydrogen.[11]

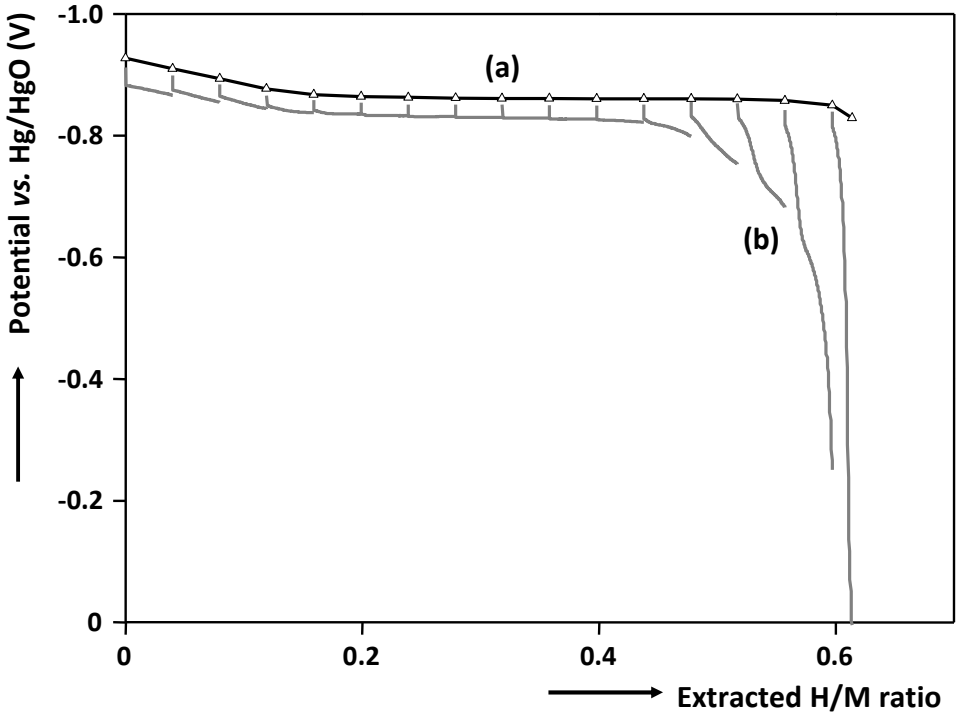

Fig. 3.1 Equilibrium curve of a 150 nm thick Pd thin film electrode. The equilibrium points (Δ) are determined by means of GITT during discharging and the corresponding isotherm is shown by curve (a). The electrochemical response during each current pulse (I=+0.12 mA) is shown by curves (b).

To simulate the thermodynamic properties of PdH_x, the recently developed lattice gas model is used.[1] Combining structural assumptions, mean field approximations and a binary alloy approach, the lattice gas model is able to describe the equilibrium potential of hydride-forming materials (E_{MH}^{eq}) as explicit functions of the normalized hydrogen concentration (x). A maximum of eight parameters is used to simulate and fit the experimental data. These parameters are the phase-transition points (x_α and x_β), the energies of the individual hydrogen atoms in their separate phases (E_α and E_β), the H-H interaction energies within the α- and β-phases ($U_{\alpha\alpha}$ and $U_{\beta\beta}$), the H-H inter-phase interaction energy

between hydrogen atoms located in different phases ($U_{\alpha\beta}$) and finally the energy of the host lattice (L) which corresponds to the energy of the unit cell of the hydride-forming material. Thus, according to the lattice gas model the total description of E_{MH}^{eq} consists of three parts: the equilibrium potential of the α- (Eq. 3.1) and β-solid solutions (Eq. 3.3) and that of the two-phase coexistence region (Eq. 3.2), according to

$$E_{MH}^{eq} = \frac{RT}{F}\begin{cases} \ln\left(\frac{1-xd}{xd}\right) - \frac{F}{RT}(E_\alpha + U_{\alpha\alpha}x), & 0 \le x < x_\alpha \quad (3.1) \\ \dfrac{\left(\frac{S_\alpha^0}{d} - S_\beta^0\right) - \frac{F}{RT}\left\{-E_\alpha x_\alpha - U_{\alpha\alpha}x_\alpha^2 x_2 + E_\beta x_\beta + U_{\beta\beta}x_\beta^2 x_1 + \frac{U_{\alpha\beta}x_\alpha x_\beta}{2}(x_2 - x_1) + L\right\}}{\left(x_\beta - x_\alpha\right)}, & x_\alpha \le x < x_\beta \quad (3.2) \\ \ln\left(\frac{1-x}{x}\right) - \frac{F}{RT}(E_\beta + U_{\beta\beta}x), & x \le x_\beta \quad (3.3) \end{cases}$$

where $x_1 = \dfrac{x - x_\alpha}{x_\beta - x_\alpha}$, $x_2 = \dfrac{x_\beta - x}{x_\beta - x_\alpha}$. The entropy terms are defined as

$$\begin{aligned} S_\alpha^0 &= x_\alpha d \ln x_\alpha d + (1 - x_\alpha d)\ln(1 - x_\alpha d) \\ S_\beta^0 &= x_\beta \ln x_\beta + (1 - x_\beta)\ln(1 - x_\beta). \end{aligned} \quad (3.4)$$

where d, the ratio between the number of host sites per unit cell in the α- and β-phase, was set to unity in all simulations.

In order to obtain a set of parameters with physical relevance, yielding continuous dependencies in Eqs. 3.1-3.3, some restrictions are imposed to the constants to preserve the continuity of the equilibrium potential at the phase transition points (x_α and x_β), namely

$$\lim_{x\uparrow x_\alpha}\left(E_{MH}^{eq}(x)\right) = \lim_{x\downarrow x_\alpha}\left(E_{MH}^{eq}(x)\right) \quad \text{and} \quad \lim_{x\uparrow x_\beta}\left(E_{MH}^{eq}(x)\right) = \lim_{x\downarrow x_\beta}\left(E_{MH}^{eq}(x)\right) \quad (3.5)$$

As an example the experimental isotherms (symbols) of the extremes of the various Pd-thicknesses (*i.e.* 10 and 200 nm) are plotted as a function of the normalized hydrogen content together with the isotherms simulated by the lattice gas model (solid lines) in Fig. 3.2 . As it is generally accepted to plot isotherms from low to high hydrogen content it should be noted that the present dehydrogenation results are plotted in this figure in accordance with this convention. First, the experimental data will be discussed in more detail. The isotherm of the 200 nm thick Pd thin film (curve (a)) shows a distinct and flat plateau at approximately -0.86 V, which is typical for bulk Pd. Contrastingly, the equilibrium curve of the 10 nm thick Pd electrode (curve (b)) shows a much more sloping plateau, which is an indication of the absence of a two-phase coexistence region. This observation is in line with results reported before that show that the critical temperature (T_c) is well below room temperature for very thin Pd films compared to 566 K for bulk Pd.[3-6,12]

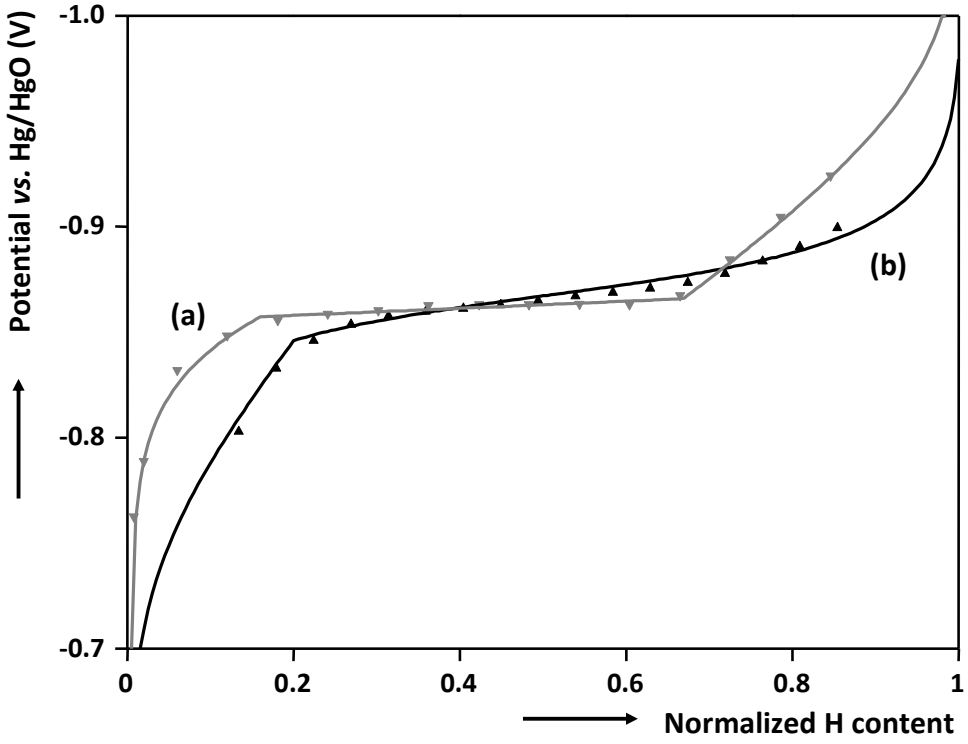

Fig. 3.2 Measured (symbols) and calculated (lines) isotherms for (a) 200 nm thick Pd and (b) 10 nm thick Pd electrode.

More insight into the thermodynamic properties of palladium hydride as a function of its thickness can be obtained by analyzing the simulated parameter values that are listed in Table 3.1. Here, the most informative parameters are the interaction energies between hydrogen atoms in various phases ($U_{\alpha\alpha}, U_{\alpha\beta}, U_{\beta\beta}$) and the host energy contribution (L). The interaction energies within the α- and β-phases change into opposite directions with increasing film thickness. $U_{\alpha\alpha}$ declines, while $U_{\beta\beta}$ increases towards higher repulsion energies, *i.e.* more positive values. Nevertheless, the average values of the equilibrium potentials of both plateau regions are, however, very similar (see Fig. 3.2). As the dependence of $U_{\alpha\alpha}$ and $U_{\beta\beta}$ with respect to the Pd thickness is found to be different, this difference should therefore, in accordance with Eqs. (3.1-3.3), be compensated by the other parameters ($U_{\alpha\beta}, L$). From Table 3.1 it is evident that $U_{\alpha\beta}$ steadily increases as the thickness of the film increases, indicating a much stronger inter-phase interaction in the case of thick Pd layers compared to thinner films. Note that for 10 nm thick Pd no value for $U_{\alpha\beta}$ is given as the two-phase coexistence region was completely absent in this case.

There are two ways to explain the increase of $U_{\alpha\beta}$ as a function of film thickness: (*i*) as $U_{\alpha\alpha}$ and $U_{\beta\beta}$ clearly depend on the Pd thickness (Table 3.1), it is expected that the H-H interaction of H atoms located in different phases is also related to the film thickness. (*ii*) the variation of $U_{\alpha\beta}$ could also be related to the grain size of the α and β phases as for a small grain size and, as a consequence, a large contact area between the phases, and the fact that the lattice gas model is based on mean field theory, a stronger interaction is to be expected between the H atoms in separate phases. Therefore, $U_{\alpha\beta}$ will by definition increase in the

case of a small grain size and implies that the grain size decreases as the Pd thickness increases.

Table 3.1 Simulation results for Pd thin films with a thickness ranging from 10 to 200 nm.

Pd Thickness (nm)	x_α	x_β	E_α (eV)	E_β (eV)	$U_{\alpha\alpha}$ (eV)	$U_{\beta\beta}$ (eV)	$U_{\alpha\beta}$ (eV)	L (eV)
10	0.196	0.196	-0.120	-0.038	0.366	-0.050	-	-0.008
50	0.130	0.370	-0.067	-0.065	0.312	0.001	0.126	0.006
100	0.140	0.473	-0.028	-0.093	0.008	0.059	0.176	0.017
150	0.149	0.600	-0.025	-0.139	0.0002	0.096	0.391	0.037
200	0.156	0.664	-0.034	-0.204	0.025	0.183	0.743	0.060

L also increases with increasing Pd thickness and this may be attributed to the substrate. More specifically, in terms of the lattice gas model, L is defined as the transformation energy of the crystal lattice and generally this transformation is accompanied by a volume-change of the unit cell. However, the Pd films discussed here are attached to a quartz substrate, and as a consequence, the rigid substrate causes resistance towards isotropic volume-expansion. Therefore it is expected that the overall volume-expansion, starting from the as-deposited state, is smaller in the case of Pd thin films comparing to bulk Pd, resulting in a decline of the host energy contribution. Overall, the large impact of the substrate on the thermodynamics of Pd thin films is in line with previous results.[3-6]

As the phase-transition points (x_α and x_β) are accurately determined using the mathematical model, it is possible to construct a phase diagram as a function of Pd thickness and normalized hydrogen content. This is depicted in Fig. 3.3. The phase boundaries x_α and x_β converge smoothly towards a single phase transition point as the thickness of the film decreases and indicates that below 10 nm Pd the miscibility gap completely vanishes.

According to our lattice gas model, the Gibbs free energy (G) of the hydrogen storage material expressed in eV/H atom can be determined according to[1]

$$G=\begin{cases}\left(E_\alpha x+\dfrac{U_{\alpha\alpha}x^2}{2}\right)+\dfrac{RT}{Fd}\left[xd\ln(xd)+(1-xd)\ln(1-xd)\right] & 0\le x<x_\alpha \quad (3.6)\\ \left(E_\alpha x_\alpha x_2+\dfrac{U_{\alpha\alpha}x_\alpha^2x_2^2}{2}+E_\beta x_\beta x_1+\dfrac{U_{\beta\beta}x_\beta^2x_1^2}{2}+\dfrac{U_{\alpha\beta}x_\alpha x_\beta x_1x_2}{2}+Lx_1\right)+\dfrac{RT}{F}\left[\dfrac{S_\alpha^0x_2}{d}+S_\beta^0x_1\right] & x_\alpha\le x<x_\beta \quad (3.7)\\ \left(E_\beta x+\dfrac{U_{\beta\beta}x^2}{2}\right)+\dfrac{RT}{F}\left[x\ln(x)+(1-x)\ln(1-x)\right]+L & x\le x_\beta \quad (3.8)\end{cases}$$

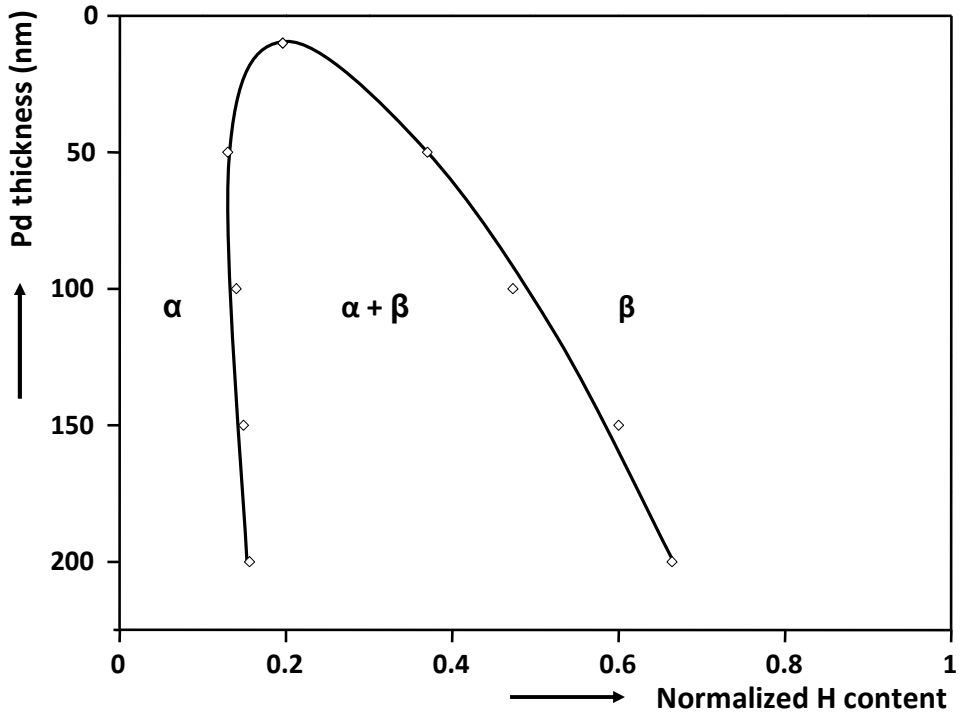

Fig. 3.3 Calculated phase diagram *vs.* the Pd electrode thickness.

Here, the Gibbs free energies for the pure solid solutions are given by Eqs. 3.6 and 3.8 accordingly, while Eq. 3.7 corresponds to the two-phase coexistence region. Fig. 3.4A shows the behavior of the Gibbs free energies for the 200 nm thick Pd layer and the behavior of the 50 nm Pd layer is depicted in Fig. 3.4B. The dashed curves (a) correspond to the Gibbs free energies of the α-phase, while the solid curves (b) correspond to the β-phase. The black lines (c) represent the Gibbs free energies of the total system. From Fig. 3.4 it is evident that the Gibbs free energies of the solid solutions are never below the energy of the total system. This observation is in line with the principle of minimal energy, which states that the Gibbs free energy in the two-phase coexistence region is always lower than it can be for systems containing only one phase.

Furthermore, from Fig. 3.4A it is apparent that for the 200 nm thick Pd film the difference between the partial energies of the individual phases at the phase-transition points (x_α and x_β) is more pronounced compared to that of the thinner film (Fig. 3.4B). Therefore, the energy gain associated with the phase-transition is relatively small for very thin Pd layers and is in accordance with the observation that the phase transformation plateau is less apparent or even completely vanishes (see Fig. 3.3).

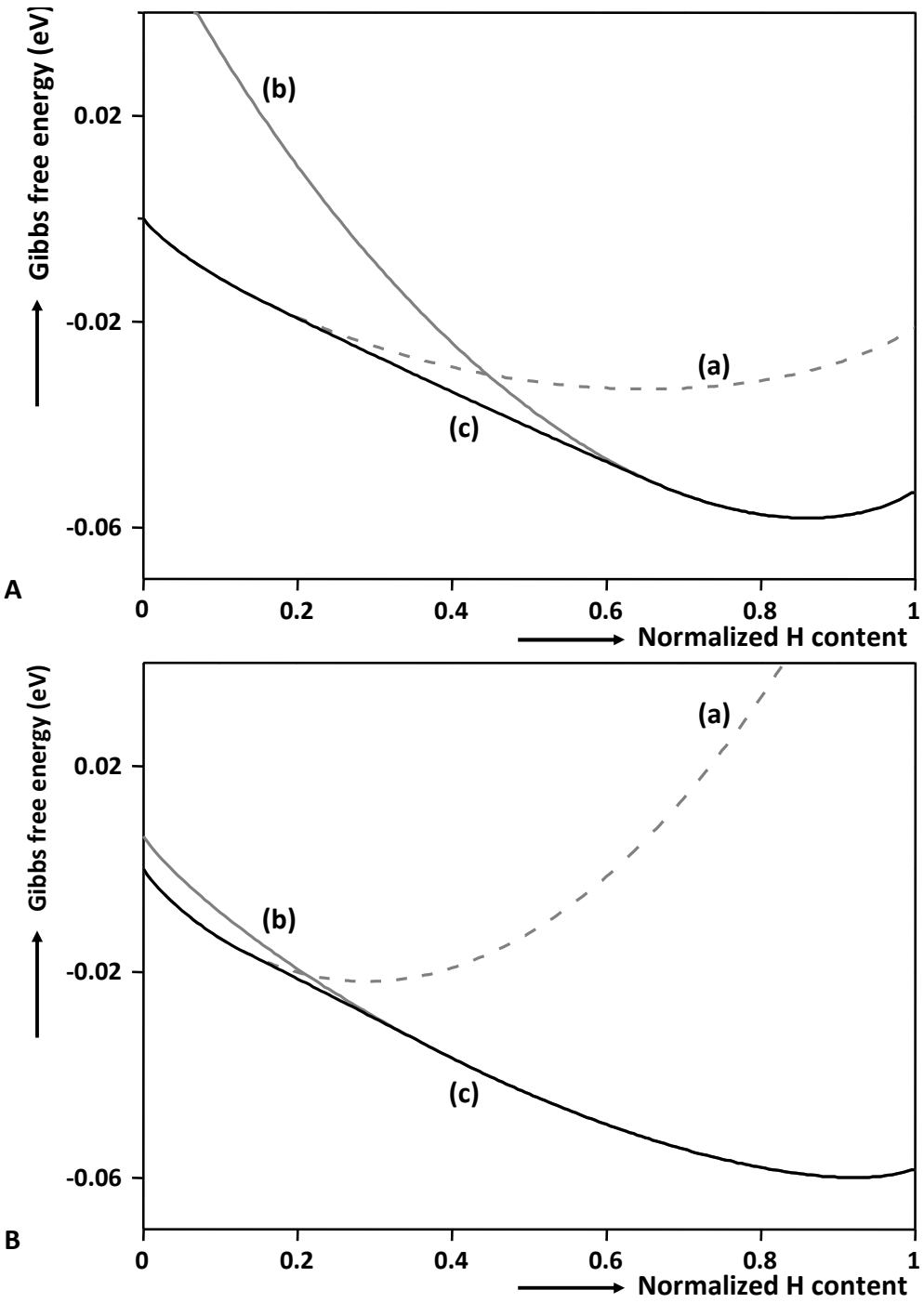

Fig. 3.4 Evolution of the Gibbs free energy as a function of hydrogen content for Pd films with a nominal thickness of 200 nm (A) and 50 nm (B). The partial energy curves of the α-phase (a) and the β-phase (b) are shown together with the Gibbs free energy curves of the total system denoted by (c).

3.2.2 Kinetics of Pd hydride thin film electrodes

In the introduction it is mentioned that a Pd topcoat is often applied to metal hydride thin film research, as it catalyzes the dissociation rate of H_2 and electrocatalyzes the reduction of H_2O.[7-10] The need for a Pd topcoat to prevent oxidation of the main constituents of the thin film alloys discussed in this thesis (Mg and Ti) readily becomes apparent by considering the large negative enthalpy of formation of the oxides compared to the hydrides, *i.e.* ΔH_f (MgO)=-602 kJ/mol O and ΔH_f (TiO_2)=-994 kJ/mol O are both much lower than the formation enthalpies of the hydrides ΔH_f (MgH_2)=-37 kJ/mol H and ΔH_f (TiH_2)=-68 kJ/mol H).[13,14] To determine the influence of the Pd topcoat on the kinetics of the entire Mg-based film (see paragraph 4.2.3.3) a 10 nm thick Pd thin film electrode is subjected independently to an EIS study. To obtain information about the electrocatalytic properties as a function of hydrogen content, the EIS measurements are combined with GITT, which can be used to systematically change the hydrogen content (see paragraph 2.3.4). However, it has to be noted that the plateau potentials of PdH_x and $Mg_yT_{1-y}H_x$ alloys are quite different, *i.e.* -0.86 V for PdH_x (see Fig. 3.2) and -0.75 V for $Mg_yTi_{1-y}H_x$ (see Fig. 4.16). To ensure enough data points at the plateau of $Mg_yTi_{1-y}H_x$ are obtained, which corresponds to the α-solid solution of PdH_x, GITT was only used to change the hydrogen content in the plateau region and in the β-solid solution of PdH_x, whereas the hydrogen content in the α-solid solution of PdH_x was changed using the Potentiostatic Intermittent Titration Technique (PITT) up to an equilibrium potential of -0.60 V.

In a recent study, Niessen *et al.* showed that, by applying Sieverts Law, ideal solid solution behavior was found for a 10 nm PdH_x film with x<0.25.[15] In this region the equilibrium hydrogen concentration in the dilute α-phase is proportional to the square root of the hydrogen pressure according to

$$C_H^{eq} = K_S \sqrt{P_{H_2}} \qquad (3.9)$$

where C_H^{eq} is the equilibrium concentration of hydrogen in the Pd (in H/M), K_s is Sieverts' constant and P_{H_2} the partial hydrogen pressure (in bar). P_{H_2} was obtained from E_{MH}^{eq} via Eq. 2.19 in paragraph 2.3.4. The value for K_S was calculated to be 3.44 $bar^{-1/2}$ and used here to determine the hydrogen content for x<0.25 H/M.[15] Above this limiting concentration, the current was used to calculate the hydrogen content accurately (see Eqs. 2.16 and 2.17). The EIS results are depicted in a Nyquist plot as a function of hydrogen content in Fig. 3.5.

To extract parameter values from the EIS data, it is necessary to fit the data with an equivalent circuit (EQC) that closely resembles the processes and reactions occurring in/at the film. The EQC, describing a two-step hydrogen absorption mechanism in which the charge transfer is coupled with absorption, is thoroughly described by MacDonald, Montella and Gabrielli *et al.* and is plotted in Fig. 3.6A.[16-18] Note that a slightly different nomenclature is used here.

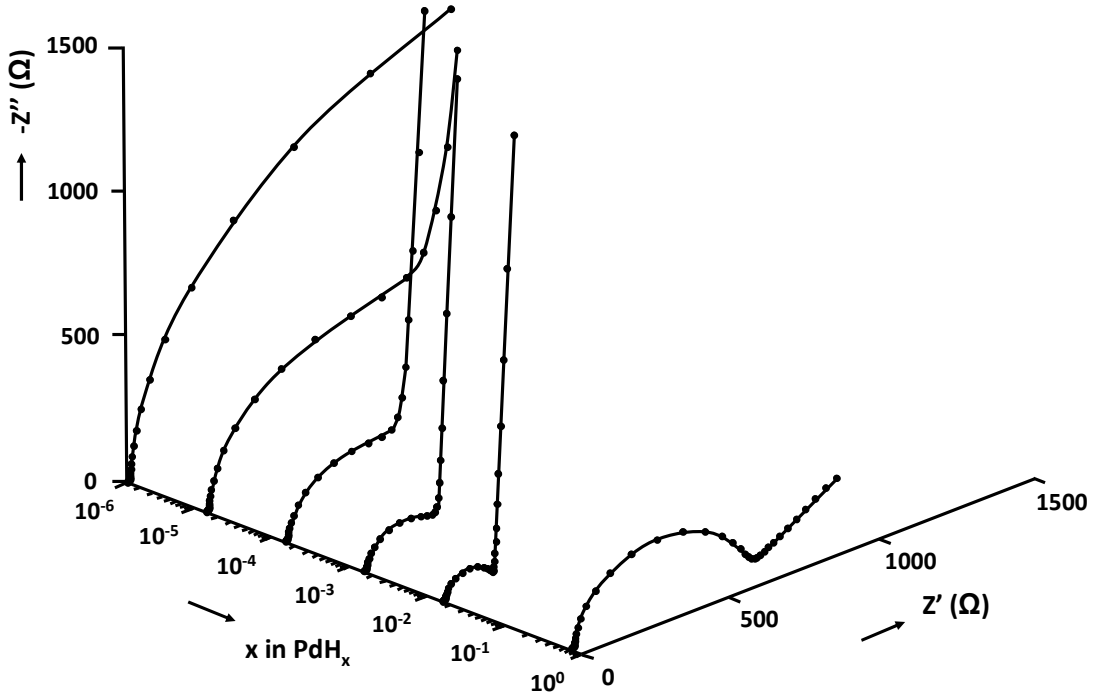

Fig. 3.5 Impedance spectra of a 10 nm thick Pd thin film electrode at various hydrogen concentrations.

The equivalent processes or reactions of the elements in Fig. 3.6A are explained below with the help of a schematic representation of the thin film Pd electrode shown in Fig. 3.6B. R_s is the solution resistance between the working electrode and the reference electrode, also known as the Ohmic (*IR*) drop. By placing the reference electrode close to the working electrode the Ohmic drop is minimized as much as possible. The Ohmic drop also comprehends possible contact resistances and resistance from the galvano/potentiostat. Charging the Pd layer changes the electrochemical potential and, consequently, an electric double layer will develop. This electric double layer is modeled by a parallel plate capacitor, denoted as C_{dl} in Fig. 3.6A. Hereafter, H_2O is reduced at the solution/solid interface of the electrode according to (step 1 in Fig. 3.6B)

$$H_2O + Pd + e^- \rightleftarrows PdH_{ad} + OH^- \tag{3.10}$$

The charge transfer reaction is modeled by a resistor (R_{ct}). In the next step the adsorbed hydrogen atoms (H_{ad}) are absorbed by the host material just below the surface, forming subsurface hydrogen (H_{ss}; step 2 in Fig. 3.6B), according to

$$PdH_{ad} \rightleftarrows PdH_{ss} \tag{3.11}$$

C_{ad} is a capacitance depending on the amount of hydrogen present at the surface. The diffusion behavior of hydrogen in the Pd bulk (see Fig. 3.6B, step 3) has been approximated by a Warburg-element (W_{Pd}), corresponding to the mass-transfer impedance for finite-length diffusion and a reflecting interface. The mathematical form of this element has been extensively treated by Lasia.[19]

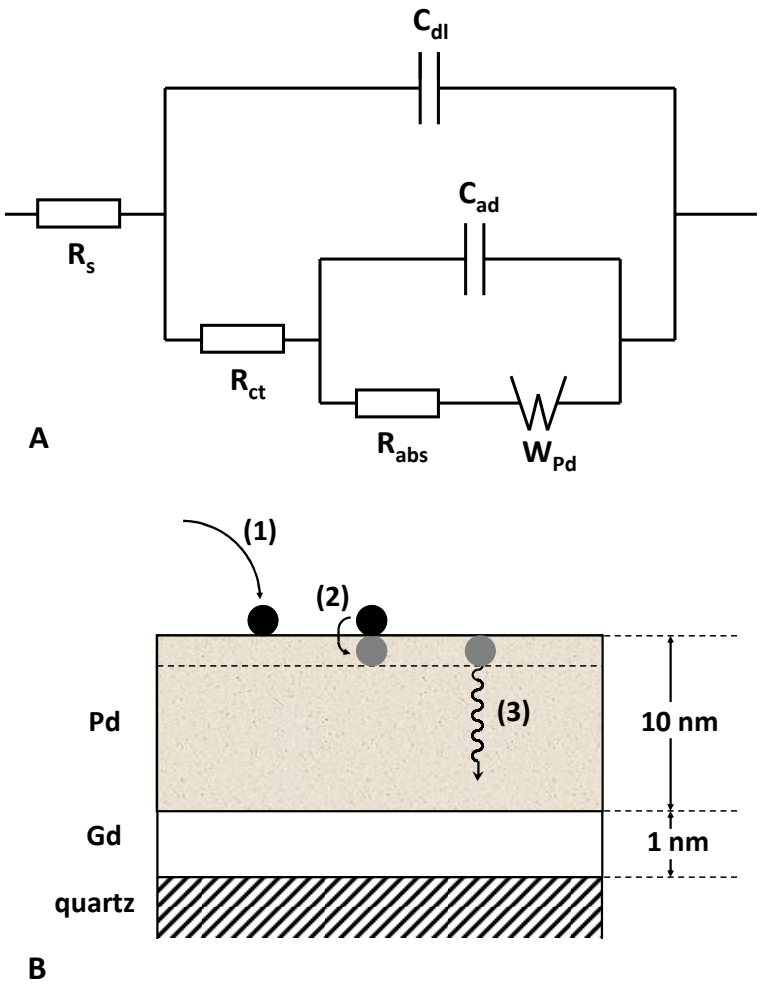

Fig. 3.6 (A) Complete equivalent circuit able to model a 1-layer Pd thin film electrode, in which the charge transfer reaction is coupled to absorption and subsequent solid-state diffusion of hydrogen in the Pd bulk. It should be noted that finite diffusion with reflective boundary conditions is used here. (B) Schematic representation of a 10 nm thick Pd thin film electrode with a 1 nm thick Gd adhesion layer. Besides the overall geometry of this 1-layer system, the main (electro)chemical processes related to hydrogen absorption are indicated at their appropriate locations: (1) charge transfer reaction, (2) adsorbed hydrogen forming subsurface absorbed hydrogen and (3) solid-state diffusion of hydrogen in the Pd bulk.

The EQC in Fig. 3.6A can readily be simplified. Firstly, Gabrielli *et al.* and Yang *et al.* showed that $R_{abs} << R_{ct}$.[18,20] Furthermore, the EIS response, shown in Fig. 3.5, consists of only a single semi-circle suggesting that either the charge transfer resistance (R_{ct}) or the absorption reaction resistance (R_{abs}) is negligible. Here, it is assumed that the absorption rate constant is very high ($R_{abs} \to 0$) and therefore the semi-circle is completely attributed to the charge transfer reaction. Secondly, the occurrence of a only a single semi-circle and the observation that the capacitance associated with this semi-circle remains constant irrespective of the hydrogen concentration in the electrode together with the fact that the absolute value of this capacitance, point to fact that this capacitive element can be ascribed to C_{dl} rather than C_{ad}.

The EQC that remains after removing R_{abs} is shown in and is equal to the EQC described by Johnsen *et al*.[21]

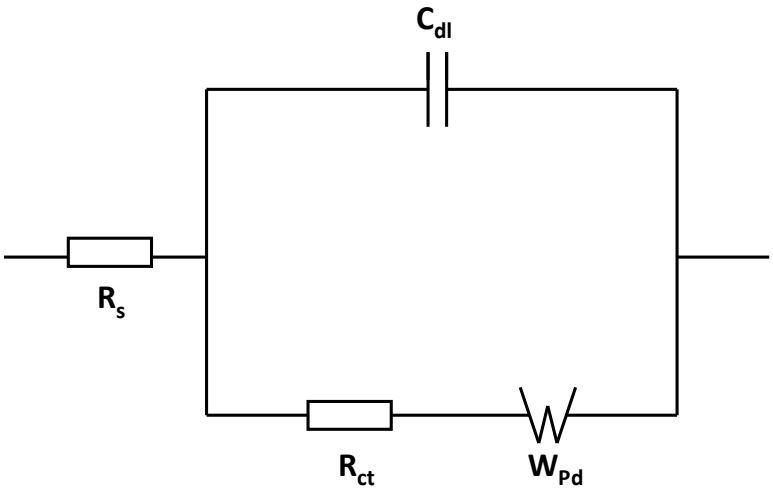

Fig. 3.7 Simplified version of the circuit shown in, obtained when assuming infinitely fast absorption ($R_{abs} \rightarrow 0$).

Note that a clear 45° Warburg diffusion line does not appear in all Nyquist plots measured for our palladium-hydrogen system (see Fig. 3.5). The origin was already experimentally determined by Gabrielli *et al.*, who showed that for Pd films thinner than 10 µm the capacitive behavior of the film becomes too dominant.[22] Therefore, the diffusion-related response at low frequencies was omitted in the present study. This essentially means that the EIS data down to $f \approx 5$ mHz can be accurately modeled as diffusion does not contribute.

Values for R_{ct} at various stages of hydrogenation of the 10 nm Pd film were obtained by using the EQC shown in Fig. 3.7 and used to calculate the more common exchange current density (i_0), using the well-known relationship[23]

$$i_0 = \frac{RT}{R_{ct}F} \tag{3.12}$$

The values of i_0 are calculated per unit surface area (3 cm^2) and plotted as a function of equilibrium potential in Fig. 3.8.

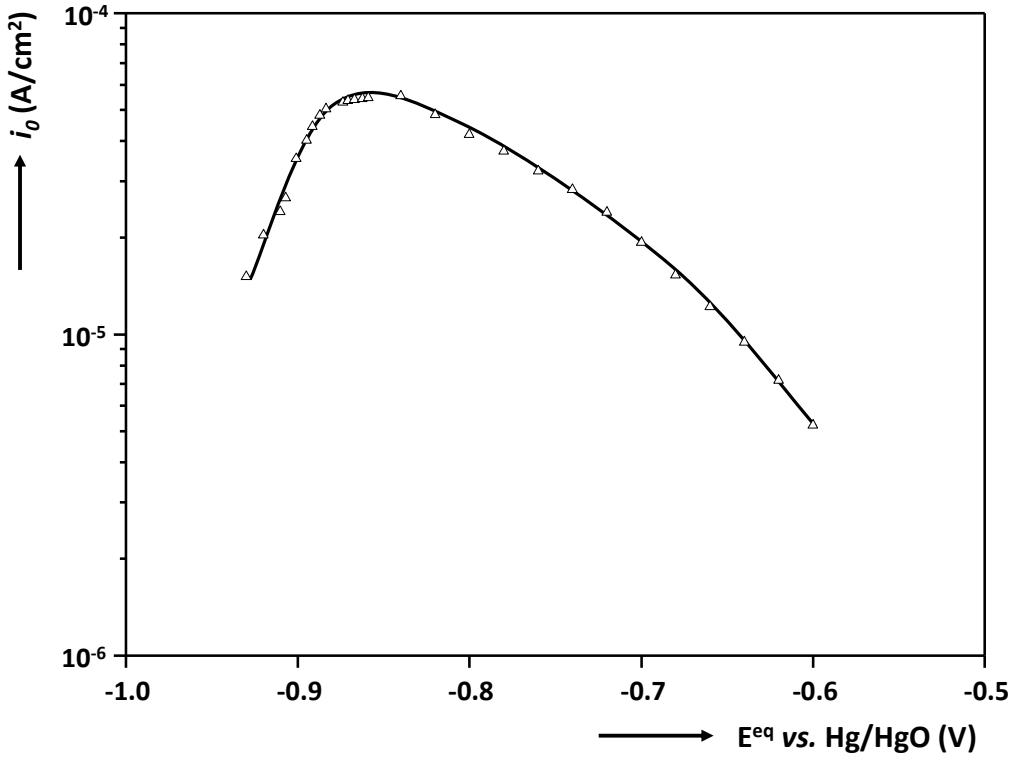

Fig. 3.8 i_0 as a function of the equilibrium potential of a 10 nm thick Pd electrode.

The results show that the exchange current density is maximal, and therefore shows the best electrocatalytic kinetics, at -0.86 V. This is, according to the isotherm presented in Fig. 3.2, just in the β-solid solution. Similar behavior of the exchange current density as a function of potential has been found for other hydride-forming compounds previously by Senoh *et al.* and it was also theoretically derived by Notten *et al.*[24,25]

3.3 Conclusions

The isotherms of Pd thin films with a nominal thickness of 10 to 200 nm are determined electrochemically and show that the isotherms change dramatically as a function of layer thickness. For the 200 nm thick Pd electrode a flat two-phase coexistence plateau is found, whereas for Pd films with a thickness of 10 nm the transformation plateau has vanished, indicating the absence of a two-phase coexistence region. The lattice gas model is used to simulate the isotherms of PdH_x electrodes and to gain more insight into the corresponding thermodynamics. The model parameters reveal a systematic change of the thermodynamic properties as a function of Pd thickness. In particular, closely analyzing the energy parameters reveals that the inter-phase interaction increases as a function of Pd thickness, which could be due to a relatively small grain size for thick Pd films. Moreover, it is shown that the influence of the substrate has a large impact, especially on the thinnest films. The phase diagram of Pd layers as a function its thickness reveals that the miscibility gap completely vanishes below 10 nm. This corresponds to the fact that the energy gain resulting from the phase transition is less in the very thin films. Finally, the successful application of

the lattice gas model to the palladium-hydrogen system illustrates that the model is an excellent tool to determine the thermodynamic properties of hydrogen storage material.

The electrocatalytic properties of a 10 nm thick Pd electrode were assessed as a function of hydrogen content by EIS in combination with GITT and PITT. The results show that the fastest surface kinetics is obtained at an equilibrium potential of -0.86, which according to the isotherm is just in the β-solid solution.

3.4 References

1 A. Ledovskikh, D. Danilov, W.J.J. Rey and P.H.L. Notten, *Modeling of hydrogen storage in hydride-forming materials: Statistical thermodynamics,* Phys. Rev. B **2006**, *73*, 014106/1-12.

2 F.A. Lewis, *The Palladium Hydrogen System*; Academic Press: London, **1967**.

3 G.A. Frazier and R. Glosser, *Characterization of thin films of the palladium-hydrogen system*, J. Less-common Met. **1980,** *74*, 89-96.

4 R. Feenstra, G.J. de Bruin-Hordijk, H.L.M. Bakker, R. Griessen and D.G. de Groot, *Critical-point lowering in thin PdH_x films*, J. Phys. F: Met. Phys. **1983,** *13*, L13-L18.

5 R. Feenstra, D.G. de Groot, J.H. Rector, E. Salomons and R. Griessen, *Gravimetrical determination of pressure composition isotherms of thin PdH_c films*, J. Phys. F **1986**, *16*, 1953-1963.

6 M. Nicolas, L. Dumoulin and J.P. Burger, *Thickness dependence of the critical solution temperature of hydrogen in Pd films*, J. Appl. Phys. **1986**, *60*, 3125-3130.

7 M. Kremers, N.J. Koeman, R. Griessen, P.H.L. Notten, R. Tolboom, P.J. Kelly and P.A. Duine, *Optical transmission spectroscopy of switchable yttrium hydride films*, Phys. Rev. B **1998**, *57*, 4943-4949.

8 T.J. Richardson, J.L. Slack, R.D. Kostecki, B. Farangis and M.D. Rubin, *Switchable mirrors based on nickel–magnesium films*, Appl. Phys. Lett. **1999**, *78*, 3047-3049.

9 R.A.H. Niessen and P.H.L. Notten, *Electrochemical hydrogen storage characteristics of thin film MgX (X = Sc, Ti, V, Cr) compounds*, Electrochem. Solid-State Lett. **2005**, *8*, A534-A538.

10 D.M. Borsa, A. Baldi, M. Pasturel, H. Schreuders, B. Dam, R. Griessen, P. Vermeulen and P.H.L. Notten, *Mg-Ti-H thin films for smart solar collectors*, Appl. Phys. Lett. **2006,** *88*, 241910/1-3.

11 Y. de Ribaupierre and F.D. Manchester, *Experimental study of the critical-point behavior of hydrogen in the palladium system 1: lattice gas aspects*, J. Phys. C: Solid State Phys. **1974,** *7*, 2126-2139.

12 M.A. Pick, J.W. Davenport, M. Strongin and G.J. Dienes, Enhancement of the hydrogen uptake rates for Nb and Ta by thin surface overlayers, Phys. Rev. Lett. **1979**, *43*, 286-289.

13 R. Griessen and T. Riesterer, *Topics in Applied Physics Hydrogen in Intermetallic Compounds*, Chapter 6: Heat of Formation Models, Vol 63 (Ed. L. Schlapbach), Springer-Verlag, Berlin, **1988**, 219-284.

14 D.R. Lide, *CRC Handbook of Chemistry and Physics* (CRC Press, Boca Raton, **2005**)

15 R.A.H. Niessen, P. Vermeulen and P.H.L. Notten, *The electrochemistry of Pd-coated $Mg_ySc_{(1-y)}$ thin film electrodes; a thermodynamic and kinetic study*, Electrochim. Acta **2006,** *51*, 2427-2436.

16 J.R. MacDonald, *Impedance spectroscopy*, John Wiley & Sons, New York, **1987**, p. 75.

17 C. Montella, *EIS study of hydrogen insertion under restricted diffusion conditions: I. Two-step insertion reaction*, J. Electroanal. Chem. **2001**, *497*, 3-17.

18 C. Gabrielli, P.P. Grand, A. Lasia and H. Perrot, *Investigation of hydrogen adsorption-absorption into palladium thin films, I. Theory*, J. Electrochem. Soc. **2004**, *151*, A1925-A1936.
19 A. Lasia, *Modern Aspects of Electrochemistry*, Vol. 35, Kluwer/Plenum, New York, **2002**, p. 29.
20 T.H. Yang and S.I. Pyun, *An investigation of the hydrogen absorption reaction into, and the hydrogen evolution reaction from, a Pd foil electrode*, J. Electroanal. Chem. **1996**, *414*, 127-133.
21 S.E. Johnsen, G. Lindbergh, A. Lundqvist and R. Tunold, *A single particle investigation on the kinetics of metal hydride materials*, J. Electrochem Soc. **2003**, *150*, A629-A637.
22 C. Gabrielli, P.P. Grand, A. Lasia and H. Perrot, *Investigation of Hydrogen Adsorption and absorption in palladium thin films, III. Impedance spectroscopy*, J. Electrochem. Soc. **2004**, 151**,** A1943-A1949.
23 A.J. Bard and L.R. Faulkner, *Electrochemical Methods-Fundamental and Applications*, John Wiley & Sons, New York, **2001**, p. 100.
24 H. Senoh, K. Morimoto, H. Inoue, C. Iwakura and P.H.L. Notten, *Relationship between equilibrium hydrogen pressure and exchange current for the hydrogen electrode reaction at $MmNi_{(3.9-x)}Mn_{(0.4)}Al_{(x)}Co_{(0.7)}$ alloy electrodes*, J. Electrochem. Soc. **2000**, 147, 2451-2455.
25 P.H.L. Notten, M. Ouwerkerk, A. Ledovskikh, H. Senoh and C. Iwakura, *Hydride-forming electrode materials seen from a kinetic perspective*, J. Alloys Compd. **2003**, 356-357, 759-763.

4

Electrochemical hydrogen storage in thin film Mg_yTi_{1-y} alloys

Abstract

The crystallographic properties of as-prepared electron-beam deposition and sputtered Mg_yTi_{1-y} thin films with *y* ranging from 0.50 to 1.00 were determined X-ray diffraction analyses, revealing that crystalline single-phase alloys were obtained. Galvanostatic (de)hydrogenation measurements were performed to unveil the effects of the Mg-to-Ti ratio on the hydrogen absorption and desorption kinetics. Increasing the Ti-content up to 15 at.% does not change these rate much and hydrogen can only be desorbed at a low rate. Beyond 15 at.% Ti the hydrogen desorption kinetics increase substantially. A superior reversible hydrogen storage capacity (>6 wt.% H), along with excellent hydrogen absorption and desorption kinetics is found for the $Mg_{0.80}Ti_{0.20}$ alloy. The close analogy of the electrochemical behavior of Mg_yTi_{1-y} and Mg_ySc_{1-y} alloys points to a fcc-structured hydride for the alloys showing fast hydrogen uptake and release kinetics, whereas for the hydrides of alloys rich in Mg (>80 at.%), that show poor kinetics, probably crystallize into the common MgH_2 bct structure. The cycling stability of electron-beam deposited and sputtered thin film $Mg_{0.80}Ti_{0.20}$ alloys is constant over the first 10 cycles, hereafter it decreases sharply caused by delamination of the film from the substrate. The intrinsic cycling stability is therefore expected to be higher. Isotherms of Mg_yTi_{1-y} thin films show that the plateau pressure is not affected strongly by the Ti-content and is almost equal to the equilibrium pressure of the magnesium-hydrogen system. Impedance analyses show that the surface kinetics can be fully attributed to the Pd-topcoat. The overall kinetic impedance, when the Mg_yTi_{1-y} thin film electrodes are in their hydrogen-depleted state, is dominated by the transfer of hydrogen across the Pd/Mg_yTi_{1-y} interface.[*]

---

[*] Part of this chapter is based on:

P. Vermeulen, R.A.H. Niessen and P.H.L. Notten, *Hydrogen storage in metastable $Mg_yTi_{(1-y)}$ thin films*, Electrochem. Comm. **2006**, *8*, 27-32.

P. Vermeulen, R.A.H. Niessen, D.M. Borsa, B. Dam, R. Griessen and P.H.L. Notten, *Effect of the deposition technique on the metallurgy and hydrogen storage characteristics of metastable $Mg_yTi_{(1-y)}$ thin films*, Electrochem. Solid-state Lett. **2006**, *9*, A520-A523.

P. Vermeulen, A. Ledovskikh, D. Danilov and P.H.L. Notten, *Thermodynamics and kinetics of the thin film Magnesium-Hydrogen system*, Acta Mater. **2008**, submitted.

4.1 Introduction

In paragraph 1.3 it was pointed out that for hydrogen storage applications Mg is often used as a starting material mainly because of its potentially high gravimetric capacity.[1] Several studies, however, show that pure Mg cannot be used as effective hydrogen storage medium, because it suffers from several drawbacks, *e.g.* the thermodynamic stability of MgH_2 is too high, it requires therefore a desorption temperature of up to 350 °C to release hydrogen at 1 bar.[2] Another major impediment toward practical applications is the poor kinetics associated with hydrogen absorption and desorption by MgH_2. It was shown that the growth of MgH_2 is rate-limited by the diffusion of hydrogen through the hydride layer, which effectively blocks hydrogen.[3-13] In spite of its apparent drawbacks, a lot of research is aimed on the development of interstitial hydrides comprising of alloys that are rich in Mg, as they are, in theory, capable of reaching high storage capacities. In other disciplines, like for instance switchable mirror research, Mg is frequently added to improve the optical transparency of the hydride.[14]

Recently, Niessen *et al.* revealed that the hydrogen uptake and release kinetics of Mg, in thin film form, can be enhanced significantly by alloying Mg with 20 at.% Ti.[15] Additionally, an excellent gravimetric capacity (>6 wt.% H) was obtained for the $Mg_{0.80}Ti_{0.20}$ thin film alloy. Under standard alloying conditions Mg and Ti do no form any intermetallics and therefore the use of a non-equilibrium preparation method is indispensable to enforce Mg and Ti to alloy.[16] At present only a limited amount of research has been done on the hydrogenation properties of Mg_yTi_{1-y} alloys. For instance, Kyoi *et al.* used 8 GPa and 873 K to synthesize metastable Mg_7TiH_x.[17] Although the complexity of the 'anvil-cell' technique is very high and the conditions applied very extreme, it does show that crystalline MgTi hydrides can exist in bulk form. Until now, only a few researchers have tried to synthesize and characterize the same compounds via a thin film approach that does not require extremes in pressure and temperature.

In this chapter a systematic approach is used to unveil the effects of the Mg-to-Ti ratio on the metallurgy and hydrogen storage properties of Mg_yTi_{1-y} thin film prepared by electron-beam deposition and sputtering. To obtain a comprehensive view of the effects of the Ti-content on the storage characteristics of Mg_yTi_{1-y} thin films, pure Mg thin films are included in the this study.

4.2 Results & discussion

A wide variety of characterization techniques are used to determine the properties of Mg_yTi_{1-y} thin film alloys with $0.50 \leq y \leq 1.00$, covering the as-deposited state as well as under different levels of hydrogenation. Firstly, the crystallographic properties of the as-prepared alloys are resolved by XRD. Secondly, the hydrogen absorption and desorption characteristics are assessed by means of electrolytic analyses. Thirdly, the thermodynamic properties and kinetics are determined by means of a combination of GITT and EIS. Fourthly, the effect of the deposition technique, *i.e.* electron-beam deposition and sputtering, is extensively studied.

4.2.1 Structural characterization of the as-prepared thin films

The crystallographic orientation of the as-deposited thin films, prepared by means of electron-beam evaporation, is resolved by XRD. As an example the diffractogram of a $Mg_{0.80}Ti_{0.20}$ thin film is depicted in Fig. 4.1. Here, the most dominant reflection is that of the (002) oriented hexagonal Mg-structure. The corresponding peak position is shifted with respect to that of pure Mg (34.4 °2θ) due to the incorporation of Ti in the Mg lattice.[18] The inset in Fig. 4.1 shows the (002) reflections of Mg_yTi_{1-y} thin films with $0.75 \leq y \leq 0.95$. Also the reflection of the (002) plane of the pure Mg thin film (y=1.00) is included. It should be noted that the XRD spectra of $Mg_{0.50}Ti_{0.50}$ and $Mg_{0.70}Ti_{0.30}$ are omitted since these only showed very weak and broad reflections of the (002) peak, suggesting that the crystallites are very small. A clear shift of the hexagonal peak position towards larger angles, *i.e.* smaller d-spacings, is apparent with increasing Ti-content. This shift is brought about by partial substitution of Mg by Ti, which has a smaller molar volume than Mg, causing the lattice to contract.[19]

Overall it is clear that crystalline single-phase compounds are obtained by means of electron-beam evaporation, which is in contrast to the observations reported by Richardson and co-workers, who showed that their sputtered Mg_yTi_{1-y} thin films were X-ray amorphous.[20,21] Additionally, Extended X-ray Absorption Fine Structure (EXAFS) analysis revealed no alloy formation in the metallic state and that their hydrides were present as distinct binary phases. The discrepancy in the observed crystallographic behavior remains unclear at this moment. Most likely, the deposition rate is an important parameter enforcing true alloying. Preliminary results also showed that the base pressure is a dominant factor that controls the crystallinity of the alloys to a significant extent. Aside from the reflections that can be attributed to the Mg_yTi_{1-y} layer, XRD peaks, which can be assigned to the (111) and (103) planes of the Pd topcoat, are observed in the diffractogram in Fig. 4.1.

According to the empirical rule known as *Vegard's Law*, a linear relationship exists between the crystal lattice parameters and the composition of a binary alloy.[22] Fig. 4.2 shows the evolution of the *c*-axis of the Mg_yTi_{1-y} thin film compositions with respect to the *c*-axis of pure Mg. Although deviations from the linear dependency predicted by *Vegard's Law* occur, it is clear that the linear trend is closely followed. Zen formulated boundary conditions for *Vegard's Law* as deviations are commonly observed.[23] It has been stated that the linear relation between the crystal lattice constants and the binary alloy composition only holds in those cases where both elements have a comparable molar volume. As the molar volumes of Mg and Ti are reported to be 14.00 and 10.64 cm^3/mol, respectively, this substantial difference can explain the small deviations found in Fig. 4.2.[24]

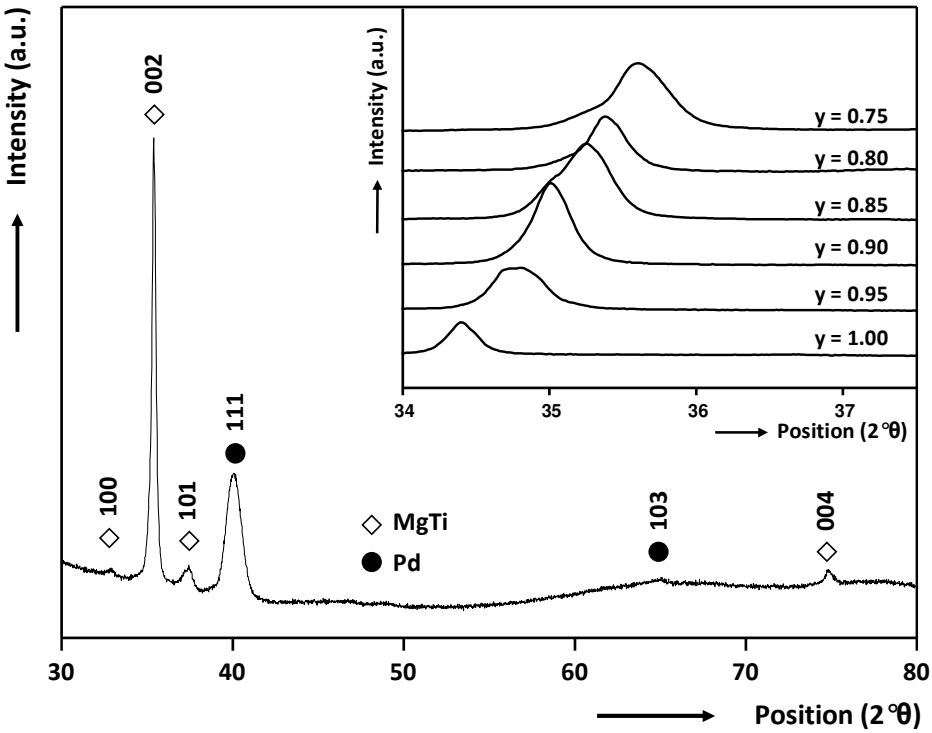

Fig. 4.1 XRD spectrum of a 200 nm thick $Mg_{0.80}Ti_{0.20}$ thin film capped with 10 nm of Pd. Indicated are the reflections and orientations of the different layers. The inset shows the evolution of the (002) reflections of Mg_yTi_{1-y} alloys with *y* ranging from 0.75 to 1.00.

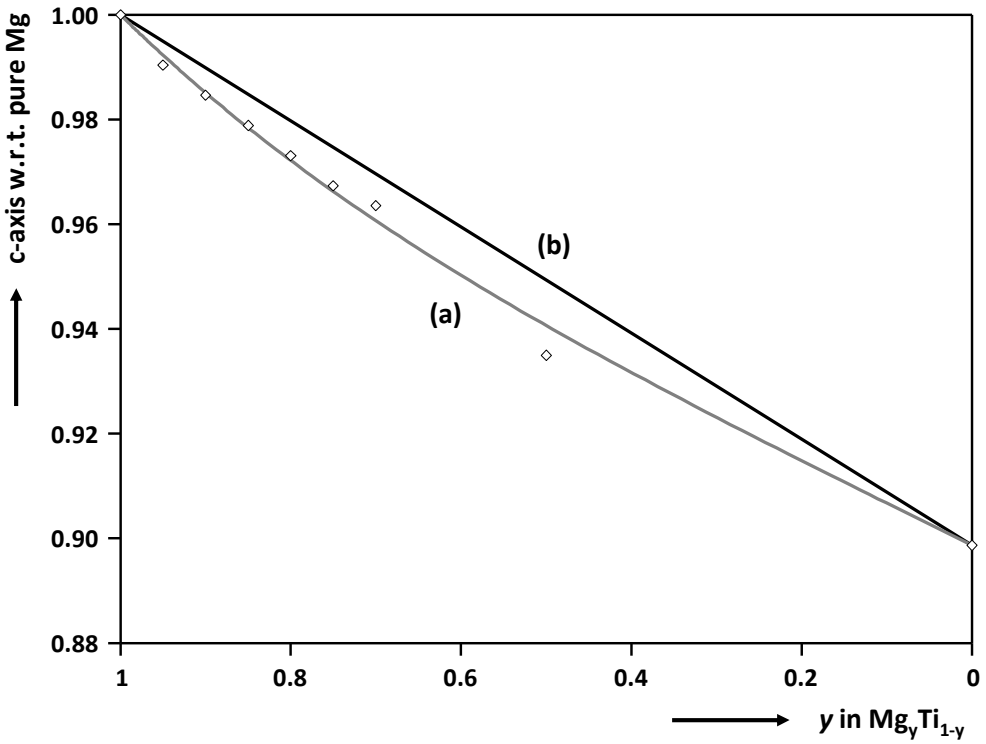

Fig. 4.2 The dependence of the *c*-axis on the composition of Mg_yTi_{1-y} thin films with respect to the *c*-axis of pure Mg (a). Also indicated is the linear dependency predicted by *Vegard's Law* (b).

4.2.2 Galvanostatic (dis)charging behavior

To determine if alloying Ti with Mg affects the hydrogen storage properties it is indispensible to characterize pure Mg first. Therefore, a 200 nm thick pure Mg film capped with 10 nm Pd was subjected to galvanostatic charging and discharging to illustrate its poor hydrogen absorption and desorption properties. Interesting to note is that up to now only a limited number of experimental studies dealing with electrochemically (de)hydriding pure Mg films have been reported in the literature, *e.g.* by Friedrichs *et al.* and Paillier *et al.*[25,26]

Firstly, a current of -0.6 mA (~5000 mA/g) was used to hydrogenate the Mg electrode. The potential response is shown by curve (a) depicted in Fig. 4.3. This response is characterized by a narrow α-solid solution during the initial stages of hydrogen insertion. Subsequently, a broad plateau, situated around -0.9 V, indicates to the α-to-β phase transition. The charging curve reveals that only about 0.85 wt.% H can be absorbed, hereafter hydrogen evolution (reaction 2.14) is observed that also manifests itself as a plateau. This extremely low absorption capacity is probably caused by the well-known blocking layer effect of MgH_2 formation.[3-13] The poor hydrogen uptake kinetics become especially apparent when considering that Mg thin films that are highly oriented along the hexagonal (002) direction in the as-deposited state, which was found for the Mg film investigated here, show relatively fast hydrogen absorption and desorption rates compared to polycrystalline Mg.[27,28]

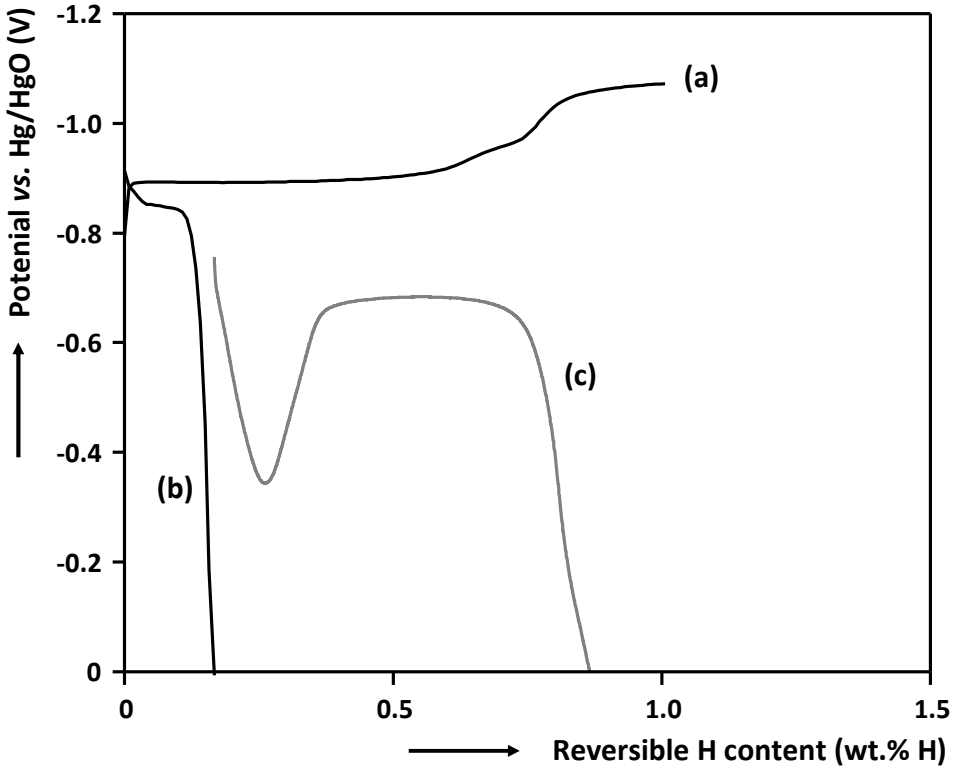

Fig. 4.3 Electrochemical response of a 200 nm thick Mg thin film capped with 10 nm Pd, showing hydrogenation at -0.6 mA (a), discharging at +0.12 mA (b) and deep-discharging at +0.012 mA (c).

After hydrogenation the Pd-capped Mg electrode was allowed to equilibrate under open-circuit conditions for one hour. Dehydrogenation with I=+0.12 mA (~1000 mA/g; curve (b)) and, after one hour of equilibration, subsequently with I=+0.012 mA (~100 mA/g; curve (c)) shows that all the hydrogen atoms can be extracted. However, again the poor diffusion properties of MgH_2 are obvious from the fact that only at a very low-rate current a substantial part of the total H concentration can be extracted.

To minimize the effect of the poor H permeability of MgH_2, and to approach more closely the intrinsic capacity of MgH_2, the charging current was lowered to a current of -0.012 mA (see Fig. 4.4 curve (a)). Hereafter, similar discharging and deep-discharging currents as above were applied to extract the absorbed hydrogen atoms. The hydrogenation response (curve (a)) is characterized by a nearly constant plateau situated around -0.81 V. After the conversion of α-Mg hydride to β-Mg hydride, a narrow plateau is observed indicative of hydrogen uptake by the Pd topcoat. Hereafter, the HER-plateau (reaction 2.14) is observed. Although the theoretical storage capacity of Mg is 7.7 wt.% H, experimentally only about 4.2 wt.% H is found. In spite of the 50 times lower charging current used here, the somewhat lower storage capacity compared to the theoretical capacity of MgH_2 suggests that the influence of the poor permeability of MgH_2 for hydrogen is still observed experimentally and, as a consequence, only about 55% of the film is fully hydrogenated. After one hour of relaxation the Mg hydride was dehydrogenated with a high-rate current (+0.12 mA; curve (b)) and results in a discharge capacity of only 0.18 wt.% H. This again illustrates the poor dehydrogenation properties of Mg hydride. After reaching 0 V, the electrode was allowed to relax for one hour before starting low-rate dehydrogenation with a current of +0.012 mA, which took about 13.5 hours. The low-rate discharging behavior (curve (c)) shows that, in line with the results in Fig. 4.3, all absorbed hydrogen can be desorbed.

The electrochemical response during the initial stages of low-current discharging (curves (c) in Figs. 4.3 and 4.4) shows a distinct evolution of the overpotential (η). In more detail, the potential increases in the early stages of dehydrogenation to about -0.4 V and decreases upon continued discharging. It remains constant until the Mg hydride reaches its H depleted state. A very similar evolution of the electrochemical potential under galvanostatic conditions is generally observed when investigating nucleation and growth mechanisms.[29] Therefore, this characteristic response might be linked to a similar process and is dealt with in more detail in paragraph 4.2.3.2.

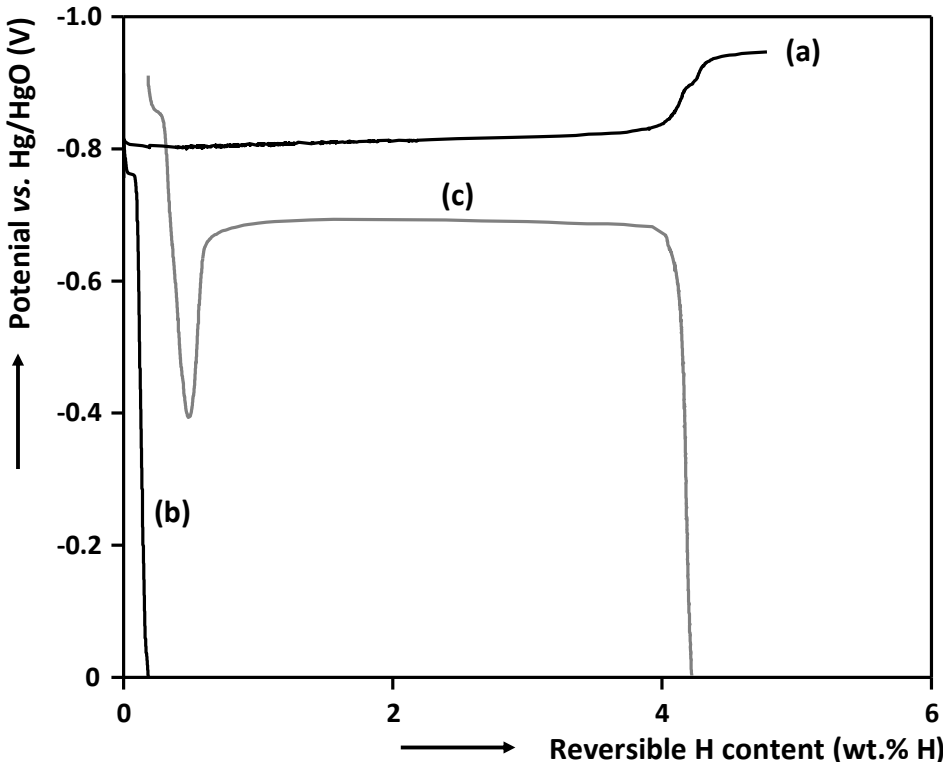

Fig. 4.4 Electrochemical response of a 200 nm thick Mg thin film capped with 10 nm Pd, showing hydrogenation at -0.012 mA (a), discharging at +0.12 mA (b) and deep-discharging at +0.012 mA (c).

From the results in Figs. 4.3 and 4.4 it is clear that pure Mg cannot be used as effective storage medium, because of, amongst others, fast hydrogen uptake and release is impeded. To determine the influence of the Mg-to-Ti ratio various Mg_yTi_{1-y} thin films containing 50 to 95 at.% Mg were galvanostatically (de)hydrogenated while monitoring the electrochemical potential of the electrode. Taking $Mg_{0.85}Ti_{0.15}$ as an example (see Fig. 4.5), the Mg_yTi_{1-y} thin films were firstly charged to their fully hydrogenated state (curve (a)) using a current of -0.6 mA. The electrochemical response is characterized by a narrow α-solid solution during the initial stages of hydrogen insertion. Subsequently, a broad plateau is situated around -1.1 V, indicating an α-to-β phase transition. After the entire thin film is transformed into the β-phase, the HER (reaction 2.14) is observed that also manifests itself as a plateau. After full conversion to the β-phase the electrodes were allowed to equilibrate under open-cell conditions for one hour. Using a high-rate current of +0.12 mA the alloys were discharged until the cut-off potential of 0 V was reached (curve (b)). Subsequently, after one hour of equilibration, the electrode was further discharged using a low-rate current of +0.012 mA (curve (c)). During discharging the thin film, firstly a β-phase solid solution is apparent, followed by a $\beta \rightarrow \alpha$ transformation plateau and finally again solid solution behavior.

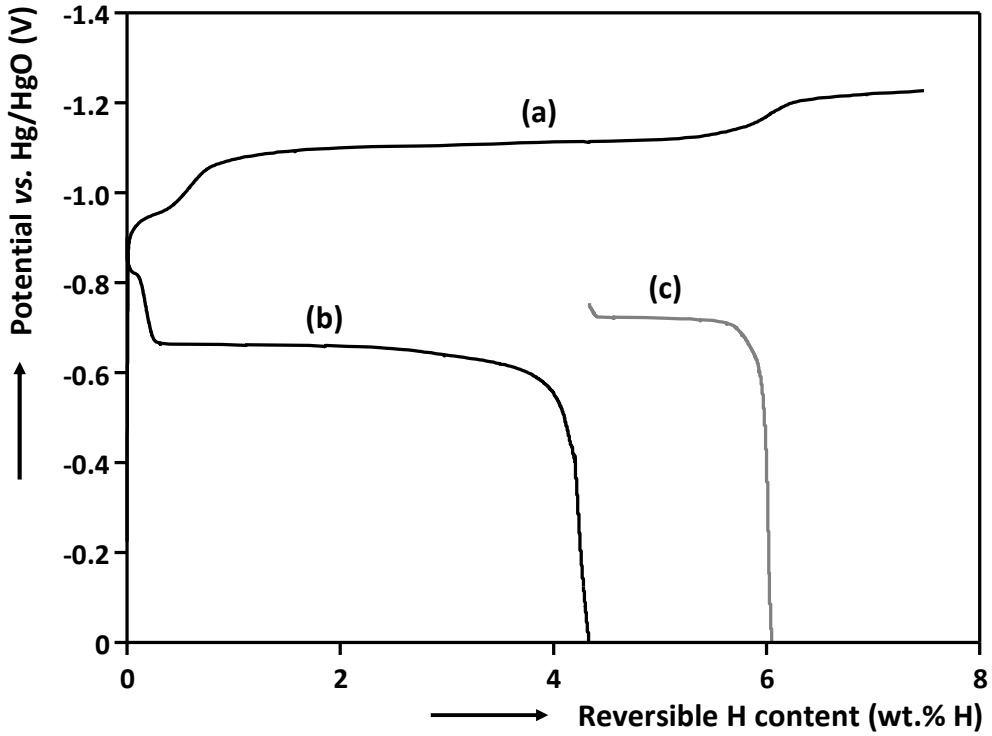

Fig. 4.5 Electrochemical response of a Pd-capped 200 nm thick $Mg_{0.85}Ti_{0.15}$ electrode, showing hydrogenation at -0.6 mA (a), discharging at +0.12 mA (b) and deep-discharging at +0.012 mA (c).

Fig. 4.6 shows the discharge capacities of thin film Mg_yTi_{1-y} alloys with $0.50 \leq y \leq 1.00$ obtained by high-rate discharging (curve (a)) and the summation of the reversible hydrogen content obtained by high-rate and subsequently low-rate discharging (curve (b)). For Mg_yTi_{1-y} thin films with *y* ranging from 0.50 to 0.80 the difference between the discharge capacities for high-rate (curve (a)) and high- and low-current (curve (b)) discharging is relatively small and nearly constant, indicating that increasing the Ti-content does not influence the rate-capability to a large extent. The increase of the discharge capacity for alloys containing more Mg is therefore solely dependent on the decrease in weight of the alloy. A sharply decreasing discharge capacity is observed for high-rate discharging for compounds with a Mg-content higher than 80 at.% (curve (a)). This is in line with the results found for pure Mg and illustrates the poor hydrogen release characteristics of alloys that are rich in Mg. An approximately similar compositional dependence of the discharge capacity for Mg_ySc_{1-y} alloys was reported in the past.[30-33] There, it was argued that the crystal structure of the hydride has a large impact on the hydrogen transport characteristics, *i.e.* fcc-structured hydrides provide fast hydrogen transport, whereas the common bct MgH_2 (rutile) structure strongly inhibits hydrogen diffusion. The analogous dependence for the Mg_yTi_{1-y} materials presented here, suggests that the same crystal symmetries are responsible for the notable differences in rate-capability. To elucidate whether the crystal structure can be held responsible for this behavior an in-depth study of the crystal symmetries as a function of hydrogen content and Mg-to-Ti ratio has been performed and is presented in chapter 5. Finally, it is interesting to note that the results of the pure Mg film (y=1.00) in Fig. 4.6 were obtained after hydrogenating the film with a current 50 times lower than that used to charge

the Mg_yTi_{1-y} alloys, emphasizing the positive effects of substituting even small amounts of Mg by Ti.

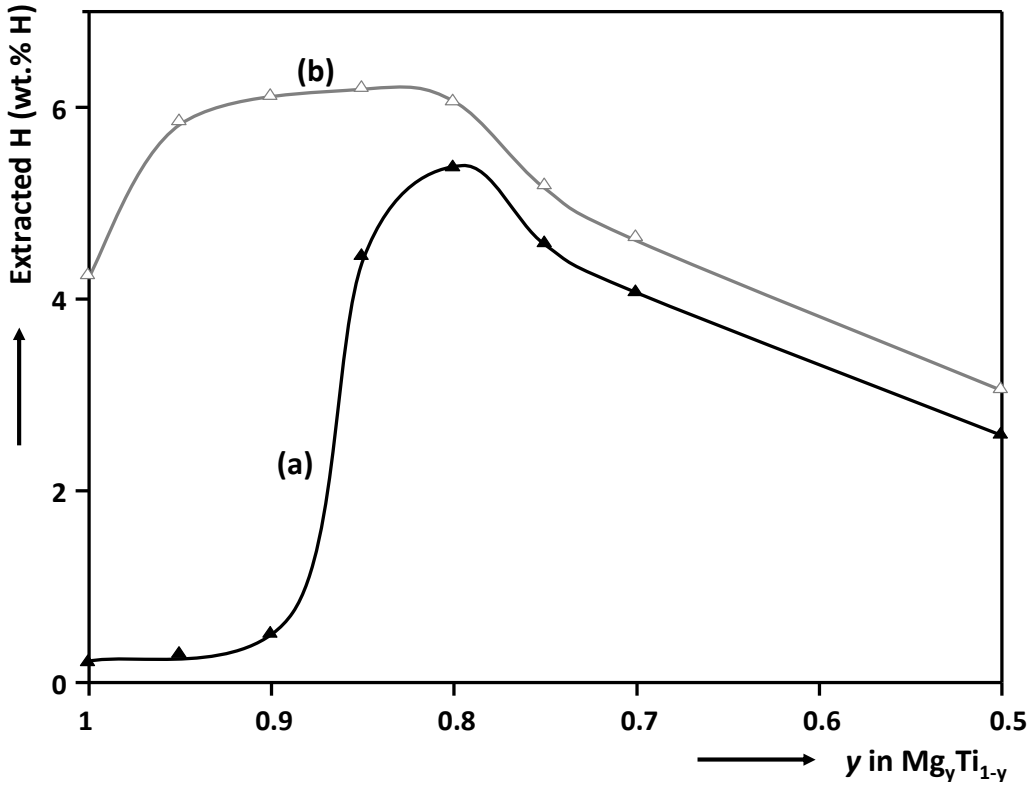

Fig. 4.6 High current (a; *I*=+0.12 mA) and low current (b; *I*=+0.012 mA) discharge capacities for Mg_yTi_{1-y} electrodes with varying composition. The Mg-content was varied in the range *y*=0.50-0.95. Additionally, pure Mg is included.

Aside from a high discharge capacity, one of the key requirements of a MH is the cycling stability. The results of cycling a $Mg_{0.80}Ti_{0.20}$ alloy are depicted in Fig. 4.7 and reveal that a high hydrogen storage capacity is still maintained up to 11 cycles. Hereafter, the discharge capacity decreases sharply. In this figure the discharge capacity shows the summation of the discharge capacities obtained at both high-rate and low-rate discharging. During each successive cycle, the discharge capacity upon high-rate discharging decreases which points to a diminishing rate-capability of the $Mg_{0.80}Ti_{0.20}$ alloy. This has been investigated more thoroughly using electrochemical impedance spectroscopy and is presented in paragraph 4.2.3.3. The origin of the decrease of the discharge capacity beyond cycle number 11 is closely related to the mechanical stability of the thin film electrode on the supporting substrate. It is likely that due to the large volume expansion of the $Mg_{0.80}Ti_{0.20}$ layer upon hydrogenation mechanical stresses are induced in the thin films. These stresses cause the thin film to slowly delaminate, effectively decreasing the storage capacity. This observation shows that the decrease of the discharge capacity is by no means related to the intrinsic cycling stability of the $Mg_{0.80}Ti_{0.20}$ alloy. In spite of the fact that the electrochemical cycling stability is not yet optimized, the initial results are very encouraging. Gas phase (de)hydrogenation has shown that the cycle-life of sputtered Mg-Ti alloys easily surpasses

100 cycles, indeed revealing good intrinsic recycle-ability properties of thin film Mg_yTi_{1-y} hydrogen storage compounds.[34]

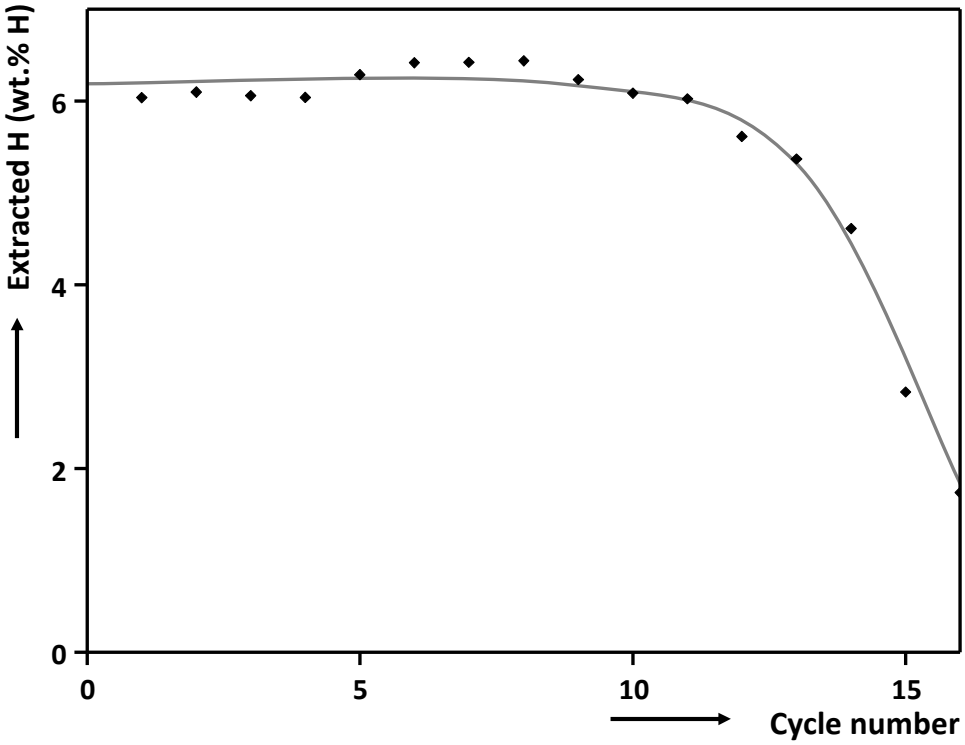

Fig. 4.7 Reversible hydrogen storage capacity, obtained for high-rate and subsequently low-rate discharging, as a function of cycle number for a $Mg_{0.80}Ti_{0.20}$ alloy.

In order to discuss the effect of the Ti-content in more detail, selected hydrogenation curves of the Mg_yTi_{1-y} thin films with *y* ranging from 0.50 to 0.95 are depicted in Fig. 4.8. It should be emphasized that these curves show the electrochemical response when hydrogenating freshly prepared thin films. It is known that the electrochemical response of subsequent (de)hydrogenation cycles may reveal somewhat different behavior.[15] At a first glance, the presented charging curves can be divided into three regions. In the early stages of hydrogenation it is evident that the width of the first plateau increases with increasing Ti-content. Hereafter, a second plateau develops, which, based on its width and position, could be attributed to the conversion of Mg to Mg hydride. These observations may suggest that Mg and Ti form separate phases once they are hydrogenated. Interesting to note is that the Mg-to-Ti ratio clearly affects the hydrogen uptake amount at a fixed absorption rate. An additional effect, evident from Fig. 4.8, is that the Ti-content affects the degree of sloping of the second plateau. Ti-rich alloys (*e.g.* y=0.50 and 0.70) are characterized by a rather sloping second plateau, whereas Mg-rich materials (*i.e.* y=0.95) exhibit a very flat plateau region.

After the hydrogenation of the Mg-Ti layer the electrochemical potential decreases further until a stable value is reached where hydrogen gas formation occurs (reaction 2.14). Surprisingly, this potential value is quite susceptible to the composition of the Mg_yT_{1-y} compound. Although the Pd/KOH interface is expected to have similar electrocatalytic properties for all Mg_yTi_{1-y} systems, the difference in potential at which hydrogen gas evolves

suggests otherwise. Apparently the surface kinetics at the Pd topcoat is significantly influenced by the composition of the underlying Mg_yTi_{1-y} layer. A possible reason for this could be that the degree of expansion of the Mg_yTi_{1-y} lattice upon hydrogenation changes with Ti-content, introducing more or less stress in the Pd film, which alters the electrocatalytic properties.

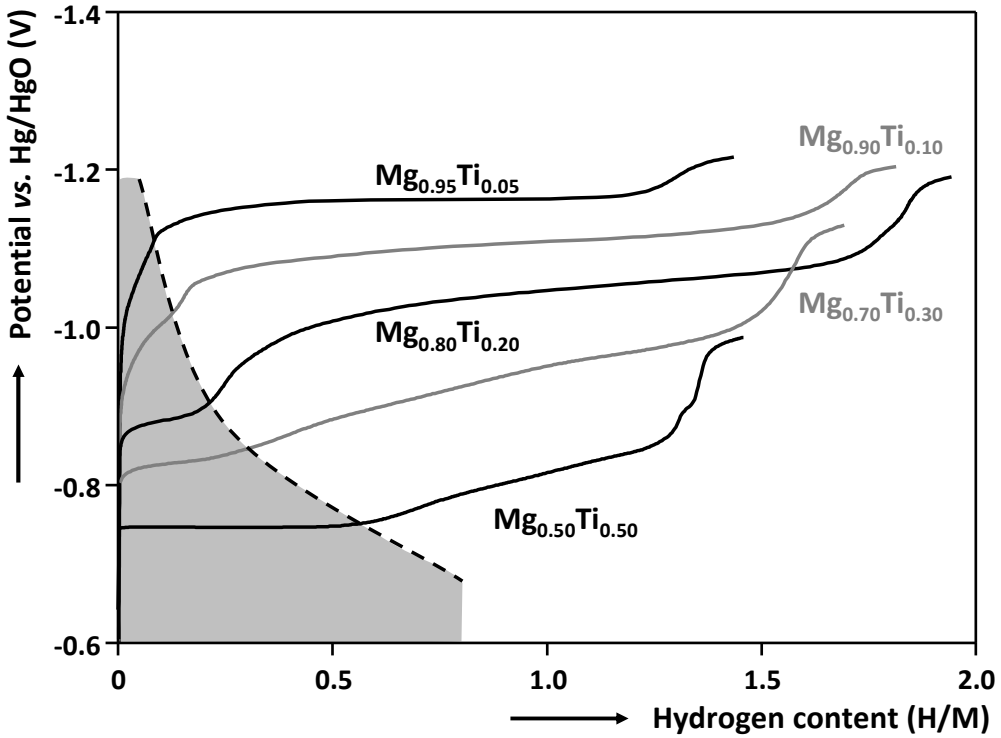

Fig. 4.8 Galvanostatic behavior of Mg_yTi_{1-y} thin films (y=0.50-0.95) showing the first hydrogenation. The applied current was -0.6 mA in all cases. The dashed line is merely a guide for the eye, indicating the transition from the first to the second plateau.

4.2.3 Thermodynamics and kinetics

As the Mg_yTi_{1-y} alloys described in this thesis all contain a substantial amount of Mg, firstly the thermodynamics and kinetics of hydrogen absorption and desorption in Mg thin films is determined by means of GITT (see paragraph 2.3.4). Secondly, the thermodynamics of electron-beam evaporated $Mg_{0.70}Ti_{0.30}$, $Mg_{0.75}Ti_{0.25}$, $Mg_{0.80}Ti_{0.20}$ and $Mg_{0.85}Ti_{0.15}$ is determined. These particular compositions were selected based on their superior storage properties, which is essential for future hydrogen storage applications. Additionally, the individual contribution of the reactions and processes to the overall uptake and release rates is resolved by Electrochemical Impedance Spectroscopy (EIS) measurements (see paragraph 2.3.6).

4.2.3.1 The thin film magnesium-hydrogen system

To determine the thermodynamic absorption and desorption properties of the magnesium-hydrogen system GITT is used (see paragraph 2.3.4). This method is based on collecting equilibrium potential data by successively applying a current pulse followed by a current-off relaxation period.

The results of hydrogen absorption by multiple current steps (I = -0.012 mA for 2100 s each) of an as-prepared Mg thin film electrode at room temperature are depicted in Fig. 4.9. Curves (a) show the electrochemical overpotential during current on conditions. After each current pulse the Mg-electrode is allowed to equilibrate for 1 hour. The symbols show the equilibrium potentials (E^{eq}) at the end of the relaxation period and the corresponding isotherm is shown by curve (b). The inset shows the potential response and subsequent one-hour relaxation period of a typical GITT pulse at the plateau (indicated by the arrow) and shows that after the current interruption the potential quickly stabilizes to the new equilibrium potential.

Equilibrium curve (b) shows the typical behavior of a conventional metal-hydrogen system. In the early stages of hydrogen absorption a narrow solid solution behavior is apparent. Upon further hydrogen absorption a two-phase coexistence is observed that manifests itself as a, nearly constant, plateau. At approximately 4.5 wt.% H the equilibrium potential increases again due to the sole existence of a hydrogen-rich β-phase. Hereafter, the Pd capping layer absorbs hydrogen, which is visible from curves (a) that show a narrow plateau-like feature in this hydrogen-rich region. After the Pd layer is saturated with hydrogen, hydrogen gas evolution starts at the surface of the electrode, according to Eq. 2.14.

It is generally accepted that hydrogenation of a Pd-capped Mg film begins with the formation of a hydride at the Pd/Mg-interface which grows into the material. The growth is rate-limited by the diffusion of hydrogen through the hydride layer, which effectively blocks hydrogen.[3-13] The electrochemical hydrogenation mechanism of a Pd-coated Mg thin film depicted in Fig. 4.10A, where the electrochemical charge transfer reaction at the Pd/electrolyte interface, solid state diffusion in the Pd layer and solid state diffusion in the MgH_2 are indicated. Thus, the largest contribution to the overpotentials (curves (a) in Fig. 4.9) required for hydrogen absorption is likely related to poor hydrogen diffusion in the MgH_2 layer. Poor diffusivity properties are probably also the origin of the fact that the overall hydrogen absorption capacity at room temperature is lower than the theoretical value of 7.6 wt.% H (see Fig. 4.9). The amount of hydrogen absorbed by the magnesium film will be even somewhat lower than the 4.5 wt.% H absorbed by the Mg layer found from the data presented in Fig. 4.9, because hydrogen evolution (Eq. 2.14) competes with the hydrogen absorption reaction.

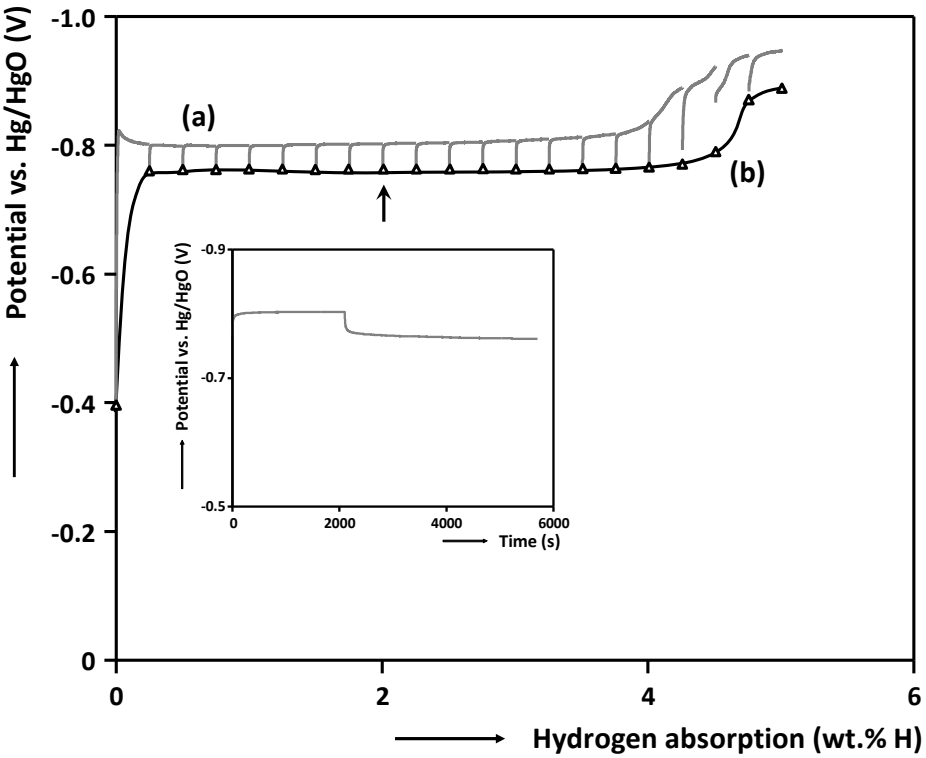

Fig. 4.9 Equilibrium absorption curve of a 200 nm thick Mg thin film electrode capped with 10 nm Pd. The equilibrium points (Δ) are determined by means of GITT during charging and the electrochemical response during each current pulse (+0.012 mA) is shown by the curves (a). The corresponding isotherm is shown by curve (b). The inset shows the corresponding potential response and subsequent relaxation at approximately half of the total absorption capacity (indicated by the arrow).

One of the most important properties of a metal-hydrogen system is the plateau pressure, *viz.* the pressure at which the hydrogen-poor α-phase transforms into a hydrogen-rich β-phase. By applying Eq. 2.19 to the plateau potential found in Fig. 4.9 (-0.76 V), the hydrogen partial pressure for hydride formation is calculated to be $1.7*10^{-6}$ bar H_2 at 298 K, which, according to Eq. 2.4, corresponds to an enthalpy of formation of -72 kJ/mol H_2. This value is in good agreement with the results previously reported by Stampfer *et al.* (-74 kJ/mol H_2) and Vigeholm *et al.* (-70 kJ/mol H_2).[1,35] Note that these experimental results were, however, determined at high temperatures (>600 K), whereas the present electrochemical experiments are performed at room temperature.

After hydrogen absorption, the Mg hydride film is dehydrogenated by changing the polarity of the current. Hydrogen is desorbed in 17 current pulses using a current of +0.012 mA for 2100 s each. The voltage response of each of these pulses is shown in Fig. 4.11 by curves (a). The inset shows the potential response of a typical GITT desorption pulse and subsequent relaxation period. The potential response shows that just after the current interruption at 2100 s the overpotential decreases and equilibrates after one hour. The equilibrium potentials at the end of the relaxation periods are indicated by the symbols and the corresponding equilibrium curve is shown by curve (b).

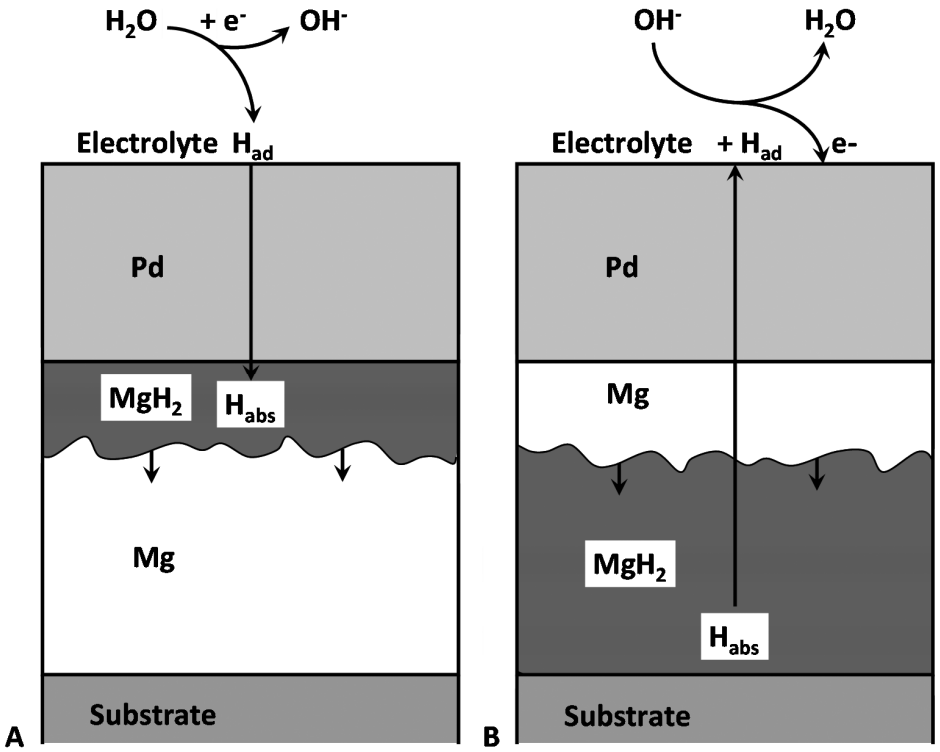

Fig. 4.10 Schematic representation of the hydrogenation (A) and dehydrogenation (B) mechanism of a Pd-coated Mg thin film.

The total amount of hydrogen that can be desorbed is somewhat lower than the amount absorbed initially (see Fig. 4.9). This is probably caused by the large driving force required to dehydrogenate the material (see the large overpotentials in curves (a) of Fig. 4.11). The equilibrium curve (curve (b)) shows similar characteristics as the hydrogenation curve shown in Fig. 4.9, however, now we start from the hydrogen-rich β-phase and finally end up with the hydrogen-poor α-phase. The average equilibrium potential of the phase transition plateau is -0.75 V, which corresponds to a hydrogen partial pressure of $7.6*10^{-7}$ bar. At 298 K this pressure relates to an enthalpy of hydride decomposition of -74 kJ/mol H_2. This value is close to the previously reported desorption data by Krozer and Kasemo (-71 kJ/mol H_2).[36] The plateau pressure of hydride formation and decomposition only shows a small hysteresis, which can be attributed to strain induction-relaxation and/or plastic deformation by the expansion-contraction of the crystal lattice during hydride formation-decomposition, respectively.[37,38]

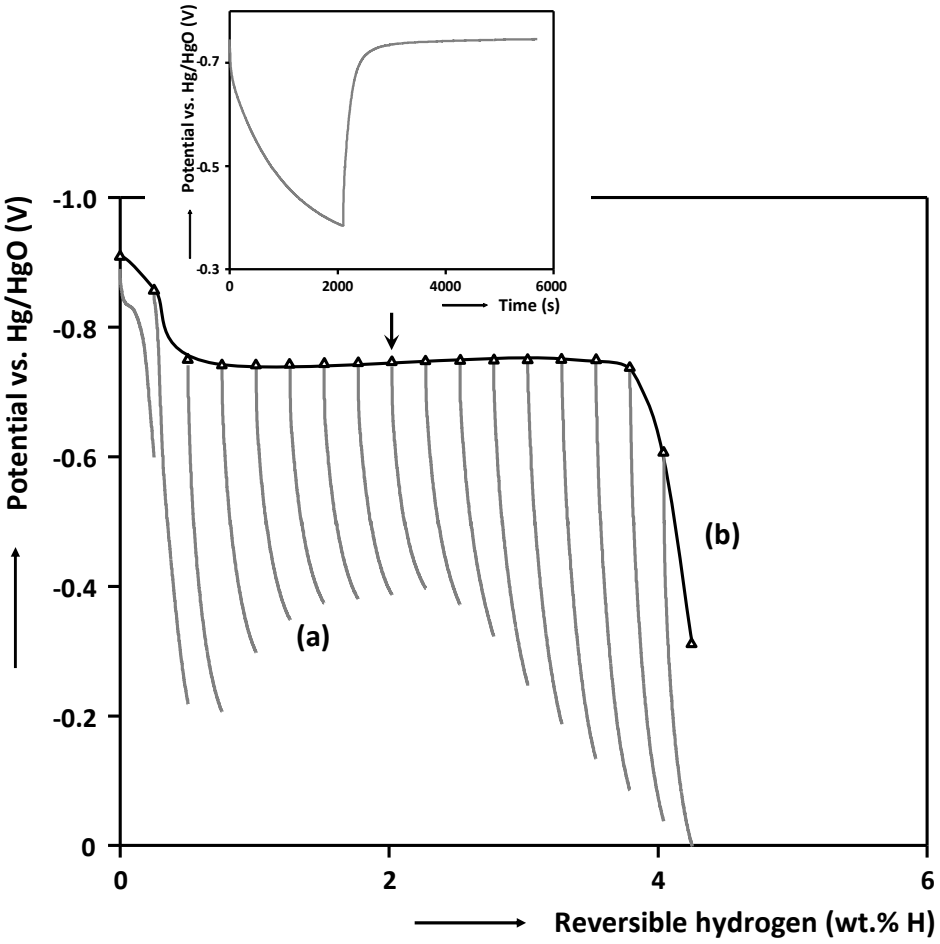

Fig. 4.11 Equilibrium desorption curve of a 200 nm thick Mg thin film electrode capped with 10 nm Pd. The equilibrium points (Δ) are determined by means of GITT during discharging. The voltage response during each current pulse (-0.012 mA) is shown by curves (a). The isotherm is shown by curve (b). The inset shows the potential response and subsequent one-hour relaxation of the GITT pulse at approximately half of the total desorption capacity (arrow).

To determine the origin of the remarkably large overpotentials in Fig. 4.11 (curves (a)), we firstly focus on a recent study where Mg thin film electrodes were galvanostatically (de)hydrogenated in a single step (see Fig. 4.4). Strikingly, curve (c) in Fig. 4.4 reveals that only in the early stages of dehydrogenation a large overpotential is required. Hereafter, the overpotential quickly decays and remains nearly constant until the hydrogen-depleted state is reached. Apparently, a strong driving force is required before dehydrogenation proceeds more facile.

Remarkably, curves (a) in Fig. 4.11 show that, if the MgH_x thin film electrodes are dehydrogenated in multiple steps, each step requires a large overpotential, whereas dehydrogenation in a single run only requires a large driving force in the early stages of dehydrogenation (see curve (c) in Fig. 4.4). Interesting to note is that it has been identified that in a hydrogenated Pd-capped Mg-hydride film, dehydrogenation will be initiated at the

Pd/MgH_2 interface.[39] Therefore, the nucleated Mg layer grows into the MgH_2 layer. The electrochemical dehydrogenation mechanism of a Pd-capped Mg thin film is depicted in Fig. 4.10B.

Hydrogen diffusion in the MgH_2 layer but also in the nucleated Mg layer and Pd layer cannot be the origin of the extremely large initial overpotentials, as a large overpotential would then be expected throughout the entire dehydrogenation process. Furthermore, the electrochemical charge transfer reaction (Eq. 2.12) at the Pd/electrolyte interface cannot be the source of the extreme overpotential as this reaction also occurs throughout the entire dehydrogenation process.

In a study by Rydén *et al.* it was shown by depth profiling of hydrogen in a Pd/Mg/Pd/Mg sandwich system that hydrogen atoms prefer to occupy host sites in Mg layers that are closest to Pd.[4] The Mg metal phase, which nucleates at the Pd/MgH_2 interface during the multiple dehydrogenation steps in Fig. 4.11, probably reabsorbs hydrogen again during the relaxation period that follows the current pulse. Consequently, in the next dehydrogenation step a Mg metal phase again has to nucleate and grow at the Pd/MgH_2 interface. This explanation is in line with the report by Milchev and co-workers as the shape of the overpotentials in Fig. 4.4 (curve (c)) and Fig. 4.11 (curves (a)) closely resembles a typical response for a nucleation and growth mechanism.[29] It also explains that in Fig. 4.4 only at the beginning of dehydrogenation (curve (c)) a large overpotential is observed, because there the Mg layer only has to nucleate once (see Fig. 4.10B).

In order to obtain more detailed information about the thermodynamics of hydrogen storage in pure Mg, the experimental desorption equilibrium data are simulated with the recently developed LGM.[40] This model has already been successfully applied to simulate the pressure-composition isotherms of Pd thin films (see paragraph 3.2.1) and $LaNi_yCu$ and Mg_ySc_{1-y} alloys.[40-42]

The experimental hydrogen desorption isotherm (symbols) and simulation results (line) of a Mg thin film electrode are plotted as a function of the normalized reversible hydrogen capacity in Fig. 4.12. Note that the desorption isotherm is now plotted as a conventional pressure-composition isotherm, *i.e.* with increasing hydrogen content. The agreement between experiment and simulation is excellent. The values of the simulation parameters are listed in Table 4.1. Three individual regions can be distinguished: the α- and β-solid solution regions with phase transition points at x_α=0.103 and x_β=0.837 and a two-phase coexistence region at $0.103 \leq x \leq 0.837$.

Table 4.1 Energy parameter values obtained by simulating the desorption isotherm of a Pd-capped Mg electrode using the LGM.

x_α	x_β	E_α (eV)	E_β (eV)	$U_{\alpha\alpha}$ (eV)	$U_{\beta\beta}$ (eV)	$U_{\alpha\beta}$ (eV)	L (eV)
0.103	0.837	-0.458	-1.408	3.206	1.407	11.85	0.522

It is interesting to compare the LGM parameters with those previously reported for the Mg_ySc_{1-y} alloys.[42] From Table 4.1 it can be seen that the interaction energies between hydrogen atoms in the α- and β-phase ($U_{\alpha\alpha}$ and $U_{\beta\beta}$) and the inter-phase interaction energy

($U_{\alpha\beta}$) are positive, which means that the interaction has a repulsive character. Compared to the results found for the Mg_ySc_{1-y} alloys the repulsive interaction is stronger for pure Mg and is probably caused by the fact that Mg is somewhat more electropositive than Sc, which may result in a larger negative charge on the hydrogen atoms ($H^{\delta-}$) and therefore stronger repulsive coulombic interactions.[43]

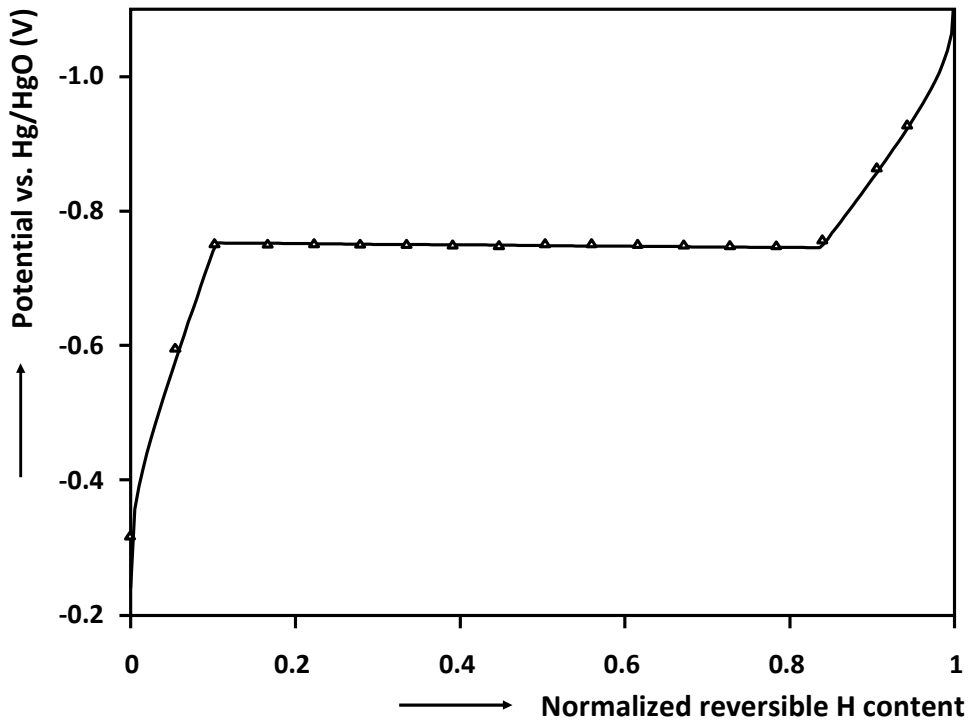

Fig. 4.12 Measured (symbols) and calculated (line) isotherm of a 200 nm thick Mg electrode with a 10 nm Pd capping layer at room temperature.

The transformation energy of the host lattice ($L = 0.522$ eV) is the highest for pure Mg compared to Mg_ySc_{1-y}, which is in line with the general trend found by decreasing the Sc-content in Mg_ySc_{1-y} alloys.[42] Phase transformation is, in general, accompanied by a volume change of the unit cell. It has been shown for Mg_ySc_{1-y} alloys with $0.50 \leq y \leq 0.80$ that the hydride forms a fcc structure, whereas MgH_2 has a bct structure.[30] The transformation to a different crystal structure, also starting from a different crystal structure, *i.e.* cubic for Mg_ySc_{1-y} alloys[32] and hcp for Mg thin films (see Fig. 4.1), requires a different value of *L*. It can be concluded that the relatively high value of *L* found for pure Mg (0.522 eV) compared to Mg_ySc_{1-y} (0.191 eV on average) indicates that the phase transformation of pure Mg to MgH_2 requires more energy.[42]

As the phase transition points (x_α and x_β) for the hydrogen desorption isotherm of the pure Mg are accurately determined using the LGM, it is possible to complete the phase diagram of Mg_ySc_{1-y} alloys (see Ref. 42) at room temperature as a function of alloy composition and normalized hydrogen concentration. The complete phase diagram is shown in Fig. 4.13 and reveals that the miscibility gap closes with decreasing the Mg-content.

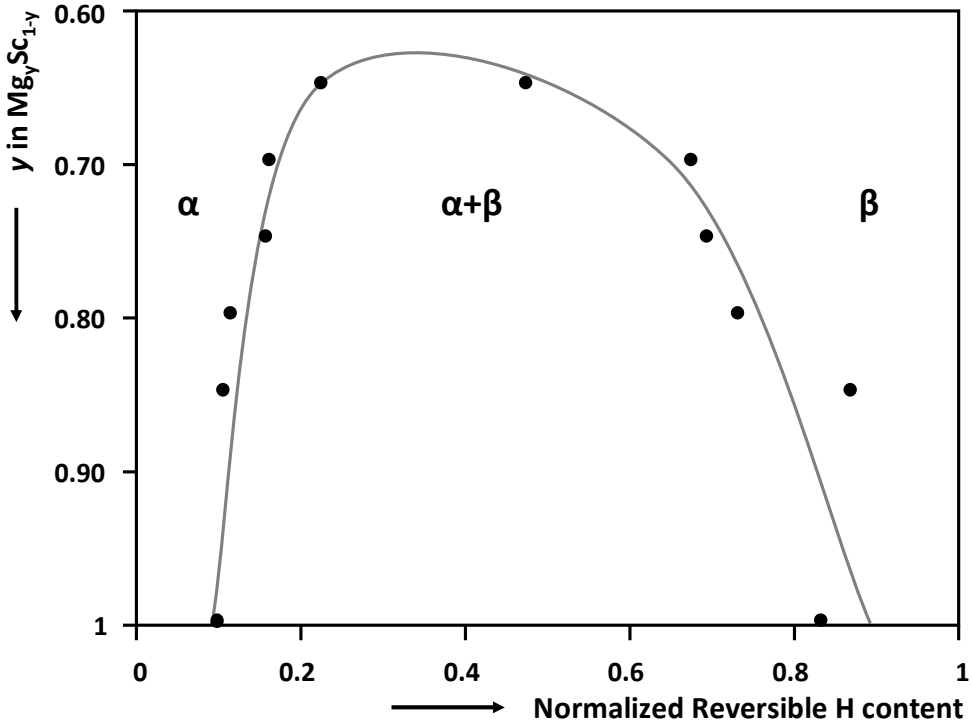

Fig. 4.13 Calculated phase diagram as a function of Mg content and normalized hydrogen concentration of Mg_ySc_{1-y} (simulations of Mg_ySc_{1-y} alloys are presented in Ref. 42).

According to the LGM, the Gibbs free energy (G) of the hydrogen storage system can be calculated according to Eqs. 3.6-3.8. Fig. 4.14 shows the contribution of the energy (curve (a)) and entropy (curve (b)) to the total Gibbs free energy (curve (c)).Evidently, the partial energies of the separate phases are never below the total energy of the system. This observation is in line with the principle of minimal energy which states that the Gibbs free energy in the two-phase coexistence region is always lower than that of the single phases. The slope of the partial energy curve for the α-phase changes from negative to positive in the vicinity of x_α. It is apparent that further hydriding the α-phase is thermodynamically unfavorable, which is the driving force for the phase transition.

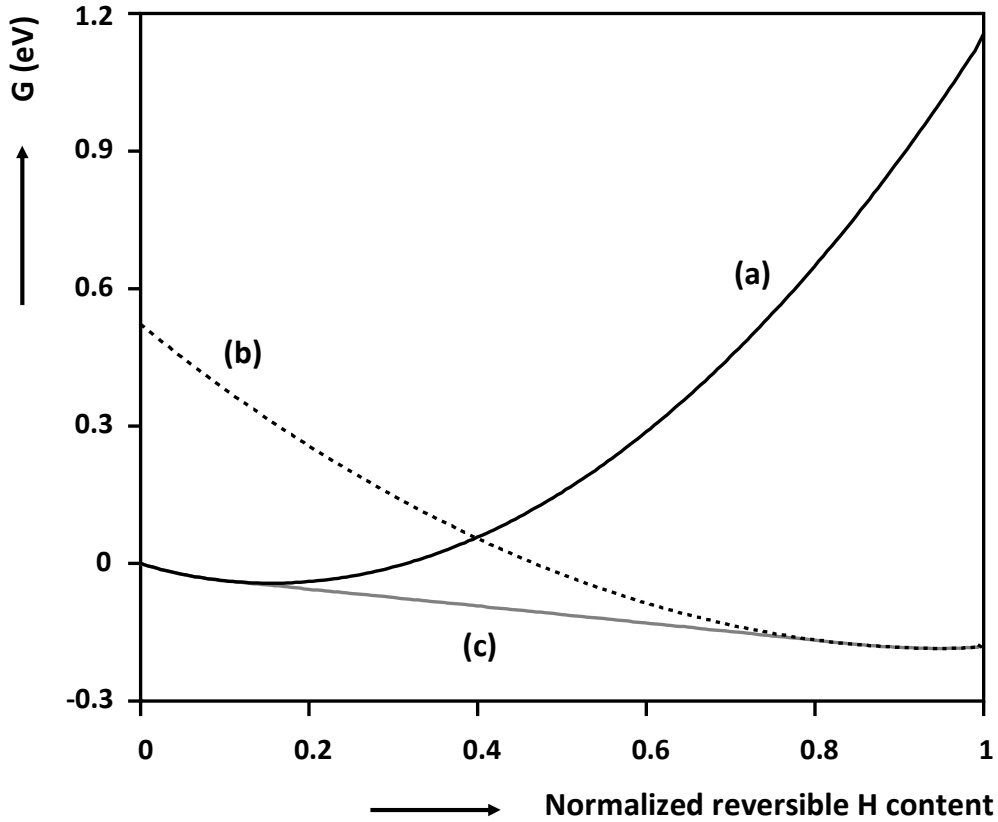

Fig. 4.14 Evolution of the Gibbs free energy as a function of normalized hydrogen content for 200 nm thick Mg film capped with 10 nm Pd. The partial energy curves of the α-phase (a) and the β-phase (b) are shown together with the Gibbs free energy curve of the total system (c).

4.2.3.2 Thermodynamics of Mg_yTi_{1-y} thin films

GITT experiments were performed by charging the as-prepared films with -0.6 mA. Hereafter, the hydrogenated alloys were discharged in approximately 20 current pulses of +0.012 mA. After each pulse the system was allowed to equilibrate for 1 hour. As soon as the potential reached 0 V *vs.* Hg/HgO the current was interrupted and followed by a relaxation period of one hour. An example of a typical GITT result is shown in Fig. 4.15 for a 200 nm thick $Mg_{0.85}Ti_{0.15}$ thin film capped with 10 nm Pd.

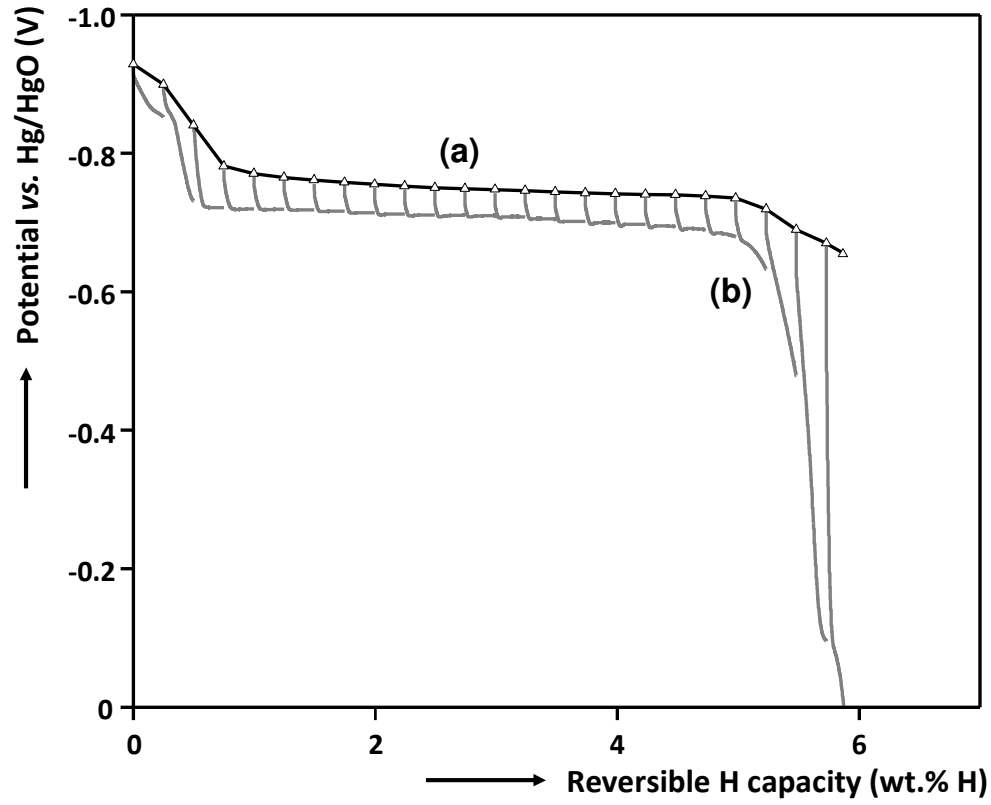

:

Fig. 4.15 Voltage equilibrium curve of a 200 nm thick $Mg_{0.85}Ti_{0.15}$ thin film electrode capped with 10 nm Pd. The equilibrium points (Δ) are determined by means of GITT during discharging and the corresponding isotherm is shown by curve (a). The electrochemical response during each current pulse (I=+0.012 mA) is shown by curves (b).

Fig. 4.15 shows the experimentally determined equilibrium points (symbols), together with the corresponding equilibrium curve (curve (a)), as well as the dynamic potential responses during each current pulse (curves (b)). The latter curves clearly show that the overpotential (η) remains nearly constant throughout the entire discharge process, only to increase significantly at the very end of the discharge process which is caused by the depleting amount of hydrogen, *i.e.* diffusion limitations. This is typical for all MgTi alloys investigated in this study.

The equilibrium desorption curves of the Mg_yTi_{1-y} compounds, with $0.70 \leq y \leq 0.85$ determined by means of GITT, are depicted in Fig. 4.16. The electrochemical equilibrium potentials are converted to hydrogen partial pressures using Eq. 2.19 to obtain pressure-composition isotherms. These electrochemically determined isotherms are presented in line with conventional pressure-composition isotherms. Note therefore that the x-axis is the reversible amount of hydrogen under the applied electrochemical dehydrogenation (oxidation) conditions. Hence it is not the absolute amount of hydrogen inside the metallic matrix, as it will be shown in chapter 5 that part of the hydrogen atoms probably remain in Ti-rich regions as these provide a high stability.

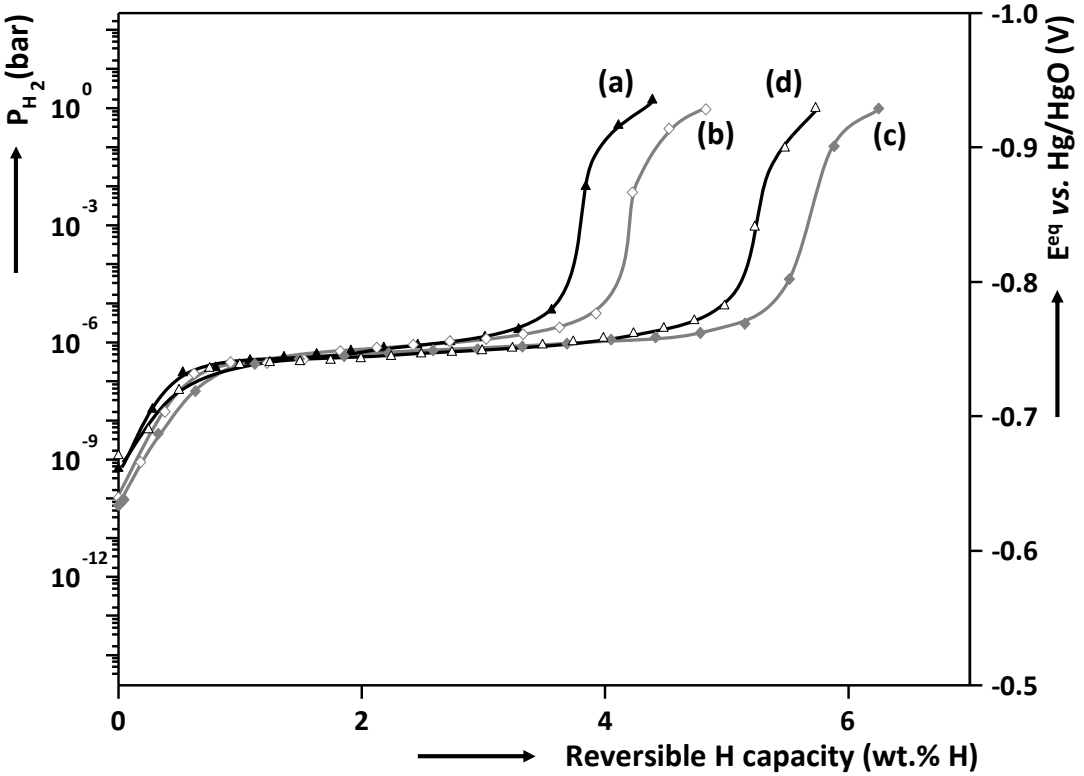

Fig. 4.16 Desorption isothermal curves of 200 nm thick (a) $Mg_{0.70}Ti_{0.30}$, (b) $Mg_{0.75}Ti_{0.25}$, (c) $Mg_{0.80}Ti_{0.20}$ and (d) $Mg_{0.85}Ti_{0.15}$ layers with a 10 nm Pd topcoat determined with GITT.

The isotherms consist of three individual regions. First, the metal hydrides are in the hydrogen depleted state also known as the α-solid solution, where hydrogen is randomly dissolved in the solid matrix. Increasing the hydrogen content nucleates the β-phase and is generally observed as a plateau in the isotherm. After further hydrogenation, only a β solid solution remains, where hydrogen is in distinct structural sites in the metal lattice.

The plateau pressure is found to be more or less independent of the Mg-to-Ti ratio and is in the order of 10^{-6} bar H_2 for all alloys, which is nearly equal to the value found for desorption of MgH_2 thin films, suggesting that the plateau pressure is dominated by this reaction.[36] This observation points to phase segregation of Mg and Ti as one would expect considering the positive enthalpy of mixing of Mg and Ti.[16] Various reports, however, show that large scale phase segregation does not occur even after repeatedly hydrogenation and subsequent dehydrogenation.[44-46] Based on this model the plateau observed in the isotherms is likely to be due to dehydrogenation of sites that are surrounded mostly by Mg, because Ti-related sites are, according to the high thermodynamic stability of TiH_2, too stable to release hydrogen at a hydrogen partial pressure of about 10^{-6} bar. This is explains why the first hydrogenation responses show in Fig. 4.8 differ from the successive hydrogenation cycles as part of the absorbed hydrogen atoms during the first hydrogenation step are not desorbed.

4.2.3.3 Kinetics of hydrogen uptake and release by Mg_yTi_{1-y} alloys

As pointed out in paragraph 2.3.6, EIS is often used to resolve the individual contributions of the reactions and processes to the overall impedance. The layered planar structure of the thin film electrodes investigated here enables a detailed study on the specific influence of the electrochemical reactions and processes that occur in the separate layers, but also at the interfaces.

Typical results of EIS experiments, often shown in a Nyquist plot, performed at 0, 20, 40, 60, 80 and 100 % of the reversible hydrogen content of a $Mg_{0.85}Ti_{0.15}$ electrode are depicted in Fig. 4.17. The electrochemical equivalent of the reversible hydrogen content is the Depth-Of-Discharge (DOD), where 0% DOD is used for a completely hydrogenated Mg_yTi_{1-y} electrode and 100% points towards a dehydrogenated electrode. The Nyquist response at 100% DOD shows two distinct semi-circles, whereas at higher hydrogen contents the second semi-circle is less pronounced or even completely absent. Moreover, the radii of both semi-circles strongly depend on the hydrogen content.

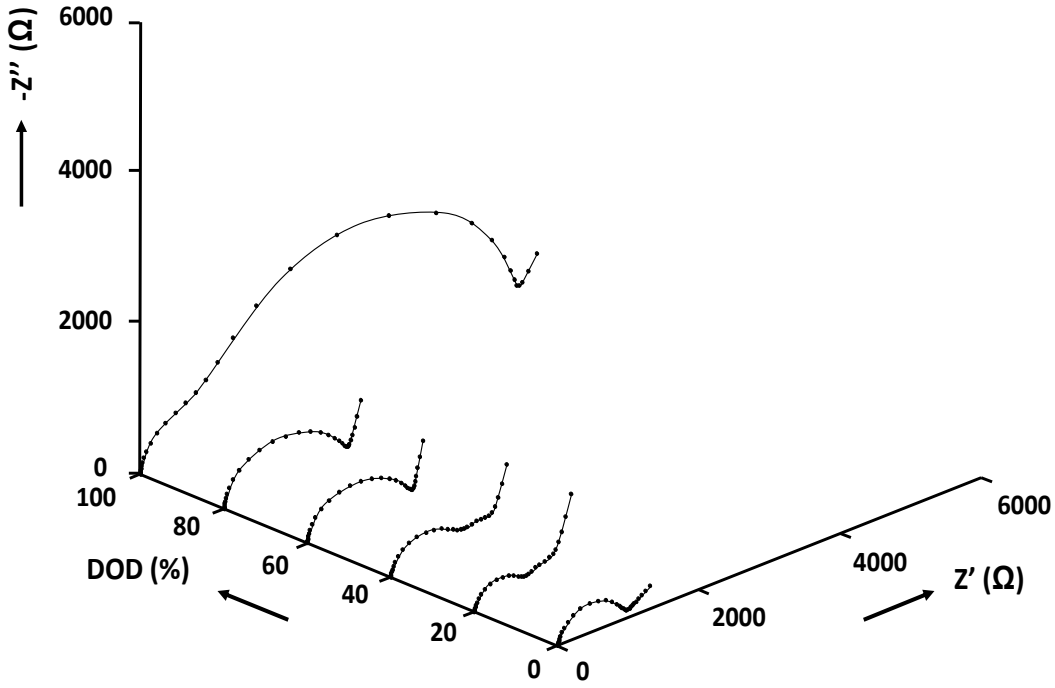

Fig. 4.17 Nyquist plot of a $Mg_{0.85}Ti_{0.15}$ thin film alloy measured at 0%, 20%, 40%, 60%, 80% and 100% of the reversible amount of hydrogen (depth of discharge (DOD)).

To obtain values for the contributions of the various reactions and processes that together make up the total impedance of the system, an equivalent circuit (EQC) is required. To construct the EQC the fact that the Mg_yTi_{1-y} layers capped with Pd can be treated as two-layer systems, as is illustrated in Fig. 4.18, is utilized.

The (electro)chemical reactions and process during hydrogenation of the layered, planar electrodes are shown in Fig. 4.18. Here, step (1) represents the reduction of H_2O at the electrolyte/Pd interface, step (2) shows the reaction of adsorbed hydrogen (H_{ad}) forming

subsurface hydrogen (PdH_{ss}), step (3) is solid-state diffusion of H_{ss} into the Pd film forming absorbed hydrogen (PdH_{abs}), step (4) represents the transfer of hydrogen across the Pd/Mg_yTi_{1-y} interface nucleating the MgTi hydride phase and finally step (5) is solid-state diffusion of hydrogen into the bulk of the Mg_yTi_{1-y} layer.

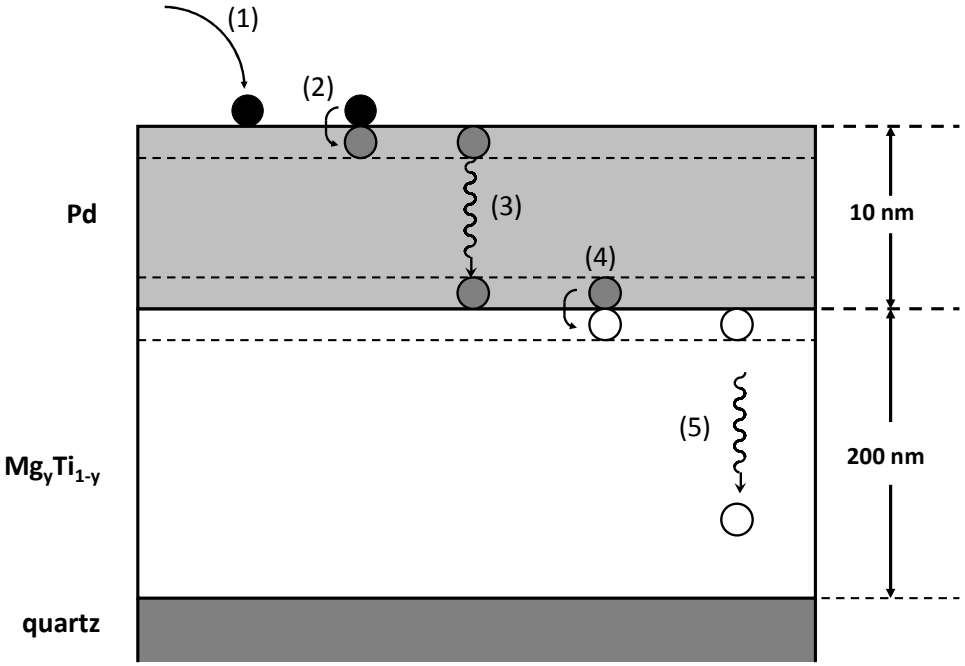

Fig. 4.18 Schematic representation of a 200 nm thick Mg_yTi_{1-y} thin film alloys covered with 10 nm Pd deposited on a quartz substrate. Indicated are the (electro)chemical reactions and processes related to hydrogen absorption.

An EQC that describes hydrogen absorption in two steps is thoroughly described by MacDonald, Montella and Gabrielli *et al.*[47-49] We can therefore use the same EQC as depicted in Fig. 3.6A as the basis for the new EQC. The complete EQC for the situation shown in Fig. 4.18 is depicted in Fig. 4.19A. The box with the broken line indicates that one complex transfer function is needed to describe the linked H-diffusion processes through the Pd layer and the MgTi layer. Here, W_{Pd}^{FLDR} is the Finite Length Diffusion/Reaction (FLDR) Warburg that is used to model finite length diffusion in the Pd layer coupled with a reaction (exchange) rate at the back plane of the Pd layer (here the interface with the MgTi layer). W_{MgTi}^{FS} is the Finite Space (FS) Warburg that theoretically models solid state diffusion in the MgTi layer. When the diffusion in the MgTi layer is much slower than in the Pd layer then the two processes may be separated as indicated by the two Warburg elements, which is a reasonable assumption as diffusion in Pd is known to be very fast and probably many order of magnitude faster than H-diffusion in the MgTi layer.

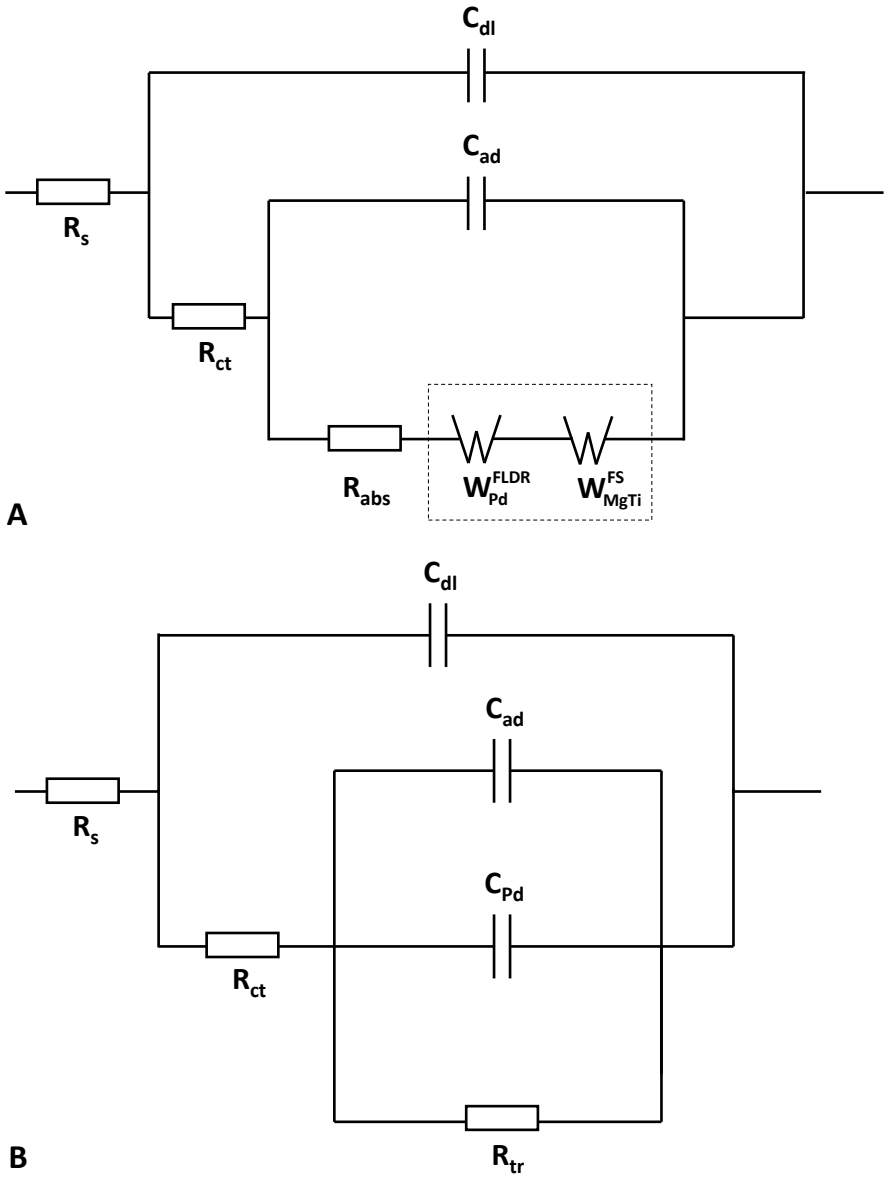

Fig. 4.19 (A) Complete equivalent circuit modeling hydrogen absorption by a two-layer Mg_yTi_{1-y} thin film electrode capped with Pd. In this circuit, the charge transfer is coupled to absorption, subsequent solid-state diffusion of hydrogen in the Pd bulk, followed by transfer of hydrogen across the Pd/Mg_yTi_{1-y} interface and solid-state diffusion of hydrogen in the Mg_yTi_{1-y} bulk and (B) simplified EQC of the circuit shown in (A) obtained when assuming infinitely fast absorption ($R_{abs}\rightarrow 0$) and omitting elements coupled to solid-state diffusion of hydrogen in the Mg_yTi_{1-y} bulk.

In paragraph 3.2.2 it was already extensively discussed that the EIS response of a single Pd layer showed only one semi-circle, consequently, the EQC in Fig. 4.19A can readily be simplified as the resistance of the hydrogen absorption/desorption reaction (R_{abs}) can be neglected. Reports by Yang *et al.* and Gabrielli *et al.* confirm that this is allowed as it was shown that generally the absorption/desorption resistance is extremely small compared to the charge transfer resistance.[49,50] It is further assumed that H-diffusion in the Pd layer is fast

with respect to the transfer kinetics at the Pd/MgTi interface. Therefore W_{Pd}^{FLDR} reduces to a chemical capacitance (C_{Pd}) parallel to a transfer resistance (R_{tr}).

Note that a clear 45° Warburg diffusion line does not appear in the Nyquist plots (see Fig. 4.17). The origin was already experimentally determined by Gabrielli *et al.*, who showed that for films thinner than 10 µm the capacitive behavior of the film becomes too dominant.[51] Therefore, the diffusion-related response at low frequencies was omitted in the present study. This essentially means that the EIS data down to $f \approx 5$ mHz can be accurately modeled as diffusion is only observed at lower frequencies. The complete simplified EQC used to fit the EIS data is shown in Fig. 4.19B.

The circuit elements that are used to fit the experimental data of our EIS measurements will be dealt with separately. Firstly the charge-transfer resistance (R_{ct}) is converted to the more commonly used exchange current density (i_0) using Eq. 3.12 (calculated per unit surface area), and is depicted as a function of the equilibrium potential in Fig. 4.20.

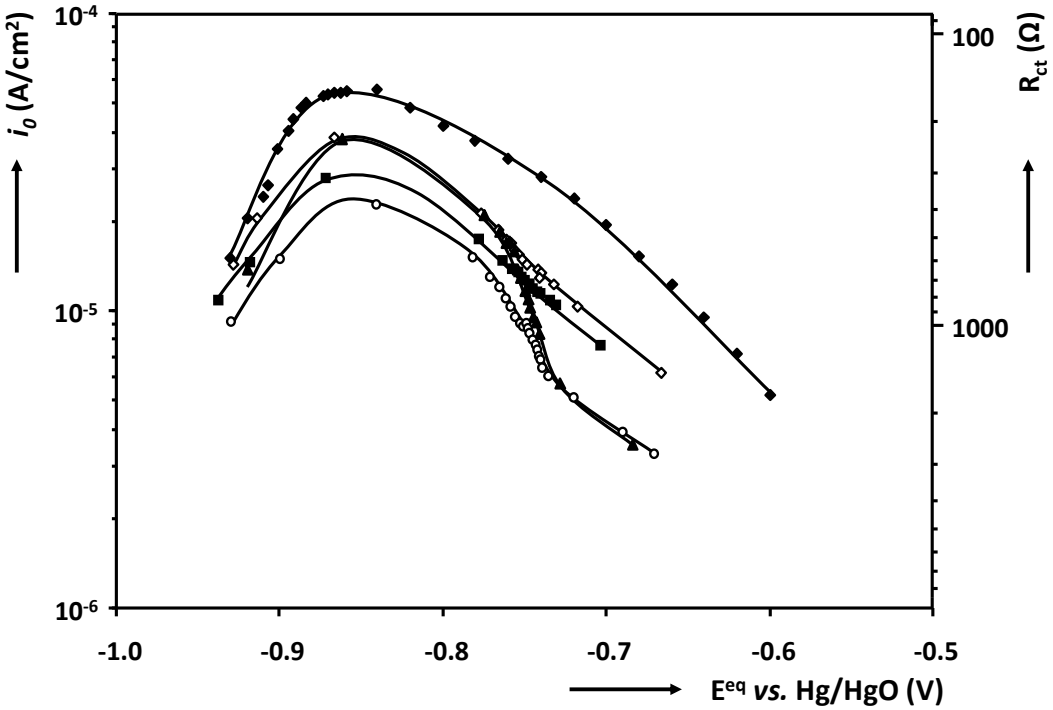

Fig. 4.20 i_0 as a function of equilibrium potential for Mg_yTi_{1-y} with y=0.70 (■), 0.75 (◇), 0.80 (▲) and 0.85 (○). Included is the exchange current density of a 10 nm Pd film (◆) deposited on quartz substrate (see paragraph 3.2.2).

The curves in Fig. 4.20 show that a similar shape is observed for all composition. The small deviations of i_0 for the different compositions are attributed to variations in surface roughness and geometric surface area. To verify that the first-semi circle in the Nyquist plot is due to the charge transfer resistance at the Pd/electrolyte interface, the results of a 10 nm thick Pd layer deposited on a quartz substrate (see paragraph 3.2.2) are included in Fig. 4.20. It indeed confirms that the first semi-circle can be fully attributed to the Pd layer and shows that the charge transfer kinetics are coupled to the electrocatalytic properties of Pd. Furthermore, the dependence of i_0 is in accordance with theory.[52]

The circuit parameter to be discussed next is the transfer resistance across the Pd/Mg_yTi_{1-y} interface denoted as R_{tr}. The results as a function of E^{eq} are depicted in Fig. 4.21. Note that the potential window is smaller compared to Fig. 4.20, because R_{tr} does not appear throughout the entire isothermal, *i.e.* a second semi-circle is not observed at all hydrogen contents (see Fig. 4.17).

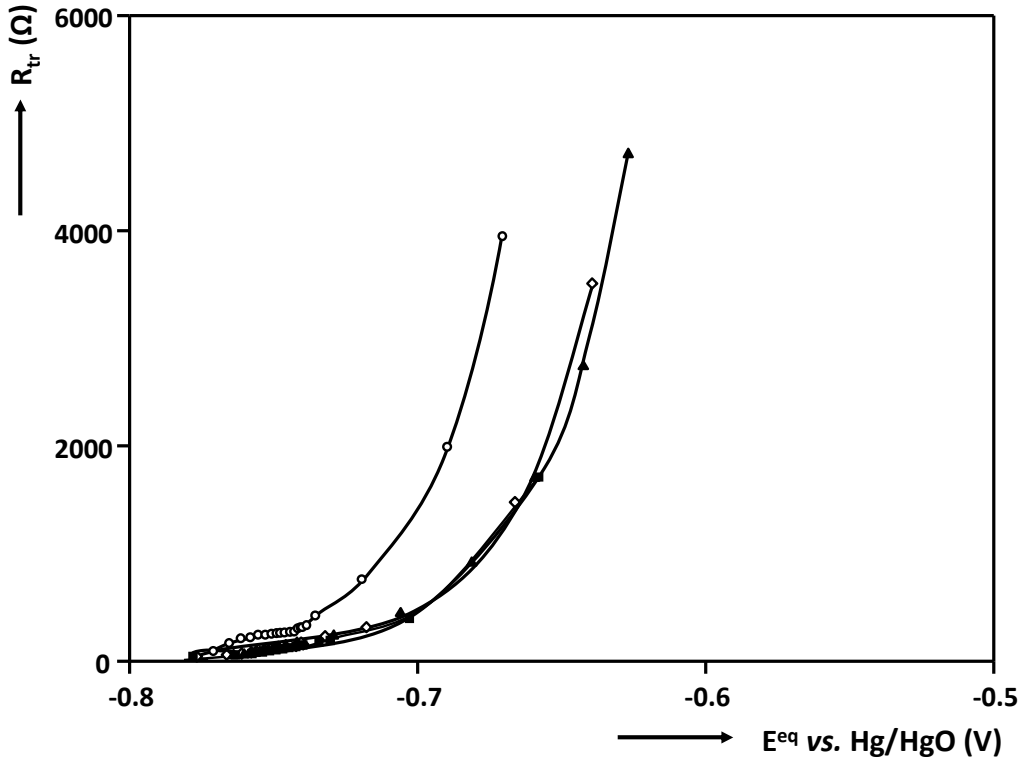

Fig. 4.21 R_{tr} for 200 nm thick Mg_yTi_{1-y} alloys with y = 0.70 (■), 0.75 (◇), 0.80 (▲) and 0.85 (○).

The fact that all alloy compositions presented here are easily (de)hydrogenated as compared to MgTi alloys with a higher Mg-content is believed to be closely related to the crystal structure of the metal hydride (see chapter 5). Fig. 4.21 shows that the values of R_{tr} are approximately similar for $Mg_{0.70}Ti_{0.30}$, $Mg_{0.75}Ti_{0.25}$ and $Mg_{0.80}Ti_{0.20}$. $Mg_{0.85}Ti_{0.15}$, on the other hand, reveals deviating behavior. At all equilibrium potentials, the $Mg_{0.85}Ti_{0.15}$ alloy displays a significantly higher R_{tr} with respect to the compounds with a higher Ti-content and R_{tr} also increases rapidly at negative potentials. Therefore, it is not only the diffusion in the specific crystallographic phases and the electrocatalytic properties of Pd that are responsible for the poor hydrogen uptake and release kinetics found for alloys with a high Mg-content, but also the transfer of hydrogen across the Pd/M_yTi_{1-y} interface contributes substantially, especially in the hydrogen-depleted state.

4.2.3.4 Cycling stability of a thin film $Mg_{0.80}Ti_{0.20}$ alloy

During each successive hydrogen absorption-desorption cycle it was found that, although the overall discharge capacity remains nearly constant (see Fig. 4.7), the discharge capacity that

is obtained by high-rate discharging decreases substantially as a function of cycle number, To investigate the origin of the loss of rate-capability of a 200 nm thick $Mg_{0.80}Ti_{0.20}$ thin film electrode capped with 10 nm Pd as a function of cycle number, EIS experiments are performed during the second, fourth, sixth and eighth dehydrogenation step. The EQC, shown in Fig. 4.19B, is used to simulate the EIS data and to extract the values for the circuit elements. The charge transfer resistance and transfer resistance are discussed in detail below.

The charge transfer resistance, converted to the exchange current density using Eq. 3.12, is shown in Fig. 4.22 as a function of equilibrium potential and cycle number. It shows that, in line with the results shown in Fig. 4.20, again the same shape is found as for pure Pd films and therefore the electrocatalytic properties are fully attributed to the Pd top-coat. The small increase of i_0 going from the second to the fourth and sixth cycle are probably caused by an activation process that enhances the electrocatalytic properties of Pd. Hereafter, the exchange current density decreases, which might be an indication of intermixing of Pd and the $Mg_{0.80}Ti_{0.20}$ layer that effectively decreases the amount of Pd available for the charge transfer reaction.[53,54]

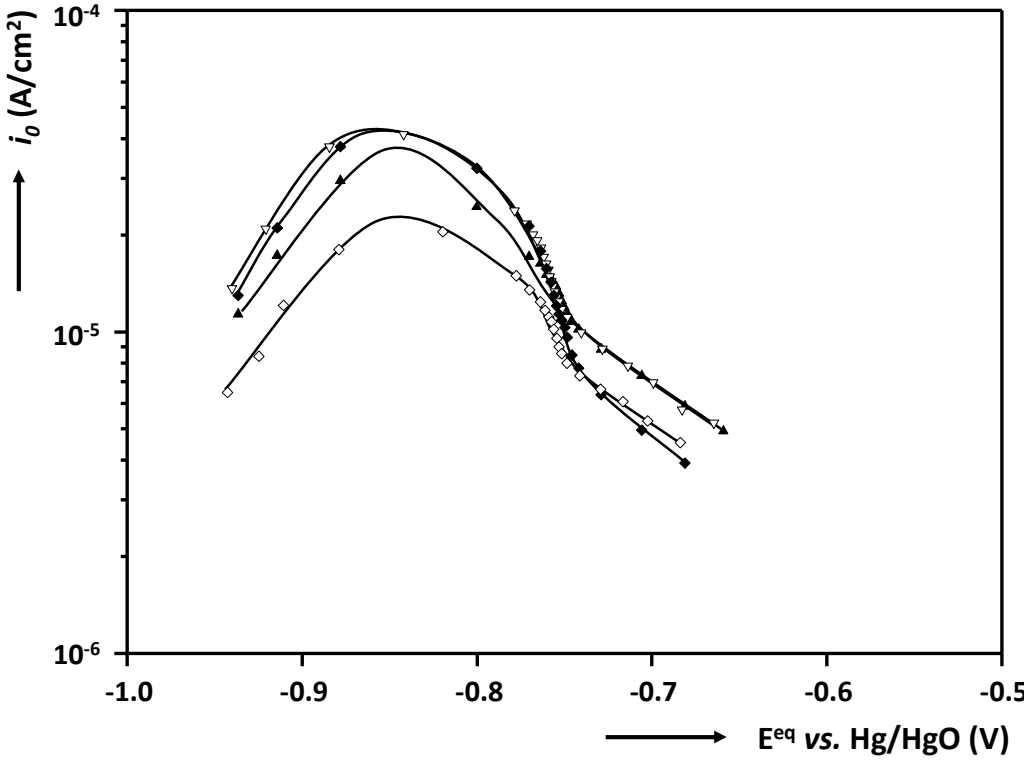

Fig. 4.22: i_0 as a function of E^{eq} measured during the 2nd (▲), 4th (▽), 6th (◆) and 8th (◇) dehydrogenation step.

The resistance related to hydrogen that crosses the $Pd/Mg_{0.80}Ti_{0.20}$ interface (R_{tr}) is monitored during the second, fourth, sixth and eighth dehydrogenation sequence. The results are depicted in Fig. 4.23. From this it is clear that R_{tr} increases after each successive (de)hydrogenation step. Although the electrocatalytic properties of Pd deteriorate somewhat after several cycles (see Fig. 4.22) the transfer resistance across the $Mg_{0.80}Ti_{0.20}$ interface increases much more and will therefore contribute to a larger extent to the decreasing cycling stability as a function of cycle number.

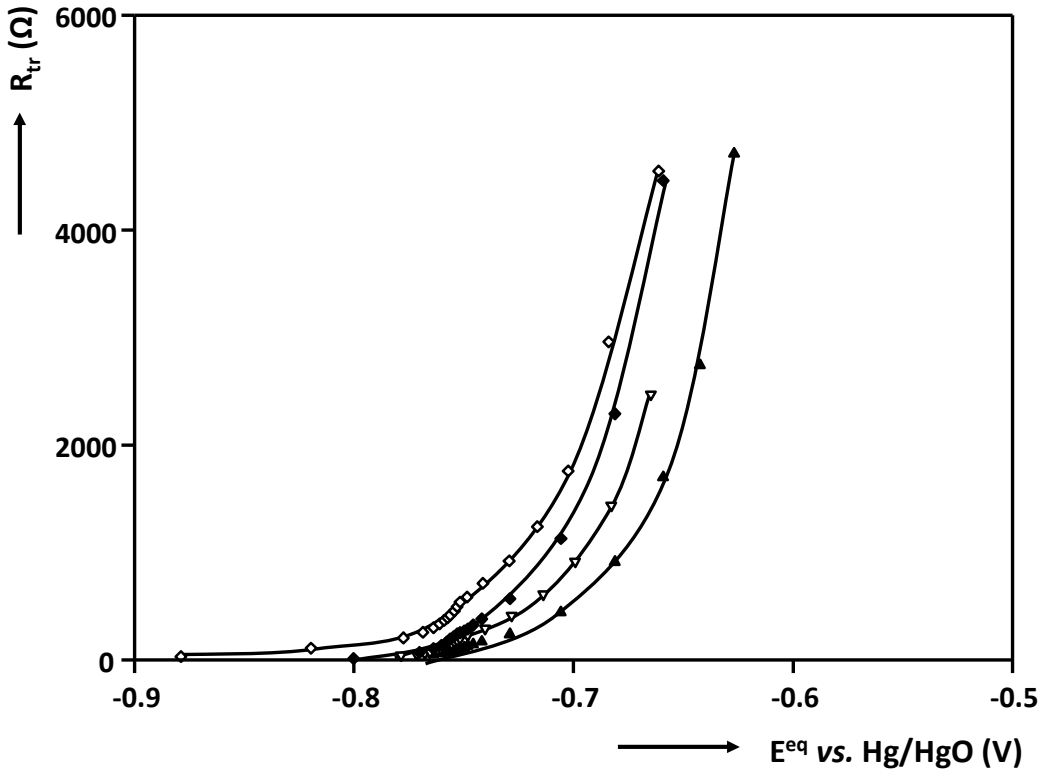

Fig. 4.23 R_{tr} as a function of E^{eq} measured during the 2nd (▲), 4th (▽), 6th (◆) and 8th (◇) dehydrogenation step.

4.2.4 Effects of the deposition technique

The recent developments regarding the promising hydrogen storage properties of thin film Mg_yTi_{1-y} alloys have triggered research that mainly focuses on the optical properties. In line with many Mg-based thin film systems, the Mg-Ti system shows remarkable optical properties.[34,44,55-59] Because these Mg_yTi_{1-y} alloys were prepared by co-sputtering instead of electron-beam evaporation it is interesting to determine if and how the deposition technique influences the characteristics of the alloy. This is especially important as the thin film systems investigated in chapter 5 are prepared by sputtering.

4.2.4.1 Structural investigation

The crystallographic orientation of the thin films prepared by magnetron co-sputtering and electron-beam deposited (EBD) is resolved by means of X-ray diffraction (see paragraph 2.3). The XRD spectrum of a sputtered $Mg_{0.80}Ti_{0.20}$ thin film is depicted in Fig. 4.24. A very intense peak is observed at 2θ=35.4° and is associated with a hexagonal closed packed (hcp) Mg-Ti unit cell. The (002) reflection is shifted with respect to the positions of both pure Mg (34.4 °2θ) and Ti (38.4 °2θ) and is due to a solid solution of Ti in Mg. The shift of the position of the 002 peak to larger angles (smaller interatomic distances) with respect to pure Mg is a direct consequence of the smaller molar volume of Ti as compared to Mg.[19] In

contrast to these findings, Richardson *et al.* and Farangis *et al.* concluded that Mg-Ti thin films, within a similar composition range and also prepared by magnetron co-sputtering, were amorphous.[20,21] Apparently, the deposition conditions (temperature, deposition rate, *etc.*) influence the crystallography of the films significantly. As a comparison, the XRD spectrum of a $Mg_{0.80}Ti_{0.20}$ alloy prepared by EBD is depicted in the inset in Fig. 4.24 (see section 4.2.1). It is apparent that the relative intensity of the peaks is different for the two deposition methods. The 002 refection is very intense for the co-sputtered compounds, whereas the EBD thin films show a much weaker reflection. This will be discussed in more detail below.

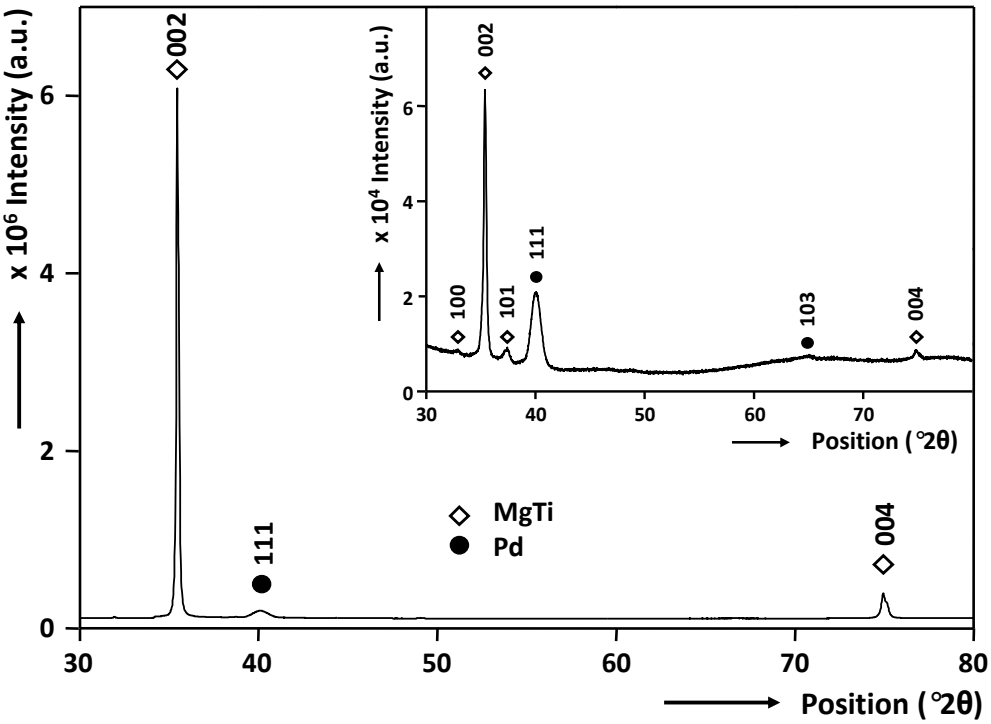

Fig. 4.24 XRD spectrum of an as-deposited $Mg_{0.80}Ti_{0.20}$ thin film with a thickness of 200 nm and a 10 nm thick Pd topcoat prepared by means of DC/RF magnetron co-sputtering. The inset shows the XRD spectrum of a similar composition prepared by means of electron beam deposition. Note the difference of the vertical intensity scales.

The 002 peaks for EBD and magnetron co-sputtered Mg_yTi_{1-y} alloys are shown in Fig. 4.25 . It should be noted that the peaks of the EBD $Mg_{0.50}Ti_{0.50}$ and $Mg_{0.70}Ti_{0.30}$ alloys are not included in this figure as their intensities were extremely low. Due to the intensity difference of the 002 reflections for both deposition techniques, the scale of the y-axis is adjusted in order to depict the peaks appropriately. The most notable observation is that the peak positions seem to be almost independent of the deposition method used, which implies that the geometries of the unit cells of the alloys are very similar. However, the width of the peaks is clearly dependent on the deposition technique. Electron beam deposited Mg_yTi_{1-y} layers reveal relatively broad peaks in comparison to sputtered films, indicating a difference in grain size. The Scherrer equation (Eq. 2.45) is used to quantify this difference.

Before calculating the grain size it should be noted that the 002 peaks of the films have a double-peak structure, which is most pronounced for the sputtered films due to their

relatively narrow peaks. This structure is caused by the fact that Cu radiation used in the XRD measurements consists of two characteristic lines, *viz.* Cu Kα_1 (λ=1.5404 Å) and Cu Kα_2 (λ=1.5443 Å). Keeping in mind that the line-width at half maximum peak intensity ($B_{1/2}$) is related to one of the peaks, we obtain, on average, a crystallite diameter of 28 nm for EBD compounds and 52 nm for sputtered alloys. This difference must be due to the deposition technique and the associated deposition conditions.

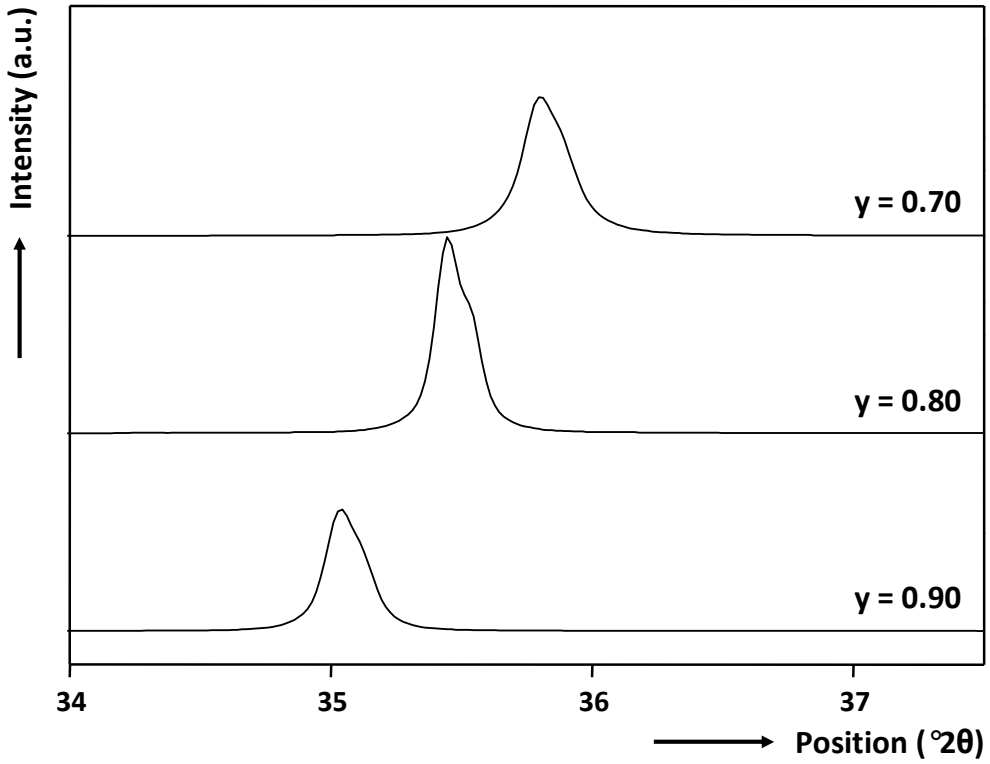

Fig. 4.25 Evolution of the (002) reflection as a function of Ti-content for magnetron co-sputtered 200 nm thick Mg_yTi_{1-y} alloys.

4.2.4.2 Electrochemical characterization

To determine the effects of the deposition technique on the hydrogen storage properties, electrochemical measurements are performed to (de)hydrogenate the metallic films. In general, two reactions are involved in (de)hydrogenation. Starting from the as-deposited state, H_2O is reduced at the metal (M) surface. Fig. 4.26 shows the cyclic voltammograms of the first two cycles of $Mg_{0.70}Ti_{0.30}$ films in the range -1.2 to 0 V using a scan rate of 0.5 mV/s. This particular range is chosen because previous galvanostatic measurements showed that within this range the (de)hydrogenation reactions of MgTi alloys take place. Starting from the as-deposited state of the e-beam deposited alloy at 0 V (Fig. 4.26, black curve), there is nearly no current flowing down to a potential of -0.7 V. Hereafter, the current decreases towards more negative values and reaches a local minimum at -0.88 V denoted by (a). This peak, which is also observed during galvanostatic measurements, has been attributed to the irreversible hydrogenation part of the compound. Decreasing the potential beyond -0.88 V

results in a small plateau, however, it quickly declines again down to -11 A/g at -1.04 V (peak (b)). The corresponding reaction is further hydrogenation of the $Mg_{0.70}Ti_{0.30}$ alloy and a phase transition is most likely involved. After the maximum H storage capacity is reached, the current increases, only to decrease rapidly at more negative potentials due to the formation of hydrogen gas according to reaction (2.14).

During scanning towards less negative potentials, the first peak (c) observed is related to a broad β-solid solution, commonly found for Mg_yTi_{1-y} alloys. Also, a small peak is observed and can be related to the dehydrogenation of the Pd topcoat. Hereafter, the $Mg_{0.70}Ti_{0.30}H_x$ transforms from β to the α-phase which manifests itself at -0.51 V (peak d)). During the second hydrogenation (grey curve), the first cathodic peak (e) corresponds to hydrogenating the MgTi alloy. Note that in line with the comments made above, the second hydrogenation does not show any features that resemble peak (a) in the first hydrogenation, illustrating its irreversible nature. The irreversibility of the hydrogenation leads to a lower hydrogenation capacity during the second hydrogen insertion. Moreover, it is evident that the overpotential necessary for the second hydrogenation reaction to proceed steadily is significantly decreased in comparison to the first cycle. Contrastingly, the peak positions and peak areas during the first and second dehydrogenation are not significantly changed illustrating that the rate-capability as well as the reversible H storage capacity are approximately constant. Fig. 4.26B shows that very similar voltammograms are observed for the magnetron co-sputtered $Mg_{0.70}Ti_{0.30}$ thin film, stressing that the electrochemistry of both layers is approximately analogous.

The effect of the Ti-content in Mg_yTi_{1-y} alloys on the reversible hydrogen content is determined by firstly hydrogenating the metallic layers with a current of -0.6 mA. Hereafter, a high-rate current (+0.12 mA) and additionally a low-rate current (+0.012 mA) are used to extract the hydrogen atoms. The corresponding reversible H discharge capacities are shown for electron-beam deposited and sputtered films in Fig. 4.27. For both preparation methods, the $Mg_{0.80}Ti_{0.20}$ composition exhibits the highest rate-capability and excellent reversible hydrogen storage capacity of approximately 6 wt.% of H. This is especially desirable for high-drain applications where the need of a high current is vital for the device to work properly. The two other composition ($Mg_{0.70}Ti_{0.30}$ and $Mg_{0.90}Ti_{0.10}$) show similar properties as the electron-beam evaporated films. As was already mentioned in paragraph 4.2.2, the graph in Fig. 4.27 shows two particular regions, *i.e.* up to 20 at.% Ti the rate-capability is poor, whereas beyond 20 at.% Ti fast hydrogen uptake and release can be attained. Most probably the crystal structure of the hydride is responsible for this behavior and this is presented in detail in chapter 5.

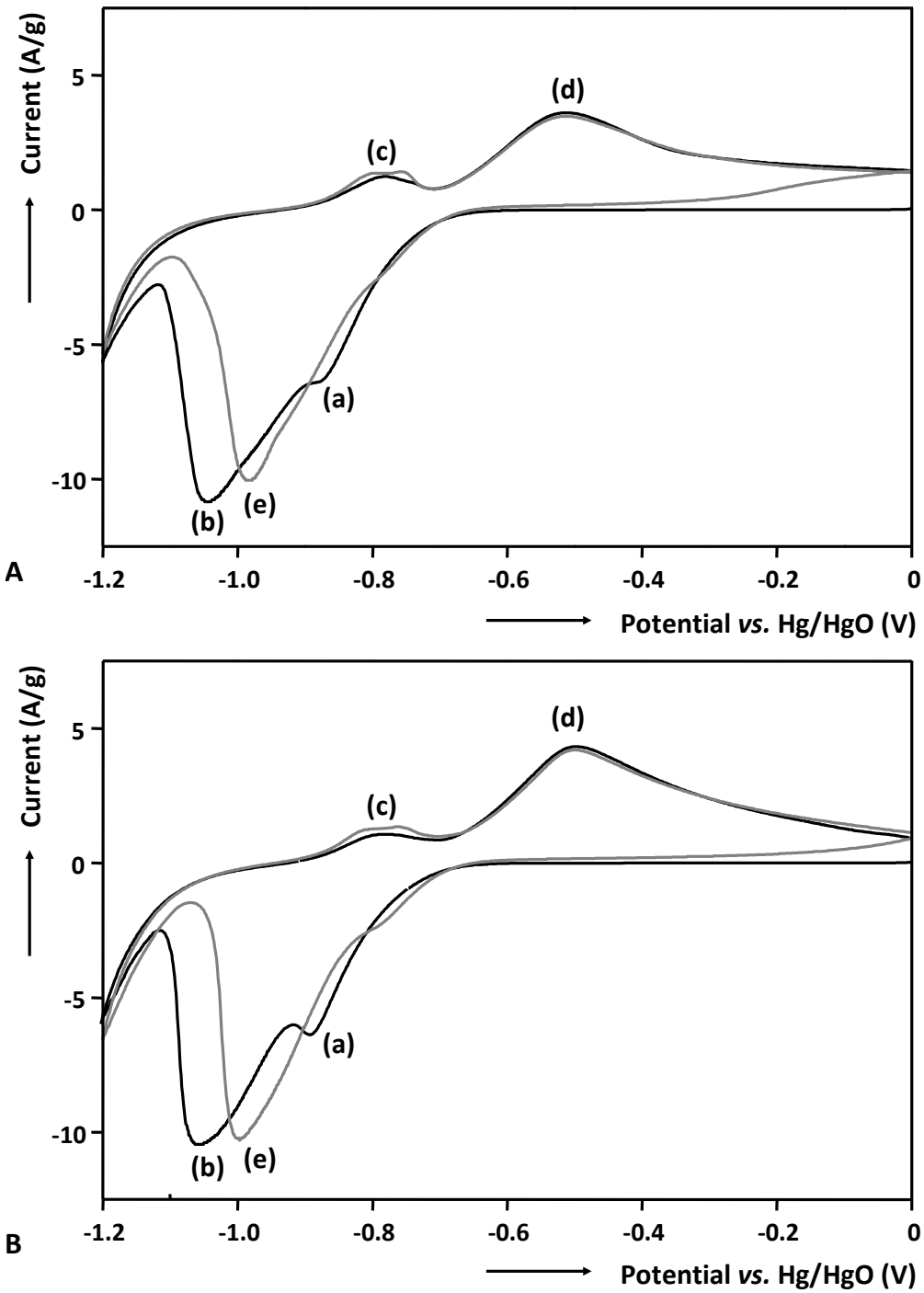

Fig. 4.26 Cyclic voltammograms of (A) electron-beam deposited and (B) magnetron co-sputtered $Mg_{0.70}Ti_{0.30}$ films within the potential range of 0 to -1.2 V using a scan rate of 0.5 mV/s. The specific features of the curves are denoted (a) to (e).

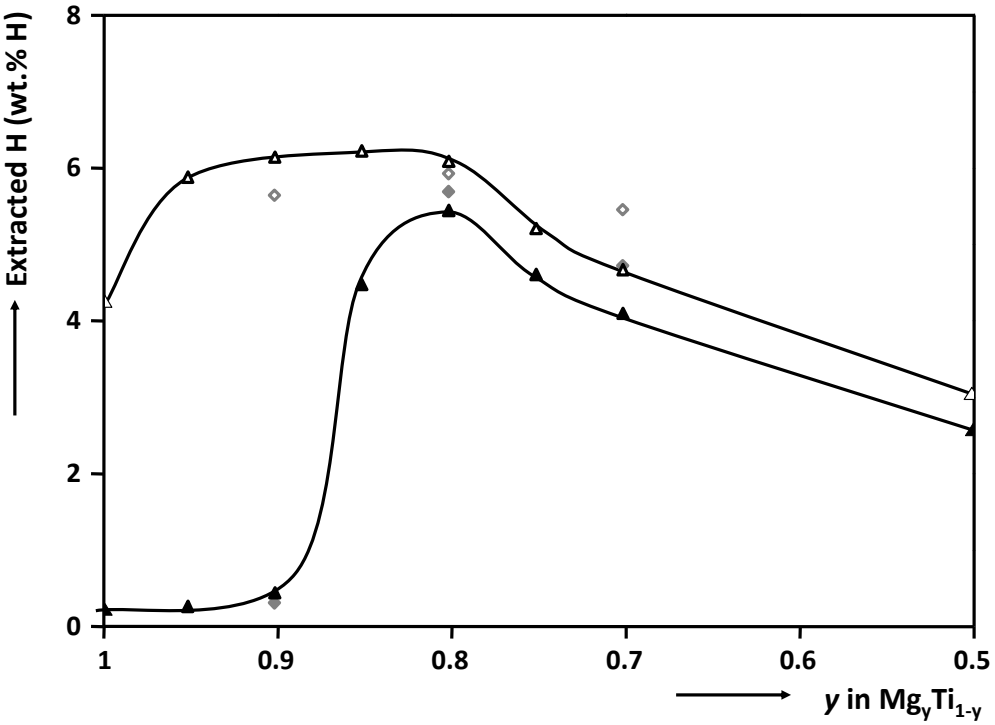

Fig. 4.27 Discharge capacity versus the Mg-content in Mg_yTi_{1-y} alloys. A distinction is made between the discharge capacity obtained using high-rate discharging (+0.12 mA; closed symbols) and low-rate discharging (+0.012 mA; open symbols). The data corresponding to electron beam deposited thin films are represented by triangles, whereas magnetron co-sputtered compounds are indicated by diamonds.

Finally, besides a high gravimetric energy density, a good cycle-life performance is one of the main requirements for future applications. The electrochemical cycle-life behavior is measured by applying a high-rate and, subsequently, a low-rate discharge current of 0.12 mA (~1000 mA/g) and 0.012 mA (~100 mA/g), respectively. The results of cycling a sputtered $Mg_{0.80}Ti_{0.20}$ thin film electrode alloy several times in depicted in Fig. 4.28. For the sputtered compounds (curve (b)), the reversible capacity is approximately constant up to 15 cycles Up to 15 cycles the sputtered film reveals a nearly constant reversible hydrogen storage capacity which, hereafter, slowly decreases. Beyond 15 cycles, delamination causes the reversible hydrogen storage capacity to deteriorate. The somewhat better cycle-life of the sputtered films compared to that of the e-beam deposited alloys (see Fig. 4.7) is related to their stronger adhesion to the substrate. Aside from this observation, gas phase (de)hydrogenation has shown that the cycle-life of sputtered Mg-Ti alloys easily surpasses 100 cycles, indeed revealing the excellent intrinsic recycle-ability of the MgTi hydrogen storage compounds.[34]

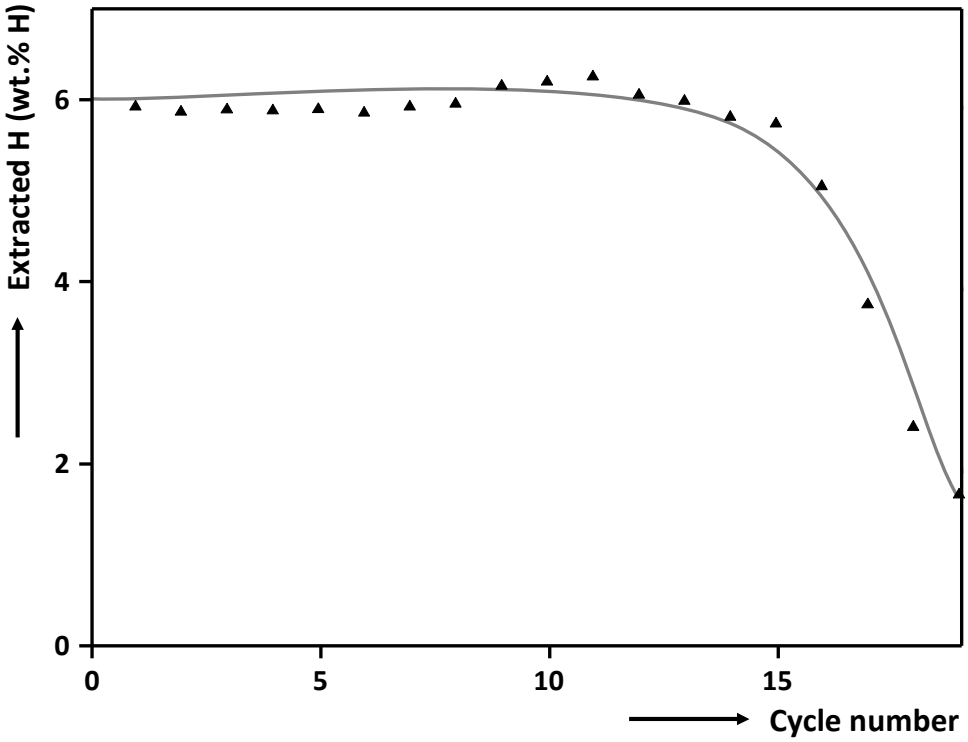

Fig. 4.28 Discharge capacity determined by high-rate (I=+0.12 mA) and additionally low-rate (I=+0.012 mA) dehydrogenation *vs.* cycle number for a sputtered Pd-coated 200 nm thick $Mg_{0.80}Ti_{0.20}$ electrode.

4.3 Conclusions

Thin films consisting of Mg and Ti with y ranging from 0.50 to 1.00 were prepared by means of electron-beam evaporation and sputtering. XRD analysis showed that incorporating Ti in the Mg lattice gradually shifts the peak assigned to the MgTi alloy in the XRD spectrum, indicating that crystalline single-phase alloys were obtained.

Galvanostatic (de)hydrogenation showed that the compositional dependence of the reversible hydrogen storage capacity consists of two parts. The first part applies to Mg-rich alloys ($0.85 \leq y \leq 1.00$) that reveal an extremely low discharge capacity upon high-rate discharging indicating a low-rate capability, whereas at lower Mg-contents the reversible hydrogen storage capacity increases substantially. An excellent rate-capability, along with a superior hydrogen storage capacity, was found for the $Mg_{0.80}Ti_{0.20}$ composition. Increasing the Ti-content beyond 20 at.% induces the storage capacity to decrease linearly with composition, which was attributed to the increasing weight of the alloys. The analogous electrochemical behavior of Mg_ySc_{1-y} and Mg_yTi_{1-y} alloys suggests that upon hydrogenation of Mg_yTi_{1-y} alloys with a Ti-content of 20 at.% and beyond a fcc-structured hydride is formed, which greatly facilitates rapid hydrogen uptake and release. Whereas the hydride of Mg_yTi_{1-y} alloys rich in Mg crystallizes into the common body-centered tetragonal MgH_2 structure, which is familiar for its poor hydrogen transport properties. The effect of the hydrogen content on the structure of the host is investigated in detail in Chapter 5.

Compared to the Mg_yTi_{1-y} alloys, the electrochemical response of pure Mg thin films shows quite deviating behavior. Experimentally only about 55% of the Mg thin films could be hydrogenated, which suggests the formation of a hydrogen diffusion blocking MgH_2 layer. Deep-discharging the Mg hydride shows a distinct evolution of the overpotential, which might be linked to a nucleation and growth process.

The cycling stability of a $Mg_{0.80}Ti_{0.20}$ thin film electrode is constant up to 11 cycles, hereafter it slowly deteriorates due to delamination of the film from the substrate. Therefore, the intrinsic cycling stability is, in line with other reports, expected to be higher.

The thermodynamic properties of $Mg \rightarrow MgH_2$ and *vice versa* are determined by means of GITT. The results are in close agreement with previous reported data, however, here the results are obtained at much lower temperatures. Electrochemical dehydrogenation revealed that for a multiple-step discharge a large driving force is required in each successive step. Probably this phenomenon is related to a nucleation and growth mechanism, which has to be overcome in the early stages of each step as the former nucleation and growth of a Mg metal phase has vanished completely. This observation is in line with reports that show that hydrogen tends to reside in interstitial on the Mg-side closest to the Pd/Mg interface.

The recently proposed thermodynamic Lattice Gas Model is applied to simulate the electrochemically measured hydrogen desorption isotherm of a Mg thin film electrode. Excellent agreement between experimental and simulation results is obtained. The values of the calculated energy parameters of the LGM have been compared with previously simulated Mg_ySc_{1-y} alloys. It is shown that the repulsive interactions in the separate phases and also between the phases is the largest for pure Mg, which is probably caused by a larger negative charge of the hydrogen atoms. Also the phase transformation of Mg to MgH_2 requires a larger energy than for the transition of Mg_ySc_{1-y} to $Mg_ySc_{1-y}H_x$. Conclusively, it has been shown that the model can successfully be applied to simulate the isotherm of Mg. The parameters yield detailed information about the magnesium-hydrogen system.

Electrochemical impedance spectroscopy measurements were performed on Mg_yTi_{1-y} alloys at different levels of hydrogen-content by combining it with GITT. The results reveal that the charge transfer kinetics can be fully attributed to the Pd topcoat. The transfer of hydrogen across the Pd/Mg_yTi_{1-y} interface has been identified to contribute a significant extent to the total impedance of the system. This resistance seems to be closely related to the alloy composition and therefore to the crystal structure of the hydride. It can therefore be concluded that not only the solid state H diffusion in lattices with different symmetries is responsible for poor hydrogen uptake and release rates, but also the transfer across the Pd/Mg_yTi_{1-y} interface contributes to the impeded hydrogen (de)hydrogenation kinetics.

The influence of the preparation method (sputtering and electron-beam deposition) on the metallurgy and electrochemical hydrogen storage properties of metastable Mg_yTi_{1-y} has been studied in detail. Only minor differences in the crystallography of the as-deposited films have been found. Although the unit cell dimensions are identical, for sputtered films the grain size is found to be larger and the preferred orientation is somewhat stronger.

The hydrogen storage properties of electron-beam deposited and co-sputtered alloys have been studied electrochemically. In spite of the fact that the overpotential is somewhat lower in the case of sputtered films, the overall response is found to be independent of the deposition technique. Moreover, a very similar compositional dependence on the

rate-capability is found, indicating to two specific regions that could be related to a fluorite-type structure for Mg_yTi_{1-y} with $y<0.85$. Above this critical composition, the diminishing rate-capability again indicates the formation of the rutile-type MgH_2 structure. Finally, an analogous cycle-life behavior is found for the two methods. The diminishing discharge capacity of the compounds after about 15 cycles is related to the delamination of the metallic films from the substrate.

4.4 References

1 F. Stampfer, C.E. Holley and J.F. Suttle, *The magnesium-hydrogen system*, J. Am. Chem. Soc. **1960**, *82*, 3504-3508.

2 K.H.J. Buschow, P.C.P. Bouten and A.R. Miedema, *Hydrides formed from intermetallic compounds of two transition metals: a special class of ternary alloys,* Rep. Prog. Phys. **1982**, *45*, 937-1039.

3 A. Krozer and B. Kasemo, *Unusual kinetics due to interface hydride formation in the hydriding of Pd/Mg sandwich layers*, J. Vac. Sci. Technol. A **1987**, 5, 1003-1005.

4 J. Rydén, B. Hjörvarsson, T. Ericsson, E. Karlsson, A. Krozer and B. Kasemo, *Unusual kinetics of hydride formation in Mg-Pd sandwiches, studied by hydrogen profiling and quartz crystal microbalance measurements*, J. Less-common Met. **1989**, *152*, 295-309.

5 V.P. Zhdanov, A. Krozer and B. Kasemo, *Kinetics of first-order phase transitions initiated by diffusion of particles from the surface into the bulk*, Phys. Rev. B **1993**, *47*, 11044-11048.

6 K.B. Gerasimov and A. Krozer and B. Kasemo, *Unusual kinetics due to interface hydride formation in the hydriding of Pd/Mg sandwich layers*, J. Vac. Sci. Technol. A **1987**, 5, 1003-1005.

7 K.B. Gerasimov and E.Y. Ivanov, *The mechanism and kinetics of formation and decomposition of magnesium hydride*, Mater. Lett. **1985**, *3*, 497-499.

8 C.M. Stander, *Kinetics of the formation of magnesium hydride from magnesium and hydrogen*, Z. Phys. Chem. Neue Folge **1977**, *104*, 229-238.

9 Z. Luz, J. Genossar and P.S. Rudman, *Identification of the diffusing atom in MgH_2*, J. Less-common Met. **1980**, *73*, 113-118.

10 J. Töpler, H. Buchner and H. Säufferer, *Measurements of the diffusion of hydrogen atoms in magnesium and Mg_2Ni by neutron scattering* J. Less-common Met. 1982, *88*, 397-404.

11 P. Spatz, H.A. Aebischer, A. Krozer and L. Schlapbach, *The diffusion of H in Mg and the nucleation and growth of MgH2 in thin films*, Z. Phys. Chem. **1993**, *181*, 393-397.

12 B. Vigeholm, K. Jensen, B. Larsen and A.S. Pedersen, *Elements of hydride formation mechanisms in nearly spherical magnesium powder particles*, J. Less-common Met. **1987**, *131*, 133-141.

13 M. Stioui, A. Grayevski, A. Resnik, D. Shaltiel and N. Kaplan, *Macroscopic kinetics of hydrogen in magnesium-rich compounds*, J. Less-common Met. **1986**, *123*, 9-24.

14 P. van der Sluis, M. Ouwerkerk and P.A. Duine, *Optical switches based on magnesium lanthanide alloy hydrides*, Appl. Phys. Lett. **1997**, *70***,** 3356-3358.

15 R.A.H. Niessen and P.H.L. Notten, *Electrochemical hydrogen storage characteristics of thin film MgX (X=Sc,Ti,V,Cr) compounds*, Electrochem. Solid-State Lett. **2005**, *8*, A534-A538.

16 H. Baker (Edt.), *ASM Handbook – Alloy Phase Diagrams*, vol. 3, ASM International, **1992**.
17 D. Kyoi, T. Sato, E. Rönnebro, N. Kitamura, A. Ueda, M. Ito, S. Katsuyama, S. Hara, D. Noreus and T. Sakai, *A new ternary magnesium–titanium hydride Mg_7TiH_x with hydrogen desorption properties better than both binary magnesium and titanium hydrides*, J. Alloys Compd. **2004**, *372*, 213-217.
18 P. Villars (Edt), *Pearson's Handbook Desk Edition*, Vol. 2, 2336, ASM International, **1997**.
19 A.R. West, *Solid state Chemistry and its applications*, 1st ed., 367, John Wiley & Sons, New York **1984**.
20 T.J. Richardson, B. Farangis, J.L. Slack, P. Nachimuthu, R. Perera, N. Tamura and M. Rubin, *X-Ray absorption spectroscopy of transition metal-magnesium hydride thin films*, J. Alloys Compd. **2003**, *356-357*, 204-207.
21 B. Farangis, P. Nachimuthu, T.J. Richardson, J.L. Slack, B.K. Meyer, R.C.C. Perera and M.D. Rubin, *Structural and electronic properties of magnesium-3D transition metal switchable mirrors*, Solid State Ionics **2003**, *165*, 309-314.
22 L. Vegard, *The constitution of mixed crystals and the space occupied by atoms*, Z. Physik **1921**, *5*, 17-26.
23 E. Zen, *Validity of "Vegard's law"*, Am. Mineral. **1956**, *41*, 523-524
24 C.N. Singman, *Atomic volume and allotropy of the elements*, J. Chem. Ed. **1984**, *61*, 137-142.
25 O. Friedrichs, L. Kolodziejczyk, J.C. Sánchez-López, A. Fernández, L. Lyubenova, D. Zander, U. Köster, K.F. Aguey-Zinsou, T. Klassen and R. Bormann, *Influence of particle size on electrochemical and gas-phase hydrogen storage in nanocrystalline Mg*, J. Alloys Compd. **2008**, *463*, 539-545.
26 J. Paillier and L. Roue, *Hydrogen electrosorption and structural properties of nanostructured Pd-Mg thin films elaborated by pulsed laser deposition*, J. Alloys Compd. **2005**, *404-406*, 473-476.
27 A. Léon, E.J. Knystautas, J. Huot and R. Schulz, *Magnesium films for hydrogen storage*, Mater. Sci. Forum **2001**, *377*, 85-94.
28 A. Léon, E.J. Knystautas, J. Huot and R. Schulz, *Influence of the evaporation rate and evaporation mode on the hydrogen sorption kinetics of air-exposed magnesium films*, Thin Solid films **2006**, *496*, 683-687.
29 A. Milchev and M.I. Montenegro, *A galvanostatic study of electrochemical nucleation*, J. Electroanal. Chem. **1992**, *333*, 93-102.
30 P.H.L. Notten, M. Ouwerkerk, H. van Hal, D. Beelen, W. Keur, J. Zhou, and H. Feil, *High energy density strategies: from hydride-forming materials research to battery integration*, J. Power Sources **2004**, *29*, 45-54.
31 R.A.H. Niessen and P.H.L. Notten, *Hydrogen storage in thin film magnesium–scandium alloys***,** J. Alloys Compd. **2005**, *404-406*, 457-460.
32 W.P. Kalisvaart, R.A.H. Niessen and P.H.L. Notten, *Electrochemical hydrogen storage in MgSc alloys: A comparative study between thin films and bulk materials*, J. Alloys Compd. **2006**, *417*, 280-291.
33 W.P. Kalisvaart, P. Vermeulen, A.V. Lyedovskikh, D. Danilov and P.H.L. Notten, *The electrochemistry and modelling of hydrogen storage materials*, J. Alloys Compd. **2007**, *446-447*, 648–654.

34 M. Slaman, B. Dam, M. Pasturel, D.M. Borsa, H. Schreuders, J.H. Rector and R. Griessen, *Fiber optic hydrogen detectors containing Mg-based metal hydrides*, Sens. Actuators B **2006**, *123,* 538-545.

35 B. Vigeholm, J. Kjøller, B. Larsen and A.S. Pedersen, *Formation and decomposition of magnesium hydride*, J. Less-common Met. **1983**, *89*, 135-144.

36 A. Krozer and B. Kasemo, *Hydrogen uptake by Pd-coated Mg: absorption-decomposition isotherms and uptake kinetics*, J. Less-common Met. **1990**, *160*, 323-342.

37 T.B. Flanagan and J.D. Clewley, *Hysteresis in metal hydrides*, J. Less-common Met. **1982**, *83*, 127-141.

38 A.T.M. van Gogh, D.G. Nagengast, E.S. Kooij, N.J. Koeman and R. Griessen, *Quenching of giant hysteresis effects in $La_{1-z}Y_zH_x$ switchable mirrors*, Phys. Rev. Lett. **2000**, *85*, 2156-2159.

39 R. Kelekar, H. Giffard, S.T. Kelly and B.M. Clemens, *Formation and dissociation of MgH_2 in epitaxial Mg thin films*, J. Appl. Phys. **2007**, *101*, 114311/1-7.

40 A. Ledovskikh, D. Danilov, W.J.J. Rey and P.H.L. Notten, *Modeling of hydrogen storage in hydride-forming materials: Statistical thermodynamics*, Phys. Rev. B **2006**, *73*, 014106/1-12.

41 P. Vermeulen, A. Ledovskikh, D. Danilov and P.H.L. Notten, *The impact of the layer thickness on the thermodynamic properties of Pd hydride thin film electrodes*, J. Phys. Chem. B **2006**, *110*, 20350-20353.

42 W.P. Kalisvaart, P. Vermeulen, A. Ledovskikh, D. Danilov and P.H.L. Notten, *The electrochemistry and modeling of hydrogen storage materials*, J. Alloys Compd. **2007**, *446-447*, 648-654.

43 D.R. Lide (Edt.), *CRC Handbook of Chemistry and Physics 88th Edition,* p. 9-81, CRC Press, Boca Raton, FL **2008**.

44 D.M. Borsa, R. Gremaud, A. Baldi, H. Schreuders, J.H. Rector, B. Kooi, P. Vermeulen, P.H.L. Noten, B. Dam and R. Griessen, *Structural, optical, and electrical properties of $Mg_yTi_{1-y}H_x$ thin films*, Phys. Rev. B **2007**, *75*, 205408/1-9.

45 R. Gremaud, A. Baldi, M. Gonzalez-Silveira, B. Dam and R. Griessen, *Chemical short-range order and lattice deformations in $Mg_yTi_{1-y}H_x$ thin films probed by Hydrogenography*, Phys. Rev B **2008**, *77*, 144204/1-10.

46 A. Baldi, R. Gremaud, D.M. Borsa, C.P. Baldé, A.M.J. van der Eerden, G.L. Kruijtzer, P.E. de Jongh, B. Dam and R. Griessen, *EXAFS study of short-range ordering in $Mg_yTi_{1-y}H_x$ thin films*, Phys. Rev. B **2008**, submitted.

47 J.R. MacDonald, *Impedance spectroscopy*, John Wiley & Sons, New York, **1987**, p. 75.

48 C. Montella, *EIS study of hydrogen insertion under restricted diffusion conditions: I. Two-step insertion reaction*, J. Electroanal. Chem. **2001**, *497*, 3-17.

49 C. Gabrielli, P.P. Grand, A. Lasia and H. Perrot, *Investigation of hydrogen adsorption-absorption into palladium thin films, I. Theory*, J. Electrochem. Soc. **2004**, *151*, A1925-A1936.

50 T.H. Yang and S.I. Pyun, *An investigation of the hydrogen absorption reaction into, and the hydrogen evolution reaction from, a Pd foil electrode*, J. Electroanal. Chem. **1996**, *414*, 127-133.

51 C. Gabrielli, P.P. Grand, A. Lasia and H. Perrot, *Investigation of Hydrogen Adsorption and absorption in palladium thin films, III. Impedance spectroscopy*, J. Electrochem. Soc. **2004**, *151*, A1943-A1949.

52 P.H.L. Notten, M. Ouwerkerk, A. Ledovskikh, H. Senoh and C. Iwakura, *Hydride-forming electrode materials seen from a kinetic perspective*, J. Alloys Compd. **2003**, *356-357*, 759-763.

53 K. Yoshimura, Y. Yamada and M. Okada, *Hydrogenation of Pd capped Mg thin films at room temperature*, Surf. Sci. **2004**, *566-568*, 751-754.

54 J. Paillier and L. Roue, *Hydrogen electrosorption and structural properties of nanostructured Pd-Mg thin films elaborated by pulsed laser deposition*, J. Alloys Compd. **2005**, *404-406*, 473-476.

55 D.M. Borsa, A. Baldi, M. Pasturel, H. Schreuders, B. Dam, R. Griessen, P. Vermeulen and P.H.L. Notten, *Mg-Ti-H thin films for smart solar collectors*, Appl. Phys. Lett. **2006**, *88*, 241910/1-3.

56 S. Bao, K. Tajima, Y. Yamada, M. Okada and K. Yoshimura, *Color-neutral switchable mirrors based on magnesium-titanium thin films***,** Appl. Phys. A **2007**, *87*, 621-624.

57 S. Bao, K. Tajima, Y. Yamada, M. Okada and K. Yoshimura, *Magnesium-titanium alloy thin-film switchable mirrors*, Solar Energy Materials & Solar Cells **2008**, *92*, 224-227.

58 R. Gremaud, A. Baldi, M. Gonzalez-Silveira, B. Dam and R. Griessen, *Chemical short-range order and lattice deformations in $Mg_yTi_{1-y}H_x$ thin films probed by Hydrogenography***,** Phys. Rev B **2008**, *77*, 144204/1-10.

59 A. Baldi, D.M. Borsa, H. Schreuders, J.H. Rector, T. Atmakidis, M. Bakker, H.A. Zondag, W.G.J. van Helden, B. Dam and R. Griessen, *Mg–Ti–H thin films as switchable solar absorbers*, Int. J. Hydrogen Energy **2008**, *33*, 3188-3192.

5

In situ XRD study of thin film Mg_yTi_{1-y} alloys

Abstract

In situ gas phase X-ray diffraction was used to identify the crystal structures of as-deposited and hydrogenated Mg_yTi_{1-y} thin film alloys containing 70, 80 and 90 at.% Mg. The preferred crystallographic orientation of the films in both the as-prepared and hydrogenated state made it difficult to unambiguously identify the crystal structure up to now. In this work identification of the symmetry of the unit cells was achieved by *in situ* recording XRD patterns at various tilt angles. The results reveal a hexagonal closed packed structure for all alloys in the as-deposited state. Hydrogenating the layers under 1 bar H_2 transforms the unit cell into face centered cubic for the $Mg_{0.70}Ti_{0.30}$ and $Mg_{0.80}Ti_{0.20}$ compounds, whereas the unit cell of hydrogenated $Mg_{0.90}Ti_{0.10}$ has a body centered tetragonal symmetry. The (de)hydrogenation kinetics changes along with the crystal structure of the metal hydrides from rapid for fcc-structured hydrides to sluggish for hydrides with a bct symmetry and emphasizes the influence of the crystal structure on the hydrogen transport properties.

X-ray diffraction and electrochemical (de)hydrogenation were performed *in situ* to systematically monitor the effects of stepwise increasing and decreasing the hydrogen content on the structure of Mg_yTi_{1-y} thin film alloys with y=0.70, 0.80 and 0.90. The relationship between the electrochemical equilibrium potential and hydrogen partial pressure is utilized to obtain pressure-composition isotherms. The X-ray diffraction patterns and electrochemical results of $Mg_{0.70}Ti_{0.30}$ and $Mg_{0.80}Ti_{0.20}$ point towards a host lattice with distinct Ti-poor and Ti-rich regions, whereas $Mg_{0.90}Ti_{0.10}$ shows the properties of a randomly mixed alloy.[*]

[*] Part of this chapter is based on:
P. Vermeulen, P.C.J. Graat, H.J. Wondergem and P.H.L. Notten, *Crystal structures of Mg_yTi_{100-y} thin film alloys in the as-deposited and hydrogenated state*, Int. J. Hydrogen Energy **2008**, *33*, 5646-5650.
P. Vermeulen, H.J. Wondergem, P.C.J. Graat, D.M. Borsa, H. Schreuders, B. Dam, R. Griessen and P.H.L. Notten, *In situ electrochemical XRD study of (de)hydrogenation of Mg_yTi_{100-y} thin films*, J. Mater. Chem. **2008**, *18*, 3680-3687.

5.1 Introduction

In chapter 4 it was shown shat the Mg_yTi_{1-y} composition strongly affects the hydrogen desorption kinetics. Very similar behavior was found previously for Mg_ySc_{1-y} alloys and there it was argued that, depending on the Sc content, the MgSc hydride is either bct-structured or fcc-structured of which the latter structure shows superior hydrogen transport properties.[1-4] The favorable fcc structure of the MgSc hydride most likely originates from the fact that the fcc structure of ScH_2 is retained, even when Sc is largely substituted by Mg. As TiH_2 also forms a unit cell with fcc-symmetry, it is expected that the same crystallographic phases are responsible for the electrochemical behavior of Mg_yTi_{1-y} thin films. Together with our electrochemical data, this hypothesis was recently confirmed as experiments showed that the crystal structure of sputtered Mg_yTi_{1-y} thin films changes together with the ability to dehydrogenate the hydrides at an appreciable rate.[5] XRD measurements point to a fcc structure, which, combined with our electrochemical results (see Fig. 5.1), reveals fast hydrogen release for alloys containing 20 at.% Ti or more and a bct lattice for alloys containing 10 at.% Ti or less where fast hydrogen transport is strongly inhibited.

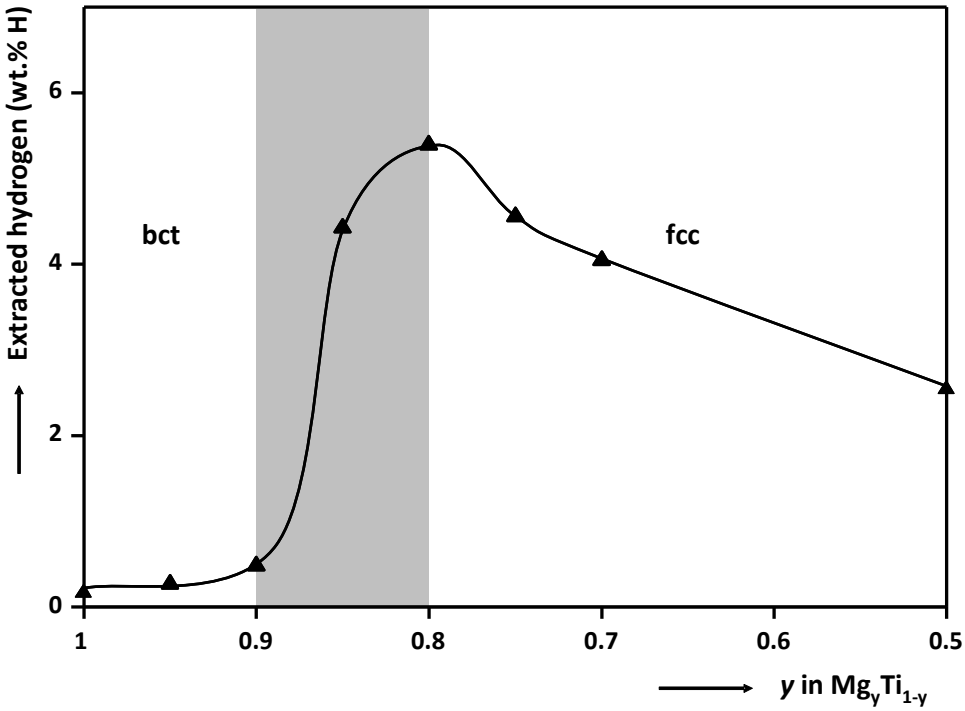

Fig. 5.1 Discharge capacities of fully hydrided $Mg_yTi_{1-y}H_x$ thin film electrodes using a current of +0.12 mA (~1000 mA/g). Indicated are the regions where the hydrides with body centered tetragonal ($y \geq 0.90$) and face centered cubic ($y \leq 0.80$) symmetry are expected to form. Between 80 and 90 at.% Mg the coexistence of both structures is presumed.

The results reported by Borsa *et al.* reveal, however, that the sputtered Mg_yTi_{1-y} thin films have a strong preferential crystallographic orientation and, consequently, not enough reflections appeared in the measured X-ray diffraction patterns that can be used to indisputably identify the symmetry of the crystal structures.[5] This problem was addressed by performing additional transmission electron microscopy (TEM) measurements of

hydrogenated Mg_yTi_{1-y} alloys. However, the results indicated that electron-beam bombardment influences the hydrogen content and also the ultra high vacuum (UHV) pressure required for TEM measurements is significantly lower than the hydrogen partial pressure required to extract hydrogen from the hydride. Therefore, the hydrogen concentration in the metal hydride was probably not constant and presumably lower than that for completely hydrogenated alloys. To overcome this problem and unambiguously identify the structure of the unit cells, in the present work XRD measurements were performed using a diffractometer equipped with a 4-circle goniometer and a closed, X-ray transparent container that could be filled with 1 bar H_2 gas (see paragraph 2.4.3). Fig. 5.1 shows that the most striking effects of hydrogen on the structure of the Mg_yTi_{1-y} host lattice are expected for y=0.70, 0.80 and 0.90 and therefore these compositions were subjected to an elaborate *in situ* gas phase XRD study of which the details can be found in paragraph 5.3.1.

The investigated Mg_yTi_{1-y} compounds, however, react with H_2 to their final hydrides as soon as they are exposed to H_2 pressures higher than 10^{-6} bar at ambient temperatures (see the isotherms in Fig. 4.16, note that these are desorption isotherms and therefore the plateau pressure for absorption could be somewhat higher, depending on the degree of hysteresis). This complicates the use of gas phase experiments as a tool to obtain detailed information about the influence of the hydrogen content on the metallic matrix. To circumvent this problem, electrochemical (de)hydrogenation at room temperature can successfully be applied to accurately monitor and tune the hydrogen content. In addition, the equilibrium potential can be related to the partial hydrogen pressure, enabling accurate construction of isotherms. To obtain detailed information about the crystal structure of Mg_yTi_{1-y} alloys as a function of hydrogen content, X-Ray Diffraction and electrochemical (de)hydrogenation were performed *in situ*. The results are discussed in paragraph 5.3.2. Again the thin film Mg_yTi_{1-y} alloys investigated contain 70, 80 and 90 at.% Mg.

5.3 Results & discussion

5.3.1 Structural characterization via *in situ* XRD gas loading

Fig. 5.2A shows the X-ray 2θ-θ scans of an as-prepared 200 nm thick $Mg_{0.70}Ti_{0.30}$ thin film alloy capped with 10 nm Pd measured at different tilt angles (ψ). The identification and position of the diffraction peaks are presented in Table 5.1. At ψ=0° the scan only shows two reflections, which in paragraphs 4.2.1 and 4.2.4.1 were ascribed to the {002} plane of a hexagonal closed packed (hcp) Mg-Ti lattice and the {111} plane of fcc-structured Pd, respectively. Additionally, two small reflections on the left side of the 002 peak appear that are caused diffraction of Cu Kβ and W Lα emission. It should be noted that the diffraction patterns are plotted on a logarithmic scale, which emphasizes the intensities of these reflections. The small peak on the left of the {111} plane of Pd at approximately 38.76 °2θ cannot readily be identified. Yet, the fact that this peak is not observed for as-prepared $Mg_{0.90}Ti_{0.10}$ where the Pd reflection is completely absent at ψ=0° (see Fig. 5.4A) suggests that these peaks can most likely be attributed to the Pd topcoat. It is therefore expected that the small peak on the left side of the Pd reflection originates from diffraction of other wavelengths than Cu Kα. Tilting the thin film in successive steps of 6° reveals the (101) and

(100) peaks of the hexagonal Mg-Ti lattice and the (200) peak of the cubic Pd lattice. The 2θ positions of the Mg-Ti peaks correspond to a hcp unit cell with lattice constants a=3.11 Å and c=5.02 Å. The 2θ positions of the Pd peaks correspond to a fcc unit cell with lattice constant a=3.90 Å (see Table 5.1).

Table 5.1 Peak identification and positions obtained from the XRD scans of the as-prepared and hydrogenated $Mg_{0.70}Ti_{0.30}$ sample depicted in Fig. 5.2. For accuracy the 2θ positions of the hydrogenated sample were determined from additional ψ scans.

As-prepared $Mg_{0.70}Ti_{0.30}$

hcp symmetry with a=3.11 Å and c=5.02 Å, V=42.04 Å^3
Pd topcoat: fcc with a=3.90 Å

identification	ψ position (°)	2θ position (°)	lattice spacing (Å)
Mg-Ti (002)	0.0	35.67	2.51
Mg-Ti (101)	60.0	37.76	2.38
Mg-Ti (100)	84.0	33.28	2.69
Pd (111)	0.0	40.11	2.25
Pd (200)	54.0	46.58	1.95
Pd (111)	72.0	40.10	2.25

Hydrogenated $Mg_{0.70}Ti_{0.30}$ (1 bar H_2)

fcc symmetry with a=4.66 Å and α=89° (V=101.18 Å^3)
Pd topcoat: fcc with a=4.03 Å

identification	ψ position (°)	2θ position (°)	lattice spacing (Å)
Mg-Ti-H (111)	0.1	32.67	2.74
Mg-Ti-H (200)	55.8	38.71	2.32
Mg-Ti-H (111)	70.8	33.59	2.67
Pd-H (111)	0.0	38.51	2.34
Pd-H (200)	55.7	44.96	2.01
Pd-H (111)	71.1	38.74	2.32

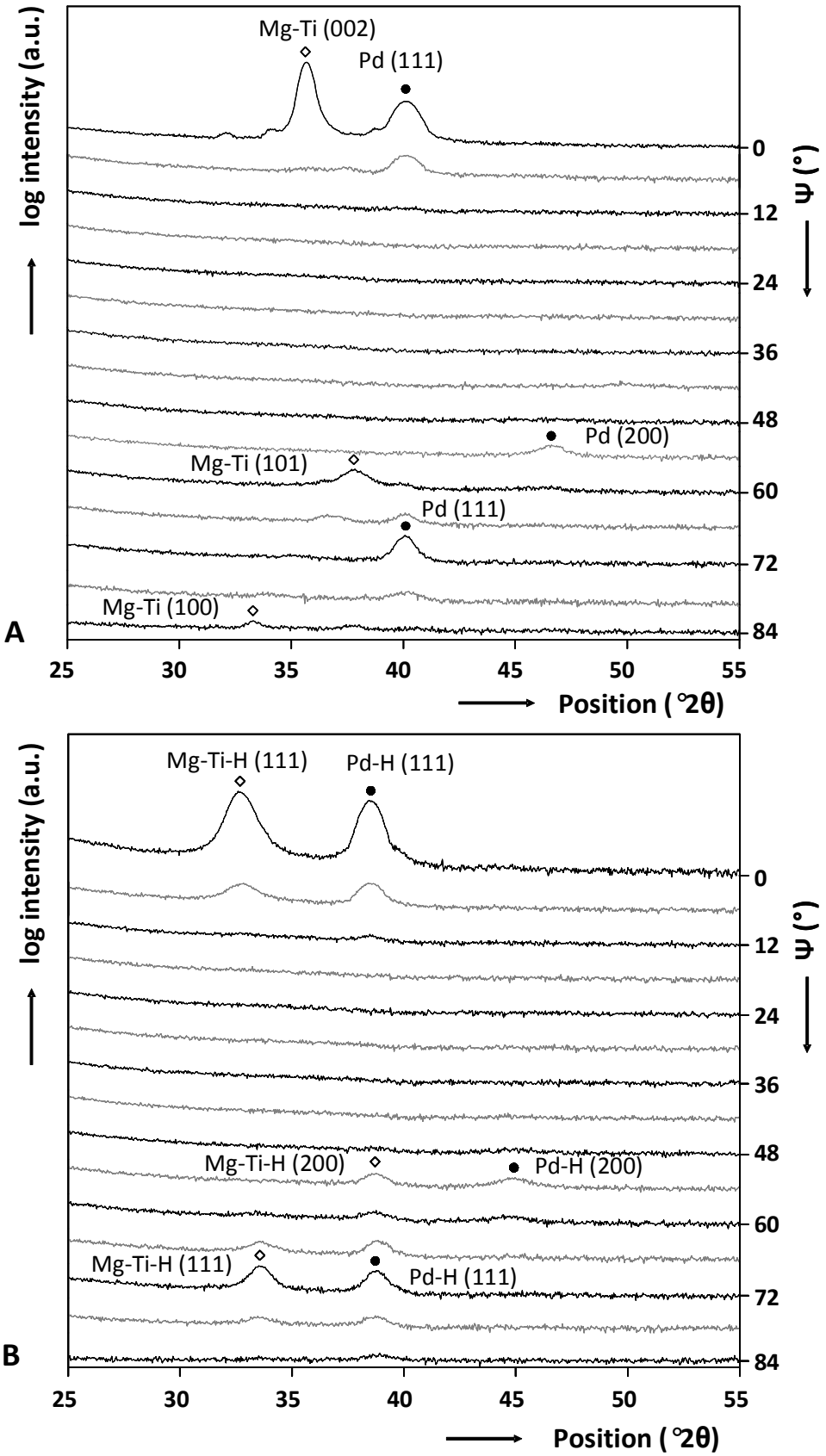

Fig. 5.2 XRD 2θ-θ scans at different tilt angels ψ of a 200 nm thick $Mg_{0.70}Ti_{0.30}$ layer capped with a 10 nm thick Pd topcoat in the as-prepared state (A)and after hydrogenation in 1 bar H_2 (B).

Fig. 5.2B shows the 2θ-θ scans obtained from the $Mg_{0.70}Ti_{0.30}$ layer after hydrogenation by filling the container with 1 bar H_2. The identification and position of the diffraction peaks are also listed in Table 5.1. The 2θ positions of the hydrogenated Mg-Ti phase correspond to a face centered cubic unit cell. However, the somewhat different 2θ position of the (111) peaks at ψ=0° and ψ=72° indicate that the material is either stressed or that the unit cell is rhombohedrally distorted, or both. As the 2θ difference is relatively large, nearly 1°, it is most likely that the unit cell is distorted. In that case the lattice constants are approximately a=4.66 Å and α=89°. The lattice parameter is larger than the value found from TEM measurements reported before (4.55 Å) and is probably due to a higher hydrogen content in the present study.[5] Also, here we take distortion of the unit cell into account otherwise the difference with the reported value would be even larger. Note that in Fig. 5.2B and Table 5.1 the hydrogenated $Mg_{0.70}Ti_{0.30}$ and Pd phases are denoted as Mg-Ti-H and Pd-H, respectively. The reason that the exact hydrogen content is not quantified is that for hydrogenated thin film alloys it is difficult to determine the hydrogen content accurately. In a recent report on hydrogenating Mg-Ti thin films the hydrogen to metal (H/M) ratio was determined from a comparison of the experimental lattice constants to those calculated by a linear combination of the lattice constants of cubic MgH_2 and TiH_2.[5] On average, it was found that H/M=2 for alloys containing less than 80 at.% Mg. However, here it is shown that the lattice of the hydrogenated $Mg_{0.70}Ti_{0.30}$ alloy is rhombohedrally distorted. Thus, determining the H/M ratio from the lattice constants assuming non-distorted unit cells will give unreliable results. Fortunately, it is known that electrochemical hydrogen insertion is an ideal tool to measure the hydrogen content and showed that the H/M ratio in the $Mg_{0.70}Ti_{0.30}$ layer is close to 1.5 (see Fig. 4.8) and that in the 10 nm thick Pd topcoat it is 0.7 H/M (see paragraph 3.2.1).[6]

Similarly, the $Mg_{0.80}Ti_{0.20}$ and $Mg_{0.90}Ti_{0.10}$ thin film alloys were investigated in the as-prepared state and after hydrogenation under 1 bar H_2. The results are depicted in Fig. 5.3 and Fig. 5.4, respectively. Fig. 5.3A shows the 2θ-θ scans of the 200 nm thick $Mg_{0.80}Ti_{0.20}$ layer in the as-deposited state. The material characteristics are presented in Table 5.2. The 2θ positions of the Mg-Ti phase correspond to a hcp unit cell with lattice constants a=3.16 Å and c=5.10 Å. In comparison to as-prepared $Mg_{0.70}Ti_{0.30}$ the values for the lattice parameters are higher because Mg has a significantly larger molar volume compared to Ti, which causes the lattice to expand.[7] The 2θ positions of the Pd phase again correspond to a fcc unit cell with lattice constant a=3.90 Å. As was observed in the diffraction patterns of $Mg_{0.70}Ti_{0.30}$, some small peaks appear on the left side of the 002 reflection of Mg-Ti that are related to the diffraction of Cu Kβ (most left) and W Lα. Note that the diffractograms are plotted on a logarithmic scale, which emphasizes the intensities of these small peaks.

Table 5.2 Peak identification and positions obtained from the XRD scans of the as-prepared and hydrogenated $Mg_{0.80}Ti_{0.20}$ sample depicted in Fig. 5.3. For accuracy, the 2θ positions of the hydrogenated sample were determined from additional ψ scans.

As-deposited $Mg_{0.80}Ti_{0.20}$

hcp symmetry with a=3.16 Å and c=5.10 Å (V=44.10 Å^3)
Pd topcoat: fcc with a=3.90 Å

Identification	ψ position (°)	2θ position (°)	lattice spacing (Å)
Mg-Ti (002)	0.0	35.23	2.55
Mg-Ti (102)	42.0	48.88	1.86
Mg-Ti (101)	60.0	37.20	2.41
Mg-Ti (100)	84.0	32.68	2.74
Pd (111)	0.0	39.96	2.25
Pd (200)	54.0	46.64	1.95
Pd (111)	72.0	40.10	2.25

Hydrogenated $Mg_{0.80}Ti_{0.20}$ (1 bar H_2)

fcc symmetry with a=4.71 Å and α=88.5° (V=104.45 Å^3)
Pd topcoat: fcc with a=4.03 Å

Identification	ψ position (°)	2θ position (°)	lattice spacing (Å)
Mg-Ti-H (111)	0.9	32.03	2.79
Mg-Ti-H (111)	72.0	33.12	2.70
Pd-H (111)	0.2	38.43	2.34
Pd-H (200)	54.0	44.85	2.02
Pd-H (111)	70.3	38.88	2.31

The results of a hydrogenated $Mg_{0.80}Ti_{0.20}$ layer are shown in Fig. 5.3B and listed in Table 5.2. Like for the hydrogenated $Mg_{0.70}Ti_{0.30}$ film the 2θ positions of the Mg-Ti-H phase correspond to a fcc unit cell. The different 2θ positions of the (111) peaks at ψ=0° and ψ=72° indicate again that the material is either stressed and/or that the unit cell is distorted. Assuming a distorted unit cell the lattice constants are a=4.71 Å and α=88.5°, which complicates an accurate estimate of the hydrogen content based on a linear combination of the lattice constants of non-distorted cubic MgH_2 and TiH_2 structures. Electrochemical measurements showed that the H/M ratio at the end of hydrogenating the $Mg_{0.80}Ti_{0.20}$ film is close to 1.8 (see Fig. 4.8). The 2θ positions of the Pd hydride phase are practically the same as for the Pd hydride topcoat found for the $Mg_{0.70}Ti_{0.30}$ layer. The lattice constant is about 4.03 Å.

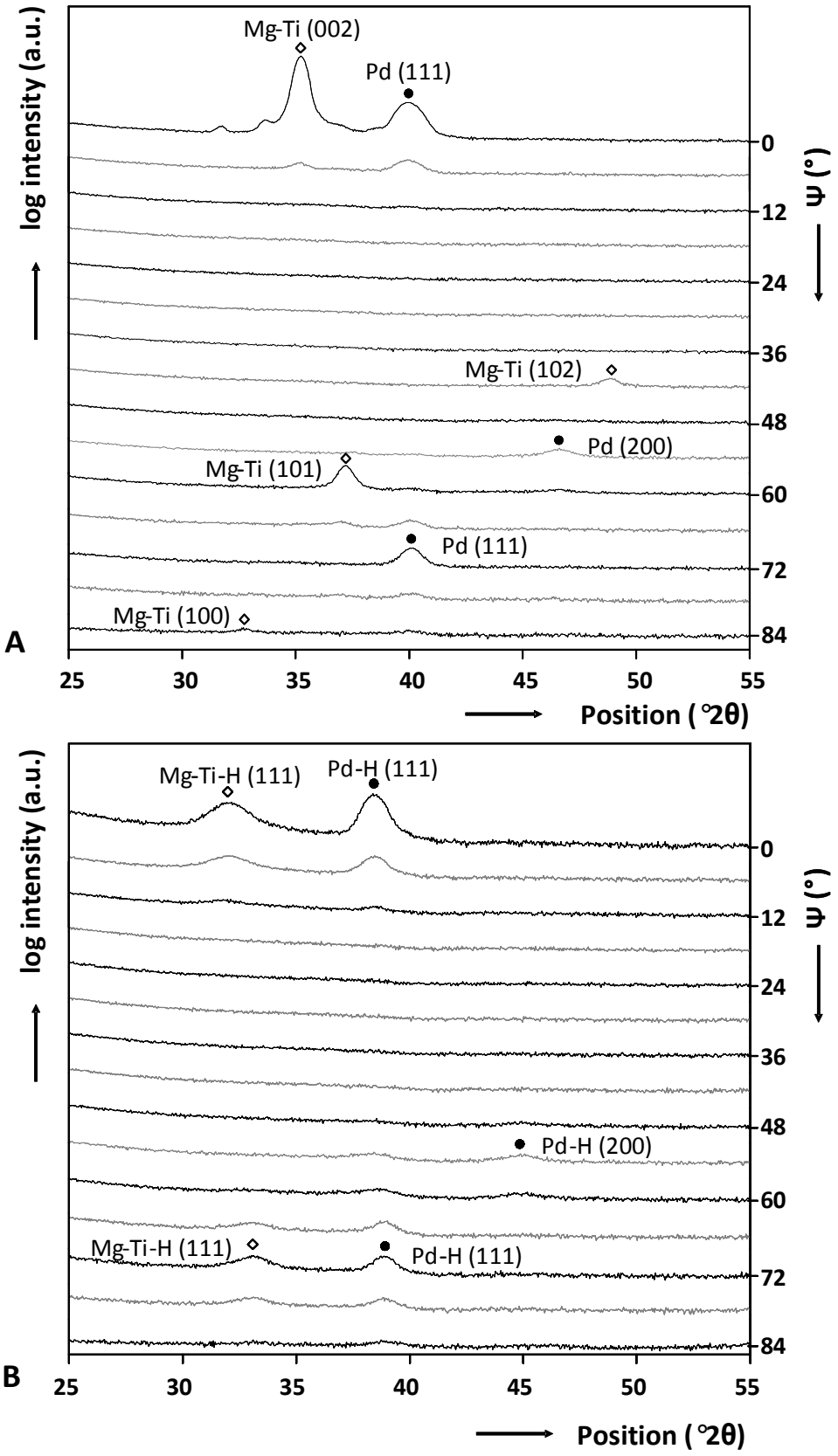

Fig. 5.3 XRD 2θ-θ scans at different tilt angles ψ of the 200 nm thick $Mg_{0.80}Ti_{0.20}$ layer capped with a 10 nm thick Pd topcoat in the as-prepared state (A) and after hydrogenation in 1 bar H_2 (B).

Fig. 5.4A shows the 2θ-θ scans of the $Mg_{0.90}Ti_{0.10}$ layer in the as-received state. The identification and position of the diffraction peaks are presented in Table 5.3. The absence of clear Pd peaks in all scans, except at ψ=84°, indicates that the Pd crystallites do not have a strong preferred orientation. The higher intensity of the Pd peaks at ψ=84° is due to a higher surface sensitivity of the measurements at ψ angles close to 90°. Again, small peaks appear on the left side of the 002 reflection of Mg-Ti, which are caused by diffraction of Cu Kβ and W Lα radiation. The 2θ positions of the Mg-Ti phase correspond to a hcp unit cell with lattice constants a=3.19 Å and c=5.12 Å. The 2θ positions of the Pd phase correspond in this case to a fcc unit cell with lattice constant a=3.88 Å.

Table 5.3 XRD characterization of the as-deposited and hydrogenated $Mg_{0.90}Ti_{0.10}$ sample obtained from Fig. 5.4. The 2θ positions of the Mg-Ti-H (110), (211) and (211) peaks of the hydrogenated sample were obtained from additional ψ scans.

As-deposited $Mg_{0.90}Ti_{0.10}$

hcp symmetry with a=3.19 Å, c=5.12 Å (V=45.12 Å^3)
Pd topcoat:fcc with a=3.88 Å

Identification	ψ position (°)	2θ position (°)	lattice spacing (Å)
Mg-Ti (002)	-0.3	34.97	2.56
Mg-Ti (102)	42.7	48.46	1.88
Mg-Ti (101)	61.5	37.00	2.43
Pd (111)	84.0	40.15	2.24

Hydrogenated $Mg_{0.90}Ti_{0.10}$ (1 bar H_2)

bct symmetry with a=4.48 Å and c=2.99 Å (V=60.01 Å^3)
Pd topcoat: fcc with a=3.99 Å

Identification	ψ position (°)	2θ position (°)	lattice spacing (Å)
Mg-Ti-H (110)	-0.3	28.03	3.18
Mg-Ti-H (211)	38.1	54.86	1.67
Mg-Ti-H (101)	66.8	35.99	2.49
Mg-Ti-H (211)	75.1	55.19	1.66
Mg-Ti-H (110)	84.0	28.39	3.14
Pd-H (111)	84.0	39.06	2.30

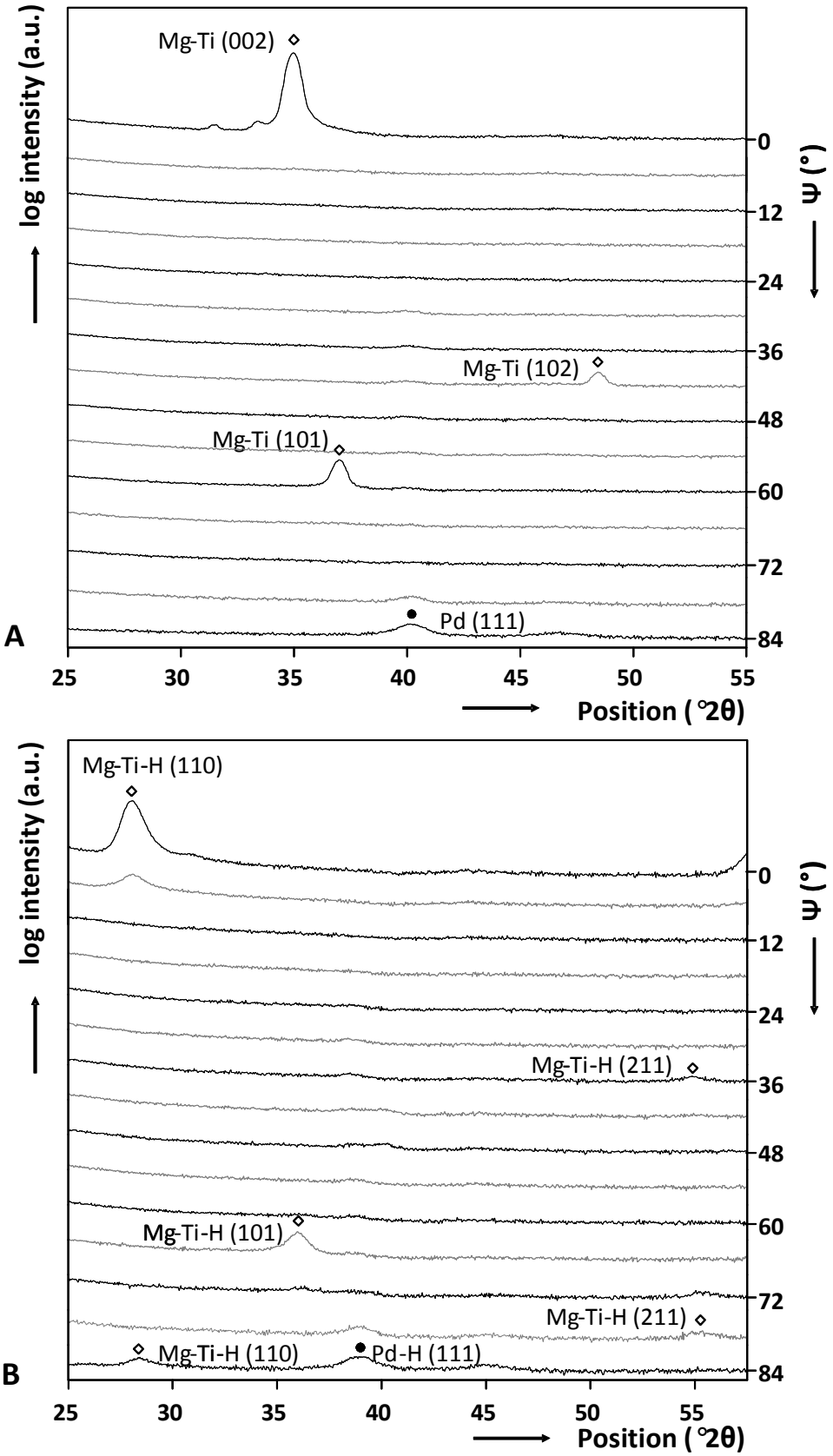

Fig. 5.4 XRD 2θ-θ scans at different tilt angles ψ of the 200 nm thick $Mg_{0.90}Ti_{0.10}$ layer capped with a 10 nm thick Pd topcoat in the as-prepared state (A)and after hydrogenation in 1 bar H_2 (B).

Fig. 5.4B shows 2θ-θ scans obtained after hydrogenating the $Mg_{0.90}Ti_{0.10}$ layer. XRD measurements were started about 3 days after filling the container with H_2, because initial measurements performed directly after filling still showed diffraction peaks of unreacted Mg-Ti alloy illustrating poor hydrogen uptake kinetics. This observation is in line with previous electrochemical results that showed that the hydrogen transportation kinetics is strongly inhibited for Mg-Ti alloys containing 90 at.% Mg or more (see Fig. 5.1 and paragraphs 4.2.2 and 4.2.4.2). The identification and position of the diffraction peaks are also presented in Table 5.3. The 2θ positions of the hydrided Mg-Ti phase correspond to a body centered tetragonal unit cell. This structure is similar to that of rutile MgH_2, which is known for its poor hydrogen insertion and extraction kinetics, thus emphasizing the influence of the structure on the (de)hydrogenation kinetics.[8] The different 2θ positions of the (110) peaks at ψ=-0.3° and ψ=84° and the (211) peaks at ψ=38.1° and ψ=75.1° again indicate that the material is either stressed or that the unit cell is distorted. The difference is, however, much smaller than found for hydrogenated $Mg_{0.70}Ti_{0.30}$ and $Mg_{0.80}Ti_{0.20}$ films. Neglecting stress and distortion, the lattice constants are approximately a=4.48 Å and c=2.99 Å. The 2θ positions of the Pd hydride phase correspond to a fcc unit cell with lattice constant of about 3.99 Å. The H/M ratio in the $Mg_{0.90}Ti_{0.10}$ layer determined by means of electrolytic hydrogenation experiments is approximately 1.7 (see Fig. 4.8).

5.3.2 Structural characterization using *in situ* electrochemical XRD

To obtain detailed information about the influence of the hydrogen content on the crystallographic properties of the host lattice, XRD and electrochemical (de)hydrogenation measurements were performed *in situ* (see paragraph 2.4.4 for the experimental details). The electrodes were fully hydrogenated in about 20 current pulses. Each current pulse of -0.12 mA was followed by a one hour relaxation period after which the XRD pattern was measured. After converting the thin film layers to their corresponding hydrides, an oxidation current of +0.12 mA was applied to extract the hydrogen atoms in about 20 current pulses. Again, after each current pulse the system was allowed to equilibrate for 1 hour before obtaining the XRD pattern. The current pulses were interrupted once the electrochemical potential reached 0 V *vs.* Hg/HgO (1 M KOH) to avoid oxidation of the thin film electrodes.

The X-ray diffractograms of a $Mg_{0.90}Ti_{0.10}$ film at various stages of hydrogenation are depicted in Fig. 5.5. The inset shows the experimental electrochemical equilibrium potentials, indicated by the symbols, and the corresponding isotherm. Starting with the as-deposited state, the X-ray diffraction pattern at the back in Fig. 5.5 shows only a single peak at 35.13 °2θ, which is due to the {002} plane of a hexagonal closed packed (hcp) MgTi unit cell. Note that initially only a single peak assigned to the MgTi alloy appears in the diffractograms as a consequence of preferential orientation, commonly observed with thin films. The (002) peak is shifted slightly to a higher 2θ angle compared to pure Mg, because the formation of a solid solution of Ti in Mg causes the lattice to contract, as Ti has a relatively small molar volume.[9-11] No peak from the Pd topcoat is present, which is in agreement with earlier reports and is probably related to the loss of preferential orientation induced by the morphology of the underlying $Mg_{0.90}Ti_{0.10}$ layer (see Fig. 4.24).[5,12]

The isotherm depicted in the inset of Fig. 5.5 shows a narrow hydrogen-poor solid solution region. Hereafter, a plateau develops, which is typical for a phase transformation. At the end

of hydrogenation the hydrogen partial pressure increases and a second plateau forms that is due to the formation of H_2 gas. The final H/M ratio of the $Mg_{0.90}Ti_{0.10}$ film is approximately 6.9 wt.% H (1.8 hydrogen per metal atom (H/M)). The actual H content is, however, somewhat lower because of the competing hydrogen evolution reaction (reaction 2.14), can take place during hydrogenation.

The plateau pressure of the hydride formation reaction is, on average, approximately 5^*10^{-5} bar at room temperature. The Van 't Hoff equation (see Eq. 2.4) can be used to estimate the enthalpy of formation (ΔH_f). The calculated average value of ΔH_f is -31.8 kJ/mol H, which is close to the value found for thin film MgH_2 formation.[13] It is nearly similar to the results found by Gremaud *et al.*, using hydrogenography.[14]

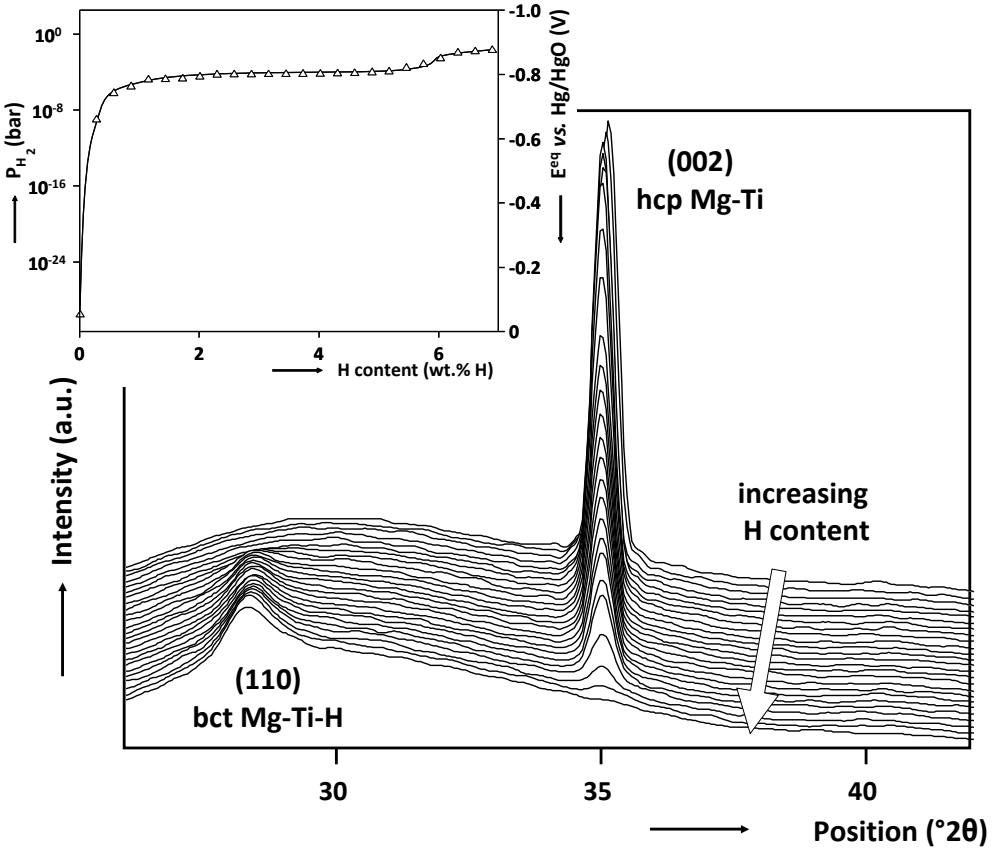

Fig. 5.5 Diffractograms, measured at various stages of hydrogenation, of a 200 nm thick $Mg_{0.90}Ti_{0.10}$ thin film deposited on 125 µm thick PEEK foil with a 1 nm Cr adhesion layer and a 10 nm thick Pd topcoat. The inset depicts the absorption isotherm at room temperature and the symbols indicate the hydrogen concentrations at which the XRD diffractograms were measured.

Hydrogenating the thin film from the as-prepared state decreases the intensity of the hexagonal 002 peak and, at the same time, a second peak emerges at 28.32°2θ. In paragraph 5.3.1 it was shown that the latter is due to the {110} plane of a hydrogen-rich, body-centered tetragonal structure. After continued hydrogenation, the intensity of the hcp reflection slowly decays and disappears completely at about 6.6 wt.% H and only the (110) bct peak remains.

After the metallic film is transformed into its hydride counterpart, the film is dehydrogenated. The diffractograms at various stages of dehydrogenation are shown in Fig. 5.6, now starting with the XRD pattern at the front. The inset shows the corresponding desorption isotherm and the positions where the diffraction patterns were obtained (symbols).

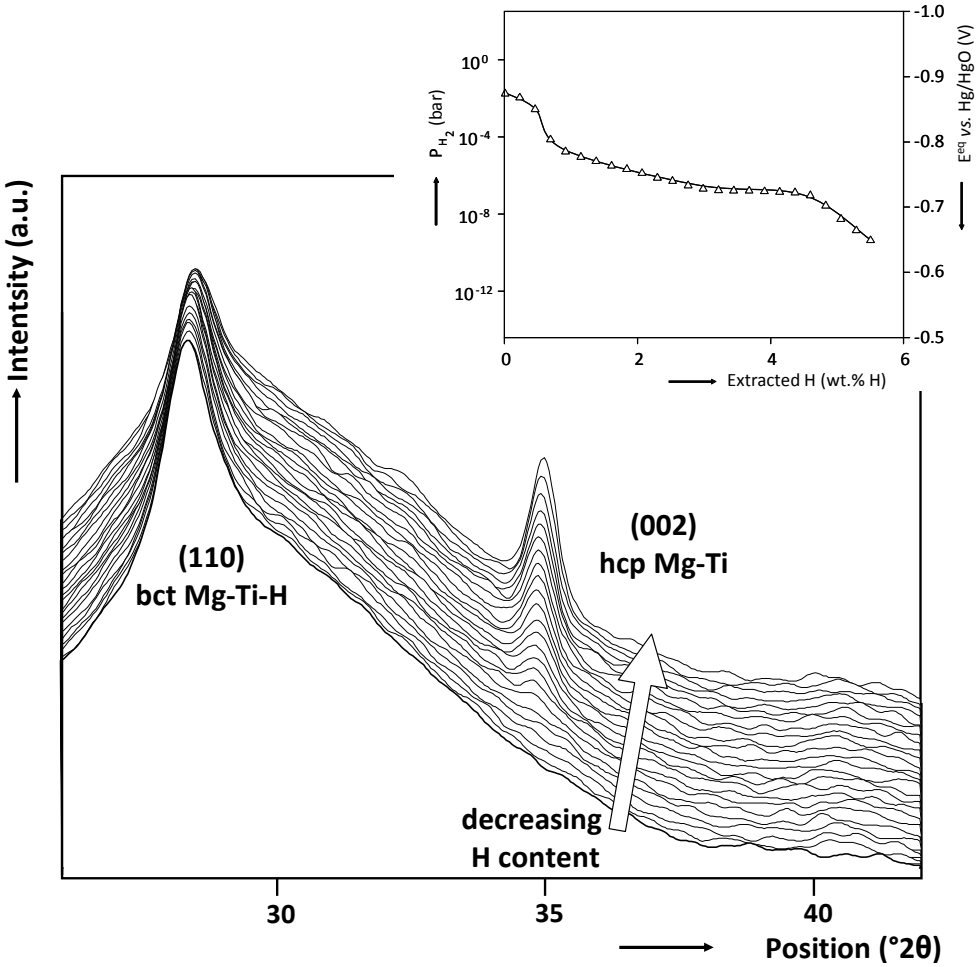

Fig. 5.6 Diffractograms of a fully hydrided $Mg_{0.90}Ti_{0.10}H_x$ thin film at various stages of dehydrogenation. The inset shows the desorption isotherm and the symbols indicate where the XRD patterns were obtained.

The position of the bct (110) peak shifts slightly towards larger angles during the first dehydrogenation steps, hereafter, it remains nearly constant for the entire dehydrogenation process. Simultaneously, the original 002 reflection grows in time. Yet, the final intensity of the 002 peak is far below the intensity of the as-prepared thin film. This observation is coupled to the fact that the hydrogen-rich tetragonal phase remains present. Apparently, the experimental conditions do not allow the entire hydrogen content to be extracted resulting in the coexistence of both the tetragonal and hexagonal structures at the end of dehydrogenation. Presumably, the poor hydrogen extraction kinetics that is associated with $Mg_{0.90}Ti_{0.10}$ hydride requires more driving force than experimentally applied. Potentiostatic dehydrogenation down to 0 V *vs.* Hg/HgO, which corresponds to $P_{H_2} \approx 10^{-33}$ bar (Eq. 2.18), was performed to completely dehydrogenate the film and showed that indeed only the hcp structure remains, which illustrates the reversibility of the phase transformation. Finally, the isotherm depicted

in Fig. 5.6 shows a sloping plateau with an average pressure of $5^{*}10^{-7}$ bar H_2 that corresponds to a enthalpy of formation of -31.7 kJ/mol H.

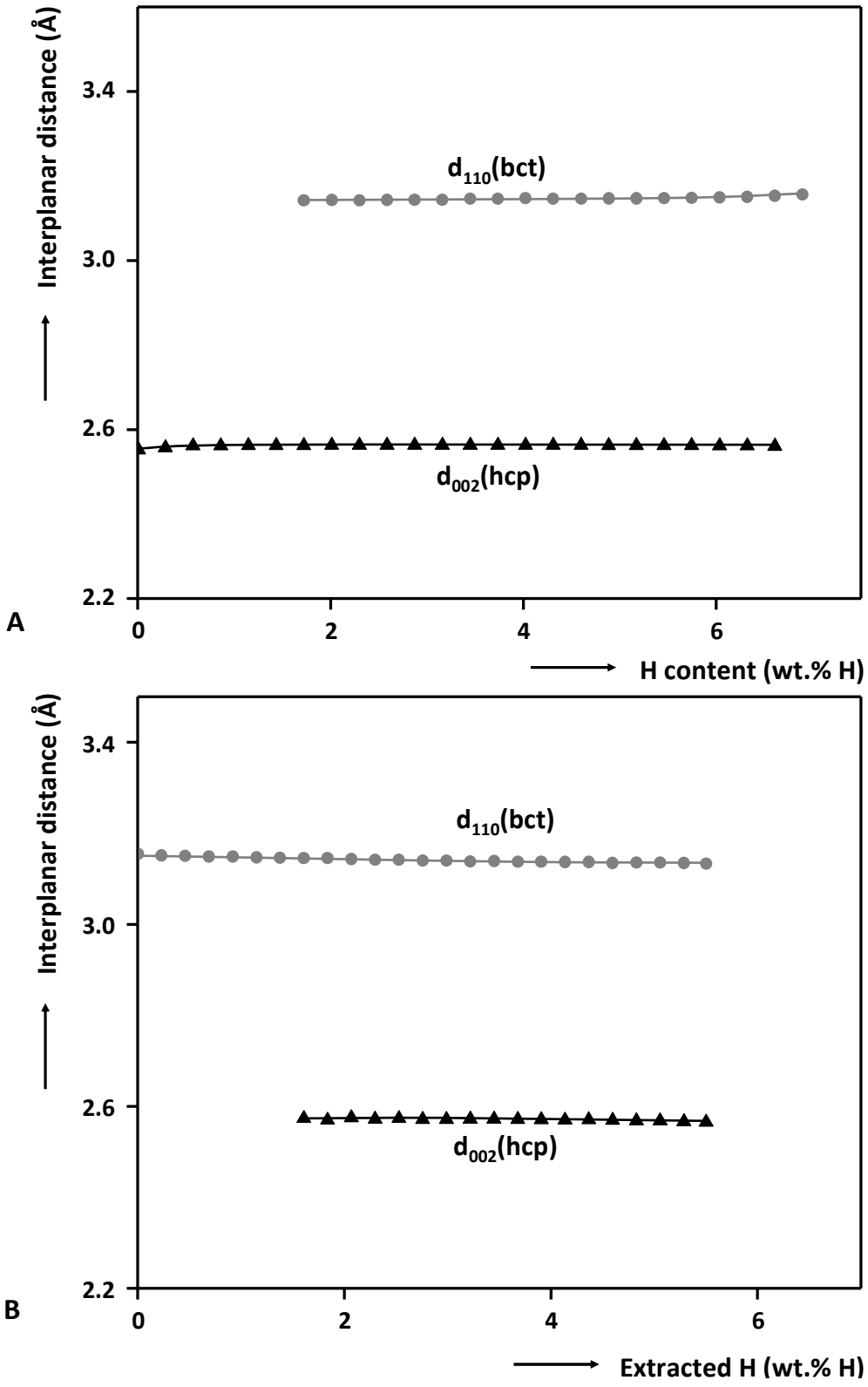

Fig. 5.7 Evolution of d_{002} (hcp) and d_{110} (bct) for $Mg_{0.90}Ti_{0.10}H_x$ as a function of hydrogen content for (A) hydrogen absorption and (B) desorption.

The interplanar distance between the hexagonal {002} and tetragonal {110} planes during (de)hydrogenation can be calculated from the peak positions using the Bragg equation. The interplanar distances of these planes, denoted as d_{002} and d_{110}, obtained from the peaks in Fig. 5.5 and Fig. 5.6, are plotted as a function of the amount of inserted (a) and extracted (b) hydrogen in Fig. 5.7. Throughout almost the entire (de)hydrogenation process the interplanar distances of the lattice planes of the hexagonal and tetragonal phases are essentially constant, only changing slightly in the single-phase regions. A constant interplanar distance during the two-phase coexistence region implies that the composition of the hydrogen-poor and hydrogen-rich phases remains unchanged and that only the relative fractions of these phases vary. It implies also that the two phases are elastically decoupled. Similar behavior was observed before for ternary $LaNi_5$ hydride.[15,16]

An as-prepared $Mg_{0.70}Ti_{0.30}$ film was subjected to the same treatment as the $M_{0.90}Ti_{0.10}$ film. The X-ray diffractograms, again showing the as-deposited state at the back and corresponding isotherm are depicted in Fig. 5.8. The diffraction pattern of the as-deposited state shows two reflections. The peak at 35.56 $^\circ 2\theta$ is due to the {002} plane of the hexagonal closed packed (hcp) MgTi lattice. Also the (111) peak of the fcc-structured Pd topcoat is visible at 40.09 $^\circ 2\theta$. Increasing the hydrogen content shifts the (002) peak to lower 2θ angles as a result of an increasing interplanar distance. Once the hydrogen content reaches about 1.2 wt.% H (see inset) a second peak appears that is related to the {111} plane of a fcc-structured MgTi lattice. After continued hydrogenation, the hcp peak gradually declines to completely disappear at about 6.1 wt.% H and only the fcc-structured hydrogen-rich phase remains. The peak widths of the (002) hcp and (111) fcc reflections broaden as a function of hydrogen content, pointing towards a decreasing grain size. Also, the peak area of the reflections gradually decreases, indicating a loss of preferred orientation.

The position of the (111) reflection of the Pd topcoat remains constant throughout almost the entire hydrogen absorption process, indicating that the H content within this layer is close to zero, which is in agreement with the results reported by Niessen *et al.*[6] Once the hydride of the magnesium-titanium mixture is saturated with hydrogen, a fcc-structured hydrogen-rich Pd phase starts to form.

In the initial stage of hydrogenation the isotherm, shown in the inset of Fig. 5.8, reveals a gradual increase of the hydrogen equilibrium pressure. Hereafter, a plateau develops and finally H_2 formation is apparent in the form of a spurious plateau at approximately 0.1 bar (≈-0.9 V). The final gravimetric capacity of the $Mg_{0.70}Ti_{0.30}$ film amounts to approximately 6.1 wt.% of H (1.7 H/M). The plateau pressure of hydride formation is approximately 2^*10^{-5} bar H_2. The average value for ΔH_f of the hydride formation plateau estimated using the Van 't Hoff equation (Eq. 2.4) is -32.9 kJ/mol H, which again is close to the value found for thin film MgH_2 formation.[13] It is remarkable that adding up to 30 at.% Ti to Mg does not change the enthalpy of formation much, which is in agreement with earlier results that also showed that replacing Ti by V, Cr or Sc does not significantly change the thermodynamics of the system.[17] Yet, the hydrogen transport kinetics heavily depends on the alloying element.

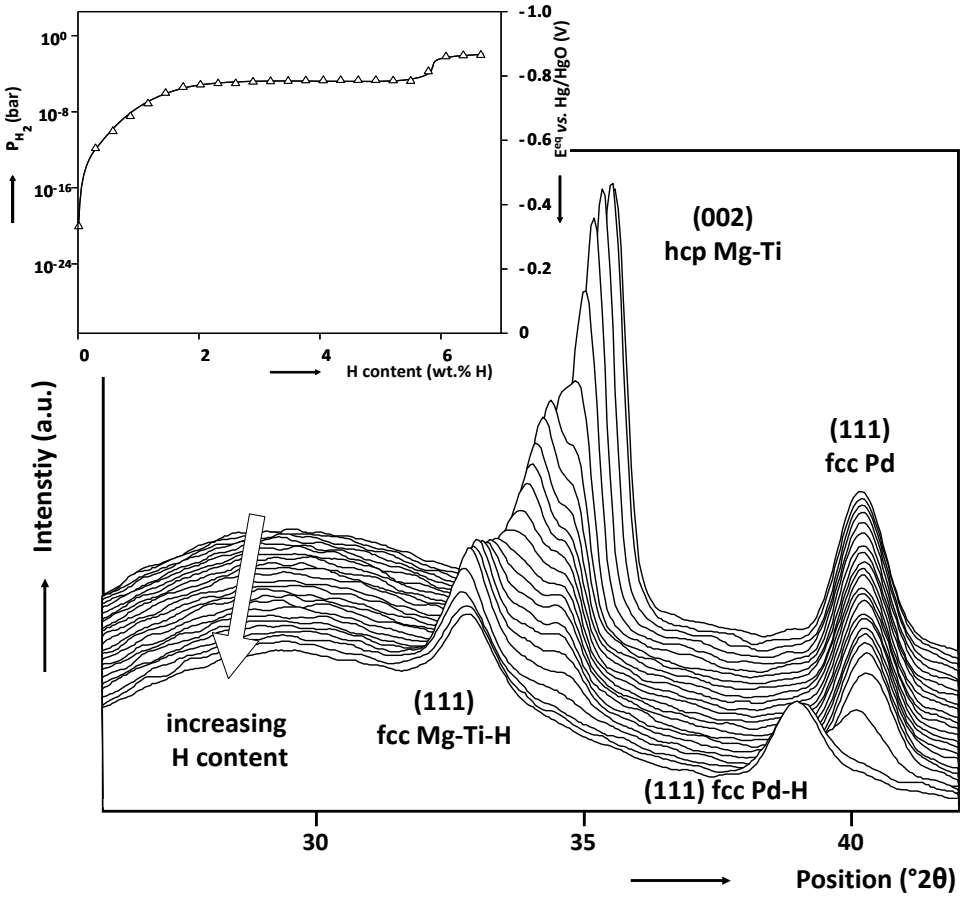

Fig. 5.8 XRD patterns of a $Mg_{0.70}Ti_{0.30}$ thin film deposited on 125 µm PEEK foil with a 10 nm Pd topcoat and a 1 nm thick Cr adhesion layer. The inset shows the pressure-composition isotherm.

The X-ray diffraction patterns and the pressure-composition isotherm during dehydrogenation of $Mg_{0.70}Ti_{0.30}H_x$ are shown in Fig. 5.9. The main features are the transformation of cubic hydrogen-rich Pd to cubic hydrogen-poor Pd, and subsequently the shift towards higher 2θ angles of the (111) reflection caused by the contracting unit cell and the transformation back to the original hexagonal MgTi structure. The positions of the (002) reflections before and after hydrogenation, however, do not coincide (as-deposited: 35.56 °2θ *vs.* dehydrogenated: 34.80 °2θ). The expanded structure after hydrogen extraction probably stems from an irreversible amount of hydrogen still present in the host lattice, which is confirmed by the desorption isotherm that shows that, instead of the 6.1 wt.% of H originally inserted, only about 5 wt.% of H is extracted. Since for gas phase measurements the peak position was fully reversible it points to certain sites where hydrogen atoms are bonded so strongly that complete electrochemical dehydrogenation is not possible under the current experimental conditions. This is in line with the electrochemical data presented in paragraph 4.2.3.1.

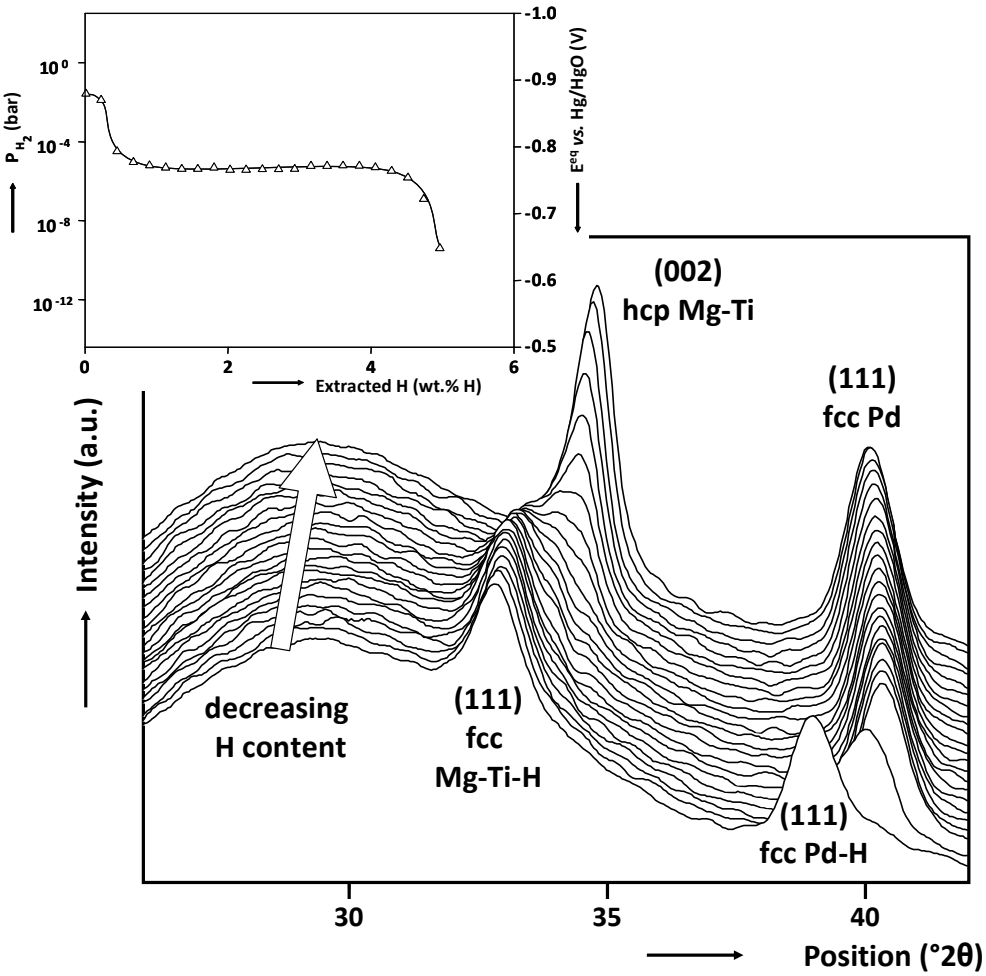

Fig. 5.9 Diffractograms of a fully hydrided Pd-capped $Mg_{0.70}Ti_{0.30}H_x$ thin film upon dehydrogenation. The inset shows the desorption isotherm.

As the thermodynamic stability of TiH_2 (ΔH_f =-68 kJ/mol H) is much larger than that of MgH_2 (ΔH_f =-37 kJ/mol H) we conclude that Ti is most likely involved in binding hydrogen irreversibly.[18] This is supported by the desorption isotherm depicted in the inset of Fig. 5.9 that shows that the experimental hydrogen partial pressure at the end of dehydrogenation (4^*10^{-10} bar H_2) is still higher than the H_2 pressure required for the $Ti \rightarrow TiH_2$ reaction (9.8^*10^{-18} bar H_2 at 298 K).

To accommodate the interesting XRD features of the MgTi alloy a model was proposed by Borsa *et al.* where Mg and Ti are assumed to be only partially segregated.[5] A schematic representation of a crystalline grain with a Mg-rich and Ti-rich region in the as-prepared state is shown in Fig. 5.10A. The local deformation is only schematic and might deviate from reality. The same crystalline grain after hydrogen uptake in the Ti-rich region and in the fully hydrogenation state is shown in Figs. 5.10B and 5.10C, respectively. This hydrogenation sequence is related to the more negative enthalpy of formation of TiH_2 as compared to MgH_2.[18] Very likely, hydrogenation of Ti-related sites in the beginning of the hydrogenation process reduces the mobility of atoms during further hydrogen uptake and thus prevents the large scale segregation, observed in many other Mg-based systems.

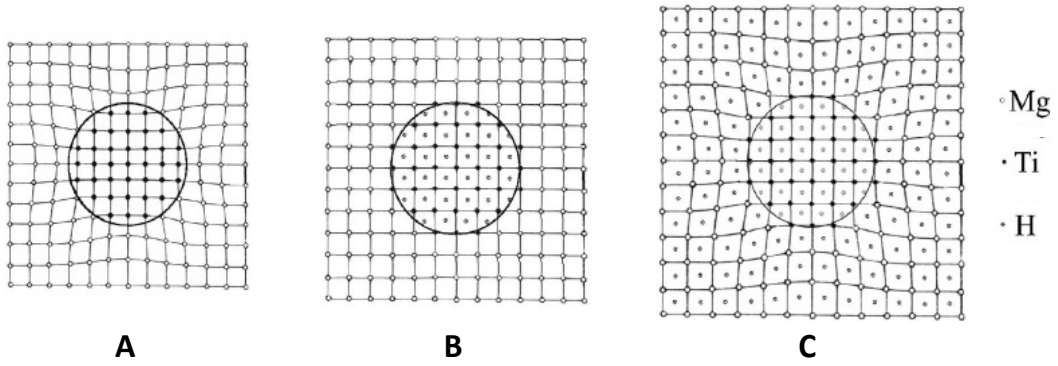

Fig. 5.10 Schematic representation of a crystalline grain consisting of a Mg and Ti region in the as-deposited state (A), the same crystalline grain after hydrogen uptake in the Ti-related sites (B) and fully hydrogenated state (C).[5]

Assuming that the irreversibly bound hydrogen atoms remain in sites that are tetrahedrally surrounded by 4 Ti atoms (this situation shown Fig. 5.10B), we would need a fraction of 19% of Ti_4-clusters. This is much higher than the fraction $(0.30)^4$=0.8% of Ti_4 sites in a random $Mg_{0.70}Ti_{0.30}$ alloy. Thus we conclude that the $Mg_{0.70}Ti_{0.30}$ system is partially segregated, which has recently been confirmed by the work of Griessen and co-workers.[12,19] A chemical short-range order (CSRO) parameter, *s*, has been introduced to quantify the degree of segregation. For $Mg_{0.70}Ti_{0.30}$ alloys s≈0.35 is found.[19] Using this value a fraction of Ti_4-clusters (f_{Ti_4}) of 4.9% can be calculated according to

$$f_{Ti_4} = (1 - y + sy)^3(1-y) \qquad (5.1)$$

which is still too low to accommodate the large amount of irreversibly bound hydrogen. Therefore, not only pure Ti_4-clusters, but also other tetrahedral sites composed of Ti and Mg atoms are likely to provide a large stability.

The X-ray diffractograms do not show, however, separate Ti and Mg phases, which leads to the conclusion that within the alloy nano-structured, Ti-rich and Ti-poor, regions coexist. This observation is in agreement with the microstructure of Mg_yTi_{1-y} alloys proposed recently.[5,19] The formation of these chemically partially segregated regions is expected, considering the large positive enthalpy of mixing of Mg and Ti.[18] The fact that these nano-structured regions do not appear separately in the diffractograms illustrates the resolution limit of conventional X-ray diffraction, in agreement with the results found for thin film multilayer systems.[20]

The inset in Fig. 5.9 shows the desorption isotherm of $Mg_{0.70}Ti_{0.30}H_x$. The plateau pressure is approximately 4^*10^{-6} bar H_2, which corresponds to an enthalpy of formation of -34.9 kJ/mol H. There is a significant hysteresis in the plateau pressure of hydrogen absorption and desorption, which is often observed for both thin film and bulk metal hydrogen systems. The origin of this hysteresis has been attributed to various stress states, induced by expansion and contraction of the lattice, during (de)hydrogenation (*i.e.* phase transformation).[21]

The interplanar distance between the hexagonal {002} and cubic {111} planes are plotted as a function of the amount of inserted (A) and extracted (B) hydrogen in Fig. 5.11. For the hcp phase, d_{002} gradually increases as a function of the hydrogen content and at about 1.2

wt.% of H the second phase appears. Remarkably, the interplanar distance d_{111} of the cubic phase increases significantly as a function of H content. Hydrogen extraction transforms the fcc phase back to the original hcp structure. Similarly as found during hydrogen absorption, the lattice spacing of the {111} planes of the fcc structure also depends on the hydrogen content.

The strong interplanar distance dependence on the hydrogen content found for $Mg_{0.70}Ti_{0.30}$ deviates clearly from the results found for $Mg_{0.90}Ti_{0.10}$ (Fig. 5.7) and $LaNi_5$.[15,16] The transition of the host lattice, from hexagonal to cubic and *vice versa*, does not only involve a change of the fractions of the phases but also points to a continuous change of phase compositions, which is likely to be coupled to a large spread in the thermodynamic stability of the available sites for hydrogen and the structural coherence of the metal lattice. For a binary system such as MgTi, this spread can only be brought about by the presence of Ti-poor and Ti-rich regions and again illustrates that the Mg and Ti atoms in $Mg_{0.70}Ti_{0.30}$ are not randomly distributed. Considering the high thermodynamic stability of TiH_2 compared to that of MgH_2, it is most likely that in the early stages of hydrogenation the hydrogen-rich phase mainly comprises of Ti-rich regions. Continued hydrogenation will eventually also fill the Mg-rich regions.

Likewise, the crystal structure of an as-prepared $Mg_{0.80}Ti_{0.20}$ film was investigated as a function of hydrogen content. The diffractograms, again showing the as-deposited state at the back and corresponding isotherm are depicted in Fig. 5.12. As was found for $Mg_{0.70}Ti_{0.30}$ the XRD pattern of as-prepared $Mg_{0.80}Ti_{0.20}$ shows two reflections, *i.e.* a reflection at 35.44 $^{\circ}2\theta$ originating from the {002} plane of the hcp MgTi lattice and a reflection at 40.30 $^{\circ}2\theta$ from the {111} plane of the fcc Pd structure. Hydrogenation shifts the hexagonal 002 peak to lower 2θ values, indicating an expansion of the interplanar distance. Further increase of the hydrogen content results in a gradual declining intensity of the hcp peak and the simultaneous formation of a fcc (111) reflection at approximately 32.5 $^{\circ}2\theta$. The decline of the intensity of the hcp reflection is evidently coupled to the decreasing amount of the hydrogen-poor MgTi phase. Yet, only a small increase of the area of the (111) reflection is observed in the diffractograms, indicating that the preferred orientation is almost completely lost.

The pressure-composition isotherm, in the inset of Fig. 5.12, shows that increasing the hydrogen concentration results in a plateau-like behavior for a large part of the isotherm. The plateau pressure is approximately $3^{*}10^{-5}$ bar H_2, which is somewhat higher than the result of $Mg_{0.70}Ti_{0.30}$ and can be related to a higher Mg-content that effectively decreases the overall stability of the magnesium-titanium hydride.

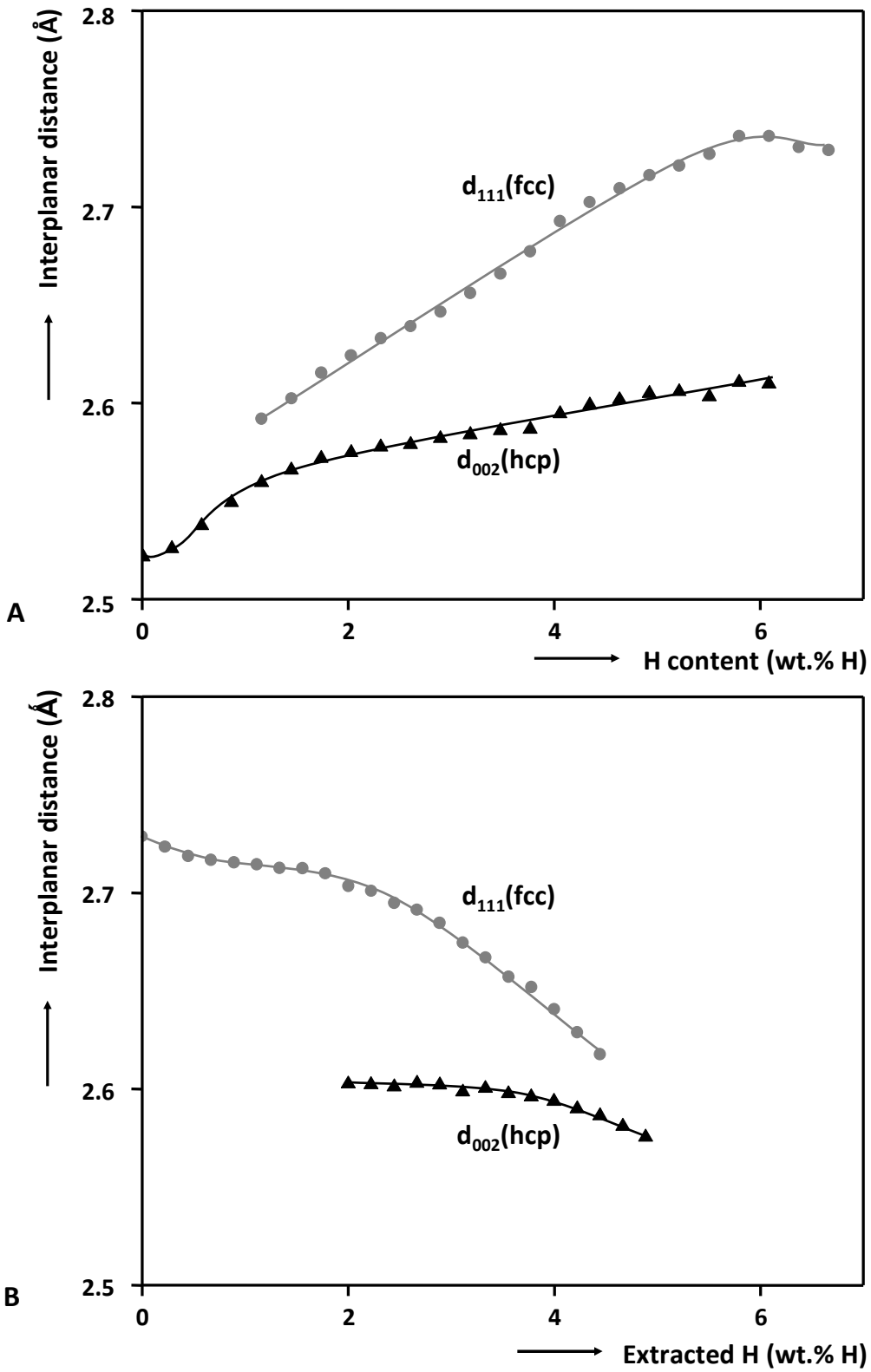

Fig. 5.11 Evolution of d_{002} (hcp) and d_{111} (fcc) for $Mg_{0.70}Ti_{0.30}H_x$ as a function of hydrogen content for (A) hydrogen absorption and (B) desorption.

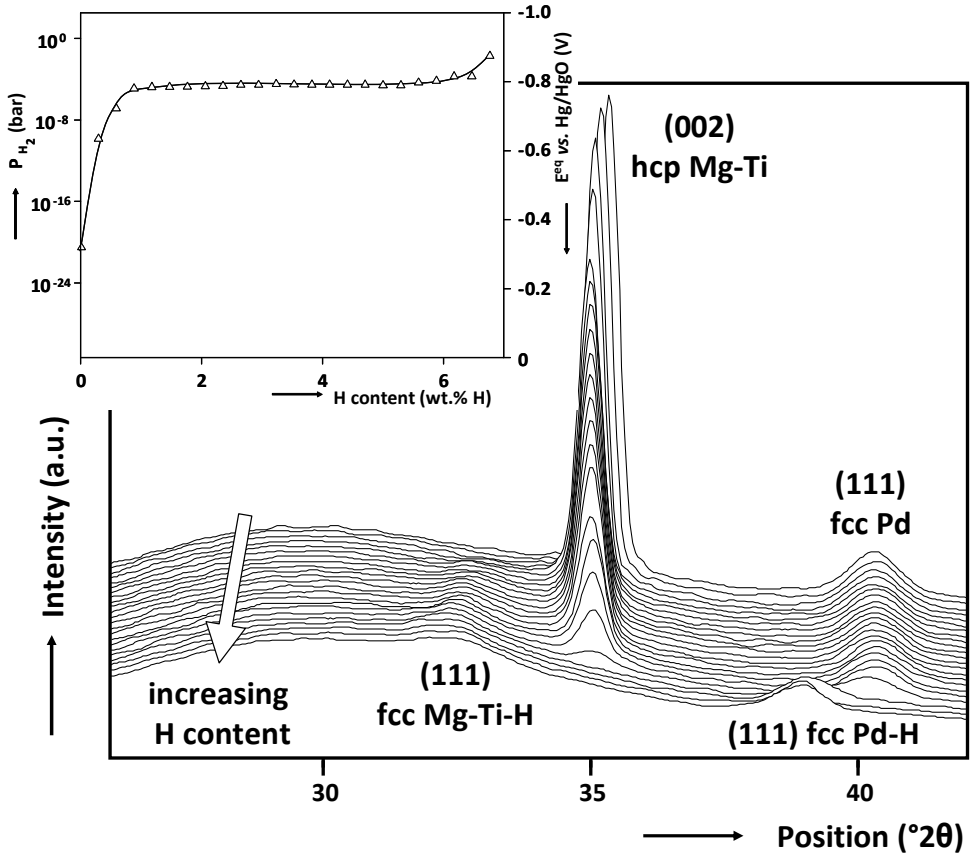

Fig. 5.12 XRD diffractograms of a 200 nm thick $Mg_{0.80}Ti_{0.20}$ thin film layer deposited on 125 μm PEEK foil with a 1 nm thick Cr adhesion layer and a 10 nm thick Pd topcoat. The inset shows the absorption isotherm.

The XRD diffractograms at various dehydrogenation stages are shown in Fig. 5.13. Hydrogen desorption is initially only perceptible in the transition of hydrogen-rich Pd to hydrogen-depleted Pd. Hereafter, the broad fcc (111) reflection of the MgTi lattice transforms back to the 002 reflection of the hcp structure. The area of the hcp reflection after hydrogen extraction is, however, significantly smaller with respect to the as-deposited state, again indicating a loss of preferential orientation. Similarly to the results found for the $Mg_{0.70}Ti_{0.30}$ alloy the interplanar distance of the {002} planes is somewhat larger after hydrogen extraction compared to the as-prepared state, indicating that hydrogen binds irreversibly to Ti-rich regions inside the metallic matrix. Support for this conclusion can be found by comparing the absorption and desorption capacity from the corresponding isotherm that indeed show that a small part of the absorbed hydrogen atoms cannot be extracted.

The isotherm in the inset of Fig. 5.13 shows that the reversible hydrogen capacity exceeds 6 wt.% of H. The plateau pressure of hydrogen desorption is $6^{*}10^{-7}$ bar, which is one order of magnitude lower than the value found for $Mg_{0.70}Ti_{0.30}$, and corresponds to an enthalpy of formation of -37.2 kJ/mol H. This value is again very similar to the result reported for MgH_2 thin films by Krozer and Kasemo.[13]

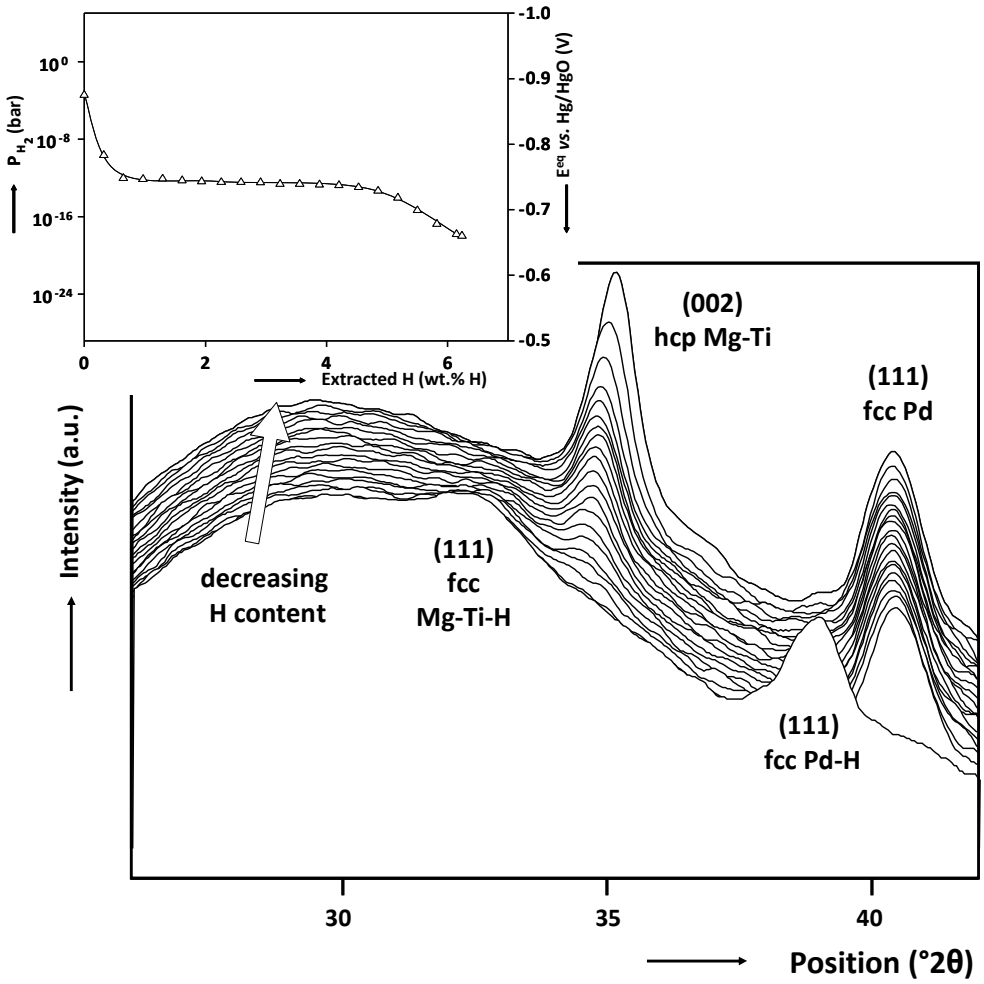

Fig. 5.13 XRD diffractograms and desorption isotherm (inset) of a fully hydrogenated Pd-capped $Mg_{0.80}Ti_{0.20}H_x$ thin film at various stages of dehydrogenation.

5.4 Conclusions

In conclusion, it is shown that $Mg_{0.70}Ti_{0.30}$, $Mg_{0.80}Ti_{0.20}$ and $Mg_{0.90}Ti_{0.10}$ thin film alloys have a hexagonal closed packed crystal structure in the as-deposited state. Hydrogenation under 1 bar H_2 transforms the structure of both $Mg_{0.70}Ti_{0.30}$ and $Mg_{0.80}Ti_{0.20}$ films into a, rhombohedrally distorted, unit cell with face centered cubic symmetry, whereas hydrogenated $Mg_{0.90}Ti_{0.10}$ has a body centered tetragonal structure. In combination with previous electrochemical data the results emphasize the importance of the crystal structure of the hydride for the hydrogen transport rate, *i.e.* a face centered cubic unit cell greatly facilitates rapid hydrogen insertion and extraction, whereas a unit cell with body centered tetragonal symmetry inhibits hydrogen uptake and release rates significantly.

The *in situ* electrochemical XRD study showed that the lattice spacings of the unit cell of $Mg_{0.90}Ti_{0.10}$ as a function of hydrogen content do not change much in the phase transformation region, indicating that only the fractions and not the composition of the phases change. Remarkably, the lattice spacings found for $Mg_{0.70}Ti_{0.30}H_x$ show a strong dependence on the composition of the phases and reveal that the Mg-to-Ti ratio of both phases

continuously changes. Evidently, there is a large spread in the thermodynamic stability of the available sites for hydrogen, which implies a nano-structured alloy with Ti-poor and Ti-rich regions and illustrates that the Mg and Ti atoms in $Mg_{0.70}Ti_{0.30}$ are not randomly distributed.

5.5 References

1 P.H.L. Notten, M. Ouwerkerk, H. van Hal, D. Beelen, W. Keur, J. Zhou and H. Feil, *High energy density strategies: from hydride-forming materials research to battery integration*, J. Power Sources **2004**, *29*, 45-54.

2 R.A.H. Niessen and P.H.L. Notten, *Hydrogen storage in thin film magnesium–scandium alloys***,** J. Alloys Compd. **2005**, *404-406*, 457-460.

3 W.P. Kalisvaart, R.A.H. Niessen and P.H.L. Notten, *Electrochemical hydrogen storage in MgSc alloys: A comparative study between thin films and bulk materials*, J. Alloys Compd. **2006**, *417*, 280-291.

4 W.P. Kalisvaart, P. Vermeulen, A.V. Lyedovskikh, D. Danilov and P.H.L. Notten, *The electrochemistry and modelling of hydrogen storage materials*, J. Alloys Compd. **2007**, *446-447*, 648-654.

5 D.M. Borsa, R. Gremaud, A. Baldi, H. Schreuders, J.H. Rector, B. Kooi, P. Vermeulen, P.H.L. Notten, B. Dam and R. Griessen, *Structural, optical, and electrical properties of $Mg_yTi_{1-y}H_x$ thin films*, Phys. Rev. B **2007**, *75*, 205408/1-9.

6 R.A.H. Niessen, P. Vermeulen and P.H.L. Notten, *The electrochemistry of Pd-coated $Mg_ySc_{(1-y)}$ thin film electrodes: A thermodynamic and kinetic study*, Electrochim. Acta **2006**, *61*, 2427-2436.

7 C.N. Singman, *Atomic volume and allotropy of the elements*, J. Chem. Ed. **1984**, *61*, 137-142.

8 K.H.J. Buschow, P.C.P. Bouten and A.R. Miedema, *Hydrides formed from intermetallic compounds of 2 transition metals: a special-class of ternary alloys*, Rep. Prog. Phys. **1982**, *45*, 937-1039.

9 A.R. West, *Solid state Chemistry and its applications*, 1st ed., p. 367, John Wiley & Sons, New York (**1984**).

10 P. Villars (Edt), *Pearson's Handbook Desk Edition*, Vol. 2, p. 2336, ASM International, **1997**.

11 L. Vegard, *The constitution of mixed crystals and the space occupied by atoms*, Z. Phys. **1921**, *5*, 17-26.

12 A. Baldi, R. Gremaud, D.M. Borsa, C.P. Baldé, A.M.J. van der Eerden, G.L. Kruijtzer, P.E. de Jongh, B. Dam and R. Griessen, *EXAFS study of short-range ordering in $Mg_yTi_{1-y}H_x$ thin films*, Phys. Rev. B **2008**, submitted.

13 A. Krozer and B. Kasemo, *Hydrogen uptake by Pd-coated Mg – absorption-desorption isotherms and uptake kinetics,* J. Less-common Met. **1990**, *160*, 323-342.

14 R. Gremaud, C.P. Broedersz, D.M. Borsa, A. Borgschulte, P. Mauron, H. Schreuders, J.H. Rector, B. Dam and R. Griessen, *Hydrogenography: an optical combinatorial method to find new light-weight hydrogen-storage materials*, Adv. Mater. **2007**, *19*, 2813-2817.

15 P.H.L Notten, J.L.C. Daams, A.E.M. Deveirman and A.A. Staals, *In-situ X-ray diffraction – a useful tool to investigate hydride formation reactions*, J. Alloys Compd. **1994**, *209*, 85-91.

16 P.H.L Notten, J.L.C. Daams and R.E.F. Einerhand, *On the nature of the electrochemical cycling stability of nonstoichiometric $LaNi_5$-based hydride-forming compounds*, J. Alloys Compd. **1994**, *210*, 233-241.

17 R.A.H. Niessen and P.H.L. Notten**,** *Electrochemical hydrogen storage characteristics of thin film MgX (X = Sc, Ti, V, Cr) compounds***,** Electrochem. Solid-State Lett. **2005**, *8*, A534-A538.

18 R. Griessen and T. Riesterer, *Topics in Applied Physics Hydrogen in Intermetallic Compounds*, *Chapter 6: Heat of Formation Models*, Vol. 63 (Ed. L. Schlapbach), Springer-Verlag, Berlin, **1988**, 219-284.

19 R. Gremaud, A. Baldi, M. Gonzalez-Silveira, B. Dam and R. Griessen, *Chemical short-range order and lattice deformations in $Mg_yTi_{1-y}H_x$ thin films probed by hydrogenography*, Phys. Rev. B **2008**, *77*, 144204/1-10.

20 C. Michaelsen, *On the structure and homogeneity of solid-solutions – the limits of conventional X-ray diffraction*, Philos. Mag. A **1995**, *72*, 813-828.

21 A.T.M. van Gogh, D.G. Nagengast, E.S. Kooij, N.J. Koeman, J.H. Rector and R. Griessen, *Quenching of giant hysteresis effects in $La_{1-z}Y_zH_x$ switchable mirrors*, Phys. Rev. Lett. **2000**, *85*, 2156-2159.

6

Hydrogen storage in ternary MgTiX alloys

Abstract

In the search for hydrogen storage materials with a high gravimetric capacity, thin film Mg_yTi_{1-y} alloys, which exhibit excellent kinetic properties, form the basis for more advanced compounds. The plateau pressure of the Mg-Ti hydride system is very low (approximately 10^{-6} bar at room temperature). A way to increase this pressure is by destabilizing the metal hydride. The foremost effect of incorporating an additional element in the binary Mg-Ti system is to increase the stability of the metallic alloy, which, according to Van Mal's rule, is expected to destabilize the metal-hydrogen system. A model to calculate the effect on the thermodynamic stability of alloying metals was developed by Miedema and co-workers. Adopting this model offers the possibility to select promising elements beforehand. Al and Si were selected to impose a stabilization of the Mg-Ti system.

The electrochemical Galvanostatic Intermittent Titration Technique was used to obtain pressure-composition isotherms of these new ternary materials, which reveal a reversible hydrogen storage capacity of more than 6 wt.%. In line with the calculations, substitution of Mg and Ti by Al or Si indeed shifts the plateau pressure of a significant part of the isotherms to higher pressures, while remaining at room temperature.

It has been proven that, by controlling the chemistry of the metal alloy, the thermodynamic properties of Mg-based hydrides can be regulated over a wide range. Hence, the possibility to increase the partial hydrogen pressure while maintaining a high gravimetric capacity creates promising opportunities in the field of hydrogen storage materials, which are essential for the future hydrogen economy.[*]

---

[*] Part of this chapter is based on:

P. Vermeulen, E.F.M.J. van Thiel and P.H.L. Notten, *Ternary MgTiX-alloys: A promising route towards low temperature, high capacity, hydrogen storage materials*, Chem. Eur. J. **2008**, *13*, 9892-9898.

E.M.F.J. van Thiel, P.H.L. Notten and P. Vermeulen, *Hydrogen storage material for use in electronic equipment, comprises magnesium alloy, transition element, and element with hydride heat of formation higher than magnesium hydride*, Patent Nr. WO2008035310-A1, **2007**.

6.1 Introduction

In chapters 4 and 5 it was shown that by incorporating a small amount of Ti in a Mg matrix positively affects the kinetics of hydride uptake and release. Furthermore, the attractive storage capacity of MgH_2 was preserved to a large extent and the reversibility of hydrogen insertion and extraction was found to be robust. The Mg_yTi_{1-y} hydrides, however, all reveal more or less the same thermodynamic stability, which is considered to be too high for practical applications, *i.e.* the isotherms show a plateau around a hydrogen partial pressure of 10^{-6} bar at room temperature (which corresponds to 10^{-4} bar H_2 at 353 K), whereas for Fuel Cell applications a pressure of 1 bar H_2 at 353 K is required (see Table 1.1). The appealing kinetic properties of Mg_yTi_{1-y} make this material, however, a good starting-point for the development of more advanced, thermodynamically less stable, metal hydrides.

A mathematical model to calculate the effect of adding an additional element in a metallic compound on the thermodynamic stability was brought forward by Miedema *et al.*[1-3] Combined with Van Mal's rule of reversed stability it enables us to carefully select an element that is expected to enforce a destabilizing effect on the Mg-Ti-H system and, consequently, increases the partial hydrogen pressure.[4] Al and Si were selected by adopting this approach. Several ternary compositions were prepared and their hydrogen storage characteristics were determined electrochemically. The effects of incorporating Al and Si in the Mg-Ti lattice on the hydrogen storage properties are discussed in this chapter.

6.2 Results & discussion

In paragraph 2.3.1 it was shown that the plateau pressure of a metal hydride is related to its thermodynamic stability via the Van 't Hoff-equation (Eq. 2.4).[5,6] This equation shows that in order to increase P_{H_2}, the metal-hydrogen system can be destabilized by increasing ΔH_f. A possible route to destabilize a MH is by increasing the stability of the metallic compound. This principle is known as the rule of reversed stability, introduced by Van Mal *et al.*[4], which states that the more stable a metallic alloy is the less stable its hydride is expected to be. In equation form this rule is represented by

$$\Delta H_f(A_nB_mH_{a+b}) = n\Delta H_f(AH_a) + m\,\Delta H_f(BH_b) - \Delta H_f(A_nB_m) \qquad (6.1)$$

Where n and m are the atomic fractions of elements A and B. a and b depend on the atomic composition of the individual hydrides of A and B.

Van Mal's rule combined with the Miedema model enables us to select an element, which is expected to impose a destabilizing effect on the metal system (*i.e.* it increases the last term of Eq. 6.1), thus increasing the partial hydrogen pressure of the metal-hydrogen system. It is noteworthy that, although the composites of interest consist of three elements, the common binary approach of the Miedema model is chosen because of its simplicity. Consequently, the results are a first-order approximation and can only be dealt with qualitatively.

6.2.1 The Miedema model

The Miedema model uses different equations to determine ΔH_f for binary alloys between two non-transition metals and between a non-transition metal and a transition metal. The former is denoted as

$$\Delta H_f = \frac{2f\left(c_A V_A^{2/3} + c_B V_B^{2/3}\right)}{\left(n_{WS}^A\right)^{-1/3} + \left(n_{WS}^B\right)^{-1/3}} \cdot \left(-P\left(\Delta\varphi^*\right)^2 + Q\left(\Delta n_{WS}^{1/3}\right)^2\right) \tag{6.2}$$

where f accounts for the concentration dependence of ΔH_f for ordered compounds, V_A and V_B are the molar volumes of the elements inside the alloy, n_{WS}^A and n_{WS}^B are the electron densities of elements A and B at the boundary of their Wigner-Seitz cell. $\Delta\varphi^* = \varphi_A^* - \varphi_B^*$ represents the difference in electronegativity between elements A and B. P and Q are experimentally determined parameters and depend on the elements involved in the alloy.

The enthalpy of formation of an alloy consisting of a non-transition metal and a transition metal is described by

$$\Delta H_f = \frac{2Pf\left(c_A V_A^{2/3} + c_B V_B^{2/3}\right)}{\left(n_{WS}^A\right)^{-1/3} + \left(n_{WS}^B\right)^{-1/3}} \cdot \left(-\left(\Delta\varphi^*\right)^2 + \frac{Q}{P}\left(\Delta n_{WS}^{1/3}\right)^2 - \frac{R}{P}\right) \tag{6.3}$$

where *R/P* is the so-called hybridization term, which represents the degree of mixing of d-states of the transition metal with the s-state of the non-transition metal.

As the Mg-Ti-H system is characterized by a high gravimetric capacity only lightweight elements are regarded as promising substitutes. These elements should preferably be cheap and readily available. On the basis of these criteria Al and Si were selected and both offer the additional advantage that their individual hydrides are relatively unstable which is expected to impose a positive effect on the stability of the MgTiX (X = Al, Si) hydride. The values of the parameters required to calculate ΔH_f of the binary constituents of Mg-Ti doped with Al or Si are listed in Table 6.1.

Table 6.1 Parameters required for the Miedema model.[2]

Element	φ^* (V)	$n_{WS}^{1/3}$ ((d.u.)$^{1/3}$)	$V^{2/3}$ (cm^2)
Mg	3.45	1.17	5.8
Ti	3.65	1.47	4.8
Al	4.20	1.39	4.6
Si	4.70	3.38	4.2

The values for *P* are 10.6 and 12.3 for binary alloys of two non-transition metals and a transition metal with a non-transition metal, respectively. For all solid state alloys *Q/P* equals 9.4 V^2 (d.u.)$^{-2/3}$ and *R/P* for Mg-Ti, Al-Ti and Si-Ti equals 0.4, 1.9 and 2.1, respectively. The

results of the calculated enthalpy of formation for the various binary alloys are depicted in Fig. 6.1.

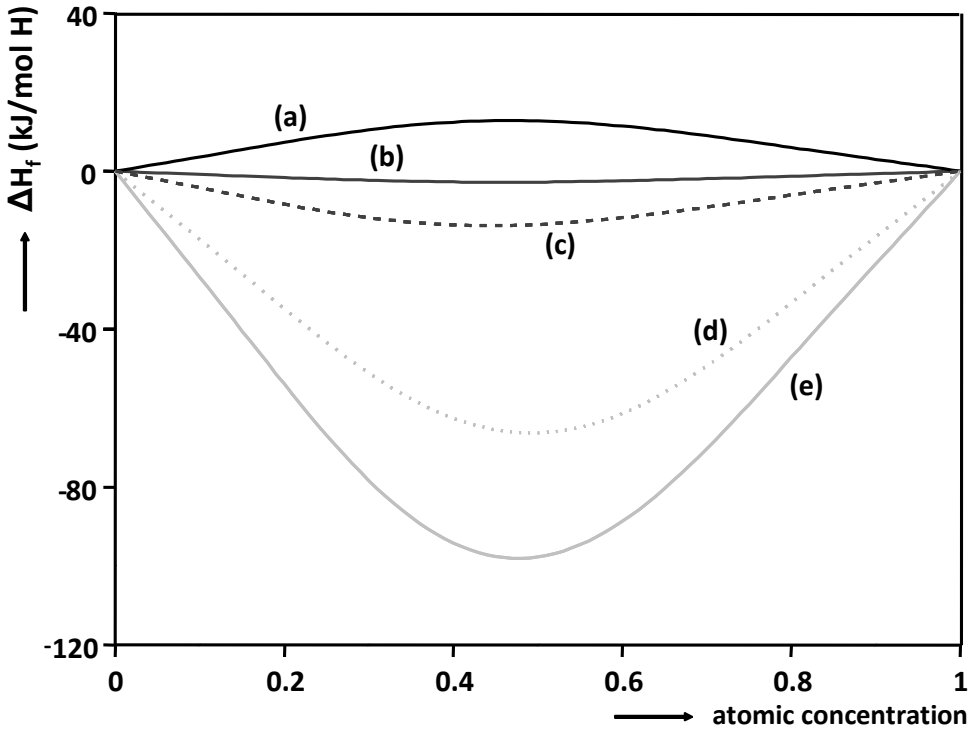

Fig. 6.1 ΔH_f as a function of composition for Mg in Ti (a), Mg in Al (b), Mg in Si (c), Ti in Al (d) and Ti in Si (e).

Fig. 6.1 shows that incorporating Al or Si in the Mg-Ti system (a) both stabilize the ternary alloy as Mg-Al (b), Mg-Si (c) and to an even larger extent Ti-Al (d) and Ti-Si (e) are characterized by a relatively low enthalpy of formation. The positive values of ΔH_f for the Mg-Ti system are in line with the literature as no intermetallics are reported for this particular alloy if standard alloying techniques are used.[7] However, using no-equilibrium techniques, like electron beam deposition and dc/rf magnetron co-sputtering, it is possible to obtain homogenous Mg-Ti alloys, which are regarded metastable (see chapter 4).

6.2.2 Thermodynamics of MgTiX hydride thin film electrodes

To verify if the partial hydrogen pressure indeed changes by incorporating Al and Si in the Mg-Ti crystal lattice, Pressure-Composition (PC) isotherms of these alloys are measured electrochemically using GITT (see paragraph 2.3.4). The GITT experiments were performed during dehydrogenation to avoid inaccuracies resulting from the hydrogen evolution reaction (see Eq. 2.14). Current pulses of + 12 μA (~100 mA/g) for a period corresponding to approximately 20 pulses to fully dehydrogenate the metal hydrides were used. As soon as the cut-off voltage of 0 V is reached, the GITT experiment is terminated to avoid oxidation of the electrode material. The measured equilibrium potentials are converted to hydrogen partial pressures using Eq. 2.19. Since conventional gas phase pressure-composition-temperature

(PCT) measurements are generally represented with increasing hydrogen content, the electrochemically determined isotherms here are plotted in accordance with this convention.

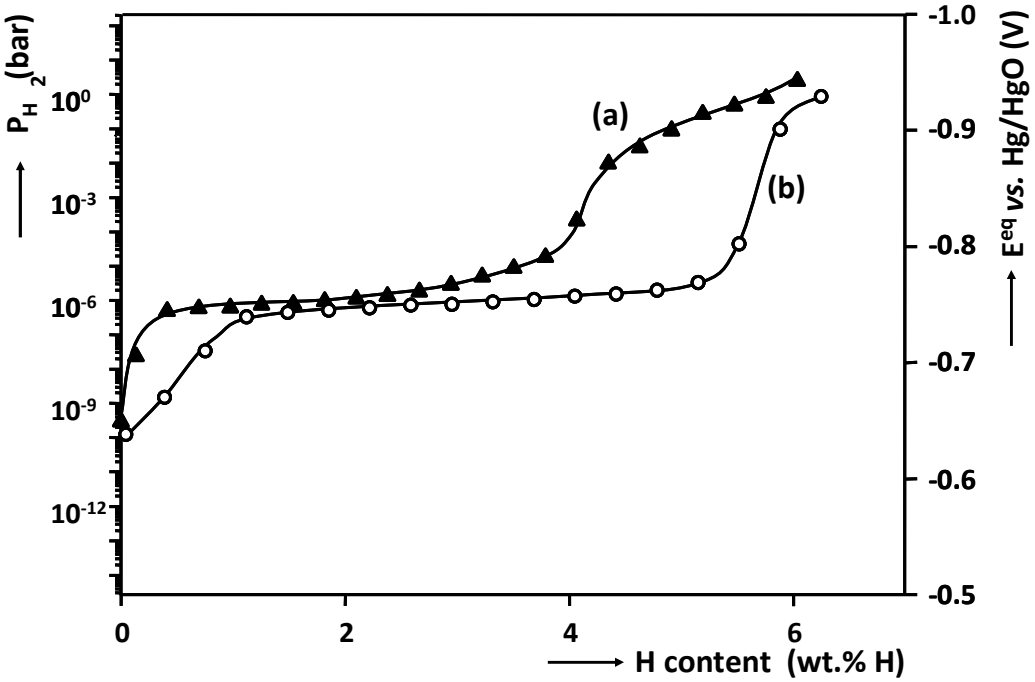

Fig. 6.2 Electrochemically determined dehydrogenation isotherms of 200 nm thick $Mg_{0.69}Ti_{0.21}Al_{0.10}$ (a) and $Mg_{0.80}Ti_{0.20}$ (b) thin films with a 10 nm Pd top-coat deposited on a quartz substrate by means of electron beam evaporation.

The isotherms of $Mg_{0.69}Ti_{0.21}Al_{0.10}$ and $Mg_{0.80}Ti_{0.20}$ thin films are depicted in Fig. 6.2. The latter is representative for Mg_yTi_{1-y} alloys within the range $0.70 \leq y \leq 0.85$ as they all reveal a single low pressure plateau (see Fig. 4.16). The isothermal curve of the $Mg_{0.69}Ti_{0.21}Al_{0.10}$ compound, on the other hand, shows two plateau-like regions, a plateau up to 4 wt.% H at ~10^{-6} bar and a second sloping plateau at higher pressures. Apparently, incorporating Al in the Mg-Ti lattice creates interstitial sites, which can be occupied by hydrogen, with a relatively positive enthalpy of formation. The occurrence of a second plateau suggests a second phase-transformation. Metal-hydrogen systems with 2 plateaus are not uncommon and were identified for the hydrides of $Mg_2CuAl_{0.375}$, $LaCo_6$, TiFe and $NdCo_5$.[8-11] However, for the Mg-Ti-Al-H system the isotherm interestingly shows a plateau close to atmospheric pressures at room temperature! Hence, it could be used to store and release hydrogen at low temperatures, which is of prime importance for most hydrogen-driven devices. It is noteworthy that the experimental setup limits the practical accessible partial hydrogen pressure to a maximum of 1 bar. Therefore, it is possible that the reversible hydrogen storage capacity is even larger than the indicated 6 wt.% H.

Adding Al to a metal-hydrogen system to increase P_{H_2} of MgH_2 has been reported by others.[12-18] However, for Mg-Al alloys it is generally observed that upon hydrogenation the alloys disproportionate under the formation of MgH_2 and Al. The PC isotherms of $Mg_{0.69}Ti_{0.21}Al_{0.10}$ and $Mg_{0.80}Ti_{0.20}$ depicted in Fig. 6.2 show an almost similar reversible H-capacity of approximately 6 wt.% H, which suggests that Al actively participates in the hydrogenation process and thus contributes to the overall hydrogen storage capacity. Note

that the hydrogen content in Fig. 6.2 corresponds to the amount that could be dehydrogenated at room temperature. These are not the absolute amount of hydrogen in the crystal lattice of the alloy as electrochemical measurements have indicated that part of the hydrogen is irreversibly bound. This observation is in accordance with the results of electrochemical (de)hydrogenation of Mg_yTi_{1-y} alloys discussed in chapter 4 and 5. The reversibility of hydrogen insertion and extraction amounts to approximately 10 cycles for the electrochemical experiments, which is similar as the Mg-Ti alloys. Hereafter, delamination is considered the cause of the declining capacity. It is therefore to be expected that the intrinsic reversibility of Mg-Ti-Al compounds, easily surpasses 100 cycles as was found for gas phase (de)hydrogenation of Mg-Ti alloys.[19]

The H-storage capacities for the proposed ternary systems are studied in more detail as a function of composition. Figures 6.3 and 6.4 show the results in combination with 3D fits obtained using a triangle-based linear interpolation Matlab® procedure (griddata). Note that the graphs are scaled to embed only the experimental range.

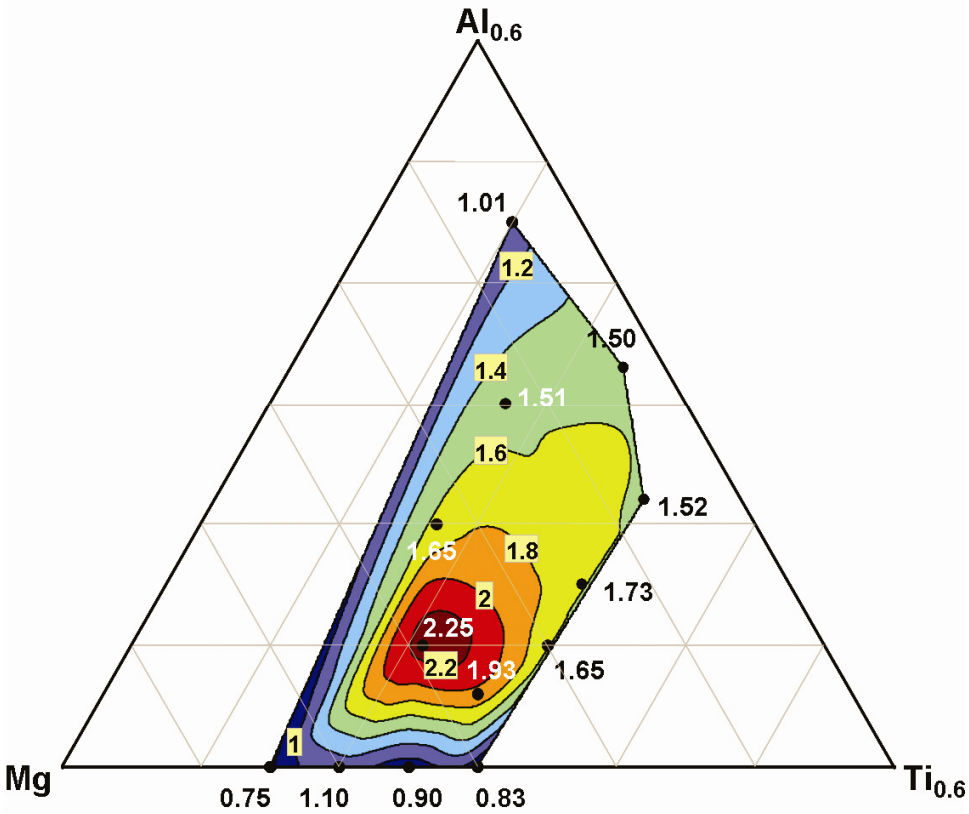

Fig. 6.3 Phase diagram showing the compositions measured experimentally (black dots) in combination with the width of the isotherm situated above the first plateau in wt.% H. The values in the framed yellow labels correspond to the calculated contour lines.

Fig. 6.3 shows the width of isotherm that is situated above the partial hydrogen pressure of the first plateau as a function of composition and allows the reader to see that even within a small composition range the width differs significantly. All experimental data points are indicated together with the contour lines obtained from the 3D-fit. It indeed shows that adding Al to a Mg-Ti alloy changes the position of the isothermal curve to a large extent. The composition characterized by the broadest plateau situated close to atmospheric pressures is

$Mg_{0.69}Ti_{0.21}Al_{0.10}$. This composition is positioned within the dark red area of Fig. 6.3 and, according to the fit, similar or potentially even broader plateaus are to be expected in this area.

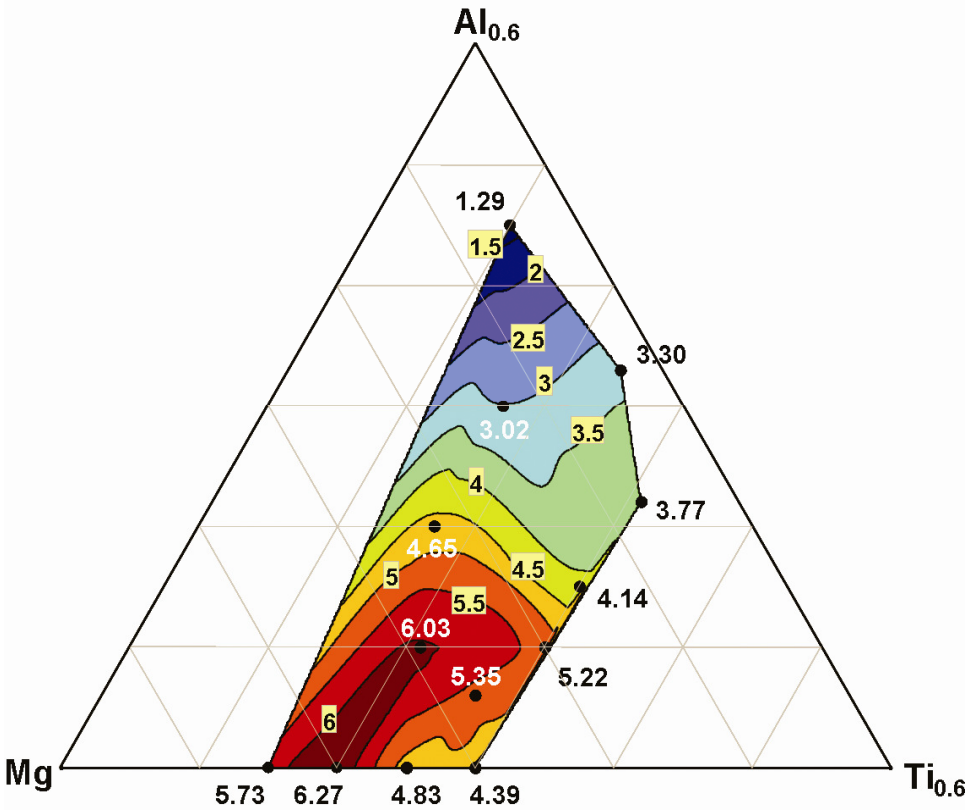

Fig. 6.4 Phase diagram showing the reversible gravimetric H-storage capacity as a function of composition (black dots) with the values representing the gravimetric capacity given in wt.% H. The values corresponding to the contour lines are depicted in the framed yellow labels.

Fig. 6.4 depicts the reversible gravimetric capacity of $Mg_yTi_zAl_{(1-y-z)}$ as a function of composition. It shows that incorporating Al in the Mg-Ti lattice leads to a decrease of the reversible capacity. Similar results were found for Mg-Ti-Al systems reported by Lupu *et al.*[20] However, the compounds they investigated have a rather high Al content and, as Fig. 6.4 clearly indicates, this leads to a low reversible hydrogen capacity as opposed to the Mg-rich alloys presented here. If only 10 at.% Al is incorporated in Mg-Ti compounds with a high Mg-content does not seem to significantly affect the reversible capacity. The declining capacity at high Al contents could be due to kinetic restrictions imposed by the material. These restrictions might be related to an unfavorable crystal structure of the metal hydride. In chapter 4 and 5 it was shown that for $Mg_yTi_{1-y}H_x$ systems the kinetics of the hydrogen insertion and extraction are largely dominated by the Mg-content. In more detail, if the metal hydride crystallizes into the body centered tetragonal MgH_2 structure the H-transport properties are dramatically inhibited, while the kinetics is very favorable for face centered cubic-structured $Mg_yTi_{1-y}H_x$ alloys.

From Figs. 6.3 and 6.4 it can be concluded that only within a small region possible improvements of the reversible H content at low temperatures are expected. It is therefore

noteworthy that significant enhancements are foreseen only by incorporating a fourth element.

In the previous section it was shown that Al, in line with calculations based on the Miedema model, can advantageously affect the position of the isothermal curve in comparison to Mg-Ti alloys. The Miedema model shows that not only Al but also Si could bring about these improvements (see Fig. 6.1). Two Si-containing Mg-Ti compounds were experimentally investigated to verify if indeed the isotherm is influenced. The results are shown in Fig. 6.5. Note that these results are preliminary results without searching for the most optimal composition.

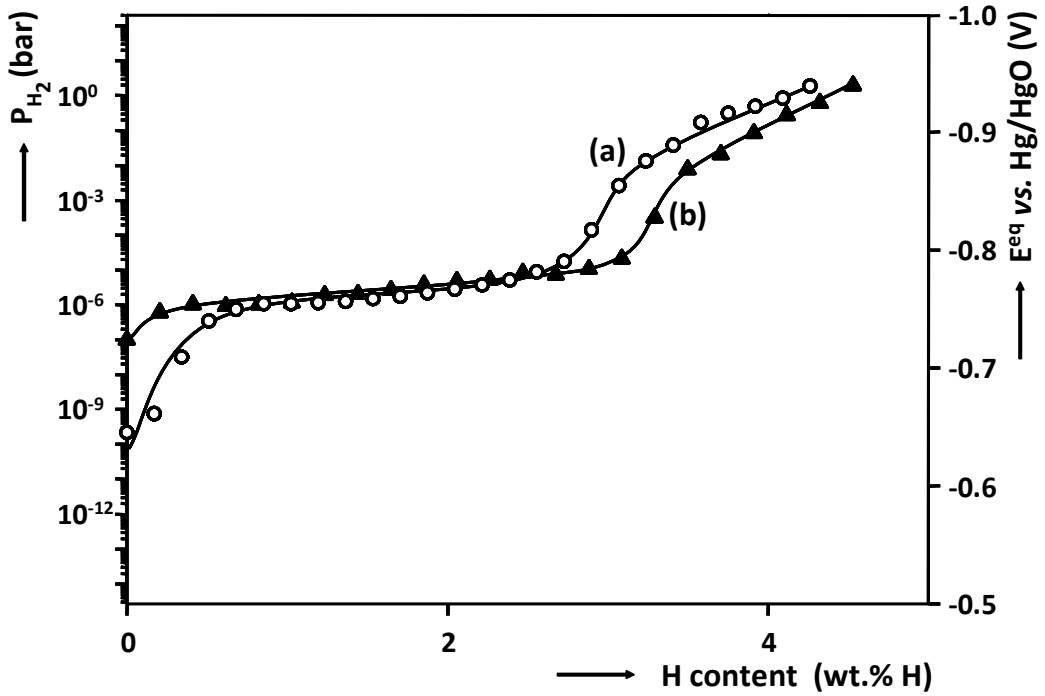

Fig. 6.5 The isothermal curves of 200 nm thick $Mg_{0.55}Ti_{0.35}Si_{0.10}$ (a) and $Mg_{0.69}Ti_{0.21}Si_{0.10}$ (b) films capped with 10 nm Pd.

In Fig. 6.5 it is apparent that incorporating Si clearly affects the position of the isotherms compared to Mg-Ti alloys (Fig. 4.16). For the Mg-Ti-Si alloys a similar shape is found as is observed for MgTiAl (see Fig. 6.2). P_{H_2} increases steeply at approximately 2.75 wt.% H and reaches soon a sloping plateau. This plateau is, similar to Al-addition, situated close to atmospheric pressures. The gravimetric reversible storage capacities of $Mg_{0.55}Ti_{0.35}Si_{0.10}$ and $Mg_{0.69}Ti_{0.21}Si_{0.10}$ at room temperature are 4.26 and 4.53 wt.%, respectively. These are somewhat lower compared to the Al-containing alloys because Si is slightly heavier. As the results are similar to Al addition, the degree of destabilization of the MgTi alloy does not seem to be influenced significantly by the chemistry of the dopant. Furthermore, it shows that the Miedema model can, as a first-order approximation, be used to screen for elements that destabilize a known metal hydrogen system.

6.3 Conclusions

Mg_yTi_{1-y} alloys are characterized by isothermal curves with plateau pressures of ~10^{-6} bar at room temperature. Increasing the plateau pressure of a metal-hydrogen system can be accomplished by destabilization of the metal hydride. The Miedema model was used to screen elements that stabilize the metallic Mg-Ti system and, consequently, destabilize the metal-hydrogen systems. Al and Si were selected to enforce this effect with the additional advantage that these elements are lightweight in order to maintain the high gravimetric capacity found for Mg_yTi_{1-y} alloys.

Using GITT, the pressure-composition isotherms of several $Mg_yTi_zAl_{(1-y-z)}$ and $Mg_yTi_zSi_{(1-y-z)}$ alloys were determined. The results clearly show that, in line with the results using the Miedema model, the plateau pressure is increased, while maintaining a high gravimetric storage capacity of approximately 6 wt.%. The partial hydrogen pressures of part of the isotherms of the new ternary systems are situated at higher pressures at room temperature. This enables hydrogen storage and release at low temperatures, which is required for many hydrogen-driven devices. The isothermal curves of Mg-Ti-Al and Mg-Ti-Si closely resemble each other and imply that the degree of destabilization does not strongly depend on the chemical properties of the dopants. Hence, in line with Van Mal's rule of reversed stability, destabilization of the MH seems to depend on the thermodynamics of the dopant with the host lattice.

Finally, the possibility to increase the partial hydrogen pressure while maintaining a high gravimetric capacity creates promising opportunities in the field of hydrogen storage, which are vital to ensure the feasibility of a future hydrogen economy.

6.4 References

1 A.R. Miedema, P.F. de Châtel and F.R. de Boer, *Cohesion in alloys – fundamentals of a semi-empirical model*, Physica B **1980**, *100*, 1-28.

2 A.R. Miedema, *Electronegativity parameter for transition-metals – heat of formation and charge-transfer in alloys*, J. Less-common Met. **1973**, *32*, 117-136.

3 F.R. de Boer, R. Boom, W.C.M. Mattens, A.R. Miedema and A.K. Niessen, *Cohesion in Metals*, North-Holland, Amsterdam **1988**.

4 H.H. van Mal, K.H.J. Buschow and A.R. Miedema, *Hydrogen absorption in $LaNi_5$ and related compounds – experimental observations and their explanation*, J. Less-common Met. **1974**, *35*, 65-76.

5 K.H.J. Buschow, P.C.P Bouten, A.R. Miedema, *Hydrides formed from intermetallic compounds of two transition metals: a special class of ternary alloys,* Rep. Prog. Phys. **1982**, *45*, 937-1039.

6 R. Griessen and T. Riesterer, *Topics in Applied Physics Hydrogen in Intermetallic Compounds*, *Chapter 6: Heat of Formation Models*, Vol. 63 (Ed. L. Schlapbach), Springer-Verlag, Berlin, **1988**, 219-284.

7 P. Villars (Edt), *Pearson's Handbook Desk Edition*, Vol. 2, p. 2336, ASM International, **1997**.

8 A. Biris, D. Lupu, R.V. Bucur, E. Indrea, G. Borodi and M. Bogdan, *The influence of aluminum on the properties of the Mg_2Cu-H_2 system*, Int. J. Hydrogen Energy **1982**, *7*, 89-94.

9 F.A. Kuijpers, *Investigation on $LaCo_5$-H and $CeCo_5$-H systems*, J. Less-common Met. **1972**, *27*, 27-34.

10 J.J. Reilly and R.H. Wiswall, Jr., *Formation and properties of iron titanium hydride*, Inorg. Chem. **1974**, *13*, 218-222.

11 M. Yamaguchi, T. Katamune and T. Ohta, *Magnetic-behavior of metal-hydrides as a function of hydrogen pressure and composition*, J. Appl. Phys. **1982**, *53*, 2788-2792.

12 M.H. Mintz, Z. Gavra and G. Kimmel, *The reaction of hydrogen with magnesium alloys and magnesium intermetallic compounds*, J. Less-common Met. **1980**, *74*, 263-270.

13 A. Zaluska, L. Zaluski and J.O. Strom-Olsen, *Structure, catalysis and atomic reactions on the nano-scale: a systematic approach to metal hydrides for hydrogen storage,* Appl. Phys. A **2001**, *72*, 157-165.

14 S. Bouaricha, J.P. Dodelet, D. Guay, J. Huot, S. Boily and R. Schulz, *Hydriding behavior of Mg-Al and leached Mg-Al compounds prepared by high-energy ball-milling*, J. Alloys Compd. **2000**, *297*, 282-293.

15 H. Takamura, T. Miyashita, A. Kamegawa and M. Okada, *Grain size refinement in Mg-Al-based alloy by hydrogen treatment*, J. Alloys Compd. **2003**, *356-357*, 804-808.

16 L. Pranevicius, D. Milcius, L.L. Pranevicius and G. Thomas, *Plasma hydrogenation of Al, Mg and MgAl films under high-flux ion irradiation at elevated temperature*, J. Alloys Compd. **2004**, *373*, 9-15.

17 A. Andreasen, M.B. Sørensen, R. Burkarl, B. Møller, A.M. Molenbroek, A.S. Pedersen, J.W. Andreasen, M.M. Nielsen and T.R. Jensen, *Interaction of hydrogen with an Mg-Al alloy*, J. Alloys Compd. **2005**, *404-406*, 323-326.

18 R. Gremaud, A. Borgschulte, C. Chacon, J.L.M. van Mechelen, H. Schreuders, A. Züttel, B. Hjörvarsson, B. Dam and R. Griessen, *Structural and optical properties of $Mg_xAl_{1-x}H_y$ gradient thin films: a combinatorial approach*, Appl. Phys. A **2006**, *84*, 77-85.

19 M. Slaman, B. Dam, M. Pasturel, D.M. Borsa, H. Schreuders, J.H. Rector and R. Griessen, *Fiber optic hydrogen detectors containing Mg-based metal hydrides*, Sens. Actuators B **2007**, *123*, 538-545.

20 D. Lupu, A. Biris, R.V. Bucur, E. Indrea and M. Bogdan, *Hydrogen absorption in aluminium-magnesium-titanium alloys*, Met.-Hydrogen Syst., Proc. Miami Int. Symp., Meeting Date 1981, **1982**, 437-443.

Summary

Hydrogen storage in Mg-Ti thin film alloys
An *in situ* characterization study

Depleting fossil fuel reserves and growing climate threats urge us towards a sustainable society. Moreover, we should preferably not solely rely on fossil fuels for our primary energy needs as part of the fossil fuels is imported from politically unstable regions. We should therefore think of new ways to ensure our energy needs are met in the near future. Most likely, a mixture of different sources will be used. These resources are preferable renewable in nature, *e.g.* solar, biomass, wind, water and geothermal, which can typically be used for stationary applications. For mobile applications, however, the use of an on-board energy storage system is indispensible. Especially for the latter, hydrogen is expected to play a dominant role. One of the important aspects of hydrogen is that only environmentally friendly products are emitted in the exothermic reaction of hydrogen with oxygen in a fuel cell. However, the feasibility of hydrogen production, storage and finally the use in fuel cells are still under debate.

In prototype applications, such as fuel cell-driven automobiles, hydrogen is generally stored in high-pressure cylinders. New lightweight composite cylinders have been developed that are capable of withstanding pressures of up to 800 bars. Even though hydrogen cylinders are expected to withstand even higher pressures in the near future, their large volumes and the energy required to compress hydrogen will limit their practical applicability. As opposed to storing molecular hydrogen it can also be stored atomically in a metal hydride (MH), which can reduce the volume significantly. In addition, MHs provide relatively safe storage as they can be handled without extensive safety precautions unlike, for example, compressed hydrogen gas.

Currently, the foremost problem of solid state hydrogen storage is to find a metal-hydrogen system with a gravimetric capacity that exceeds 6 wt.% H and absorbs/desorbs hydrogen at atmospheric pressures at ambient temperatures. One of the most promising elements that can reversible absorb and desorb a significant amount of hydrogen is magnesium, which has an intrinsic gravimetric storage capacity of 7.7 wt.% H. In spite of its excellent gravimetric storage capacity, the high desorption temperature (279 °C) and extremely slow hydrogen (de)sorption kinetics prevent Mg from being employed commercially. Mg is, however, often a large constituent of new hydrogen storage materials as it lowers the weight of the material and therefore increases the gravimetric capacity, which is necessary to fulfill the weight restrictions. In this thesis the hydrogen storage characteristics of Mg alloyed with other metals are addressed. The primary aim is to enforce a high absorption and desorption rate, and limit the weight of the alloys.

Chapter 2 describes the experimental settings of the thin films preparation methods and characterization techniques. The thin films were prepared by means of electron beam deposition and magnetron co-sputtering and hereafter investigated by means of Rutherford Backscattering Spectroscopy to accurately determine the film thickness and composition.

Electrochemistry was used as the main tool to investigate the hydrogen storage properties of the films in detail. One of the advantages of using electrochemistry is that the electrochemical equilibrium potential can be used to calculate the equivalent hydrogen partial pressure, which gives information about the thermodynamics of the metal-hydrogen system. The electrochemical setup is not straightforward as it requires a special three-electrode setup to obtain reliable experimental data. The experimental pitfalls and solutions, like for instance the need of an oxygen scrubber, to avoid incorrect electrochemical analyses are described in detail. By applying a fixed current, which is equivalent to a fixed (de)hydrogenate rate, the possibility to rapidly insert or extract hydrogen from the hydrogen absorbing medium can be addressed. Electrochemical control also offers the possibility to calculate and tune the hydrogen content in the films with high precision. The former was used to determine if the materials are interesting from a gravimetric point-of-view, while the latter was adopted in combination with other characterization techniques, like for example X-ray diffraction, which provides new insights into the effects of the hydrogen content on the host material. The theoretical background and experimental settings of several electrochemical techniques, *e.g.* amperometry, cyclic voltammetry, Galvanostatic Intermittent Titration Technique and impedance spectroscopy, were discussed. X-ray diffraction was used throughout the thesis to resolve the crystallography of the phases in the as-prepared samples. To acquire crystallographic data as a function of the hydrogen content custom made *in situ* X-ray diffraction setups were used. The theoretical background of X-ray diffraction and a detailed description of the experimental setups and settings are described.

A Pd topcoat is often applied to hydride-forming thin film materials to protect them from oxidation and catalyze the dissociation of H_2 or electrocatalyze the reduction of H_2O. As a 10 nm Pd caplayer was applied to all Mg-based alloys described in this thesis, it is useful to determine its thermodynamic and electrocatalytic properties separately, which is presented in Chapter 3.

A lattice gas model was presented recently and successfully applied to simulate the absorption/desorption isotherms of various hydride-forming materials. The simulation results are expressed by parameters corresponding to several energy contributions, *e.g.* interaction energies. The use of a model-system is indispensable in order to show the strength of these simulations. The palladium-hydrogen system is one of the most thoroughly described metal hydrides found in the literature and is therefore ideal for this purpose. The effects of decreasing the Pd thickness on the pressure-composition isotherms were monitored experimentally and subsequently simulated. An excellent fit of the lattice gas model to the experimental data was obtained and the corresponding parameters were used to describe several thermodynamic properties. It was found that the contribution of H-H interaction energies to the total energy and the influence of the host lattice energy are significantly and systematically changing as a function of Pd thickness. Conclusively, it was verified that the lattice gas model is a useful tool to analyze the thermodynamic properties of hydrogen storage materials.

Also, the electrocatalytic properties of a 10 nm thick Pd film were determined by means of electrochemical impedance spectroscopy, which revealed that the best electrocatalytic properties are found for β-phased Pd hydride. Determining the properties of a single-layer 10 nm thick Pd film was valuable as it was used to determine its influence on the Pd-coated Mg-based thin film alloys that were the topic of investigation for the remainder of the thesis.

Recently, a thin film approach revealed that new lightweight alloys of Mg with Ti, V or Cr can be prepared that cannot be synthesized via standard alloying techniques, because the alloys are thermodynamically unstable. Electrochemical measurements showed that especially the Mg-Ti system possesses the ability to reversibly store a considerable amount of hydrogen, which can be absorbed and desorbed at relatively high rates compared to pure Mg. The systematic investigation of hydrogen storage properties of the binary Mg_yTi_{1-y} alloy composition is described in Chapter 4.

It is shown from X-ray diffraction (XRD) measurements that as-prepared electron-beam deposited and sputtered Mg_yTi_{1-y} thin films with *y* ranging from 0.50 to 1.00 are crystalline and single-phase. Galvanostatic (de)hydrogenation measurements were performed to unveil the effects of the Mg-to-Ti ratio on the hydrogen absorption and desorption rates. Increasing the Ti-content up to 15 at.% does not change these rates much and hydrogen can only be desorbed at a relatively low rate. Beyond 15 at.% Ti, however, the hydrogen desorption rate increases substantially. A superior reversible hydrogen storage capacity that exceeds 6 wt.% H, along with excellent hydrogen absorption and desorption rates, was found for the $Mg_{0.80}Ti_{0.20}$ alloy. The close analogy of the electrochemical behavior of Mg_yTi_{1-y} and Mg_ySc_{1-y} alloys points to a face-centered cubic-structured hydride for the alloys showing fast hydrogen uptake and release rates, whereas for the hydrides of alloys rich in Mg (>80 at.%), that show a slow desorption rate, probably crystallize into the common MgH_2 body-centered tetragonal structure. The cycling stability of electron-beam deposited and sputtered thin film $Mg_{0.80}Ti_{0.20}$ alloys was found to be constant over the first 10 cycles, hereafter it decreased sharply caused by delamination of the film from the substrate. The intrinsic cycling stability is therefore expected to be higher. Isotherms of Mg_yTi_{1-y} thin films showed that the desorption plateau pressure is not strongly affected by the Mg-to-Ti ratio and is almost equal to the equilibrium pressure of the magnesium-hydrogen system. Impedance analyses showed that the surface kinetics can be fully attributed to the Pd-topcoat. The impedance, when the Mg_yTi_{1-y} thin film electrodes are in their hydrogen-depleted state, was found to be dominated by the transfer of hydrogen across the Pd/Mg_yTi_{1-y} interface.

In Chapter 4 it was argued that the symmetry of the crystal lattice of the host material probably strongly affects the hydrogen uptake and release rates. The largest difference for the (de)hydrogenation rates was found for Mg_yTi_{1-y} alloys containing 70 to 90 at.% Mg. Therefore, the crystallography of these alloy compositions was resolved by *in situ* XRD and the results are presented in Chapter 5. Firstly, i*n situ* gas phase XRD measurements were performed to identify the crystal structures of as-deposited and hydrogenated Mg_yTi_{1-y} thin film alloys. The preferred crystallographic orientation of the films in both the as-prepared and hydrogenated state made it difficult to unambiguously identify the crystal structure and therefore the identification of the symmetry of the unit cells was achieved by *in situ* recording XRD patterns at various tilt angles. The results reveal a hexagonal closed packed structure for all alloys in the as-deposited state. Hydrogenating the layers under 1 bar H_2 transforms the unit cell into face-centered cubic for the $Mg_{0.70}Ti_{0.30}$ and $Mg_{0.80}Ti_{0.20}$ compounds, whereas the unit cell of hydrogenated $Mg_{0.90}Ti_{0.10}$ has a body-centered tetragonal symmetry. The (de)hydrogenation kinetics changes along with the crystal structure of the hydrides from rapid for face-centered cubic-structured hydrides to sluggish for hydrides with a body-centered tetragonal symmetry and emphasized the influence of the symmetry of the crystal lattice on the hydrogen transport properties.

Subsequently, the experimental results of *in situ* electrochemical X-ray diffraction are discussed. The main advantage of electrochemical control is that it can be used to systematically increase or decrease the hydrogen content, which in combination with X-ray diffraction was used to monitor the effects of the hydrogen content on the phase composition and structure of Mg_yTi_{1-y} thin film alloys with y=0.70, 0.80 and 0.90. The X-ray diffraction patterns and electrochemical results of $Mg_{0.70}Ti_{0.30}$ and $Mg_{0.80}Ti_{0.20}$ point towards a host lattice with distinct Ti-poor and Ti-rich regions, whereas the $Mg_{0.90}Ti_{0.10}$ alloy shows the properties of a randomly mixed alloy.

In the search for hydrogen storage materials with a high gravimetric capacity, thin film Mg_yTi_{1-y} alloys, which according to the experimental results discussed in Chapter 4 exhibit excellent kinetic properties, form the basis for more advanced compounds. The plateau pressure of the Mg-Ti hydride system is very low (approximately 10^{-6} bar at room temperature). A way to increase this pressure is by destabilizing the metal hydride and this was enforced by incorporating an additional element in the binary Mg-Ti system. According to Van Mal's rule of reversed stability, any additional element that stabilizes the metallic alloy should destabilize the metal-hydrogen system. A model to calculate the effect on the thermodynamic stability of alloying metals was developed by Miedema and co-workers. Adopting this model offers the possibility to select promising elements beforehand. Al and Si were selected to impose a stabilization of the Mg-Ti system. The electrochemical Galvanostatic Intermittent Titration Technique was used to obtain pressure-composition isotherms of these new ternary materials. In line with the calculations, substitution of Mg and Ti by Al or Si indeed shifts the plateau pressure of a significant part of the isotherms to higher pressures, while remaining at room temperature. Moreover, part of the ternary alloys has a reversible hydrogen storage capacity that exceeds the restrictions on the gravimetric capacity. Conclusively, it was been proven that, by controlling the chemistry of the metal alloy, the thermodynamic properties of Mg-based hydrides can be regulated over a wide range. Hence, the possibility to increase the partial hydrogen pressure while maintaining a high gravimetric capacity creates promising opportunities in the field of hydrogen storage materials, which are essential for the future hydrogen economy to become feasible.

Samenvatting

Waterstofopslag in Mg-Ti dunne film legeringen
Een *in situ* karakteriseringsstudie

Het opraken van de fossiele brandstoffen en toenemende klimaatsveranderingen sporen ons aan naar een duurzame samenleving. Ook moeten we bij voorkeur niet alleen afhankelijk zijn van fossiele brandstoffen voor onze primaire energiebehoeften, omdat een deel afkomstig is van politiek instabiele regio's. Daarom moeten we andere manieren bedenken om onze energiebehoeften voor de nabije toekomst veilig te stellen. Hoogstwaarschijnlijk zal dit bestaan uit een combinatie van verschillende energiebronnen. Deze bronnen zijn bij voorkeur duurzaam, voorbeelden hiervan zijn zonne-energie, energie uit biomassa, windenergie en geothermische energie. Deze kunnen vooral worden gebruikt voor vaste toepassingen. Voor mobiele toepassingen is het echter een vereiste dat de energie kan worden opgeslagen en meegenomen. Verwacht wordt dat waterstof voornamelijk voor mobiele toepassingen een belangrijke rol zal spelen. Eén van de belangrijkste aspecten van waterstof is dat alleen milieuvriendelijke afvalstoffen worden gevormd in de exothermische reactie van waterstof met zuurstof in een brandstofcel. Echter, de haalbaarheid van waterstofproductie, de opslag ervan en uiteindelijk het gebruik in een brandstofcel is nog steeds aan debat onderhevig.

In prototype toepassingen, zoals een auto aangedreven door de elektriciteit die wordt opgewekt in een brandstofcel, wordt waterstof vaak onder hoge druk opgeslagen in gascilinders. Nieuwe lichte composiet gascilinders zijn ontworpen en kunnen een druk tot 800 bar verdragen. Hoewel verwacht wordt dat deze cilinders in de nabije toekomst waterstof zelfs bij hogere drukken kunnen opslaan, zal hun grote volume en de energie die nodig is om waterstofgas te comprimeren hun praktische toepasbaarheid sterk verhinderen. In tegenstelling tot het opslaan van moleculair waterstof kan het ook worden atomair worden opgeslagen als een metaalhydride. Hierdoor neemt het opslagvolume drastisch af en tevens bieden metaalhydrides een relatief veilige manier om waterstof op te slaan, aangezien ze zonder omvangrijke veiligheidsvoorzieningen kunnen worden toegepast, dit in tegenstelling tot bijvoorbeeld gecomprimeerd waterstofgas.

Momenteel is het voornaamste probleem van waterstofopslag in een metaalhydride het vinden van een metaalhydride-systeem dat aan de gravimetrische eis van tenminste 6 gewichtsprocent voldoet en waterstof tevens bij atmosferische drukken en lage temperaturen ab- en desorbeerd. Eén van de meest veelbelovende elementen is magnesium, dat een intrinsieke opslagcapaciteit van 7.7 gewichtprocent waterstof heeft. Ondanks deze uitstekende gravimetrische opslagcapaciteit wordt de toepasbaarheid van Mg in commerciële toepassingen sterk verhinderd door de hoge desorptietemperatuur (279 °C), lage plateaudruk en extreem trage ab- en desorptiekinetiek. Mg is echter vaak een grote component van nieuwe waterstofopslagmaterialen, omdat Mg het gewicht verlaagt en daardoor de gravimetrische capaciteit verhoogt hetgeen nodig is om aan de gewichtsbeperkingen te voldoen. In dit proefschrift worden de waterstofopslageigenschappen van puur Mg en van Mg dat gelegeerd is met andere metalen beschreven. De primaire doelstellingen zijn het behalen van een hoge ab- en desorptiesnelheid, het verlagen van de desorptietemperatuur en het beperken van het gewicht van de legering.

Hoofdstuk 2 beschrijft de experimentele instellingen van het vervaardigen en karakteriseren van dunne films. Deze films werden gemaakt door middel van elektronenbundel-depositie en magnetron co-sputteren en hierna onderzocht met Rutherford Backscattering Spectroscopie om de laagdikte en compositie nauwkeurig te bepalen.

Elektrochemie werd gebruikt als voornaamste techniek om de waterstofopslageigenschappen van de films in detail te bestuderen. Eén van de voordelen van het gebruik van elektrochemie was dat de elektrochemische evenwichtpotentiaal kon worden gebruikt om de equivalente waterstofpartiaaldruk, welke informatie gaf over de thermodynamica van het metaal-waterstof systeem, te berekenen. De elektrochemische opstelling was niet eenvoudig aangezien een speciale 3-elektroden opstelling moest worden gebruikt om betrouwbare resultaten te krijgen. De experimentele valkuilen en oplossingen, zoals een noodzakelijke opstelling voor de verwijdering van zuurstof, om foutieve elektrochemische analysen te voorkomen, worden in detail beschreven. Het aanleggen van een vaste stroom, dat equivalent is aan een vaste ab- en desorptiesnelheid, bood de mogelijkheid om vast te stellen of het waterstofabsorberende medium in staat was snel waterstof op te nemen of af te staan. Tevens boden elektrochemische analysen de mogelijkheid om de waterstofconcentratie in de films met hoge nauwkeurigheid te berekenen en te reguleren. Het berekenen van de waterstofconcentratie werd gebruikt om vast te stellen of de materialen interessant waren vanuit een gravimetrisch oogpunt, terwijl het reguleren van de waterstofconcentratie werd gebruikt in combinatie met andere analysetechnieken, zoals röntgendiffractie, dat nieuwe inzichten gaf in de effecten van de waterstofhoeveelheid op het waterstofopslagmateriaal. De theoretische achtergronden en experimentele instellingen van verschillende elektrochemische methodes, bijvoorbeeld amperometrie, cyclische voltametrie, galvanostatische intermitterende titratie techniek en impedantiespectroscopie, worden behandeld. Röntgendiffractie werd door het gehele proefschrift gebruikt om de kristallografie van de fasen in de gedeponeerde samples te bepalen. Om kristallografische data als functie van de waterstofconcentratie te verkrijgen werd gebruik gemaakt van speciale röntgendiffractieopstellingen. De theoretische achtergrond van röntgendiffractie en een gedetailleerde beschrijving van de experimentele opstellingen en instellingen worden beschreven.

Een Pd toplaag wordt vaak toegepast bij hydridevormende dunne films om ze te beschermen tegen oxidatie en voor het katalyseren van waterstofdissociatie of het elektrokatalyseren van waterreductie. Omdat een 10 nm dikke Pd toplaag wordt toegepast bij alle Mg-gebaseerde legeringen beschreven in dit proefschrift is het nuttig om de thermodynamische en elektrokatalytische eigenschappen afzonderlijk te bepalen en worden behandeld in hoofdstuk 3.

Een kristalrooster gas model werd recent gepresenteerd en succesvol toegepast om de absorptie/desorptieisothermen van verscheidene hydridevormende materialen te simuleren. De simulatieresultaten worden uitgedrukt door parameters die overeenkomen met verschillende energiebijdragen, bijvoorbeeld interactie-energieën. Het gebruik van een modelsysteem is zeer belangrijk om de kracht van deze simulaties aan te tonen. Het palladium-waterstof systeem is één van de meest grondig bestudeerde metaalhydrides en daardoor ideaal voor dit doel. De effecten van het verlagen van de Pd laagdikte op de druk-compositie isothermen werd experimenteel bepaald en vervolgens gesimuleerd. Een zeer goede fit tussen het kristalrooster gas model en de experimentele data werd gevonden en

de overeenkomstige parameters werden gebruikt om verscheidene thermodynamische eigenschappen te beschrijven. Gevonden werd dat de bijdrage van de H-H interactie-energieën op de totale energie en de invloed van de kristalroosterenergie significant zijn en systematisch veranderen als functie van de Pd dikte. Tenslotte werd het gebruik van het kristalrooster gas model als nuttige toepassing om de thermodynamische eigenschappen van waterstofopslagmaterialen te bepalen bevestigd.

Ook werden de elektrokatalytische eigenschappen van een 10 nm dikke Pd film bepaald, gebruikmakende van elektrochemische impedantiespectroscopie en deze studie toonde aan dat de beste elektrokatalytische eigenschappen werden gevonden voor β-Pd hydride. Het bepalen van de eigenschappen van enkel een 10 nm dikke Pd film was nuttig, omdat het gebruikt kan worden om de invloed van een Pd toplaag op de eigenschappen van Mg-gebaseerde dunne film legeringen, die centraal staan in het resterende deel van dit proefschrift, te bepalen.

Recentelijk werd getoond dat nieuwe lichte legeringen bestaande uit Mg en Ti, V of Cr kunnen worden gemaakt d.m.v. een dunne film methode, terwijl deze niet kunnen worden gesynthetiseerd via standaard legeringstechnieken, omdat ze namelijk thermodynamisch instabiel zijn. Elektrochemische metingen toonden aan dat met name het Mg-Ti systeem de mogelijkheid biedt om een aanzienlijke hoeveelheid waterstof reversibel op te slaan en dat dit, vergeleken met puur Mg, met relatief hoge ab- en desorptiesnelheden kan worden gedaan. Het systematische onderzoek van de waterstofopslageigenschappen van binaire Mg_yTi_{1-y} legeringen wordt beschreven in hoofdstuk 4.

Röntgendiffractiemetingen toonden aan dat de elektronenbundel gedeponeerde en gesputterde Mg_yTi_{1-y} dunne films met $0.50 \leq y \leq 1.00$ kristallijn en éénfasig zijn. Galvanostatische (de)hydrogeneringsmetingen werden uitgevoerd om de effecten van de Mg:Ti ratio op de waterstofabsorptie en desorptiesnelheden te onthullen. Verhoging van het Ti-gehalte tot 15 at.% veranderde deze snelheden nauwelijks en waterstof kon enkel bij een relatief lage snelheid worden onttrokken. Echter, het vermogen om de materialen met een hoge snelheid te dehydrogeneren nam drastisch toe vanaf een Ti-gehalte van 15 at.%. Een superieure reversibele waterstofopslagcapaciteit van meer dan 6 gewichtsprocent waterstof en uitstekende waterstofabsorptie en desorptiesnelheden werden gevonden voor de $Mg_{0.80}Ti_{0.20}$ legering. Deze afhankelijkheid was nagenoeg gelijk aan die van de Mg_ySc_{1-y} dunne films en dit suggereerde dat deze afhankelijk is toe te schrijven aan de kristalstructuur van het hydride: legeringen met snelle absorptie en desorptiesnelheden hebben een kubisch vlakkengecentreerd metaalrooster, terwijl Mg-rijke legeringen (>80 at.%) met een trage desorptiesnelheid hoogstwaarschijnlijk de gebruikelijke MgH_2 tetragonale lichaamsgecentreerde structuur aannemen. Opeenvolgende belaad- en ontlaadcycli werden gebruikt om de stabiliteit van elektronenbundel gedeponeerde en gesputterde $Mg_{0.80}Ti_{0.20}$ dunne film legeringen te bepalen en toonden aan dat deze voor de eerste 10 cycli constant was, hierna nam de stabiliteit sterk af doordat de films delamineerden. Daarom werd verwacht dat de intrinsieke (de)hydrogeneringsstabiliteit hoger is. Aangetoond werd dat de plateaudruk van de desorptie-isothermen van Mg_yTi_{1-y} dunne films nagenoeg niet beïnvloed werd door de Mg:Ti ratio en vrijwel gelijk was aan de evenwichtsdruk van het magnesium-waterstof systeem. Impedantiemetingen toonden aan dat de oppervlaktekinetiek volledig kon worden toegeschreven aan de Pd toplaag. De totale kinetische impedantie,

wanneer de Mg_yTi_{1-y} dunne film elektrodes in de waterstofarme toestand waren, werd gedomineerd door de overdracht van waterstof van de Pd naar de Mg_yTi_{1-y} laag.

In hoofdstuk 4 werd beschreven dat de ab/desorptiekinetiek hoogstwaarschijnlijk sterk werd beïnvloed door de symmetrie van het kristalrooster van het waterstofopslagmedium. Het grootste verschil in de (de)hydrogeneringssnelheden werd waargenomen voor Mg_yTi_{1-y} legeringen die 70 tot 90 at.% Mg bevatten. Daarom werd de kristallografie van deze legeringcomposities onderzocht d.m.v. *in situ* röntgendiffractie en de resultaten worden gepresenteerd in hoofdstuk 5. Eerst werden *in situ* gasfase röntgendiffractie experimenten uitgevoerd om de kristalstructuren van de gedeponeerde en hydrogeneerde Mg_yTi_{1-y} legeringen te bepalen. De preferentiële kristalgrafische oriëntatie van de films in zowel de gedeponeerde als de hydrogeneerde toestand bemoeilijkten de onomstotelijke bepaling van de kristalstructuur en daarom werd de identificatie van de symmetrie van de eenheidscellen gedaan d.m.v. het *in situ* opnemen van diffractiepatronen bij verschillende hellingshoeken. De resultaten toonden aan dat een hexagonale dichtgepakte structuur werd gevonden voor alle legeringen in de gedeponeerde toestand. Hydrogeneren van de lagen onder een waterstofdruk van 1 bar transformeerde de eenheidscellen naar kubisch vlakkengecentreerd voor $Mg_{0.70}Ti_{0.30}$ en $Mg_{0.80}Ti_{0.20}$ legeringen, terwijl de eenheidscel van gehydrogeneerd $Mg_{0.90}Ti_{0.10}$ een tetragonale lichaamsgecentreerde symmetrie had. De gecombineerde resultaten van de (de)hydrogeneringskinetiek en de kristalstructuur van de hydrides benadrukten het effect van de symmetrie van het kristalrooster op de waterstoftransporteigenschappen.

Vervolgens werden de experimentele resultaten van *in situ* elektrochemische röntgendiffractie gepresenteerd. Het voornaamste voordeel van elektrochemische controle was de mogelijkheid om de waterstofconcentratie systematisch te verhogen of te verlagen en dit werd in combinatie met diffractieanalysen gebruikt om de effecten van de waterstofconcentratie op de structuur en compositie van de fasen in Mg_yTi_{1-y} dunne film legeringen met y=0.70, 0.80 en 0.90 te bepalen. De diffractiepatronen en elektrochemische resultaten van $Mg_{0.70}Ti_{0.30}$ en $Mg_{0.80}Ti_{0.20}$ wezen op een rooster met duidelijke Ti-arme en Ti-rijke gebieden, terwijl $Mg_{0.90}Ti_{0.10}$ de eigenschappen toonde van een volledig homogene legering.

In de zoektocht naar waterstofopslagmaterialen met een hoge gravimetrische capaciteit vormen Mg_yTi_{1-y} legeringen, die volgens de experimentele resultaten gepresenteerd in hoofdstuk 4 uitstekende kinetische ab- en desorptie-eigenschappen bezitten, de basis voor meer geavanceerde verbindingen. De plateaudruk van het Mg-Ti hydride systeem is erg laag (ongeveer 10^{-6} bar bij kamertemperatuur). Een manier om deze druk te verhogen was door het metaalhydride te destabiliseren en dit kon worden bewerkstelligd door de toevoeging van een additioneel element in het binaire Mg-Ti systeem. Volgens Van Mal's regel van omgekeerde stabiliteit zou elk additioneel element dat een stabiliserend effect op de metallische legering had het metaal-waterstof systeem moeten destabiliseren. Een model om het effect van het legeren van elementen op de thermodynamische stabiliteit te berekenen was ontwikkeld door Miedema en medewerkers. Toepassen van dit model bood de mogelijkheid om veelbelovende elementen op voorhand te selecteren. Aluminium en silicium wedren zodoende geselecteerd om het Mg-Ti systeem te stabiliseren. De elektrochemische galvanostatische intermitterende titratie techniek werd gebruikt om druk-compositie

isothermen van deze nieuwe ternaire materialen te bepalen. In overeenstemming met de berekeningen schoof de plateaudruk van een aanzienlijk deel van de isotherm naar hoge drukken bij kamertemperatuur door substitutie van Mg en Ti door Al of Si. Bovendien heeft een gedeelte van de ternaire legeringen een reversibele waterstofopslagcapaciteit die de eis voor de minimale gravimetrische capaciteit overschrijdt. Tenslotte werd aangetoond dat door het beïnvloeden van de chemie van de metaallegering de thermodynamische eigenschappen van Mg-gebaseerde hydrides over een groot gebied gereguleerd konden worden. De mogelijkheid om de waterstofpartiaaldruk te verhogen, terwijl een hoge gravimetrische capaciteit wordt behouden biedt veelbelovende perspectieven op het gebied van waterstofopslagmaterialen die noodzakelijk zijn voor het realiseren van de waterstofeconomie.

List of publications

Publications related to this thesis

1. R.A.H. Niessen, P. Vermeulen and P.H.L. Notten, *The electrochemistry of Pd-coated $Mg_ySc_{(1-y)}$ thin film electrodes: A thermodynamic and kinetic study*, Electrochim. Acta, **2005**, *51*, 2427-2436.

2. P. Vermeulen, R.A.H. Niessen and P.H.L. Notten, *Hydrogen storage in metastable $Mg_yTi_{(1-y)}$ thin films*, Electrochem. Comm. **2006**, *8*, 27-32.

3. P. Vermeulen, R.A.H. Niessen, D.M. Borsa, B. Dam, R. Griessen and P.H.L. Notten, *Effect of the deposition technique on the metallurgy and hydrogen storage characteristics of metastable $Mg_yTi_{(1-y)}$ thin films*, Electrochem. Solid-State Lett. **2006**, *9*, A520-A523.

4. D.M. Borsa, A. Baldi, M. Pasturel, H. Schreuders, B. Dam, R. Griessen, P. Vermeulen and P.H.L. Notten, *Mg-Ti-H thin films for smart solar collectors*, *Appl. Phys. Lett.* **2006**, *88*, 241910/(1-3).

5. P. Vermeulen, O. Lyedovskykh, D. Danilov and P.H.L. Notten, *The impact of the layer thickness on the thermodynamic properties of Pd hydride thin film electrodes*, J. Phys. Chem. B **2006**, *110*, 20350-20353..

6. D.M. Borsa, R. Gremaud, A. Baldi, H. Schreuders, J.H. Rector, B. Kooi, P. Vermeulen, P.H.L. Notten, B. Dam and R. Griessen, *Structural, optical, and electrical properties of $Mg_yTi_{1-y}H_x$ thin films*, Phys. Rev. B **2007**, *75*, 205408/(1-9).

7. W.P. Kalisvaart, P. Vermeulen, O. Lyedovskykh, D. Danilov and P.H.L. Notten, *The electrochemistry and modelling of hydrogen storage materials*, J. Alloys Compd. **2007**, *446*, 648-654.

8. P. Vermeulen, E.F.M.J. van Thiel and P.H.L. Notten, *Ternary MgTiX-alloys: A promising route towards low temperature, high capacity, hydrogen storage materials*, Chem. Eur. J. **2007**, *13*, 9892-9898.

9. P. Vermeulen, P.C.J. Graat, H.J. Wondergem and P.H.L. Notten, *Crystal structures of Mg_yTi_{100-y} thin film alloys in the as-deposited and hydrogenated state*, Int. J. Hydrogen Energy **2008**, 33, 5646-5650.

10. P. Vermeulen, H.J. Wondergem, P.C.J. Graat, D.M. Borsa, H. Schreuders, B. Dam, R. Griessen and P.H.L. Notten, *In situ electrochemical XRD study of (de)hydrogenation of Mg_yTi_{100-y} thin films*, J. Mater. Chem. **2008**, *18*, 3680-3687.

11. A. Ledovskikh, D. Danilov, P. Vermeulen and P.H.L. Notten, *Electrochemical modeling of hydrogen storage in hydride-forming electrodes*, Electrochem. Acta **2008**, submitted.

12. P. Vermeulen, A. Ledovskikh, D. Danilov and P.H.L. Notten, *Thermodynamics and kinetics of the magnesium-hydrogen system*, Acta Mater. **2008**, submitted.

13. A. Ledovskikh, D. Danilov, P. Vermeulen and P.H.L. Notten, *Surface kinetic effects of hydrogen storage: Complete electrochemical kinetic model*, in preparation.

Other publication

14. P.S. Peijzel, P. Vermeulen, W.J.M. Schrama, A. Meijerink, M.F. Reid, G.W. Burdick, *High-resolution measurements of the vacuum ultraviolet energy levels of trivalent gadolinium by excited state excitation*, Phys. Rev. B **2005**, *71*, 125126.

Intellectual property

15. E.M.F.J. van Thiel, P.H.L. Notten and P. Vermeulen, *Hydrogen storage material for use in electronic equipment, comprises magnesium alloy, transition element, and element with hydride heat of formation higher than magnesium hydride*, Patent Nr. WO2008035310-A1, **2007**.

Curriculum Vitae

Paul Vermeulen werd geboren op 16 december 1980 te Eindhoven. Na het behalen van het HAVO diploma aan het Eckart College te Eindhoven in het jaar 1998 vervolgde hij met een HLO studie aan Fontys Hogescholen te Eindhoven. Na het afronden van deze studie startte hij op 1 september 2002 met de Master "Chemistry and Physics" aan de Universiteit Utrecht. Daar specialiseerde hij zich in het in kaart brengen van de hogere energieniveaus van gadolinium. Het doctoraal diploma werd in juni 2004 behaald (with honours).

Met ingang van 1 oktober 2004 werkte hij als promovendus in de sectie "Energy Materials and Devices" binnen de vakgroep "Anorganische Chemie en Katalyse" aan de Scheikunde Technologie faculteit van de Technische Universiteit Eindhoven. Hij verrichtte daar onderzoek naar de waterstofopslageigenschappen van interstitiële metaalhydrides in dunne film vorm. Elektrochemie werd hierbij als voornaamste karakteriseringtechniek gebruikt om de potentie van nieuwe waterstofopslagmaterialen te bepalen. De combinatie van standaard elektrochemische meetmethoden en andere analysetechnieken, waaronder impedantiespectroscopie en röntgendiffractie, werd gebruikt om diepgaande kennis over de effecten van de waterstofconcentratie op het waterstofopslagmedium te vergaren. Een aanzienlijk deel van zijn promotieonderzoek heeft hij doorgebracht bij Philips Research Laboratories te Eindhoven, waar hij de mogelijkheid kreeg om dunne films te prepareren en te karakteriseren. De resultaten van het uitgevoerde onderzoek beschreven in dit proefschrift zijn gepubliceerd in een aantal wetenschappelijke publicaties en hebben geleid tot een patent. Naast schriftelijke output heeft hij zijn resultaten gepresenteerd op enkele conferenties: 'MRS 2006' in San Francisco, Californië, 'Gordon conference 2007' in Waterville, Maine (financiering mede mogelijk gemaakt door een zogenaamde "Young scientist award" beschikbaar gesteld door General Motors Corp.) en 'MH2008' in Reykjavik, IJsland.

Naast het verrichten van onderzoek, heeft hij de mogelijkheid gekregen zijn praktische kennis over impedantiespectroscopie over te dragen op studenten d.m.v. een gastcollege binnen het keuzevak Elektrochemie. Tevens heeft hij meerdere bijvak- en hoofdvakstudenten begeleid en als contactpersoon voor energiegerelateerde multidisciplinaire projecten gefungeerd. In 2007 heeft hij aan de summerschool "Instrumental Methods in Electrochemistry" aan de Universiteit van Southampton deelgenomen.

Dankwoord

Allereerst wil ik Peter Notten bedanken voor het vervullen van zijn taak als eerste promotor. Jouw enthousiasme, kennis en hulpvaardigheid zijn onlosmakelijk verbonden met het positief afronden van mijn promotie. De mogelijkheden die je mij hebt gegeven om gebruik te maken van de faciliteiten bij Philips Research hebben overduidelijk bijgedragen aan de verscheidenheid aan analysetechnieken die ik gebruikt heb om de materialen te karakteriseren. Tevens wil ik co-promotor Bert Hintzen bedanken voor het lezen en corrigeren van verscheidende manuscripten. De daaruit voortvloeiende discussies zijn uitermate waardevol geweest. Ook ben ik je dankbaar voor de fijne sfeer binnen de sectie en de kans die je me gegeven hebt om mijn theoretische maar vooral praktische kennis van complexe elektrochemische impedantiespectroscopie binnen het vak “Electrochemistry” over te dragen.

Emile van Thiel wil ik bedanken voor het opdampen van de metaallegeringen, zelfs als dit betekende dat je een uurtje eerder moest beginnen. Hoewel het opdampen van een ternaire metaallegering door sommigen werd afgeraden, heb je toch doorgezet, hetgeen de basis was voor een publicatie en een patent.

Röntgendiffractie is de analysetechniek bij uitstek om de verschillende fasen en de kristalstructuren van de dunne films te karakteriseren. De professionele hulp van Harry Wondergem, Peter Graat en Renee Bakker zijn hierbij onontbeerlijk geweest.

De compositie en de homogeniteit van de Mg-gebaseerde dunne films zijn standaard gecontroleerd met Rutherford Backscattering Spectroscopy. Het deskundige werk van Peer Zalm, Thuy Dao en Yde Tamminga ligt hieraan ten grondslag.

Rogier Niessen wil ik bedanken voor de begeleiding tijdens mijn beginperiode. Vlak voor het einde van jouw promotieonderzoek kwam je met magnesium-titaan legeringen op de proppen. Dit gaf mij een vliegende start om, als functie van de compositie, de waterstofopslageigenschappen systematisch te onderzoeken.

Tijdens mijn promotieonderzoek heb ik bijzonder prettig samengewerkt met de medewerkers van de vakgroep “Condensed Matter Physics” aan de Vrije Universiteit van Amsterdam onder leiding van Ronald Griessen, waarvoor mijn oprechte dank.

Mijn collega’s binnen de sectie “Energy Materials and Devices” wil ik bedanken voor de prettige promotietijd: Thijs, Alexander, Dmitry, Peter K., Jos, Loïc, Frank, Merijn, Jiang, Tom, Peter V., Van-Ahn, Anneke, Marcel, Ad, Gabi, Ilkin, Shu Xia, Pieter, Harrison en Kaushik. Voor de fijne sfeer binnen de vakgroep SKA wil ik alle medewerkers bedanken. In het bijzonder wil ik vermelden: Jos, Michèle, Emiel, Gilbère, Jarno, Tiny, Freek, Patrick, Arjan, Katharina, Ojwang, Evgeny, Mathijs, Gijsbert, Bart, Erik, Christian, Laura en Leandra.

Tijdens mijn promotie heb ik het genoegen gehad studenten te mogen begeleiden. Peter van Delft, Romain Metaye, Jan van Kemenade, Gerrit Sitters en Matthijs Cox wil ik dan ook graag bedanken voor hun inzet.

Ontspanning is naast het drukke promotiebestaan zeer belangrijk, ook al is het soms moeilijk om de pen neer te leggen en op een andere manier van het leven te genieten. Mijn vrienden spelen hierin een centrale rol. In het bijzonder wil ik hiervoor de volgende personen bedanken (in willekeurige volgorde): Kasper, Yvonne, Peter, Dana, Jeroen, Floor, Roel, Imke, Milan, Chantal, Matthijs, Deborah, Rob, Niek, Johan en Manoelle. Verder mogen

Gerrie, Andy, Marvin, Ilonka, Lindsay, Kevin, Johan, Angelique en Harry niet onvermeld blijven en dank ik hen voor de gezellige dartavonden die altijd met een rode pen omcirkelt in mijn agenda stonden.

Familie is gebleken een belangrijke en constante factor te zijn om het werk als promovendus en de daarbij komende frustraties te bespreken. Mijn vader (tevens de drukker van dit proefschrift), moeder en broer wil ik dan ook bedanken voor het bieden van een luisterend oor, hulpvaardigheid, interesse en steun. Mijn vriendin Marieke wil ik uiteindelijk bedanken voor de steun, liefde en de mogelijkheid om na even lekker uitgewaaid te zijn met Dommel er weer fris tegenaan te kunnen.